LEABHARLANN CHOLÁISTE NA TRÍONÓIDE, BAILE ÁTHA CLIATH | TRINITY COLLEGE LIBRARY DUBLIN
Ollscoil Átha Cliath | The University of Dublin

Terms and Conditions of Use of Digitised Theses from Trinity College Library Dublin

Copyright statement

All material supplied by Trinity College Library is protected by copyright (under the Copyright and Related Rights Act, 2000 as amended) and other relevant Intellectual Property Rights. By accessing and using a Digitised Thesis from Trinity College Library you acknowledge that all Intellectual Property Rights in any Works supplied are the sole and exclusive property of the copyright and/or other IPR holder. Specific copyright holders may not be explicitly identified. Use of materials from other sources within a thesis should not be construed as a claim over them.

A non-exclusive, non-transferable licence is hereby granted to those using or reproducing, in whole or in part, the material for valid purposes, providing the copyright owners are acknowledged using the normal conventions. Where specific permission to use material is required, this is identified and such permission must be sought from the copyright holder or agency cited.

Liability statement

By using a Digitised Thesis, I accept that Trinity College Dublin bears no legal responsibility for the accuracy, legality or comprehensiveness of materials contained within the thesis, and that Trinity College Dublin accepts no liability for indirect, consequential, or incidental, damages or losses arising from use of the thesis for whatever reason. Information located in a thesis may be subject to specific use constraints, details of which may not be explicitly described. It is the responsibility of potential and actual users to be aware of such constraints and to abide by them. By making use of material from a digitised thesis, you accept these copyright and disclaimer provisions. Where it is brought to the attention of Trinity College Library that there may be a breach of copyright or other restraint, it is the policy to withdraw or take down access to a thesis while the issue is being resolved.

Access Agreement

By using a Digitised Thesis from Trinity College Library you are bound by the following Terms & Conditions. Please read them carefully.

I have read and I understand the following statement: All material supplied via a Digitised Thesis from Trinity College Library is protected by copyright and other intellectual property rights, and duplication or sale of all or part of any of a thesis is not permitted, except that material may be duplicated by you for your research use or for educational purposes in electronic or print form providing the copyright owners are acknowledged using the normal conventions. You must obtain permission for any other use. Electronic or print copies may not be offered, whether for sale or otherwise to anyone. This copy has been supplied on the understanding that it is copyright material and that no quotation from the thesis may be published without proper acknowledgement.

Biogeochemical Patterns During Cold-Water Coral Growth and Their Potential Application for Environmental Interpretation



Alexandra Oppelt

A Thesis submitted to the University of Dublin, Trinity College,
for the Degree of Doctor of Philosophy

TRINITY COLLEGE DUBLIN
8 JUN 2016
ACADEMIC REGISTRY

School of Natural Sciences
Discipline of Geography
Biogeochemistry Research Group

The University of Dublin
Trinity College

PhD
Natural Sciences

May 2016

50690578
50690578

THESIS
11302

TRINITY LIBRARY
0 8 MAR 2017
DUBLIN

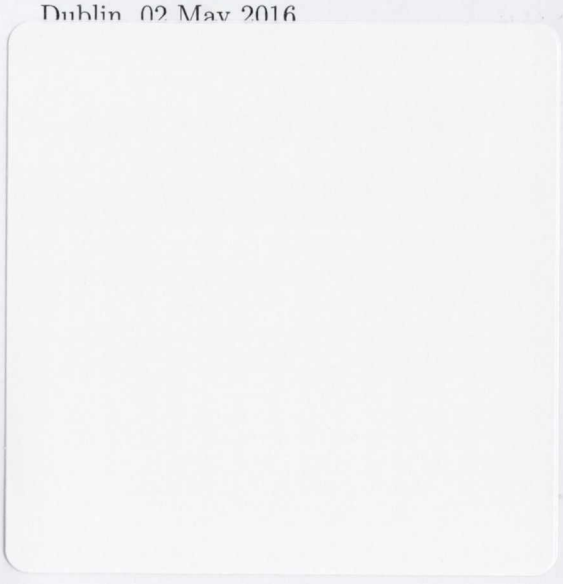
Thesis 11302

Declaration

I declare that this thesis has not been submitted as an exercise for a degree at this or any other university and it is entirely my own work.

I agree to deposit this thesis in the University's open access institutional repository or allow the library to do so on my behalf, subject to Irish Copyright Legislation and Trinity College Library conditions of use and acknowledgment.

Dublin, 02 May 2016



Summary

In the light of changing marine environments as a consequence of climatic shifts it is essential to gain a better understanding of such vulnerable habitats especially when they are located out of sight in the deep sea. The aragonitic skeletons of colonial scleractinian cold-water corals offer a unique opportunity to learn more about remote ocean areas and climate-driving current systems. A detailed study on biomineralisation to decode the information in these $CaCO_3$-based recording units is therefore essential.

A selection of three scleractinian species most common above 1,000 m depth in the NE Atlantic was studied here to deliver additional insight and new tools to extent our understanding. The presented thesis successfully applied major, minor and trace element analysis to show variations in the geochemical composition of coral skeletons in association with microstructure and growth. This correlation and association is shown in detail for the aragonitic skeletons of scleractinian species *Lophelia pertusa* and *Madrepora oculata*. The study highlights small-scale variations in geochemical composition in association with microstructures along the precipitation of a complete *Lophelia pertusa* theca combining two dimensions of growth. A selection of analysed elements suggested ^{238}U (in antithetical correlation with ^{25}Mg) to be the most reliable indicator of periods of low growth rate. The same methods was applied to highlight growth patterns along corallite and branch growth of *Madrepora oculata*, a species so far neglected in environmental studies. The resulting image of growth shows a strong focus on branch thickening which seems to take up most of the growth process and therefore provides the best basis to locate environmental information. Two different and well-classified CWC habitats were compared to the geochemically recorded signals to show a potential characterisation of oceanographic influences on coral growth. The results suggest a method to detect relative local differences in current systems and nutrient supply (here represented by nepheloid layers). All results emphasise the potential for a relative environmental reconstruction while the reconstruction of absolute values of environmental parameters (like temperature or salinity) appears inaccurate so far using the applied methods.

Finally a novel approach focuses on the contact region of corallite and calcified polychaete tube for a comparison of patterns in microstructure and geochemistry and reveals high similarities between both areas and a direct connection in the form of shared layers. The absence of differences between the regions suggests a common calcification mechanism which in turn, based on previous research, suggests mucus as a major part of the calcifying medium.

This provides a new perspective for a discussion of calcification mechanisms and ties in with earlier mentioned observations on skeletal precipitates. A model like this also has implications for the carbon and nutrient cycle in the deep sea since mucus is an important contributor.

Acknowledgements

The presented research was undertaken as part of the Earth and Natural Science Doctoral Studies Programme (ENS). The Earth and Natural Science Doctoral Studies Programme is funded by the Higher Education Authority (HEA) through the Programme for Research at Third Level Institutions, Cycle 5 (PRTLI-5) and is co-funded by the European Regional Development Fund (ERDF). Part of this research was carried out under the Sea Change strategy with the support of the Marine Institute and the Marine Research Subprogramme of the National Development Plan 2007-2013. All I would also like to thank master and crew of the RV Celtic Explorer (cruise CE11006, CE12006, CE13008, CE14009), Chief Scientists Dr. Mark Johnson and Dr. Louise Allcock and the ROV pilots for their amazing support and team work.

All used *Holland I* ROV images captured during the research cruises are subject to the following image data policy and copyright agreement: *The Marine Institute (MI) and NUI Galway (NUIG) shall each retain copies of all images (still and video) captured using the ROV (Holland I) during the course of the Survey. The MI shall retain exclusive ownership of such images and controls all rights or copyright with regards commercial use. The MI shall provide royalty-free rights to the grantee to reproduce the material, or portions thereof, in connection with their research and promotion of their activity, in perpetuity. All uses of the images, or portions thereof, by any party shall acknowledge: here: (i) ownership of the images: Marine Institute; (ii) the originator of the images: NUI Galway; (iii) the source of funding provided for the survey: Marine Institute and Marine Research subprogramme of the National Development Plan 2007-2013 (see above).*

I would like to thank my supervisor Prof. Carlos Rocha and the Biogeochemistry Research Group for fruitful discussions and support all through the project. Special thanks to Prof. Balz Kamber for his support with LA-Q-ICP-MS analysis and for his comments and discussion to help improve the work. I would like to thank Matthias López Correa (Friedrich-Alexander-Universität Erlangen-Nürnberg) for his help, collaboration in stable isotope ratio analysis, discussions and access to sample material, and Prof. Michael Joachimski (GeoZentrum Nordbayern), Dr. Robbie Goodhue (Trinity College Dublin) and Dr. Kai Knöller (Helmholtz-Zentrum für Umweltforschung, Halle) for help with stable isotope ratio analysis. I would like to thank Vincent Mouchi (Trinity College Dublin) for running XRD tests on some of my samples and for collaboration and support over the years, Annette Wilson (National University of Ireland Galway) for providing the processed CTD data for ROV dives, and Helka Folch (Marine Institute) for access to the archived cruise materials. I would also like to thank Niall McGinty for discussions on statistics and R, Aristodemo 'Mino' Vitelli for hours of photo sessions with my corals, and Friederike Wetter, Andrea Nachtigall, Shane McGuiness and Mark Johnson for proof reading, feedback and layout advice. I would also like to thank my examiners Dr. Louise Allcock and Dr. Quentin Crowley for fruitful discussions during my viva and for comments to help improve the thesis.

I would like to thank my family and friends for their patience and support during the last four years of putting together this thesis. The work would have never been possible without you. You were there during hard times and gave me the strength to overcome the obstacles. Special thanks goes to Jørgen Fulsebakke for always believing

in me, for endless proof reading, discussions and advice, and music. To Ana Alonso for being my personal 'life coach' during stressful situations. And to Andrea Nachtigall and Steffen Macy Friedersdorf for being there when I needed to talk and for keeping me grounded. To my sister Martina Oppelt for her neverending support and for never doubting the path I chose.

I dedicate this work to those who touched my life but are not here anymore. You all left an impression. And to my two wonderful nieces, Jule and Karlie, who joined during the last years and are the light in my life. Last but not least to the corals that died for the research.

Contents

I Introduction 1

1 Research Aim and Relevance 3
- 1.1 Contextual Overview . . . 3
- 1.2 Research Aims and Proposed Methodology . . . 6
- 1.3 Thesis Organisation . . . 7

2 Literature Review 9
- 2.1 Biology of Cold-Water Corals (CWCs) . . . 9
  - 2.1.1 Selection of Common Scleractinian Species in the NE Atlantic . 9
  - 2.1.2 Feeding Habits . . . 19
  - 2.1.3 Reproduction Strategies and Connectivity of CWCs . . . 20
  - 2.1.4 The Role of Mucus . . . 21
  - 2.1.5 Symbiosis with the Polychaete *Eunice norvegica* . . . 22
  - 2.1.6 Limiting Factors of CWC Occurrence . . . 23
  - 2.1.7 CWC Habitat Mapping and Modelling . . . 25
- 2.2 Oceanography of Studied Areas . . . 27
  - 2.2.1 NE Atlantic . . . 27
  - 2.2.2 Mediterranean Sea . . . 30
  - 2.2.3 Indian Ocean . . . 33
- 2.3 Skeletal Formation of Scleractinian CWCs . . . 34
  - 2.3.1 (Micro-)Structural Growth . . . 34
  - 2.3.2 Ultrastructural Growth . . . 38
  - 2.3.3 Models of Coral Biomineralisation and Elemental Incorporation . 40
- 2.4 Biogeochemistry . . . 43
  - 2.4.1 Analytical Techniques - State-of-the-Art . . . 43
  - 2.4.2 Stable Oxygen and Carbon Isotope Ratios . . . 43
  - 2.4.3 Stable Boron Isotope Ratios . . . 46
  - 2.4.4 Trace and Minor Element Concentrations . . . 47

II Material and Methods 53

3 Material 55
- 3.1 Scleractinian Samples . . . 55

4 Methods 57
- 4.1 Field Operations . . . 57
- 4.2 Video Transects and Habitat Classification . . . 58
- 4.3 Sample Preparation . . . 59

4.4 Microscopy 59
4.5 Sampling Strategies for Geochemical Analysis 60
4.5.1 Surface Sampling 60
4.5.2 Microdrill Bulk Sampling 61
4.5.3 Microdrill Line Sampling 61
4.5.4 Laser Ablation *in-situ* Sampling 62
4.6 Analysis 62
4.6.1 Gas Chromatograph Isotope Ratio Mass Spectrometry (GC-IRMS) 62
4.6.2 Laser Ablation Quadropole Inductively Coupled Plasma Mass Spectrometry (LA-Q-ICP-MS) 63
4.7 Data Processing 67

III Results and Discussion **71**

5 CWC Habitats **73**
5.1 Introduction to Canyon Habitats 75
5.1.1 Porcupine Bank 75
5.1.2 Whittard Canyon 76
5.1.3 CTD Data and Scleractinian Occurrences 84
5.2 Discussion 90
5.2.1 Environmental Parameters and Scleractinian Occurrence 90
5.2.2 Testing Existing Habitat Predictions 93
5.2.3 Habitat Geomorphology 94

6 Comparative Study - Different CWC Species **97**
6.1 $\delta^{13}C$ and $\delta^{18}O$ Correlation 98
6.2 Discussion 99

7 Case Study *Lophelia pertusa* **103**
7.1 Patterns in Coral Growth 104
7.1.1 Microstructures 104
7.1.2 $\delta^{18}O$ and $\delta^{13}C$ Analysis along *L. pertusa* Growth 105
7.1.3 Trace and Minor Element Compositions 108
7.2 Discussion 112
7.2.1 Magnesium Incorporation Mechanisms 112
7.2.2 Uranium Incorporation into the Skeleton 113
7.2.3 Geochemistry and Growth Rate 115
7.2.4 Nutrient Availability and Geochemical Signals 117
7.2.5 Growth Details - Individual Corallite 119
7.2.6 Approaches of pH Reconstruction 121

8 Case Study *Madrepora oculata* **123**
8.1 Patterns in Coral Growth 124
8.1.1 Microstructures 124
8.1.2 Trace and Minor Element Compositions 125
8.1.3 Trace and Minor Element Compositions along Branches 128
8.1.4 Discussion - *M. oculata* Growth Patterns 131
8.2 Temperature Reconstruction 135
8.2.1 $\delta^{18}O$ and $\delta^{13}C$ - 'Lines Technique' 135

8.2.2 Li/Mg Ratios 139
8.2.3 Discussion - Temperature Reconstruction 142

9 Case Study *Eunice norvegica* tubes 145
9.1 Microstructures 146
9.2 Patterns in Geochemistry 149
9.2.1 $\delta^{18}O$ and $\delta^{13}C$ Analysis 149
9.2.2 Trace and Minor Element Compositions 149
9.3 Discussion 167
9.3.1 Variations in Geochemical Composition 167
9.3.2 Patterns in Geochemical Compositions and Implications 168
9.3.3 Implications for Biomineralisation Models 169

IV Summary and Conclusion 173

V References 179

VI Appendix 209

A Selected Scleractinians 211
A.1 *Lophelia pertusa* Specimens 212
A.2 *Desmophyllum dianthus* Specimens 214
A.3 *Solenosmilia variabilis* Specimens 216
A.4 *Madrepora oculata* Specimens 218
A.5 *Enallopsammia rostrata* Specimens 219

B *M. oculata* Branch Cross Sections 221

C Initial Tests for LA-ICP-MS 223
C.1 Specifying Spotsize and Scan Speed 223
C.2 Testing Potential Nutrient Proxies 226

D Additional Information LA-ICP-MS 229
D.1 Interference in Calcium Concentrations 229
D.2 Experiments corresponding with different chapters 229
D.3 Signal-Noise-Ratios (SNRs) 230

E Cellspace Images 237
E.1 Cellspace Images *Lophelia pertusa* L1 237
E.2 Cellspace Images *Madrepora oculata* Single Corallite 239
E.3 Cellspace Images *Madrepora oculata* Branches 240
E.4 Cellspace Images *Eunice norvegica* Tubes 248

List of Figures

1.1 MPAs in the NE Atlantic 4

2.1 Structural features of corals (Cairns & Kitahara, 2012) 10
2.2 Overview over polyp and corallum 11
2.3 *Lophelia pertusa* 12
2.4 *Lophelia pertusa* environment 12
2.5 *Madrepora oculata* 14
2.6 *Madrepora oculata* environment 14
2.7 *Desmophyllum dianthus* 15
2.8 *Desmophyllum dianthus* environment 15
2.9 *Solenosmilia variabilis* 16
2.10 *Solenosmilia variabilis* environment 17
2.11 *Enallopsammia rostrata* 18
2.12 *Enallopsammia rostrata* environment 18
2.13 CWC occurrence in the Guilvinec Canyon 26
2.14 NE Atlantic current patterns (Buhl-Mortensen et al., 2014) 27
2.15 NE Atlantic currents (Dullo et al., 2008) 28
2.16 Whittard Canyon CWC occurrence (Huvenne et al., 2011) 29
2.17 Characterisation of water masses in the Whittard Canyon (Wilson et al., 2015) 30
2.18 Currents in the Mediterranean Sea (Freiwald et al., 2009) 31
2.19 Water masses of the Mediterranean Sea (Astraldi et al., 2002) 32
2.20 Water masses of the South Indian Ocean (Park et al., 1991) 33
2.21 Growth layer development (Mortensen & Rapp, 1998) 35
2.22 Corallite growth patterns *L. pertusa* L1 35
2.23 Growth layer formation model (Cuif & Dauphin, 2005) 39
2.24 Calcification model (McConnaughey et al., 1997) 41
2.25 Amorphous calcium carbonate model (Rollion-Bard et al., 2010) 41
2.26 Linear regression $\delta^{13}C/\delta^{18}O$ model 44
2.27 Lines technique connected to temperature regimes (Smith et al., 2000) . 45
2.28 Li/Mg-T reconstruction 48

4.1 Cross section orientation 60
4.2 Sampling strategy - surface samples 60
4.3 Sampling strategy - individual layers 61
4.4 Sampling strategy - microdrill lines 61

5.1 Map: ROV dives along the Irish shelf 73
5.2 Overview over ROV dives in the Whittard Canyon 76
5.3 ROV track CE13008 - event 39 77

5.4 ROV track CE13008 - event 52 . . . 77
5.5 ROV track CE13008 - event 76 . . . 78
5.6 ROV track CE14009 - event 7 . . . 79
5.7 ROV track CE14009 - event 9 . . . 80
5.8 ROV track CE13008 - event 62 . . . 80
5.9 ROV track CE14009 - event 12 . . . 81
5.10 ROV track CE14009 - event 31 . . . 82
5.11 ROV track CE14009 - event 5 . . . 83
5.12 Images canyon habitats . . . 85
5.13 CWC occurrence event 7 (PB) . . . 86
5.14 CWC occurrence event 25 (PB) . . . 86
5.15 CWC occurrence event 39 (WC) . . . 87
5.16 CWC occurrence event 39 (WC) temporal variations . . . 87
5.17 CWC occurrence event 52 (WC) . . . 88
5.18 CWC occurrence event 76 (WC) . . . 88
5.19 CWC occurrence event 7 and 9 (WC) . . . 88
5.20 CWC occurrence event 62 (WC) . . . 89
5.21 CWC occurrence event 12 (WC) . . . 89
5.22 CWC occurrence event 25 (WC) . . . 89
5.23 CWC occurrence event 5 (WC) . . . 90
5.24 Comparison *L. pertusa-S. variabilis* occurrence . . . 91
5.25 Model predictions (Rengstorf et al., 2013) in comparison . . . 93
5.26 Deep sea ridges (Correa et al., 2012) . . . 94

6.1 Map: Whittard Canyon different species . . . 98
6.2 Regression lines for different species in the Whittard Canyon . . . 99
6.3 Regression lines *M. oculata* and *D. dianthus* . . . 100
6.4 Variations in regression lines of *D. dianthus* . . . 101

7.1 Map: L1 sampling location . . . 103
7.2 *Lophelia pertusa* under reflected light . . . 104
7.3 *Lophelia pertusa* under transmitted light . . . 105
7.4 Stable carbon isotope ratios in L1 . . . 106
7.5 Stable oxygen isotope ratios in L1 . . . 107
7.6 Correlation ^{25}Mg-^{238}U . . . 109
7.7 Microstructures and ^{238}U, ^{25}Mg and ^{137}Ba . . . 111
7.8 Boron isotope ratios . . . 112
7.9 Energy budget . . . 118
7.10 Linear and radial extension in L1 . . . 120

8.1 *Madrepora oculata* 459-M1 microstructures . . . 124
8.2 *Madrepora oculata* 1009 microstructures . . . 125
8.3 *M. oculata* (459-M1) thecal variations . . . 127
8.4 *M. oculata* (459-M1) branch elemental variations . . . 129
8.5 *M. oculata* (1009) branch elemental variations . . . 130
8.6 *M. oculata* calcification model . . . 132
8.7 *M. oculata* regression layer thickness . . . 133
8.8 Map: Different *M. oculata* sampling locations . . . 135
8.9 Stable isotope ratios variations along *M. oculata* growth . . . 136
8.10 Stable isotope regression lines *M. oculata* . . . 137

8.11 *Madrepora oculata* samples from different locations in comparison 138
8.12 Li/Mg variations for different parameters 140
8.13 ^{7}Li, ^{25}Mg and $^{7}Li/^{25}Mg$ 141
8.14 $^{7}Li/^{25}Mg$ ratios for different locations 141
8.15 $^{7}Li/^{25}Mg$ ratios compared to literature 142

9.1 Map: *E. norvegica* sample locations 145
9.2 Thin section of 1447-E 147
9.3 Thin sections of 459-M1-E and 459-M2-E 147
9.4 Thin section of 1036-E 148
9.5 Thin section of 1587-E 148
9.6 Tube contact in 459-M1-E 151
9.7 Tube contact in 459-M2-E 152
9.8 Mg-U transects in 459-M1-E 153
9.9 Mg-U transects in 459-M2-E 154
9.10 Tube contact in 1009-E 156
9.11 Mg-U transects in 1009-E 157
9.12 Tube contact in 1033-E 158
9.13 Mg-U transects in 1033-E 159
9.14 Tube contact in 1036-E 161
9.15 Mg-U transects in 1036-E 162
9.16 Tube contact in 1447-E 163
9.17 Mg-U transects in 1447-E 164
9.18 Tube contact in 1587-E 165
9.19 Mg-U transects in 1587-E 166
9.20 Mucus-mediated calcification model 170
9.21 Ridged surface of *M. oculata* 171
9.22 Encalcified CWCs 171
9.23 Ridged surface of tube openings 172

A.1 Plate *L. pertusa* specimens 213
A.2 Plate *D. dianthus* specimens 215
A.3 Plate *S. variabilis* specimens 217
A.4 Plate *M. oculata* specimens 218
A.5 Plate *E. rostrata* specimens 219

B.1 *M. oculata* branch cross sections 221
B.2 *M. oculata* samples - different locations 222

C.1 Initial test 1 - ^{238}U, ^{25}Mg, ^{137}Ba 225
C.2 Initial test 4 - ^{25}Mg, ^{238}U, ^{55}Mn, ^{31}P 226
C.3 Initial test 5 - ^{25}Mg, ^{238}U, ^{137}Ba, ^{111}Cd, ^{66}Zn 227
C.4 Initial test 6 - ^{25}Mg, ^{238}U, ^{51}V, ^{57}Fe, ^{63}Cu 227

E.1 Cellspace images L1-a 237
E.2 Cellspace images L1-a 238
E.3 Boron isotope ratios 238
E.4 Cellspace images M1 239
E.5 Cellspace images 1009-1 branch 240
E.6 Cellspace images 1009-2 branch 241
E.7 Cellspace images 1009-3 branch 242

E.8 Cellspace images 1009-4 & 5 branch 243
E.9 Cellspace images 459-M1-1 & 2 branch 244
E.10 Cellspace images 459-M1-3 branch 245
E.11 Cellspace images 459-M1-4 branch 246
E.12 Cellspace images 459-M1-5 branch 247
E.13 Cellspace images 459-M1-E a 248
E.14 Cellspace images 459-M1-E b 249
E.15 Cellspace images 459-M1-E c 250
E.16 Cellspace images 459-M1-E d 250
E.17 Cellspace images 459-M2-E a 251
E.18 Cellspace images 459-M2-E b 252
E.19 Cellspace images 1009-E a 253
E.20 Cellspace images 1009-E b 254
E.21 Cellspace images 1033-E 255
E.22 Cellspace images 1036-E 256
E.23 Cellspace images 1447-E 257
E.24 Cellspace images 1587-E 258

List of Tables

2.1 Taxon tree of Hexacorallia 9
2.2 Depth ranges of scleractinian 23
2.3 *Lophelia pertusa* tolerance range environmental parameters 24
2.4 CWC extension rates 36
2.6 CWC accumulated extension rates 37
2.8 Structural feature descriptions 38
2.9 Analytical techniques 43

3.1 List of PB and WC samples 56

4.1 List of ROV dives 58
4.2 List of thin sections 60
4.3 Laboratory standards SIA 63
4.4 Results of LA-ICP-MS initial tests 64
4.5 Fluence, energy and gas flow 64
4.6 LA-ICP-MS experiment parameters 65
4.7 Accepted elemental concentrations of NIST analysis 68
4.8 Polyatomic interferences in ICP-MS 68
4.9 Signal-Noise-Ratio Categories 69

5.1 Analysed ROV dives 74
5.2 List of discussed CTD casts 84
5.3 Environmental parameters of CWC occurrence in study area 92
5.4 Combined environmental parameters of CWC occurrence in study area . 92

6.1 Stable isotope ratios for different species in the Whittard Canyon 98
6.2 Regression lines and T reconstruction 100

7.1 Stable isotope ratios in *L. pertusa* L1 105
7.2 Trace and minor element compositions in NIST612 108
7.3 Trace and minor element compositions in L1 108
7.4 NIST612 boron concentration 108
7.5 Boron compositions in L1 108
7.6 Growth phase lengths in *L. pertusa* L1 119

8.1 Precision & accuracy NIST612 (459-M1 corallite) 126
8.2 Trace and minor element compositions in 459-M1 corallite 126
8.3 Precision & accuracy NIST612 (459-M1 branch analysis) 128
8.4 Trace and minor element compositions in 459-M1 branch 128
8.5 Precision & accuracy NIST612 (1009 branch analysis) 128

8.6 Trace and minor element compositions in 1009 branch 131
8.7 *Madrepora oculata* layer succession model 132
8.8 SIA in *M. oculata* from different locations 137
8.9 *Madrepora oculata* temperature reconstruction 139
8.10 Li/Mg - parameter determination 139
8.11 *Madrepora oculata* $^{7}Li/^{25}Mg$ 141
8.12 Li/Mg methods 142

9.1 Sample list polychaete tubes 146
9.2 Precision & accuracy NIST612 (459-M1-E) 150
9.3 Trace and minor element compositions in 459-M1-E 150
9.4 Precision & accuracy NIST612 (459-M2-E) 152
9.5 Trace and minor element compositions in 459-M2-E 152
9.6 Precision & accuracy NIST612 (1009-E) 155
9.7 Trace and minor element compositions in 1009-E 155
9.8 Precision & accuracy NIST612 (1033-E) 158
9.9 Trace and minor element compositions in 1033-E 158
9.10 Precision & accuracy NIST612 (1036-E) 160
9.11 Trace and minor element compositions in 1036-E 160
9.12 Precision & accuracy NIST612 (1447-E) 163
9.13 Trace and minor element compositions in 1447-E 163
9.14 Precision & accuracy NIST612 (1587-E) 167
9.15 Trace and minor element compositions in 1587-E 167

C.1 Initial test 1 - spotsize & scan speed 223
C.2 Initial tests 2 & 3 - spotsize & scan speed 223
C.3 Initial tests - nutrient proxies 226

D.1 Thesis chapters and corresponding LA-Q-ICP-MS experiments 229
D.2 Signal-Noise-Ratios (SNRs) 230

List of Acronyms and Abbreviations

AADW	Antarctic Deep Water
ACC	Amorphous Calcium Carbonate
ADW	Adriatic Dense Water
ASH	Aragonitic Saturation Horizon
BNL	Benthic Nepheloid Layer
Chl α	Chlorophyll α
CoC	Centers of Calcification
CoM	Common Water
CTD	Conductivity-Temperature-Depth
CWC	Cold-Water Corals
DIC	Dissolved Inorganic Carbon
DRS	Data Reduction Scheme
ECF	Extracytoplasmic Calcifying Fluid, Extracytosolic Calcifying Fluid
EMDW	Eastern Mediterranean Deep Water
EMZ	Early Mineralization Zone
ENAW	East North Atlantic Water
ENFA	Ecological Niche Factor Analysis
FAU	Friedrich-Alexander-Universität
HNLC	High Nitrate Low Chlorophyll
ICP-MS	Inductively Coupled Plasma Mass Spectrometry
INL	Intermediate Nepheloid Water
IpHRAC	Internal pH Regulation Abiotic Calcification
IRMS	Isotope Ratio Mass Spectrometry
LA-ICP-MS	Laser Ablation Inductively Coupled Plasma Mass Spectrometry
LOD	Limits of Detection
LIW	Levantine Intermediate Water
LSW	Labrador Sea Water
MAW	Modified Atlantic Water
MC-IRMS	Multi-Collector Isotope-Ratio Mass Spectrometry
MOW	Mediterranean Outflow Water
MAS NMR	Magnetic Angle Spinning Nuclear Magnetic Resonance
NADW	North Atlantic Deep Water
NIST	National Institute of Standards and Technologies
NL	Nepheloid Layer
PB	Porcupine Bank
POM	Particulate Organic Matter
ppb	parts per billion
ppm	parts per million
psu	practical salinity unit
PT	Permanent Thermocline
RAD	Rapid Accretion Deposits
ROV	Remotely Operated Vehicle
SD	Standard Deviation
SIA	Stable Isotope Analysis
SIMS	Secondary Ion Mass Spectrometry
SNR	Sample-Noise-Ratio
SPM	Suspended Particulate Matter
sPOM	Suspended Particulate Organic Matter
TD	Thickening Deposit
TIMS	Thermal Ionization Mass Spectrometry
WC	Whittard Canyon
WoRMS	World Register of Marine Species

Part I

Introduction

Chapter 1

Research Aim and Relevance

1.1 Contextual Overview

The presented study is part of the strand 'Ecology & Evolutionary Biology' of the PhD Programme in Earth and Natural Sciences (ENS), and aims to contribute to the understanding of cold-water coral ecosystem functioning. At the starting point of the project in September 2011 a number of international projects focused on the investigation of CWC environments were in the process of finalising their results. The concluding meeting of the HERMIONE (Hotspot Ecosystem Research and Man's Impact On European Seas) project, for example, took place in September 2012. This interdisciplinary project had started in April 2009 as a continuation of the HERMES project (2005-2009). One focus was on understanding complexity and functioning of deep-sea ecosystems like cold-water coral (CWC) reefs, identifying the impact of natural and anthropogenic changes on these, as well as finding possibilities for a sustainable use of these habitats (Weaver et al., 2009). The strong influence of heavy fishing on the population of deep sea fish species and the destructive impact and degree of bottom trawling on vast marine areas were key findings of the project.[1] Another project at the time, CoralFISH, attempted, among other aims, to integrate fish into coral ecosystem models and to produce habitat suitability maps (e.g. Foley et al., 2012). Although many questions were answered, the knowledge about the complex deep sea systems is still underdeveloped when it comes to contributing more effectively to decision making in EU environmental policies. Protection from trawling and other human impact is an important step in assuring the survival of these vulnerable reefs which recover only slowly (Althaus et al., 2009).

The protection of deep sea coral reefs through the establishment of Marine Protected Areas (MPA), Ecologically or Biologically Significant Areas (ESA or BSA) is still rather based on their role as fishing grounds for the deep-water fishing industry than on the scientific and ecological value of the corals themselves (for example, as indicators of environmental changes and even climate history). Trawling activity has already destroyed wide areas of reef structure and changed the sedimentological environment (e.g. Puig et al., 2012). The danger of losing fish habitats and breeding grounds is only slowly accepted by policymakers as a reason for protecting these environments. The Norwegian government was among the first to protect large areas

[1] The final report for HERMIONE findings sums up the key findings from 170 peer-reviewed papers produced during the course of the project. For details see references here: `http://www.eu-hermione.net/component/content/article/215`; last accessed Jan 8, 2016.

(Røst Reef, Sula Reef, Iver Ridge, Tautra Ridge) of the Norwegian cold-water coral reefs through the 1999 Coral Protection Regulation and the Nature Conservation Act (Roberts et al., 2009a, 2009b, Tveteraas & Bryant, 2003). Other governments follow only slowly. In 2003 the Endangered Seas Programme of WWF contained these two objectives: sustainable fisheries and an increase in the number of MPAs to protect cold-water coral habitats. Today still only 2.18% of the total world ocean area is protected from destructive fishing practices with a total of 13,674 MPAs worldwide and only 1.03% globally defined as 'No Take Areas'[2] (fig. 1.1). While deep sea canyon morphologies might provide some protection from trawling activity the impact of lost fishing gear entangled in coral colonies is still evident. The establishment of MPAs is an ongoing process that will be promoted by a better understanding of the dynamics and vulnerabilities of the CWCs and their reef habitats. To date the vast canyon systems along the Irish shelf slope are still not officially recognized as vulnerable and protected environments.

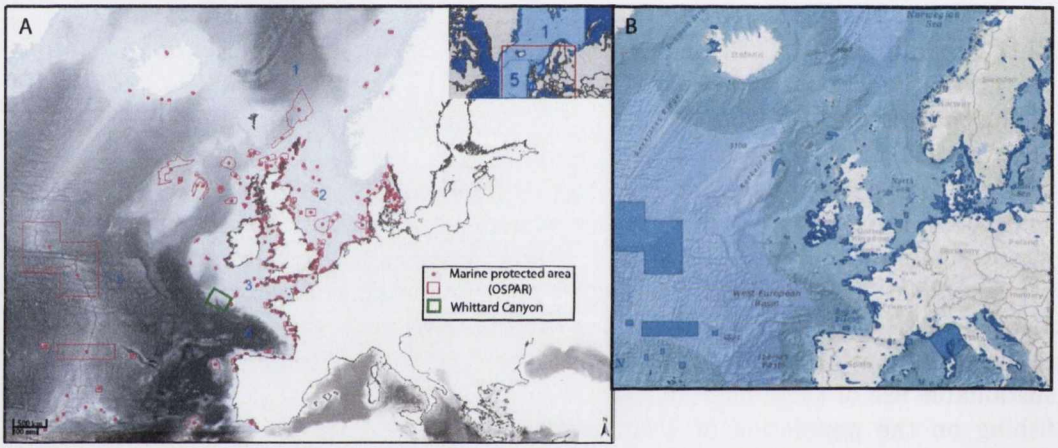


Figure 1.1: Different online sources visualising the constantly updated coverage of MPAs in the NE Atlantic. A) OSPAR map with MPAs in pink. OSPAR ('OS' for Oslo, 'PAR' for Paris) is the cooperation of 15 Governments to protect marine environments of the NE Atlantic (`http://carto.mpa.ospar.org/1/ospar.map`; last accessed July 2015). b) Excerpt from the MPAtlas (MPAs in blue).(`http://www.mpatlas.org`; last accessed July 2015). Both maps show that the shelf edge including the area of the Whittard Canyon (green box) is still largely unprotected.

HERMIONE reported strong reactions of CWCs to warming climate (from northward migration to decreasing abundance) (e.g. Frank et al., 2011). Still, due to a lack of understanding of their reproductive strategies, metabolisms and biomineralisation, the impacts of anthropogenic activity and changing climate on CWC environments and the role of the coral reef structures as archives recording changing deep sea environments remains a weak argument for enforcing protection and changing policies.

Research at Trinity College Dublin revealed a link between echinoids as bioeroders and the deep sea corals (Stevenson & Rocha, 2013). Species interaction could further increase or decrease the vulnerability of the CWCs to changes in environmental conditions as well as influence the level of stress in a setting where ocean acidification already shifts the aragonite saturation horizon (ASH) upwards and hence aggravates

[2]For updated maps see: `http://www.mpatlas.org`; last accessed Jan 8, 2016.

biomineralisation. In order to understand the extent of this danger a wider understanding of the processes involved in biomineralisation in these animals is necessary but not yet available.

Despite past efforts our knowledge of the metabolism, growth mechanisms and growth rates of the scleractinian deep sea corals is still underdeveloped. A large number of recent investigations focused on the biology of the CWCs (especially reproduction, conductivity and dispersal) and the microbiology associated with these (assemblies of bacteria within the CWCs) (e.g. Galkiewicz et al., 2011, Strömberg et al., 2010). When it comes to biomineralisation, analysis of the biogenic carbonates is usually limited to bulk sampling or focuses on one growth direction, either linear or radial (e.g. Rollion-Bard et al., 2003, Mortensen & Rapp, 1998). This is a significant deficiency since fine-scale biomineralisation processes potentially capture environmental variations in multi-directional growth in the isotopic ratios and trace and minor elemental concentrations incorporated from the ambient water during carbonate precipitation. The calcification of the coral skeleton is comparable to that of tree rings; the skeleton grows in length but also expands through the continuous addition of new layers, hence building a 3-dimensional archive. The skeleton, therefore, holds potential to record signals of seasonal cyclicity in the availability of nutrients or trace elements important for growth, for instance, barium or magnesium. A full view over all growth directions over the full extent of the coral theca can fill in gaps in our understanding.

Metabolic (or 'vital') effects can alter the retained signals. A differentiation between the degree of metabolic and kinetic fractionation is necessary to uncover the potential of CWCs as archives of small-scale environmental change. Often time-consuming research towards a better understanding is neglected in favour of immediate results on a lower level. The correlation of $\delta^{18}O$ and $\delta^{13}C$ or the so-called 'lines technique' (Smith et al., 2000) is currently the most popular method to interpret stable isotope ratios in terms of reconstruction of average ambient temperature, recent and historical, and to quantify the extent of metabolic fractionation involved. The method appears to successfully display changes through space (different temperature regimes) and time (glacial vs. interglacial periods) (e.g. Marali et al., 2013, Lopéz Correa et al., 2010, Smith et al., 2000) at a low resolution without further knowledge of biomineralisation mechanisms. It does not provide insight into seasonal or annual variations (like detritus influx), which depend on higher resolution techniques. The lack of a general sampling protocol for the application of this technique also causes difficulties for the comparability of results from different studies. To fully comprehend the vulnerability of these habitats and to promote sustainability, detailed knowledge of small-scale processes is essential. To overcome metabolic effects multi-proxy approaches combining different minor and trace elements and stable isotope ratios were suggested (e.g. Gaetani et al., 2011).

In addition the number of studies comparing different locations using material from the same coral species is very limited which is partly due to the limited availability of specimens. The same goes for extended studies on geochemical signals in different coral species from the same location. In general, *Madrepora oculata* has often been neglected, which might be on account of its complicated growth pattern, while *Lophelia pertusa* is the best examined species in the North Atlantic so far.

1.2 Research Aims and Proposed Methodology

At the beginning of the presented study the original objective was focused around the effects of species interaction and bioerosion on aragonitic CWCs based on the observed echinoid parasitism (Stevenson & Rocha, 2013). However, it soon became obvious that more effort had to go into advancing our understanding of biomineralisation mechanisms of the CWCs before influencing factors can be isolated and interpreted.

Therefore, the focus of this PhD thesis is the investigation of the biogeochemical composition of aragonitic cold-water scleractinian coral skeletons, possible species-specific differences and variations between different locations. Understanding the underlying mechanisms and patterns of biomineralisation and the degree of biological control over these is a necessary basis for identifying the biological impact on biomineralisation and, consequently the extent of any vital effects. This will allow for the isolation of external factors which imprinted on the skeletal formation directly (addition of trace elements) or indirectly (kinetic effects which influence isotopic composition/ratios). As mentioned before, this requires a sound understanding of the principles of biomineralisation in the scleractinians.

The presented study was constructed on the following hypotheses based on published research on the subject matter (introduced in the literature review):

(1) variations in microstructures are associated with geochemical variations

(2) metabolic effects are reflected in lower $\delta^{13}C$ values and deviations from a linear correlation between $\delta^{13}C$ and $\delta^{18}O$ (following McConnaughey et al., 1997)

(3) polychaete tube calcification is connected to higher metabolic activity as a reaction to stress which might be reflected in lower $\delta^{13}C$ values

(4) trace and minor element concentrations are connected to metabolic and kinetic effects

(5) uranium and magnesium variations are related to growth rate while barium as a nutrient proxy marks variations in food availability

(6) nepheloid layers influence the geochemical signals recorded in the coral skeleton

(7) *Madrepora oculata* has a high potential to record variations in environmental parameters and possibly shows lower vital effects

To test these hypotheses a variety of major, minor and trace elements will be investigated for variations in isotope ratios and elemental concentration during biomineralisation in association with microstructures as well as for their potential as environmental recorders. This will be realised by detailed high-resolution analysis on two of the most common colonial scleractinian species, and a subsequent comparison of different regions of biomineralisation. Different potential proxies will be investigated using different sampling techniques (microdrill, laser ablation) and utilising different analytical methods (gas chromatography isotope-ratio mass spectrometry (GC-IRMS),

laser ablation quadropole inductively coupled plasma mass spectrometry (LA-Q-ICP-MS), microscopy).

Additionally, the subject of species-interaction will be addressed by taking a closer look at the attached polychaete tubes which are calcified by the coral. This interaction has been reported before and classified as reef-building but has so far been neglected in studies on biomineralisation mechanisms (e.g. Roberts, 2005, Mortensen, 2001). In connection with *M. oculata* the thesis will also test a series of temperature reconstruction approaches for their feasibility and discuss the results in context with earlier findings. All of these discussions will be based on *in-situ* observations in different environments during a series of research cruises. This will allow for a detailed evaluation of observed geochemical characteristics in context with different habitats.

1.3 Thesis Organisation

The presented thesis starts with an overview over existing literature with regard to the state-of-the-art around the research topic. It then introduces the available material and the applied methodologies. Since the same analytical methods are used in several of the chapters they are summed up at the start. The first result chapter focuses on different habitat types found at the study sites along the Irish shelf in combination with available water parameters (Chapter 5). The chapter aims to provide insight into possible influencing environmental factors and differences between different habitat types which might cause imprints on biomineralisation. The study on coral skeleton geochemistry starts with a comparison between different scleractinian species from the Whittard Canyon in terms of temperature reconstruction (Chapter 6). It is then followed by a case study on one of the species (*L. pertusa*) discussing geochemical patterns over a multi-proxy approach (major, minor and trace elements) which sets up the basis for further discussion (Chapter 7). The so far underrepresented species *M. oculata* is then investigated based on methods established in Chapter 7 to look at corallite and colony growth in association with different habitat types (Chapter 8). Chapter 9 finally highlights the impact of species-interaction on biomineralisation in both investigated species by looking at the polychaete *E. norvegica*, an important contributor to reef stability (e.g. Roberts, 2005). Its tube is calcified by the corals which also provides additional insight into mechanisms of biomineralisation. Finally the conclusion re-evaluates exisiting biomineralisation models and suggests adaptions.

Chapter 2

Literature Review

The presented thesis focuses on cold-water scleractinian corals with aragonitic skeletons. Starting with a brief introduction to five of the most common genera in the study area along the Irish continental shelf slope, state-of-the-art knowledge on their zoology and live cycles are summarised together with an overview of the oceanography of the further-on represented areas and habitat observations. Following, the review turns to the skeletal formation and geochemistry of biomineralisation with regard to commonly used analytical methods. The review focuses on creating a context for further-on selected approaches and discussions of the results.

2.1 Biology of Cold-Water Corals (CWCs)

2.1.1 Selection of Common Scleractinian Species in the NE Atlantic

The existence of cold-water corals has been known since the 18^{th} century but only during the last decades did they receive increased attention from the environmental research community (e.g. Tambutté et al., 2011, Roberts et al., 2009b). For the presented thesis a selection of the most common scleractinian CWCs was studied *in situ* and collected in canyons along the Irish shelf in the NE Atlantic. The focus lies on five species from three different families of scleractinians (Anthozoa - Hexacorallia) (table 2.1).

Table 2.1: Excerpt from the taxon tree for the five investigated scleractinian genera as published in the World Register of Marine Species (WoRMS).

Kingdom	**Animalia**			
Phyllum	**Cnidaria**			
Class	**Anthozoa**			
Subclass	**Hexacorallia**			
	Order	**Scleractinia**		
		Family	**Caryophylliidae**	
			Genus	***Desmophyllum***
				Lophelia
				Solenosmilia
		Family	**Dendrophylliidae**	
			Genus	***Enallopsammia***
		Family	**Oculinidae**	
			Genus	***Madrepora***

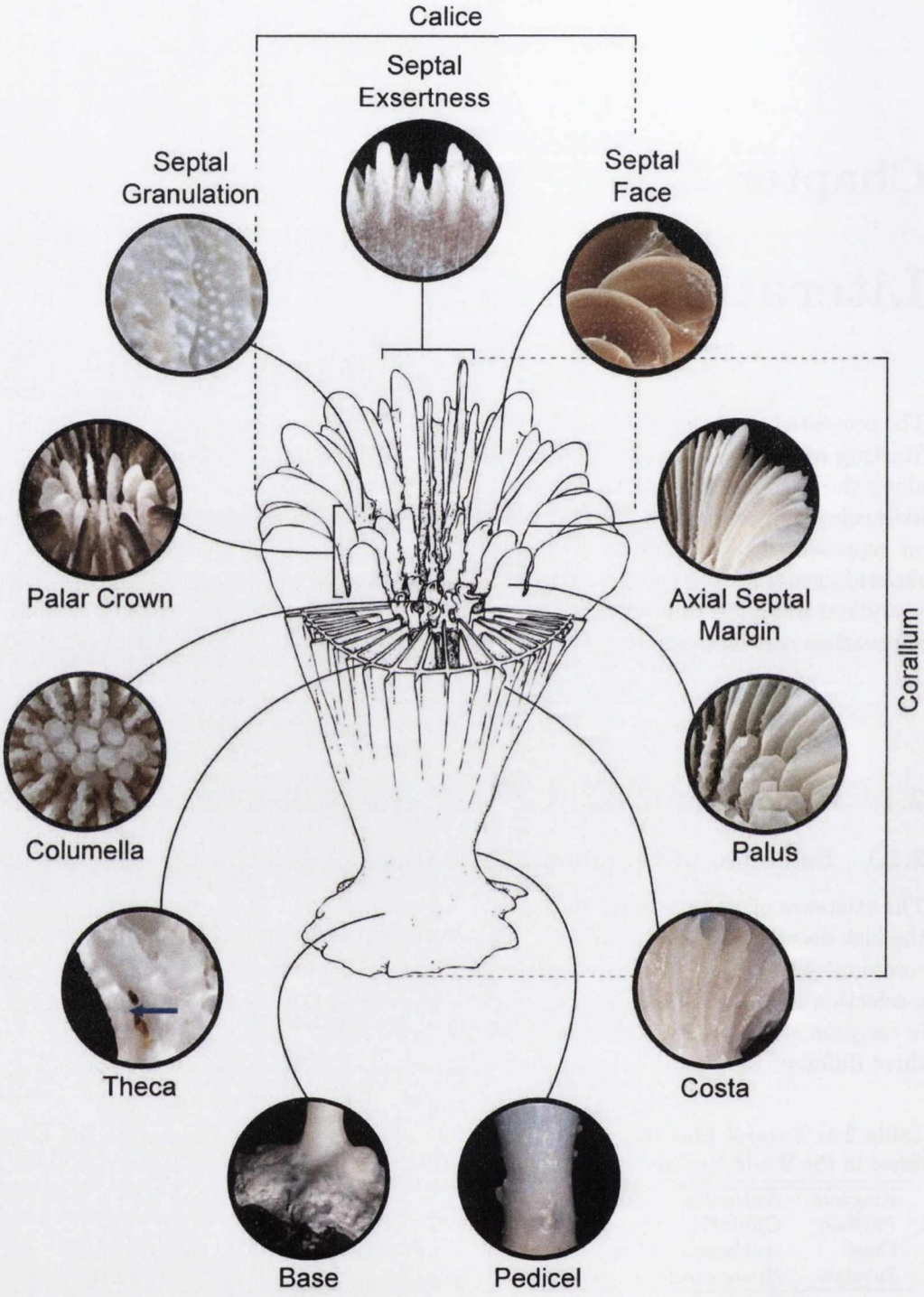


Figure 2.1: Overview over different structural features of coral skeletons (from Cairns & Kitahara, 2012).

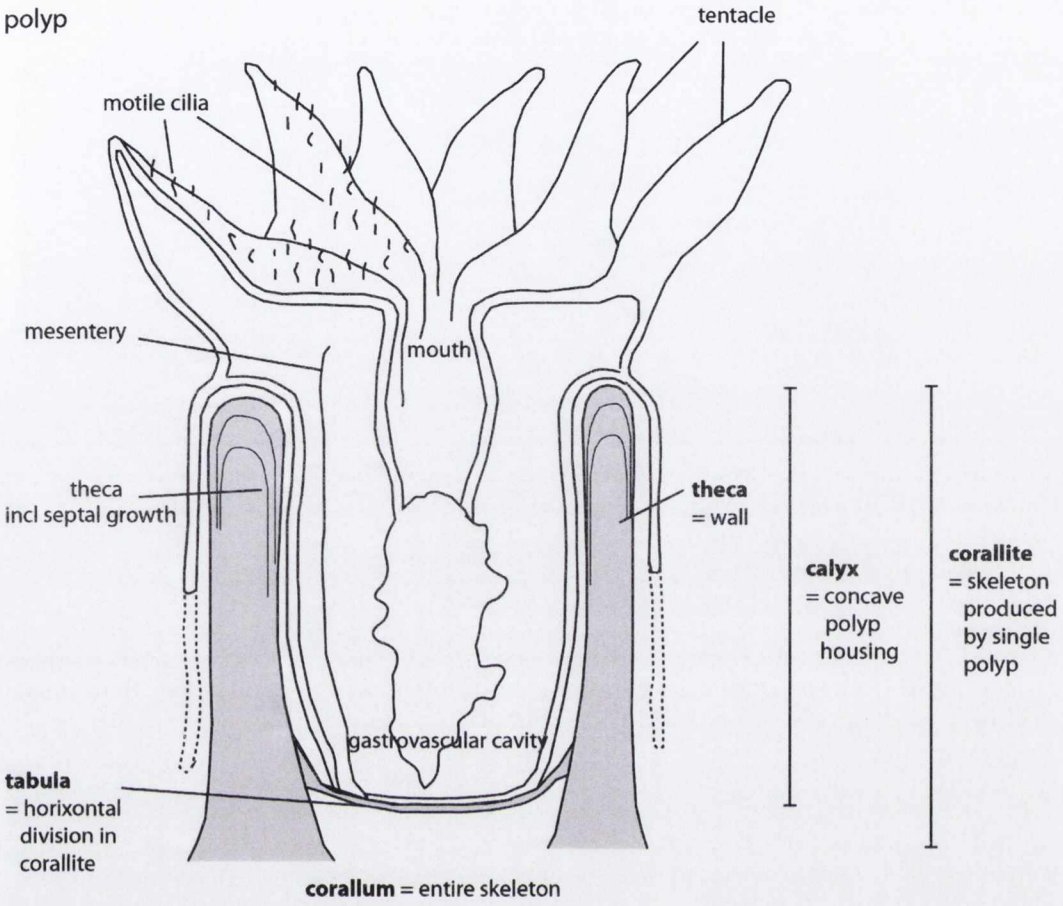


Figure 2.2: Overview over polyp (soft tissue) and corallum (skeleton) (modified after Roberts et al., 2009b). The main body of the polyp with its gastrovascular cavity sits within the corallite with the polyp mouth at the opening. The tentacles surround the mouth (*L. pertusa* has around 25-30 tentacles (Freiwald, 1998)). Motile cilia on the surface of tentacles and mouth disc provide ciliary currents to support particle transport (Shelton, 1980). The soft tissue is in contact with the inner and the upper outer part of the theca. The location of mesenteries is connected to septal precipitations on the inside of the calyx. The term coenosteum refers to skeletal material between the theca of individual adjacent corallites.

Lophelia pertusa (Linnaeus, 1758) (Family Caryophylliidae)

In the first place scleractinians are differentiated based on their skeletal features and morphologies (fig. 2.1 and 2.2). The genus *Lophelia* is the best studied scleractinian species in the NE Atlantic and forms firmly attached, bushy structures by branching intratentacularly (inside the ring of tentacles) (Cairns & Kitahara, 2012) (fig. 2.3). Asexual (vegetative) reproduction (budding) takes place unequally and single-mouthed resulting in one separate 'bud' per event (Cairns & Kitahara, 2012). It commonly attaches to hard substrate like rocks or coral rubble (fig. 2.4) and was originally categorised as colonial but since polyps are not interconnected by soft tissue *L. pertusa* has to be regarded as 'pseudo-colonial' (Freiwald, 1998, Jensen & Frederiksen, 1992).

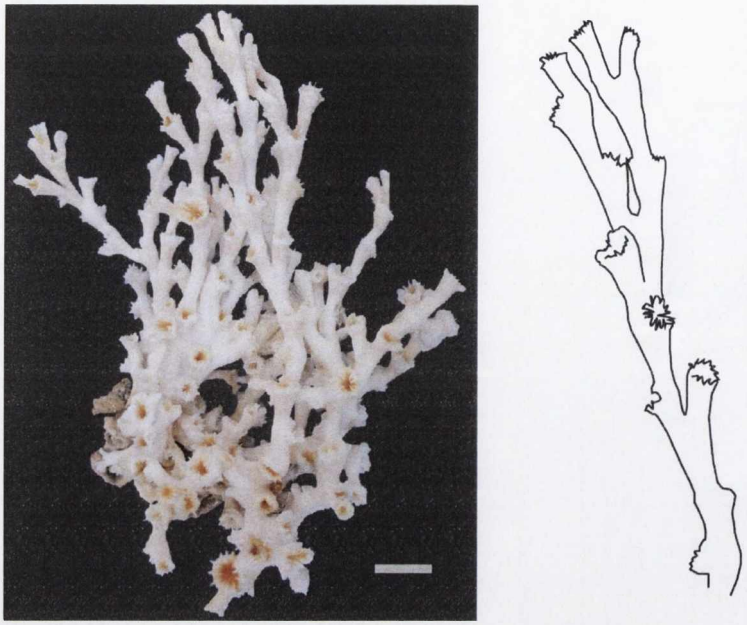


Figure 2.3: *Lophelia pertusa* extends its branches to bushy colonies (without a clear morphological pattern) that can reach more than 1 m in diameter. Scale bar equals 2 cm. Here sample 1447 from the Whittard Canyon (49.0098°N/10.9488°W).

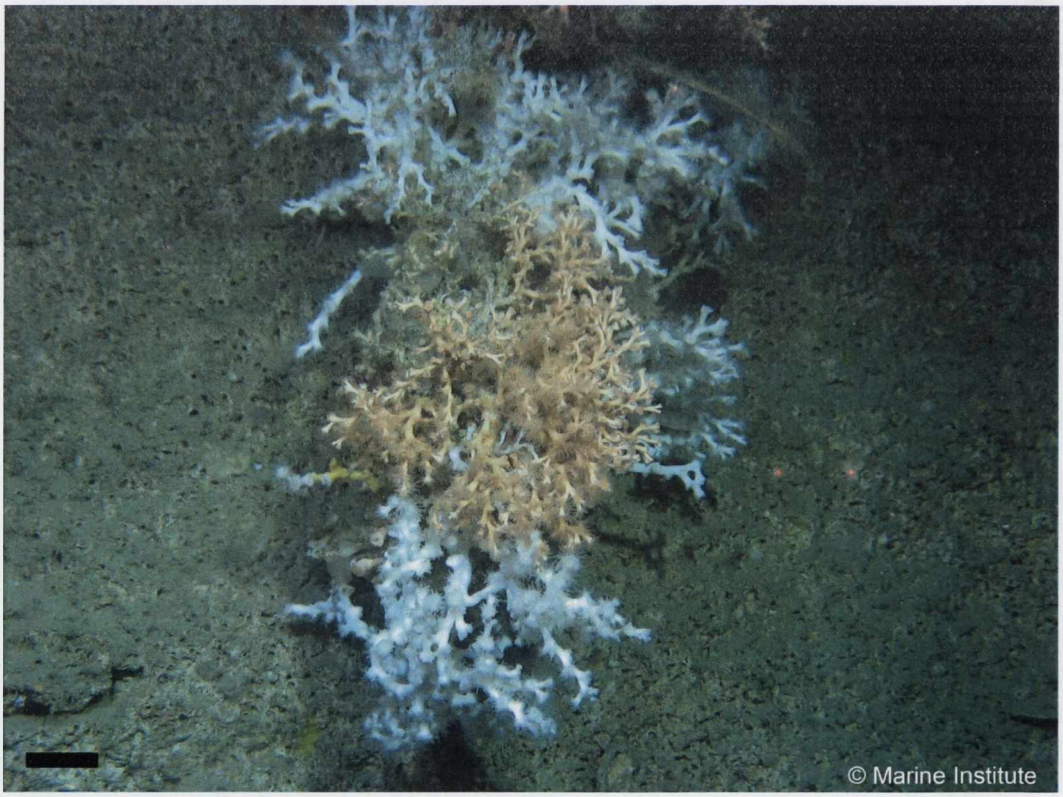


Figure 2.4: *Lophelia pertusa* is typically found along vertical walls in the higher parts of the Whittard Canyon. White and orange *L. pertusa* form colonies together; orange specimens often appear thinner branched. Here: Whittard Canyon (48.6663°N/9.9453°W). Scale bar equals 10 cm. Lower areas are settled by smaller colonies on rubble on the canyon floor. For copyright information see Acknowledgements.

The species shows a range of phenotypic plasticity from heavily calcified ('brachycephala') to fragile ('gracilis') (Lumsden et al., 2007). Freiwald (1998) reported two different branching modes from the Sula Ridge: (1) repeated 'zig-zag' budding with long and elongated colony segments; (2) bushy and dendroid with varying growth directions. The mean distance between consecutive corallites in context with published growth rates (see table 2.5) points to one budding event per year with most of the linear extension taking place within the first year (Gass & Roberts, 2011). Aquarium observations, however, revealed an extension of four polyps/year (Orejas et al., 2008). This shows that without live observations the variability of budding events and the dependency on environmental factors is hard to estimate. Generally three colour varieties of *L. pertusa* are known and possibly controlled by bacteria: white (colourless) soft tissue and mucus, yellowish soft tissue and mucus, red soft tissue and orange-reddish or colourless mucus (Neulinger, 2009, 2008, Freiwald, 1998).

Madrepora oculata Linnaeus, 1758 (Family Oculinidae)

The genus *Madrepora* includes five species of which *M. oculata* is the most common one in the NE Atlantic and Mediterranean Sea. It is described as a secondary framework builder with a highly variable colony morphology (bushy or flabellate) (Lumsden et al., 2007). The colonies attach to hard substrate (rock, dead coral). The colonial genus *Madrepora* branches extratentacular (outside of the ring of tentacles) with symmetric hexameral septa arranged in multiple cycles around a papillose columella (Cairns & Kitahara, 2012). The theca can generally be smooth, granular or ridged (Cairns & Kitahara, 2012). Our samples all show a ridged surface. The axial septal ridges are smooth (Cairns & Kitahara, 2012). *Madrepora* can have pali (small flattened lobes on the axial septal edge, one per septum) (Cairns & Kitahara, 2012). The branches are typically 'zig-zag' shaped (sympodial branching) (Lumsden et al., 2007) (fig. 2.5).

The species is very common on vertical canyon walls in the Whittard Canyon in assemblages with high densities of *D. dianthus* and bivalves (*Acesta excavata, Neopycnodonte zibrowii*) (Johnson et al., 2013) (fig. 2.6). In canyons of the Cap de Creus region (W Mediterranean Sea) the *M. oculata* cover was reported in species densities more than 50 times higher than *L. pertusa* and up to 30 times higher than *D. dianthus* (Orejas et al., 2009). In the Mediterranean Sea generally with relatively high temperature, salinities and densities above NE Atlantic values, *M. oculata* is often more common than *L. pertusa* in most areas (Freiwald et al., 2009, 2004, Orejas et al., 2009).

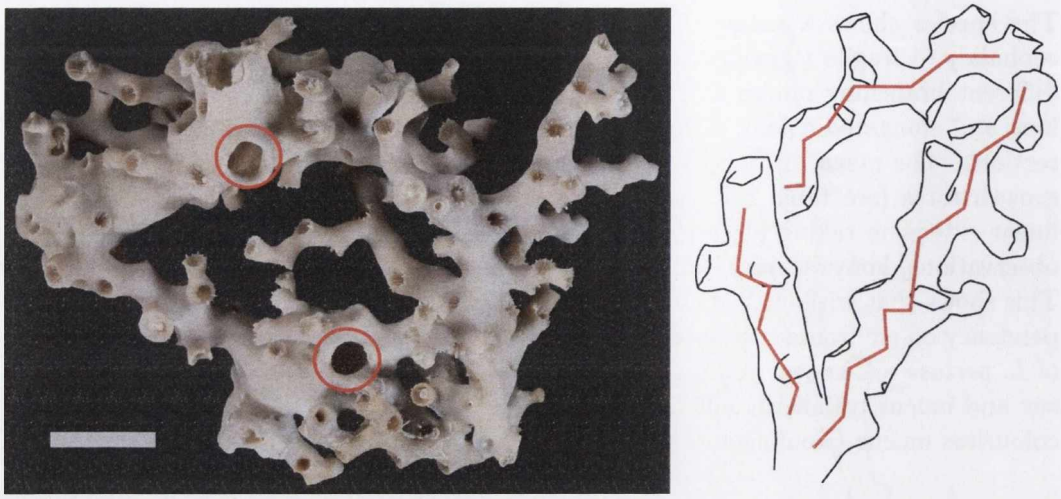


Figure 2.5: *Madrepora oculata* with the typical 'zig-zag' growth (illustrated on the right). The species often grows with *E. norvegica* tubes (two tube openings are marked by red circles). Here: sample 459-M2 from the Whittard Canyon (48.7607°N/10.4608°W). Scale bar is 1 cm.



Figure 2.6: *Madrepora oculata* is very common along the vertical walls of the Whittard Canyon and often found in white and orange phenotypes. Here: Whittard Canyon (48.7607°N/10.4608°W). Scale bar is 10 cm. For copyright information see Acknowledgements.

Desmophyllum dianthus (Esper, 1794) (Family Caryophylliidae)

The solitary corallum is found attached to hard substrate. The theca is granular, usually with longitudinally oriented costae (continuations of the septum on the outside wall) (Cairns & Kitahara, 2012) (fig. 2.7). The genus does not build a columella (Cairns & Kitahara, 2012).



Figure 2.7: Individuals of *Desmophyllum dianthus* are often found growing together in 'pseudo-colonies' (see also appendix A.3). Scale bar is 2 cm. Here: sample 1526 from the Whittard Canyon (48.8856°N/10.9229°W).

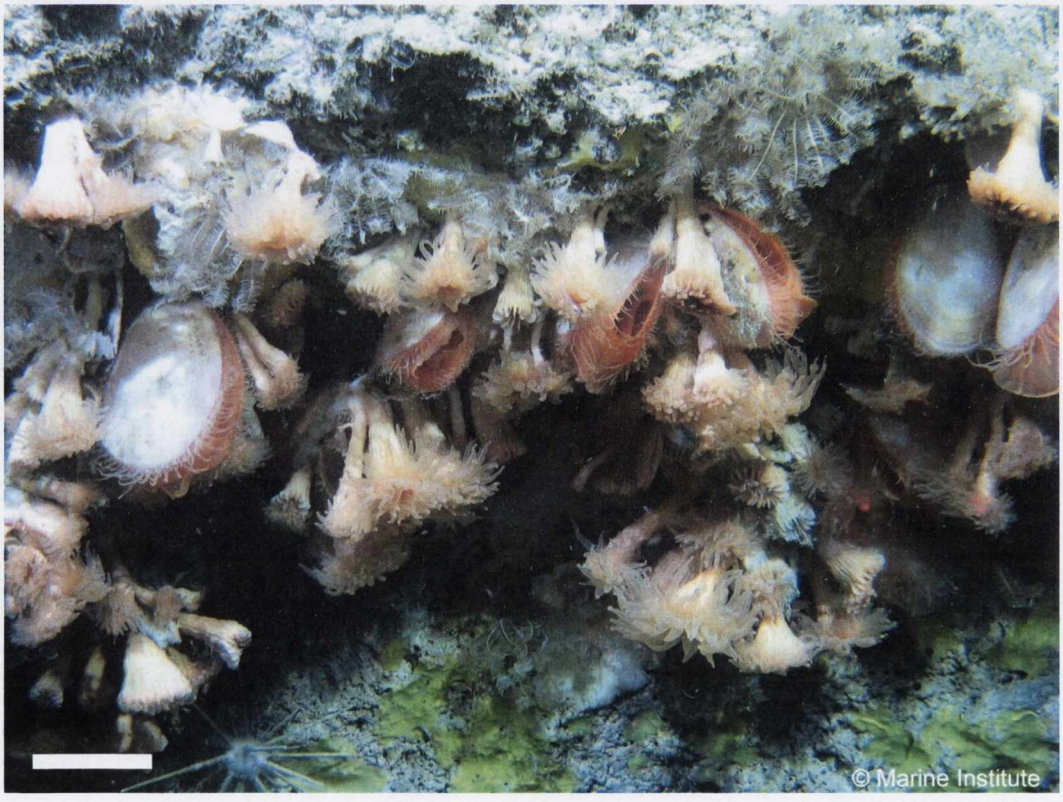


Figure 2.8: *Desmophyllum dianthus* densities along the vertical walls can be significantly higher than that of colonial species. Here: Whittard Canyon (48.7607°N/10.4608°W). Scale bar is 10 cm. For copyright information see Acknowledgements.

Along vertical walls in the Whittard Canyon *D. dianthus* was reported with densities 8 times higher than the co-occurring *M. oculata* (fig. 2.8) (*L. pertusa* is absent on the studied wall) (Johnson et al., 2013). Respiration rates for *D. dianthus* were found substantially higher than for *L. pertusa* pointing to a species-specific difference in metabolism (Naumann et al., 2011). Extensive endolithic borings are commonly found in recent and fossil *D. dianthus* (Hassenrueck et al., 2013, Marali et al., 2013, Beuck et al., 2007, Robinson et al., 2006).

Solenosmilia variabilis Duncan, 1873 (Family Caryophylliidae)

The cosmopolitan, colonial genus grows on hard substrate in bushy or arborescent structures with intratentacular branching in an equal distomadeal form (two polyps develop within a common tentacular ring) (Cairns & Kitahara, 2012) (fig. 2.9 and 2.10). The corallum is smooth (or costate) with normally arranged septa (Cairns & Kitahara, 2012). The samples collected from the Irish continental shelf often appear extremely 'swollen' probably in connection with increased radial calcification near calcified polychaete tubes (own observations) (see also appendix A.3).

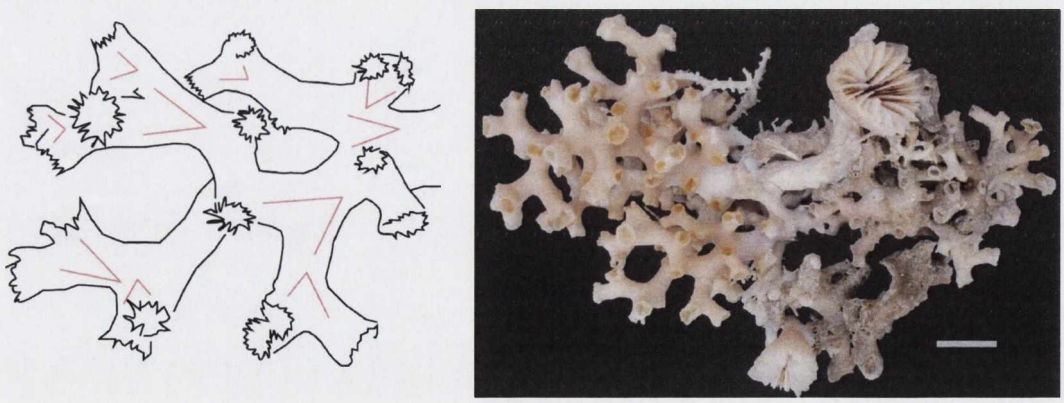


Figure 2.9: The equal distomadeal form of *S. variabilis* reflects in v-shaped branching (left). The species is often found in association with *D. dianthus* specimens around the base (right). Scale bar is 2 cm. Here: sample 1351 from the Porcupine Bank (54.0537°N/12.5963°W).

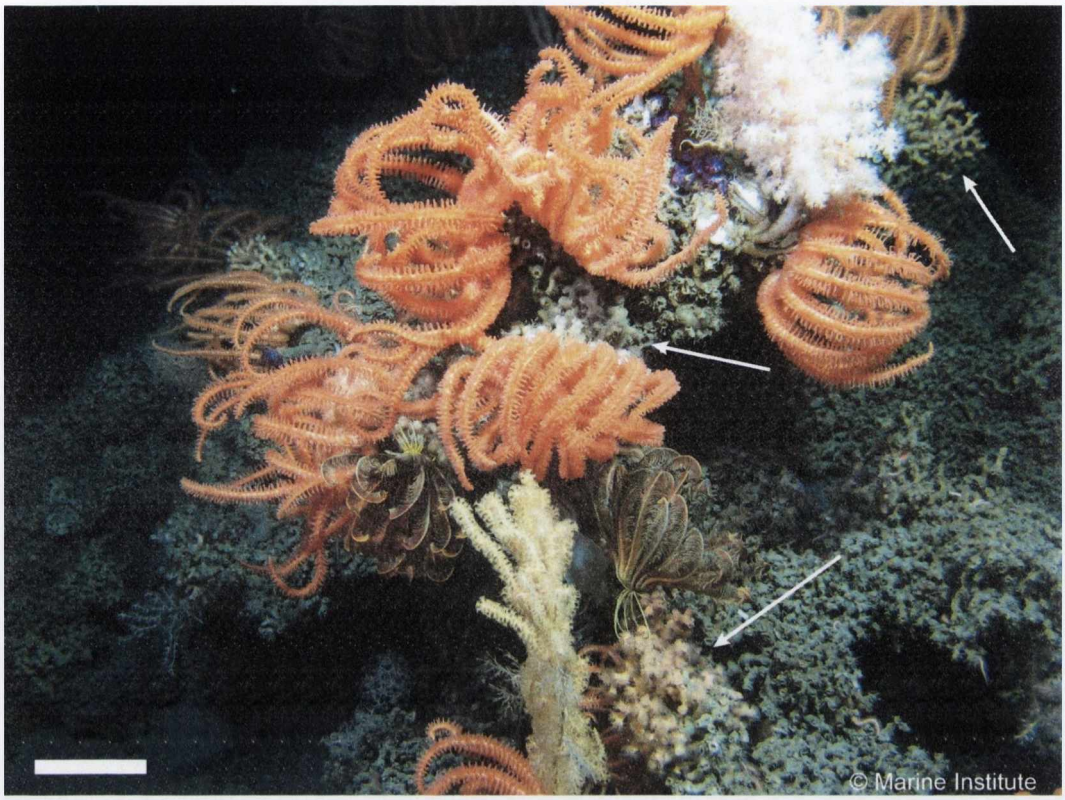


Figure 2.10: *Solenosmilia variabilis* (arrows) is found growing on top of large dead colonies along deep sea ridges. Here: Whittard Canyon (48.4872°N/10.3967°W). Scale bar is 10 cm. For copyright information see Acknowledgements.

Enallopsammia rostrata (Pourtalès, 1878) (Family Dendrophylliidae)

The colonial genus branches extratentacular (Cairns & Kitahara, 2012). All polyps are arranged on one side of the branch (Cairns & Kitahara, 2012) (fig. 2.11). The septa grow hexameral in multiple cycles around a papillose or fascicular (or absent) columella (Cairns & Kitahara, 2012). Theca and septa are rough (Cairns & Kitahara, 2012). The species is not very common in the study area and usually occurs in isolated colonies in deeper canyon regions (fig. 2.12) (own observations).

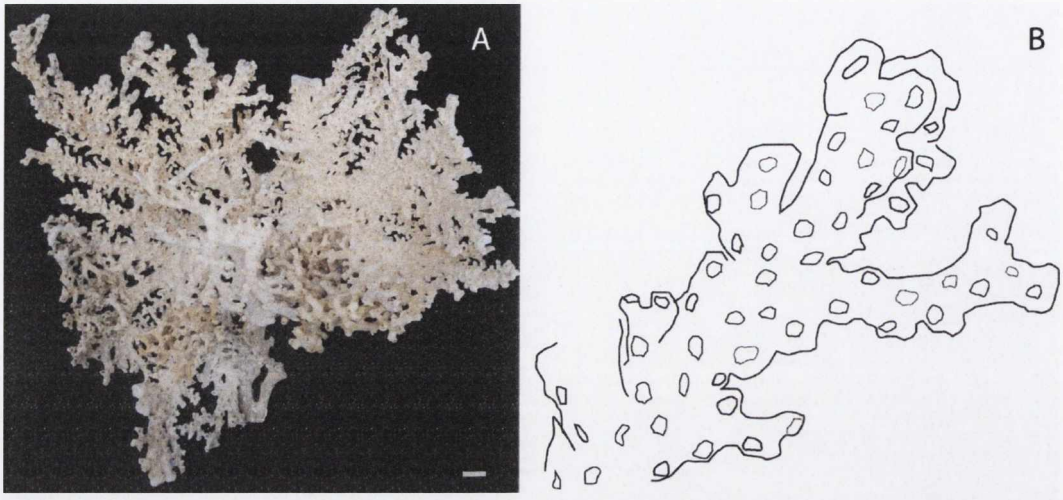


Figure 2.11: *Enallopsammia rostrata* polyps all accumulate on the inside of the fan (A). The corallite arrangement shows no specific patterns (B). The ridged back of the branches is free of corallites. Other coral species are often found growing in the center of the fan (here e.g. *S. variabilis*). Scale bar is 2 cm. Here: sample 1234 from the Porcupine Bank (54.0599°N/12.5493°W).

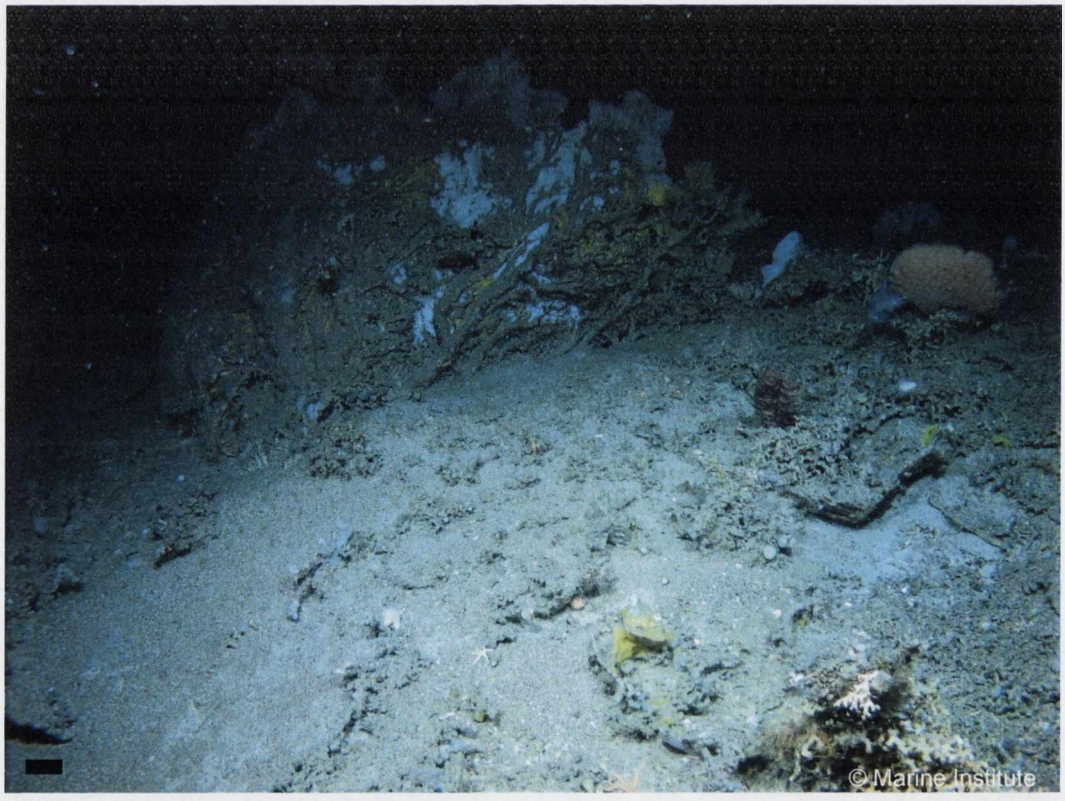


Figure 2.12: *Enallopsammia rostrata* can grow in fan-shaped colonies >1 m in diameter providing shelter for diverse CWC habitats in the inside of the 'fan'. Here: Porcupine Bank (54.0552°N/12.5457°W). Scale bar is 10 cm. For copyright information see Acknowledgements.

2.1.2 Feeding Habits

The feeding habits of CWCs are still to a quite large part open to discussion as it is hard to study them *in situ*, and aquarium experiments can only reflect natural conditions to a certain extent as many details and small-scale variability might be biased by the inherent artificiality of the environment. The animals were often reported in the vicinity of hotspots of primary production, and a direct connection to steep slopes with local flow fields and turbulence regimes was observed (Davies et al., 2009, Roberts et al., 2009a, Kiriakoulakis et al., 2007, Thiem et al., 2006). White et al. (1998) reported cold, nutrient-rich waters in dome-like structures above CWC mound habitats in the Porcupine Bank during the winter months. The increased phytoplankton production due to nutrient-rich waters in spring there persists till summer (White et al., 1998). Over the following months (depending on layer height) this layer sinks downslope through the benthic boundary layer (Ekman drainage) and delivers food particles to the CWC reefs (Davies et al., 2009, Thiem et al., 2006, White et al., 2005). Other investigations also found resuspended organic particles spreading downslope in particle-rich tongues (so-called 'nepheloid layers') which contribute to food supplies (e.g. Khripounoff et al., 2014, Klitgaard et al., 1997).

The Porcupine shelf area experiences seasonal phytoplankton blooms in July (Waller & Tyler, 2005). Satellite images of the last decade for the NE Atlantic show high chlorophyll α (Chl α) values over the area between April and July[1]. This presents a clear shift in seasonality from the double peak in surface productivity that was available until the 1980s (Martinez et al. 2011). In deeper areas Chl α is reflected in fluorescence variations. In addition to this, nepheloid layers were observed on a regular basis in the studied canyons around Ireland.

Studies on δ^{15}N indicated that at least the two scleractinian species *L. pertusa* and *M. oculata* are on the same trophic level (Duineveld et al., 2007, 2004). Both species range two trophic levels above phytodetritus and close to the level of zooplankton (Duineveld et al., 2007, 2004). Kiriakoulakis et al. (2005) found *L. pertusa* and *M. oculata* one trophic level above suspended particulate organic matter (sPOM) when comparing δ^{15}N values. Studies in CWC environments in the NE Atlantic and Mediterranean Sea identified zooplankton as the most probable main source of nutrition for the CWCs (Carlier et al., 2009, Duineveld et al., 2007, 2004). Variations in δ^{15}N might occur during photosynthesis influenced by environmental factors, therefore, allowing a possible reflection of surface water conditions in CWC δ^{15}N (Kiriakoulakis et al., 2005). Analysis of fatty acids again points to mesozooplankton being a major food source with species-specific differences in feeding and metabolism (Kiriakoulakis et al., 2005). Feeding experiments around *L. pertusa* and *M. oculata* were successful with a diet of mesozooplankton or a mixture of zoo- and phytoplankton, though at different degrees which points to possible metabolic differences between both species (Orejas et al., 2011, Duineveld et al., 2007, 2004, Kiriakoulakis et al., 2005). Labelling experiments identified *L. pertusa* as an opportunistic feeder which appears a likely strategy for most CWCs in the deep sea (Mueller et al., 2014). Diurnal vertical migration patterns of the zooplankton and sinking remnants of primary productivity, accumulates as 'marine snow' which possibly imprints on nutritional habits of deep sea corals (Roberts et al., 2009a, Kiriakoulakis et al., 2005, Beaulieu, 2002, Gooday,

[1] `http://neo.sci.gsfc.nasa.gov/view.php?datasetId=MY1DMM_CHLORA`; last accessed Jan 8, 2016.

2002, Diercks & Asper, 1997). Existing cycles in nutritional pulses can cause seasonal variations in biological processes, reflected in growth signals and reproductional ecology, and consequently also in the carbonate geochemistry (Roberts et al., 2009a, Kiriakoulakis et al., 2005, Beaulieu, 2002, Gooday, 2002, Diercks & Asper, 1997). $\delta^{15}N$ studies on coral mucus might contribute to our understanding but were so far not available (Carlier et al., 2009).

2.1.3 Reproduction Strategies and Connectivity of CWCs

There is not much research available on the reproduction of scleractinian CWCs which can again be attributed to the hard accessibility of deep-sea environments. An earlier study on *L. pertusa* and *M. oculata* in the NE Atlantic revealed rapid growth of oocytes between August and October co-occurring with an increase in particle flux to the benthic zone (Waller & Tyler, 2005). Research undertaken in shallower areas in Norwegian fjords indicated the start of gametogenesis in January with an increase in oocyte growth rate in autumn (Brooke & Järnegren, 2013). Spawning on the other hand was reported between January and early March for both regions (Brooke & Järnegren, 2013, Le Goff-Vitry & Rogers, 2005, Waller & Tyler, 2005). The studies suggested a possible resting phase after spawning in areas further south, and longer gametogenesis before spawning in northern regions (Brooke & Järnegren, 2013, Waller & Tyler, 2005). The reproduction of *L. pertusa* in the SW Atlantic off the coast of Brazil showed a peak in spawning between May and July (Pires et al., 2014). For the southern hemisphere this again places spawning within the winter months. The same study also reported continuous reproduction of *M. oculata* and *E. rostrata* as well as a year-round fertility for *S. variabilis* with a peak between April and September (Pires et al., 2014). All species were found mostly gonochoric with cases of hermaphrotism in both, *L. pertusa* and *M. oculata* (Pires et al., 2014, Waller & Tyler, 2005).

Planktotrophic planula larvae of *L. pertusa* were described as active swimmers which spend the first three to five weeks vertically migrating to the upper part of the water column before settling in the benthic zone (Larsson et al., 2014). This behaviour allows for high dispersal distances and different directions depending on upper currents (Larsson et al., 2014). An estimated vertical migration speed of approx. 50 m/d was suggested (Larsson et al., 2014). Since larval dispersal also influences the connectivity of different populations across the oceans the genetic structure of common CWCs was studied and microsatellites developed. Le Goff-Vitry et al. (2004a, b) found significant genetic diversity between different *L. pertusa* sites in the NE Atlantic and off the coast of Brazil but also suggested a high level of inbreeding. Further studies focused on *L. pertusa* in the Gulf of Mexico and the West Atlantic (Morrison et al., 2011, 2008a, 2008b). Additional observations around Australia and New Zealand revealed low levels of genetic variations for *Madrepora* and *Solenosmilia* while *Desmophyllum* shows differences between different sites (Miller et al., 2010). Insight into connectivity together with tracers of different water masses provided insight into migration patterns and pathways (Henry et al., 2014, Frank et al., 2011, Colin et al., 2010, Copard et al., 2010).

M. oculata and *L. pertusa* are known for asexual (vegetative) reproduction and for resuming growth after fragmentation which can be seen in *L. pertusa* when man-made structures like shipwrecks and oil platforms are rapidly colonised (Orejas et al., 2008, Gass & Roberts, 2006). *L. pertusa* and *M. oculata* colonies were also found growing on

lost fishing lines entangled in the Whittard Canyon (own observations). This suggests the existence of effectively dispersing planulae with higher dispersal rates, a possible effect of the cold waters (Roberts et al., 2009b). O'Connor et al. (2007) reported an exponential inverse relationship between length of larval stage and water temperature. Higher water temperatures would consequently result in a reduced capability for dispersal and migration.

2.1.4 The Role of Mucus

The exact role of mucus excretion in corals in relation with metabolism is widely discussed. The composition of mucus from cold-water corals and tropical corals is poorly known so far but does not seem to show significant differences and is primarily composed of carbohydrates and contains proportions of proteins, polysaccharids, monosaccharids, lipids and amino acids (Wild et al., 2010, Ducklow & Mitchell, 1979b). Mucus is commonly seen as a particle trap (Bythell & Wild, 2011, Mayer & Wild, 2010, Huettel et al., 2006, Wild et al., 2004). A typical reaction of corals to stress (e.g. during collection or when exposed to air or in times of increased sediment settlement) is an increased secretion of mucus (e.g. Larsson & Purser, 2011, Huettel et al., 2006). Huettel et al. (2006) reported large amounts of nutrient-containing mucus being exuded by shallow-water corals during phases of tidally induced air exposure (i.e. a regular event). The mechanism is interpreted as protection against dessication and UV radiation (Huettel et al., 2006). In these shallow water environments the returning water detaches this mucus and dissolves most of it thereby adding organic carbon and nutrients to the reef water (Huettel et al., 2006). This trigger can be excluded in deep sea environments where UV radiation or dessication only come into play when specimens are collected and brought to the surface. Nevertheless mucus might act as a carrier of nutrients across the reef when detached. The fraction of detached mucus which is not dissolved forms strings, flocs or layers incorporating suspended particles from the water (Huettel et al., 2006). Here the mucus phase contributes to Chl α, C and N increases as sinking strings provide nutrition for the benthic community (Mayer & Wild, 2010, Huettel et al., 2006). Similar observations are not easily possible in deep-sea environments. Gorgonian corals were found to cover their energy demands by feeding on exuded coral mucus (Coffroth, 1984). This contributes to a rapid nutrient recycling process (Mayer & Wild, 2010, Huettel et al., 2006). In terms of nutrient recycling mucus was found in connection with the so-called 'sponge loop' (Rix et al., 2016). Sponges consume the coral mucus and return parts as detritus, thereby converting Dissolved Organic Matter (DOM) into Particulate Organic Matter (POM) which then becomes available as coral nutrition (Rix et al., 2016). Reitner (2005) even suggested that growth rates might be controlled by the mucus production rate i.e. correlated with it, and phases of environmental stress promoting an increased production of mucus co-occur with periods of higher growth rates. Mortensen & Rapp (1998) also interpreted white layers in *L. pertusa* (correlated with high growth rates) as 'stress layers' while the banding pattern is discussed as a consequence of mineralisation under tissue cover alternating with mineralisation beyond cover (Freiwald & Wilson, 1998).

Freiwald (1998) observed films of mucus covering skeletal areas without tissue cover in *L. pertusa* and *M. oculata* thus contributing to carbonate precipitation. The degree of mucus-thickening of colonies is also discussed in direct connection with the eutrophication in surface waters and the consequent particle rain to areas beneath

(Freiwald, 1998). A high nutritional state of surface waters is suspected to increase mucus production in CWCs and reef framework stabilisation (Freiwald, 1998). On the other hand, mucus functions as a medium to remove sediment cover from the tissue surface (Larsson & Purser, 2011). Even anticalcification properties to avoid spontaneous overcrusting of soft tissue by external parameters were attributed to mucus (Marin et al., 1996). The geochemical signal recorded within the coral skeleton under high mucus influence might consequently experience higher fractionation effects due to increased calcification rates. Although this carries potential to add to geochemical studies it has not been investigated further so far.

A large part of research on coral mucus to date focused on metabolically active microbial communities in mucus, tissue and skeleton (Ducklow & Mitchell, 1979a). Bacterial community composition (BCC) was found to show stronger diversity differences between colonies than between environments (Hansson et al., 2009). For *L. pertusa* the differences appear pronounced between different colour varieties (Neulinger et al., 2009, 2008). Even different parts of *L. pertusa*, like mucus, tissue and skeleton show differences in BCC (Galkiewicz et al., 2011). A higher diversity is found in direct connection with the coral habitat in relation to surroundings, seawater and sediment (Schöttner et al., 2009). The diversity differences may also contribute to a higher resistence to extreme environmental parameters (Neulinger et al., 2008). Neulinger et al. (2008) suspected a greater influence of currents, oxygen saturation, geochemistry, even macrofaunal association and developmental stages of corals on bacterial community structures rather than temperature and salinity. To our knowledge a possible influence of microbial community structures in the mucus on skeleton biomineralisation has not been investigated so far. Neither are there studies on a possible metabolic effect of microbial activity on biomineralisation.

2.1.5 Symbiosis with the Polychaete *Eunice norvegica*

Scleractinian CWCs commonly grow in symbiosis with other species. Like *L. pertusa*, *M. oculata* and *S. variabilis* are often found in symbiotic relationships with the polychaete *E. norvegica* whose organic tubes are being calcified over by the coral (e.g. Roberts, 2005). The process assumed responsible for most of the tube calcification is the secretion of mucus over the tube, and the subsequent mineralisation of the mucus (e.g. Reitner, 2005, Mortensen, 2001). Mortensen (2001) reports an attachment of the tube directly to the coral branch through the coenosarc which later then covers the tube as well. Roberts (2005) describe the process of calcification of the coral tubes as a multistep process: after the secretion of the parchment-like tube by *Eunice* it gradually turns opaque due to a contribution of new layers from the inside of the tube. These thickened tubes will then be calcified over by the involved coral (Roberts, 2005). The polychaete irritates and stresses the coral which as a reaction releases increased amounts of mucus to remove the disturbance (Larsson & Purser, 2011, Reitner, 2005, Mortensen, 2001, Freiwald & Wilson, 1998). While the relationship was originally described as 'commensialistic' with *E. norvegica* stealing food from the CWCs (Mortensen, 2001), recently it is more often referred to as 'mutualistic' since the polychaete is contributing to reef stability by connecting coral fragments and initiating thickening of the skeleton (Roberts, 2005).

2.1.6 Limiting Factors of CWC Occurrence

The distribution of different CWC species is primarily connected to the ambient temperature of their habitat which is often a function of depth and in connection with salinity and density it can deviate from this relationship in environments with episodes of upwelling cold waters, in cold seeps, or in glacially fed waters (Roberts et al., 2009a). The animals can survive in shallower waters (e.g. in Norwegian fjords) where such events occur (Fosså et al., 2002). The temperature optimum is species-specific (Roberts et al., 2009a) (details in table 2.2).

Table 2.2: The reported depth ranges for different scleractinian species (Roberts et al., 2009a, Lumsden et al., 2007):

Species	Minimum Depth	Maximum Depth
Lophelia pertusa	39 m	3,383 m
Madrepora oculata	55 m	1,950 m
Desmophyllum dianthus	8 m	2,460 m
Solenosmilia variabilis	220 m	2,165 m
Enallopsammia rostrata	110 m	2,165 m

Although all species show distinct sensitivity to increasing temperatures, it seems to be lower in *L. pertusa* (Maier et al., 2012, Roberts et al., 2009a). A study on temperature ranges reported *M. oculata* in ambient seawater temperatures between 3.8 and 16.0°C in intermediate waters of the Pacific, between 1.8 and 15.0°C in surface, intermediate and deep waters of the Atlantic, and between 5.5 and 25.5°C in surface and intermediate waters of the Indian Ocean (Keller & Os'kina, 2008). *D. dianthus* was found in ambient seawater temperatures of 5°C in intermediate waters of the Pacific, and ambient temperature between 1.8 and 8.0°C in surface, intermediate and deep waters of the Atlantic (Keller & Os'kina, 2008). *S. variabilis* was reported in temperatures between 3.3 and 14.5°C in the Atlantic (Keller & Os'kina, 2008). *E. rostrata* is known to thrive in temperatures ranging between 2.4 and 17.9°C in the Pacific but is absent from lists for the Atlantic and Indian Ocean (Keller & Os'kina, 2008).

Other factors, like salinity, are quite stable in these depths and, therefore, not seen as major factors for habitat suitability (Roberts et al., 2009a, Dullo et al., 2008). While salinities are quite stable over short time scales, shifts in water masses and current systems might cause significant changes over longer times. The reaction of CWCs to changing currents in connection with changes in temperature and salinity input can result in migration to more favourable environments (e.g. Henry et al., 2014). Density on the other hand as a function of temperature and salinity appears to be a more decisive factor in present environments (Davies & Guinotte, 2011, Dullo et al., 2008). A clearly defined density envelop seems to be consistent for different environments in the NE Atlantic (between 27.35 and 27.65 kg/m^3) (e.g. Huvenne et al., 2011). The species *L. pertusa* was found in assemblages with a variety of octo- and hexacorals as well as other benthic invertebrates (e.g. the bivalve *Acesta excavata* (e.g. Purser et al., 2013)), however, it is also suspected to be a limiting factor to suspension feeder diversity as it possibly out-competes other taxa (Morris et al., 2013). Food supply and the involved flow systems also play an important role (e.g. Davies et al., 2009, Thiem et al., 2006, White et al., 2005). Not only do CWC reefs grow in areas of increased current speeds but also do their colonies actively

contribute to an increase in current speed (Guihen et al., 2013). Semi-diurnal flow modulation in connection with CWC occurrence was discovered in the Norwegian shelf (Guihen et al., 2013). The reef structures increase shear stress and consequently current speed which contributes to a re-suspension of particulates (Guihen et al., 2013).

Järnegren & Kutti (2014) summarised the published tolerance range for *L. pertusa* in the NE Atlantic as follows (see also references in Järnegren & Kutti, 2014) (table 2.3).

Table 2.3: Summary of known tolerance range concerning environmental parameters of *L. pertusa* as published in Järnegren & Kutti (2014).

Parameter	Total Range	Perfect Range
Temperature	4-14°C	6-9°C
Salinity	32-38.8 psu	ca. 35 psu
Oxygen	3.8-7.2 ml/l	
DIC	< 21.70 mol/kg	
Density	27.35-27.65 kg/m^3	

The reported ideal range for *L. pertusa* in oxygen levels of 6 ml/l with a minimum for the NE Atlantic at 4.3 ml/l is in accordance with the observed absolute minimum at 3.3 ml/l (Dodds et al., 2007). Dissolved oxygen within CWC reef areas in the Mediterranean Sea lies between 3.98 and 4.54 ml/l (Freiwald et al., 2009). Here *L. pertusa* was reported within the upper range of temperature and salinity tolerance limits while the observed density between 29.07 and 29.12 kg/m^3 is clearly above the reported limit from the NE Atlantic (Freiwald et al., 2009) (see table 2.3). Comparable density ranges are not found within the depths where CWCs thrive in the N Atlantic; a difference that can be attributed to the high salinities in the Mediterranean Sea which in turn suggests that temperature is more likely to be the decisive factor which controls density as well. The association between coral occurrence and density might also be influenced by higher particle load and consequently higher nutrient availability (to some degree) in the water column.

The aragonite saturation horizon (ASH), located at approximately 2,000 m depth in the NE Atlantic, is clearly an additional limiting factor when it comes to the distribution of the CWCs in general (Guinotte et al., 2006). The ASH describes the depth above which the water is still oversaturated in CO_3^{2-} and consequently the precipitation of carbonates is thermodynamically favoured. The North Pacific e.g. shows visibly limited potential as a habitat due to the shallow aragonite saturation horizon (Roberts et al., 2009a).

A number of studies on the effects of ocean acidification on carbonate precipitation rates in CWCs showed a variety of results from a reduced growth rate (for *M. oculata*) (Maier et al., 2012), over long-term acclimation mechanisms after initial calcification rate decline (for *L. pertusa*) (Form & Riebesell, 2012), to no changes in growth or respiration rates with increased pCO_2 (*L. pertusa* and *M. oculata*) (Maier et al., 2013a, 2013b). Latest studies showed that tropical corals might be able to overcome ocean acidification effects on calcification rates by increasing their feeding rate and, consequently, energy input (Towle et al., 2015). The global pCO_2 is predicted to rise up to 788 ppmv by the year 2099 which makes a shoaling of the ASH a very

real concern for CWC habitats (Guinotte et al., 2006). Models by Guinotte et al. (2006) predicted an approximately 70% decrease of current habitats by 2099. Models naturally vary with input parameters.

2.1.7 CWC Habitat Mapping and Modelling

Scleractinian CWCs have been reported from a variety of locations all over the world. The NE Atlantic (e.g. the Porcupine Seabight or Rockall Bank) is among the best studied regions when it comes to CWC habitat mapping. Most studies focused on cold-water coral mounds or so-called carbonate mounds (e.g. Foubert et al., 2011, Wheeler et al., 2011, Dorschel et al., 2007) and vertical walls (e.g. Johnson et al., 2013, Huvenne et al., 2011). So far cold-water coral ridges were rarely described (Correa et al., 2012).

A variety of approaches for CWC habitat descriptions is available so far, both qualitative and quantitative ones. Commonly the descriptions were based on available maps or accompanied by simultaneous multibeam surveys to gain additional bathymetric data (e.g. Savini et al., 2014, Rengstorf et al., 2013, Wienberg et al., 2013, Guinan et al., 2009a, 2009b, Henry et al., 2009). A series of quantitative descriptors (slope, aspect (orientation), curvature and relative position (BPI = Bathymetric Position Index), terrain variability (TRI = Terrain Ruggedness Index)) to classify the terrain were obtained from multibeam surveys and can be linked to CWC occurrences and habitat mapping using different sampling and observation techniques (Guinan et al., 2009a, Henry et al., 2009, Wilson et al., 2007).

Information about CWC assemblages can be summarised of existing reports from previous cruises, fishermen, and industrial surveys (e.g. Guinotte & Davies, 2014, Braga-Henriques et al., 2013, Roberts et al., 2003), gravity cores (e.g. Mastrototaro et al., 2010, Huvenne et al., 2009, Mienis et al., 2009), box and grab cores (e.g. Henry et al., 2009, Mienis et al., 2009, Masson et al., 2003), photo and video imaging (e.g. Johnson et al., 2013, Morris et al., 2013, Purser et al., 2013, Huvenne et al., 2011, Mastrototaro et al., 2010, Orejas et al., 2009, Dolan et al., 2008). A popular practise to evaluate CWC cover is the analysis of visual data provided by ROV tracks across the investigated terrain (straight lines or crisscrossing) often in connection with pointwise sample collection (Wienberg et al., 2013, De Mol et al., 2011, Guinan et al., 2009a, 2009b, Orejas et al., 2009, Schroeder 2002). Flying the ROV in a straight line with a constant distance from the ocean floor, a downward facing camera and a constant speed provides the best basis to gain quantitative data from the video footage, e.g. by extracting video frames over regular temporal or spatial intervals (e.g. every 5 s or 5 m) for 'presence/absence' data or a direct coral count (e.g. Morris et al., 2013, Purser et al., 2013, Guinan et al., 2009b). Where ROV flight parameters are less consistent data correction is applied or a more qualitative description of the visual data is provided (e.g. De Mol et al., 2011). Orejas et al. (2009), for example, used the central 1.5 m of the frame for the full length of the video footage (after removing sampling pauses and poor quality sections) for a study of *M. oculata* density along a crisscrossing transect.

The classification of different habitat types (e.g. 'live coral', 'dead coral', 'coral rubble', 'coral absence') is one alternative to quantifying coral occurrence (e.g. Morris

et al., 2013, Purser et al., 2013, Wienberg et al., 2013, De Mol et al., 2011, Orejas et al., 2009). In connection with Conductivity-Temperature-Depth (CTD) data and information on currents an environmental interpretation is possible (Johnson et al., 2013, Wienberg et al., 2013, De Mol et al., 2011, Huvenne et al., 2011, White et al., 2007). In literature different combinations of these techniques are applied depending on the species in focus. For solitary corals or easily identifiable branching single colonies (octocorals, antipatharians, *D. dianthus*) a quantitative approach from video frames is more applicable than for large scleractinian colonies (e.g. *L. pertusa*) which are better quantified in m^2 coverage (e.g. Morris et al., 2013, Purser et al., 2013, Orejas et al., 2009).

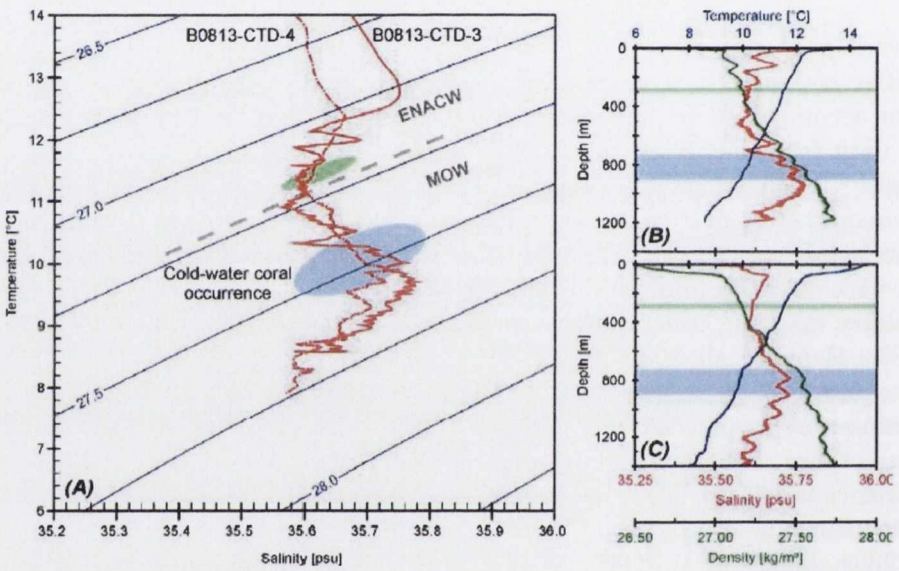


Figure 2.13: A) Hydrography of the Guilvinec Canyon. B)+C) Water parameters measured in the Penmarc'h and Guilvinec Canyon with shallow-water (green) and deep-water (blue) CWC occurrence (from De Mol et al., 2011).

A detailed study of the Guilvinec Canyon (Bay of Biscay), for example, highlighted the relationship between water parameters and coral occurrence in the canyon systems combining CTD data with ROV observations (fig. 2.13) (De Mol et al., 2011). A number of studies evolved around predictive mapping of the CWC habitats, partly using Ecological Niche Factor Analysis (ENFA) or Maximum Entropy Modelling which combines the collected data on the actual distributions of the corals with environmental information on the locations ('ecogeographical variables') and calculates a basis for the prediction of further undiscovered habitats (e.g. Rengstorf et al., 2013). Davies et al. (2008) presented habitat parameters for *L. pertusa* that included intermediate depths, productive waters and an above-average current speed. The calculated temperature range, however, was not consistent with direct observations which might have been caused by too low resolution (Davies et al., 2008). Then again, model resolution is constantly increasing and overcoming such obstacles.

2.2 Oceanography of Studied Areas

2.2.1 NE Atlantic - Whittard Canyon, Porcupine Bank, Iceland

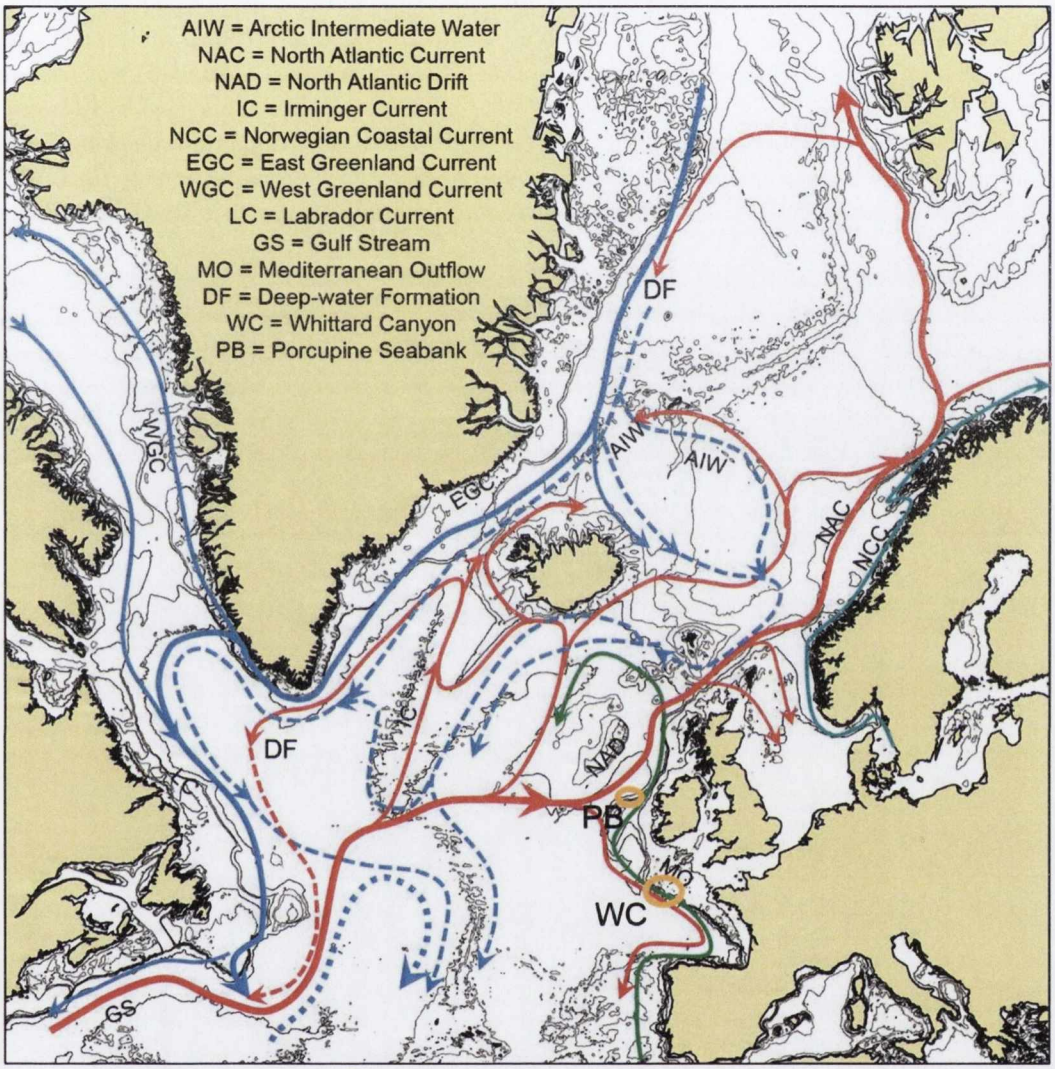


Figure 2.14: The map shows a compilation of North Atlantic currents as a basis for CWC occurrence (modified from Buhl-Mortensen et al., 2014). orange = investigated locations (this study); red = surface currents; blue = deep currents.

The NE Atlantic generally comprises surface waters in the uppermost 50-100 m separated from lower water masses by a seasonal thermocline (Dullo et al., 2008). Between 100 m and 400-600 m the East North Atlantic Water (ENAW) with temperatures $\geq$ 10.9°C and salinities between 35.2 and 36.7 psu (possibly influenced by Mediterranean Outflow Water (MOW) and Subarctic Intermediate Water (SAIW)) (Huvenne et al., 2011, Dullo et al., 2008). The permanent thermocline in the NE Atlantic is found between 600 and 1,000 m depth, connected to enhanced baroclinic tidal motions (at 400 to 700 m), and often coincides with the occurrence of cold-water coral mounds (Johnson et al., 2013, White & Dorschel, 2010). Semi-diurnal internal waves with high loads of fluorescent material are also reported from the Mingulay Reef, the Rockall Trough, the Ionian Sea (Mastrototaro et al., 2010, Guinan et al.,

2009a, 2009b, Roberts et al., 2009a, Genin et al., 1986). Underneath the ENAW the water of two branches of the MOW dominates regions in the eastern North Atlantic (fig. 2.14) with temperatures ranging from 2.6 to 11°C and high salinities (35-36.6 psu) down to a depth of 1,500 m (Johnson et al., 2013, Dullo et al., 2008) (fig. 2.15). From 1,500 to 3,000 m depth the North Atlantic Deep Water (NADW) which was formed in the Greenland-Norwegian Sea takes over with the Labrador Sea Water (LSW) (temperature = 3-4.5°C, salinity = 34.9-35.1 psu) dominating depths between 1,800 and 2,000 m (Dullo et al., 2008). Knowledge about variations in current systems and connected water masses through time (e.g. SPG gyre) and the impact on CWC occurrences is important to understand current settings (e.g. Douarin et al., 2013).

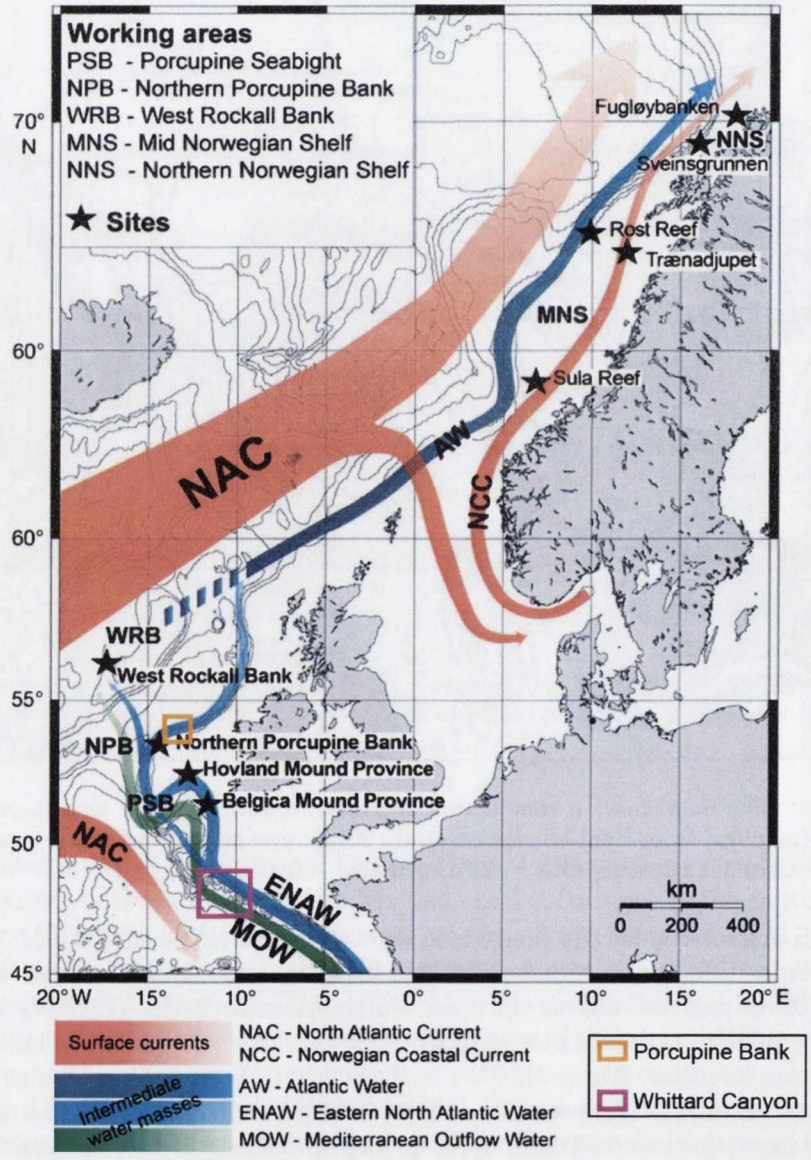


Figure 2.15: The map also shows the reaches of different currents in the NE Atlantic including the areas of Whittard Canyon, Porcupine Bank and Iceland (modified from Dullo et al., 2008). The path of the MOW around the area of the PB here varies from fig. 2.14.

Environmental studies in the presented thesis on different species will have a main focus on the Whittard Canyon (Chapters 5 to 9) which is located 400 km south of Mizen Head (Ireland). The ~200 km long canyon channels connect the continental shelf at about 200 m depth with the deep sea (Porcupine Abyssal Plain) down to around 4,300 m. Complex oceanographic systems regularly supply the local fauna with nutrients from the shelf (e.g. De Mol et al., 2011, Cunningham et al., 2005). The ecosystem in the canyons is rich, diverse and complex, and provides a perfect basis for the attempted research project.

Parallel to the study on biodiversity during research cruises CE12006 and CE13008 intensive oceanographic studies were performed along the different canyons (Wilson et al., 2015, Johnson et al., 2013). In the Whittard Canyon specifically the ENAW is found within the upper 500 m with temperatures around 12°C, a salinity range between 35.2 and 36.7 psu and densities around 27.2 kg/m^3 (fig. 2.16) (Huvenne et al., 2011). Below this the MOW with temperatures from 2.6 to 11°C, salinities from 35 to 36.2 psu and densities around 27.5 kg/m^3 includes the permanent thermocline which is associated with the occurrence of vertical walls with CWC assemblages (Johnson et al., 2013). The LSW is present with a core between 1,900 and 2,000 m (Johnson et al., 2013). The Whittard Canyon data indicates the presence of a strong benthic nepheloid layer (BNL) and several intermediate nepheloid layers (INL) with intenser INLs at 750 and 1,000 m and a possible connection with the MOW (Wilson et al., 2015) (fig. 2.17). Between 500 and 750 m the amount of measured suspended material was higher in spring (Johnson et al., 2013).

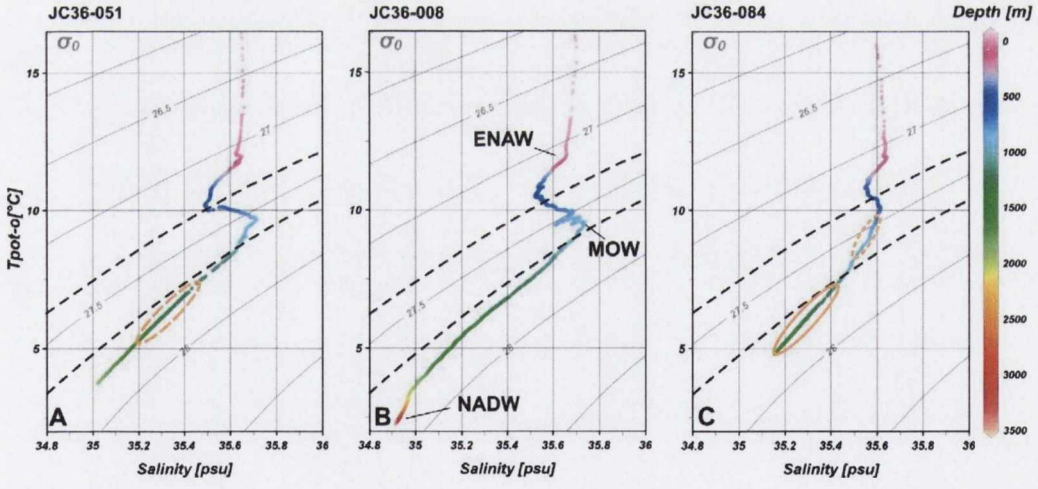


Figure 2.16: A study of CWC habitats in an eastern branch of the Whittard Canyon displays CWC occurrences along the recorded water profiles (from Huvenne et al., 2011).

Over the time of three years the study of BNLs and INLs in the Whittard Canyon found indications of a permanent presence of these layers (Wilson et al., 2015). The depths of resuspension of Suspended Particulate Matter (SPM) are defined as 400-500 m, 900-1,600 m and 1,700-1,800 m (in connection with baroclinic motions), 600-900 m (with reference to the permanent thermocline), as well as 700-1,100 m (related to the boundaries of the MOW) (Wilson et al., 2015). The surveys in spring 2011 and 2012 probably coincided with the onset of the phytoplankton spring bloom visible in SPM in the uppermost 500 m of the water column (Wilson et al., 2015). The

distribution of SPM found in Nepheloid Layers (NLs) is driven by local hydrodynamics and topographic interactions and influenced by density stratification (Wilson et al., 2015). The 2013 survey in June was marked by the absence of this feature which was interpreted as a progression of particles to deeper regions (Wilson et al., 2015). The study also showed the mixing efficiency of storm events in the area which initiates the fragmentation of INLs into thinner layers (Wilson et al., 2015). BNLs were present down to >2,500 m depth in all studied canyon branches (Wilson et al., 2015). The study found nitrogen (N) maxima between 575 and 975 m coinciding with the permanent thermocline (600-900 m) and the occurrence of INLs (~500-850 m) (Wilson et al., 2015). The periodicity of baroclinic tidal motions was discussed in context with sediment resuspension, transport and the formation of INLs (White & Dorschel, 2010). In two canyon arms a series of N peaks was detected in 725 m and 975 m (Wilson et al., 2015). The MOW in the canyons between 700 and 1,100 m showed indications of dilution of salinities (35.6-35.8 psu) and coincided with extensions of BNL and INL (Wilson et al., 2015). High SPM concentrations were observed between 1,000 and 1,100 m which cannot be related to MOW presence directly (Wilson et al., 2015).

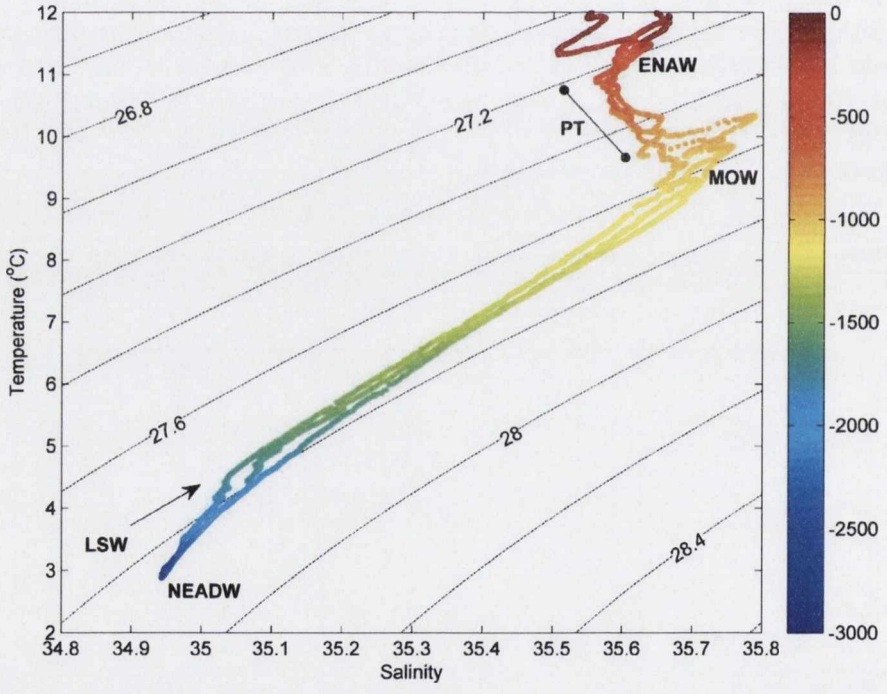


Figure 2.17: Characterisation of water masses in the Whittard Canyon from CTD profiles >2,000 m depth studied during research cruises CE11006, CE12006 and CE13008 (Wilson et al., 2015). Dashed lines represent isopycnals (in kg/m^3) (from Wilson et al., 2015). The colour scale represents depths. ENAW = Eastern North Atlantic Water; MOW = Mediterranean Outflow Water; LSW = Labrador Sea Water; NEADW = North Eastern Atlantic Deep Water; PT = permanent thermocline.

2.2.2 Mediterranean Sea - Santa Maria di Leuca reef province

The so-called White Coral Bank in the Santa Maria di Leuca area in the Mediterranean Sea receives oxygenated water from the south Adriatic Basin with temperatures around 12.92°C and salinities around 38.64 psu dominating depths between 600 and 1,000 m

(Savini et al., 2014, Taviani et al., 2005) (fig. 2.18). The Adriatic Dense Water (ADW) mixes with bottom water and turns into Eastern Mediterranean Deep Water (EMDW) with changed thermohaline properties (Savini et al., 2014). The reef province mainly consists of coral mounds within 300 to 1,100 m depth (Taviani et al., 2005).

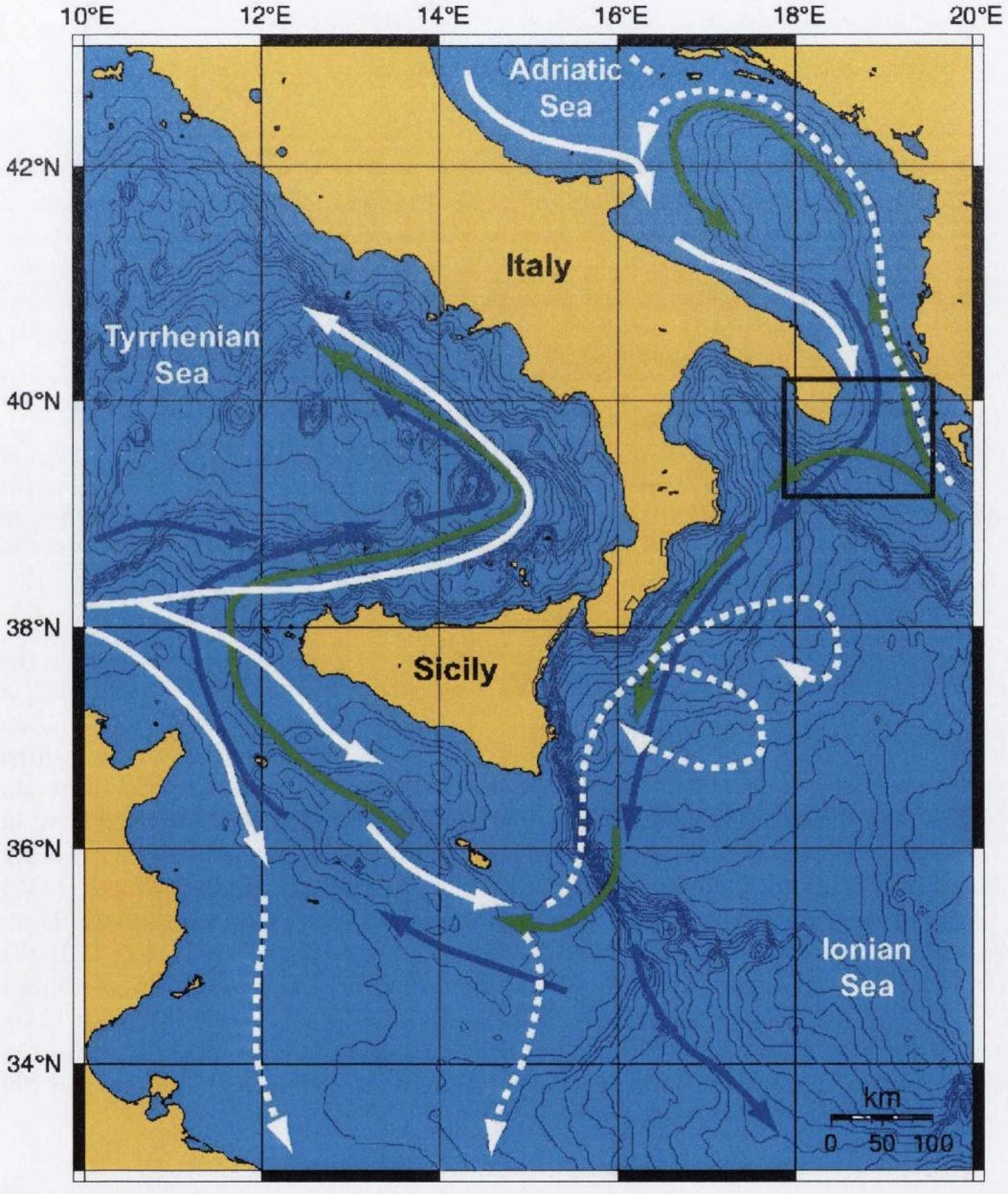


Figure 2.18: The map visualises the different currents and water masses around the Santa Maria di Leuca reef area (black box) (modified from Freiwald et al., 2009). White arrows = surface water Modified Atlantic Water (MAW) (annual); dashed white arrows = surface water MAW (seasonal); green arrows = intermediate water Levantine Intermediate Water (LIW); blue arrows = deep-water Eastern Mediterranean Deep Water (EMDW) (and WMDW in Tyrrhenian Basin (Freiwald et al., 2009)).

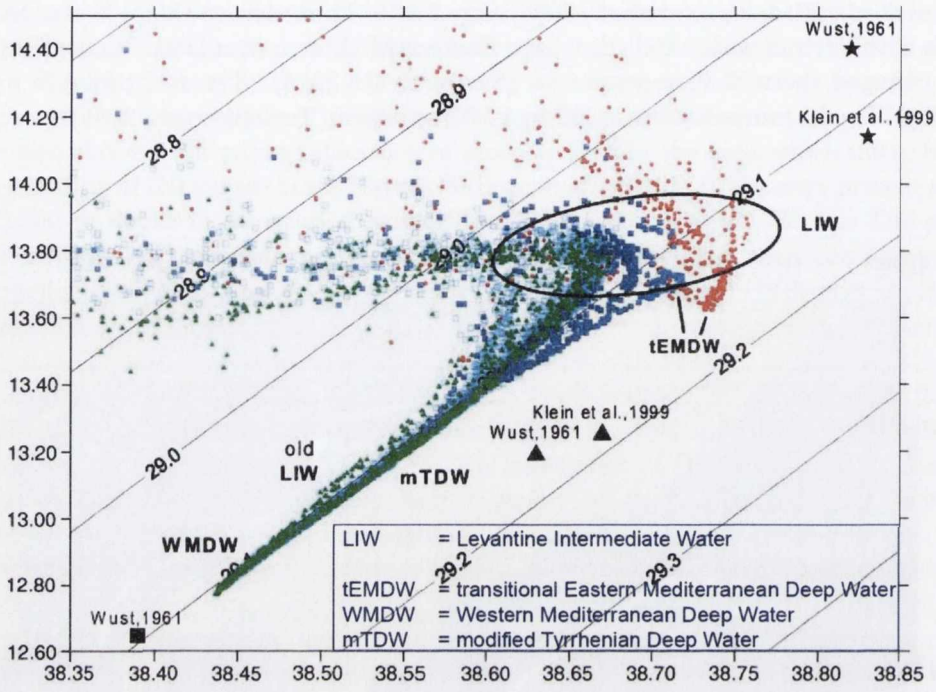


Figure 2.19: The plot shows temperature and salinity ranges with water densities for different water masses in the Mediterranean Sea (modified from Astraldi et al., 2002). Colours represent different study areas of Astraldi et al. (2002). Black stars represent typical values of Ionian LIW; black triangles of EMDW in the Ionian Basin; black squares of WMDW in the Algerian Basin (references see plot) (Astraldi et al., 2002).

A surface inflow of Atlantic water enters the Mediterranean Sea through the Strait of Gibraltar and spreads throughout the whole Mediterranean basin with a progressively increasing density (Freiwald et al., 2009, Astraldi et al., 2002) (fig. 2.19). While one part returns to the Atlantic as intermediate water the rest turns into deep water in the Mediterranean basin (Freiwald et al., 2009, Astraldi et al., 2002). The so-called Modified Atlantic Water (MAW) represents the surface layer in the central Mediterranean and represents an inflow into the Ionian Sea (among other areas) (Freiwald et al., 2009) (fig. 2.18). The Levantine Intermediate Water (LIW) experiences seasonal mixing with the MAW in winter and forms the Adriatic Deep Water (ADW), it becomes part of the Eastern Mediterranean Deep Water (EMDW) (Freiwald et al., 2009). The LIW is involved in the formation of all Mediterranean Deep Water, the North Adriatic Deep Water (NAdDW) is the densest water mass in the Mediterranean Sea with densities of up to 29.8 kg/m^3 and flows south to the Ionian Sea (mixing with the ADW) where it is seasonally present between 400 and 700 m overlain by the LIW (Freiwald et al., 2009).

In the Mediterranean Sea *L. pertusa* and *M. oculata* are found along steep walls and on the gently sloping shelf within temperatures between 13.5 and 13.8°C, salinities between 38.65 and 38.67 psu, densities from 29.07 to 29.12 kg/m^3 and dissolved oxygen contents between 3.98 and 4.54 ml/l (Freiwald et al., 2009). The salinities and consequently densities found here are beyond the reported tolerance range connected with CWC reef occurrences in the NE Atlantic (e.g. Dullo et al., 2008). In the Atlantic comparable densities would be rare and well beyond the reported coral occurrences.

2.2.3 Indian Ocean

The Indian Ocean basin is by far more extensive, more complex, and yet less intensively studied than, for example, the North Atlantic (Schott & McCreary, 2001). The current systems in the Indian Ocean are influenced by input from different basins and by seasonal variations due to monsoon activity present in currents down to 400 m depth (e.g. Schott & McCreary, 2001). Central waters consist of the Indian Equatorial Central Water (IECW) and South Indian Central Water (SICW) (Kennish, 2000). The IECW with salinities between 34.9 and 35.5 psu is found north of the equator down to depths of 1,000 m, while the SICW with salinities between 34.5 and 36.0 psu is found in depths around 500 m south of the equator (Kennish, 2000). The Atlantic and Antartic oceans play a major role in the formation of water masses in the Indian Ocean (Kennish, 2000). Kennish (2000) reported Common Water (CoW) to be the most extensive water mass below 1,000 m depth. It is a mixture of North Atlantic Deep Water (NADW) (upper CoW) and Antarctic Deep Water (AADW) (lower CoW) (Kennish, 2000). In addition to this simplified current system two types of overturning and seasonal variability produce a series of regional water masses with varying reaches depending on the time of year (Schott & McCreary, 2001).

A location of interest here is found close to the Amsterdam-St. Paul islands north of the Kerguelen Plateau and Antarctica. To the South of the Amsterdam islands a large part of the Antarctic Circumpolar Current (ACC) passes by (Park et al., 1991). North of the frontal zone at 1,000 m depth the Antarctic Intermediate Water (AAIW) is identified by its salinity minimum of 34.35 psu and an oxygen maximum (around 5 ml/l) (Park et al., 1991). The South Indian Central Water (SICW) then forms the thermocline water between the base of the subtropical surface water and the AAIW (Park et al., 1991). The relatively homogeneous so-called Mode Water is formed in winter and presents the upper part of the SICW down to ca. 500 m depth with temperatures of 11.5°C and salinities around 35.0 psu (fig. 2.20) (Park et al., 1991).

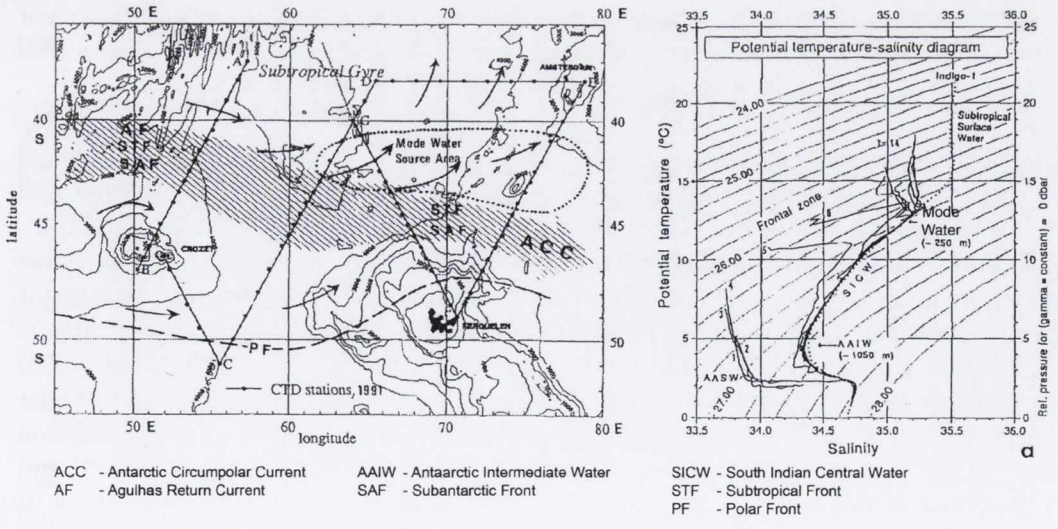


Figure 2.20: Flow pattern and characterisation of different water masses in the south Indian Ocean (modified from Park et al., 1991).

2.3 Skeletal Formation of Scleractinian Cold-Water Corals

This thesis attempts to identify signals of external parameters recorded in the precipitated skeleton. To discuss and understand geochemical patterns within the CWC skeleton it is important to look into biomineralisation processes of the corals, and physiological effects which might influence the incorporation of elements into the skeletal structure. Such physiological effects are commonly known as 'vital effects' (Weiner & Dove, 2003). They can occur in the form of fractionation effects caused by variations in kinetics during uptake, transport and/or deposition of isotopes, and as taxonomic effects which describe species-specific control over the isotopic composition to different degrees (metabolic effects) (Weiner & Dove, 2003). The process of biomineralisation (with regard to vital effects) has been subject to several published modelling attempts which will be discussed in the following sections.

2.3.1 (Micro-)Structural Growth

The idea of sclerochronology evolves around the study of periodicities in the microstructure to learn about age, growth rates and recorded environmental signals (e.g. Helmle & Dodge, 2011). The concept is similar to that of Dendrochronology which interprets the growth rings in trees. To connect skeletal geochemistry to environmental parameters the temporal factor of skeletal formation must be known. The available information on rates of multidirectional growth of scleractinian skeletons is mostly restricted to rates of longitudinal (linear) extension (growth in length) and varies widely depending on applied methodologies (Roberts et al., 2009b, Freiwald & Roberts, 2005) (table 2.4). Along the primary extension axis (growth in length, linear or longitudinal growth), the growth rate of *L. pertusa* is relatively low and usually reported as either the carbonate precipitation rate for a single polyp or as a colony expansion rate (table 2.4 and 2.6). *L. pertusa* and *D. dianthus*, for example, also expand their corallites (at a lower rate) by precipitating new layers on top of existing ones thereby thickening and stabilising the colony framework (Marali et al., 2013, Gass & Roberts, 2011, Mortensen & Rapp, 1998) (fig. 2.21 and 2.22). This radial growth or secondary growth axis is directly connected to steps in linear growth including septal growth (fig. 2.21) (e.g. Mortensen & Rapp, 1998).

Theca as well as septa show alternating opaque (white) and translucent (beige) layers parallel to the longitudinal growth axis indicating stepwise longitudinal and radial growth (Cohen et al., 2006, Mortensen & Rapp, 1998) (fig. 2.21 and 2.22). Variations within a third, latitudinal growth direction have been reported but never further investigated (Smith et al., 2002). The variation in layer colour may be a result of variations in growth rate and mineral density (white layers = high growth rates = low mineral density) (Marali et al., 2013, van de Locht et al., 2013). Freiwald (1998) suspected an intraskeletal organic matrix within areas of brownish impregnations under transmitted light equivalent to white layers. Young polyps show higher calcification rates during this early growth stage (Brooke & Young, 2009, Maier et al., 2009) and the majority of the skeletal extension appears to happen during the first year (Gass & Roberts, 2011).

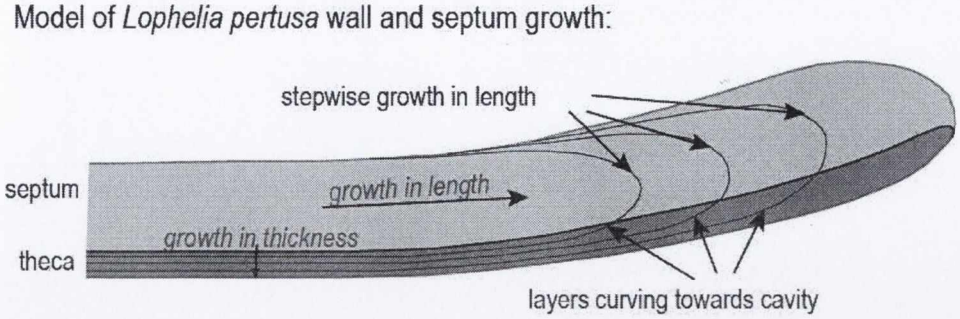


Figure 2.21: Stepwise growth of *L. pertusa* theca and septa influences the orientation of alternating layers (i.e. curving) (modified after Mortensen & Rapp, 1998).

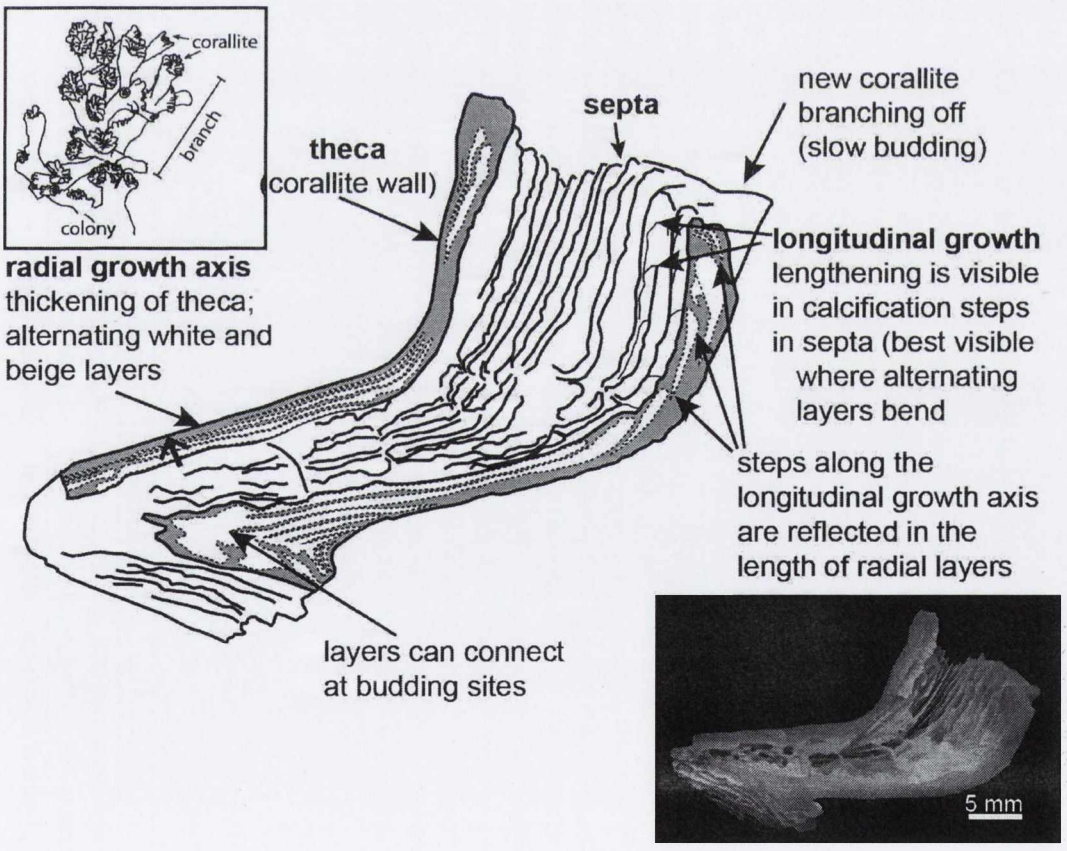


Figure 2.22: Sketch of *L. pertusa* microstructures in sample L1 as an example for corallite growth. The theca displays alternating white and beige (here grey) layers. For details on stepwise coral growth and origin of layer orientation see fig. 2.21.

Table 2.4: List of selected published research on annual CWC extension rates for the scleractinian species in focus.

species	depth	growth rate	method	reference
Lophelia pertusa	955-1006 m	7 mm/a	linear extension; man-made structure	Duncan (1877)
Lophelia pertusa	800 m	6 mm/a	linear extension; man-made structure	Wilson (1979)
Lophelia pertusa	300 m	25 mm/a	linear extension; SIA	Mikkelsen et al. (1982)
Lophelia pertusa	250 m	19 mm/a	linear extension; SIA	Freiwald et al. (1997)
Lophelia pertusa	200-350 m	6 mm/a	linear extension; SIA	Mortensen & Rapp (1998)
Lophelia pertusa	60-109 m	26 mm/a	linear extension; man-made structure	Bell & Smith (1999)
Lophelia pertusa	100 m	5 mm/a	linear extension; man-made structure	Roberts (2002)
Lophelia pertusa	220 m	2.2-5 mm/a	U series	Pons-Branchu et al. (2005)
Lophelia pertusa	94-115 m	19-34 mm/a	linear extension; man-made structure	Gass & Roberts (2006)
Lophelia pertusa	aquarium	15-17 mm/a	linear extension; aquarium	Orejas et al. (2008)
Lophelia pertusa	430-520 m	2.14-3.77 mm/a	staining, linear extension	Brooke & Young (2009)
Lophelia pertusa	146-160 m	27.4±5 mm/a	linear extension; man-made structure	Gass & Roberts (2011)
Lophelia pertusa	300-350 m	~8 mm/a	linear extension; $^{226}Ra/^{210}Pb$	Sabatier et al. (2012)
Lophelia pertusa	127-134 m	up to 12 mm/a	^{14}C dating	Douarin et al. (2013)
Lophelia pertusa	520 m	7.5±1.2mm/a	staining, linear extension (young)	Lartaud et al. (2013)
Lophelia pertusa	520 m	1.3±1.5mm/a	staining, linear extension (young)	Lartaud et al. (2013)
Madrepora oculata	aquarium	3-18 mm/a	linear extension	Orejas et al. (2008)
Madrepora oculata	aquarium	5 mm/a	linear extension	Orejas et al. (2011)
Madrepora oculata	aquarium	0.2±0.09%/d	buoyant weight technique	Orejas et al. (2011)
Madrepora oculata	300-350 m	14.4±1.1 mm/a	linear extension; $^{226}Ra/^{210}Pb$	Sabatier et al. (2012)
Madrepora oculata	520 m	3.5±2.1 mm/a	staining, linear extension (mature)	Lartaud et al. (2013)
Madrepora oculata	520 m	1.2±1.2 mm/a	staining, linear extension (mature)	Lartaud et al. (2013)
Solenosmilia variabilis	1238/1454 m	~1 mm/a	linear extension	Fallon et al. (2014)
Enallopsammia rostrata	1410 m	0.07 mm/a	radial extension; $^{226}Ra/^{210}Pb$	Adkins et al. (2004)
Enallopsammia rostrata	1410 m	5 mm/a	linear extension; $^{226}Ra/^{210}Pb$	Adkins et al. (2004)
Desmophyllum dianthus	421-2180 m	0.1-3.1 mm/a	linear extension; septa; U/Th	Cheng et al. (2000)

species	depth	growth rate	method	reference
Desmophyllum dianthus	n/a	0.5-1 mm/a	linear extension; coupled U/Th and ^{14}C	Risk et al. (2002)
Desmophyllum dianthus	395 m	0.5-2 mm/a	linear extension; $^{226}Ra/^{210}Pb$	Adkins et al. (2004)
Desmophyllum dianthus	aquarium	0.1-0.3%/d	total alkalinity (TA) technique	Naumann et al. (2011)
Desmophyllum dianthus	14-22 m	1.18-2.76 μm/d	septal extension	Hassenrück et al. (2013)
Desmophyllum dianthus	18 m	0.25$\pm$0.18%/d	weighing	Jantzen et al. (2013)

Table 2.6: Accumulated CWC extension rates for the scleractinian species listed in 2.5.

species	accumulated growth rate
Lophelia pertusa	1.3-34 mm/year
Madrepora oculata	1.2-18 mm/year
Solenosmilia variabilis	$\sim$1 mm/a
Enallopsammia rostrata	5 mm/year
Desmophyllum dianthus	0.1-3.1 mm/year

While aquarium observations revealed a growth rate of 15-17 mm/year for *L. pertusa* with the addition of four corallites per year (Orejas et al., 2008), *in-situ* colony growth was estimated to up to 26 mm/year from observations on oil platforms (Gass & Roberts, 2006). The experiment setup showed 3-18 mm/year extension with five corallites per year for *M. oculata* (Orejas et al., 2008). Roberts et al. (2009b) compiled existing research results to show that the growth rates (extension and expansion) display an apparent linear correlation with increasing depth of the habitat. The summary of published growth rates generally shows higher rates for shallower depths but no statistically significant linear or exponential correlation (compare table 2.3). Recent staining experiments highlighted areas of growth over short periods of time (Lartaud et al., 2013, Brooke & Young, 2009). This type of study, however, is rather suited for providing very detailed insight into momentary growth rates and complexity of growth than for observations over longer time intervals and presents no option for deeper open ocean studies.

2.3.2 Ultrastructural Growth

The analysis of microstructural units in coral skeletons started with tropical corals and was extended to CWCs during the last decades (Motai et al., 2012, Cuif & Dauphin, 2005a, b, Cuif et al., 1999b, Mortensen & Rapp, 1998, Constantz, 1986). *L. pertusa* was the first CWC species to receive detailed attention and is still the best studied species in the NE Atlantic (Cuif & Dauphin, 2005a, Cuif et al., 1999b, Mortensen & Rapp 1998). The solitary species *D. dianthus*, on the other hand, has provided an additional basis for detailed research due to its high abundance, larger size and longer lifespan (Marali et al., 2013, Cuif et al., 1999b, Lazier et al., 1999). Unfortunately *D. dianthus* is also strongly affected by bioerosion which is assumed to influence growth rate, cause deformation and may cause additional fractionation (Hassenrück et al., 2013, Boerboom et al., 1998).

From the onset of coral studies, an agreement was reached that all corals show a clear differentiation between two basic microstructural units: 'centers of calcification' (CoCs) and fibres (Juillet-Leclerc et al., 2009, Meibom et al., 2008, Cuif & Dauphin, 2005a, 1998, Reitner, 2005, Meibom et al., 2004, Cuif et al., 1999b, Lazier et al., 1999, Constantz, 1986, Ogilvie, 1896). During later studies structures known as CoCs were described as 'early mineralization zones' (EMZs) which more accurately describes their connection to ontogenic phases (Rollion-Bard et al., 2010, 2009). The CoCs and fibres have also been referred to as 'rapid accretion deposits' (RAD) and 'thickening deposits' (TD), respectively, with regard to the observed difference in growth rates (Rollion-Bard & Blamart, 2015, Domart-Coulon et al., 2014, Stolarski, 2003). This terminology allows for the possibility of more than one phase with high biomineralisation rates (table 2.8).

Table 2.8: Summary of terms for different structural features identified in coral skeletons with abbreviations throughout literature.

Abbreviation	Structure	Growth Rate	Reference
CoC	centres of calcification	high	e.g. Constantz, 1986
EMZ	early mineralisation zones	high	e.g. Cuif et al., 2003
RAD	rapid accretion deposits	high	e.g. Stolarski, 2003
	fibres	low	e.g. Constantz, 1986
TD	thickening deposits	low	e.g. Stolarski, 2003

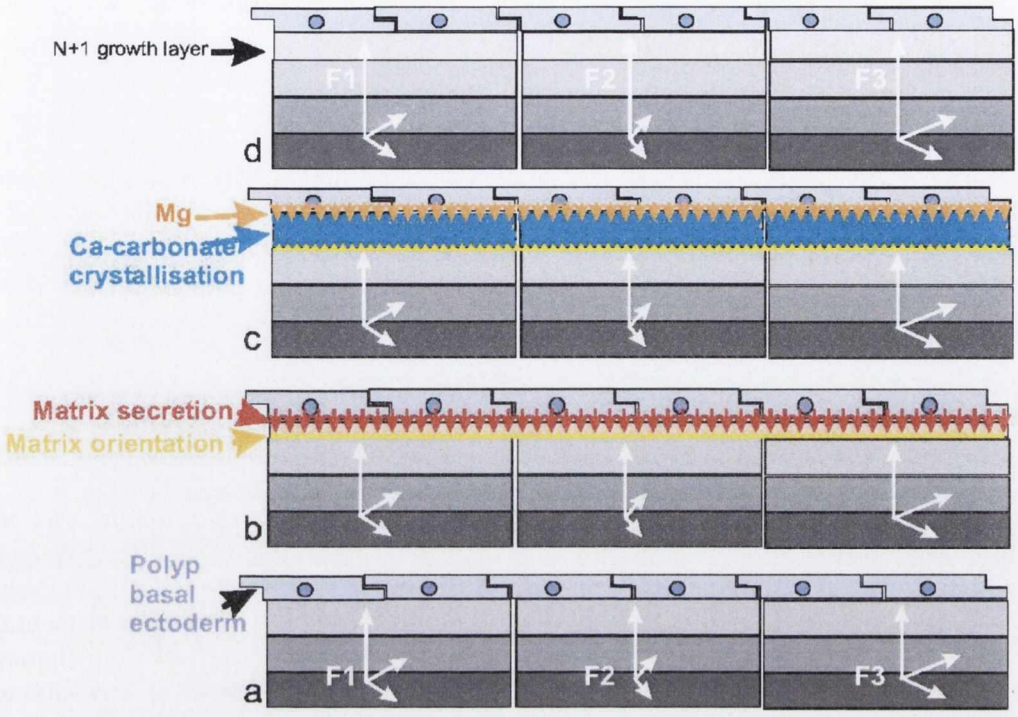


Figure 2.23: Growth layer formation model based on studies on tropical corals (from Cuif & Dauphin, 2005b). F1, F2 and F3 present three adjacent fibre bundles in the uppermost layers (3D growth indicated by arrows).

CoCs are composed of granular crystals, also described as trabecular nuclei, and organic components (e.g. Stolarski, 2003, Cohen et al., 2001, Lazier et al., 1999, Constantz, 1986). The proximity of these granules to each other and the shape they form differentiates between coral species (Cohen & McConnaughey, 2003, Cuif et al., 1999b, Cuif & Dauphin, 1998, Constantz, 1986, Bryan & Hill, 1941). For *L. pertusa* and *D. dianthus* the formation of continuous CoC lines was reported (Cuif et al., 1999b, Lazier et al., 1999). Scanning electron microscope (SEM) images confirmed these structures along theca (Mouchi et al., 2014, Gass & Roberts, 2011, Rollion-Bard et al., 2010) and septum (Rollion-Bard et al., 2010, Blamart et al., 2007, Cuif et al., 2003) of *L. pertusa*.

CoCs and fibres show biochemical differences in organic components (Gautret et al., 2000). The fibres or so-called 'sclerodermites' (Reitner, 2005, Cohen & McConnaughey, 2003) or 'fascicles' (Ogilvie, 1896) or 'fasciculi' (Constantz, 1986) are elongated along the crystallographic *c*-axis and arranged in fans (Cuif et al., 1999b). In Scanning Electron Microscopy (SEM) images these often show bands cutting across them, which causes a layer-like appearance without the general structure of the fibres appearing interrupted (Mouchi et al., 2014, Marali et al., 2013, Motai et al., 2012, Reitner, 2005, Cuif et al., 2003, Cuif et al., 1999b). Some authors suspect a repetition of crystal nucleation cycles and growth (Cohen et al., 2006, Cuif et al., 1999b). Some suggested sheets of organic matrix to function as fibre nucleation sites and organic envelops which surround fibres (Gautret et al., 2000, Cuif & Dauphin, 1998, Freiwald, 1998). Others reported networks of thin organic-rich lines among fibrous material (Holcomb et al.,

2009, Stolarski, 2003). High amounts of organic sulfates were also found within the EMZs which suggests that organic secretions lay the foundation for the crystallisation of the mineral phase as shown in a 2-step-model (Cuif & Dauphin, 2005a, b, Cuif et al., 2003, Cuif et al., 1999b) (fig. 2.23). In the illustrated model (fig. 2.23) the organic phase is reduced to the space between minerals as a cortex surrounding the nanograins after Ca-carbonate crystallisation (Cuif & Dauphin, 2005b). The soluble organic matrix in *L. pertusa* and *M. oculata* differs from tropical corals in amino acid composition (Cuif et al., 1999a, Gautret et al., 1997). This concept in connection with crystal formation can help explain trace and minor element compositions incorporated into different biomineralisation zones.

2.3.3 Models of Coral Biomineralisation and Elemental Incorporation

Biomineralisation describes the process by which organisms form minerals, and in many cases also incorporate organic components into the crystal matrix (Weiner & Dove, 2003). Corals generally calcify their aragonitic skeleton extracellularly (Allemand et al., 2004, Weiner & Dove, 2003). A number of mechanisms for elemental incorporation into coral skeletons based on calcification with (e.g. McConnaughey et al., 1997) and without (e.g. Allemand et al., 2004) the existence of a calcifying fluid i.e. absence or presence of direct contact between tissue and skeleton during growth have been discussed so far and will be introduced in the following paragraphs: pH regulation in an extracytosolic (extracytoplasmic) calcifying fluid (ECF) due to ion pumping (via enzymes, ion channels, vacuoles), the existence of a carrier phase (e.g. Amorphous Calcium Carbonate (ACC)), precipitation rate effects, and Rayleigh fractionation (RF) (see e.g. Rollion-Bard & Blamart, 2015).

McConnaughey et al. (1997) suggested a model for biomineralisation processes in tropical corals based on a semipermeable membrane, the existence of a pumping mechanism for divalent cations and passive transport of anions in connection with a pH gradient (fig. 2.24). The model is based on pH control in the ECF between cell layer and skeleton by an ATP-driven ion pump which promotes the exchange of H^+ for Ca^{2+}. The ECF is modeled as a (semi-)isolated pool which is episodically or continuously replenished with seawater as the source of Ca^{2+} and trace elements (Sinclair & Risk, 2006). This influences the pCO_2 in the ECF where a high pH facilitates calcification (McConnaughey et al., 1997). The original model (fig. 2.24) included removal of CO_2 by photosynthetic activity of zooxanthellae as one of the different suggested pathways but allowed for alternatives (McConnaughey et al., 1997). Adkins et al. (2003) suggested the exchange of $[CO_2]_{aq}$, instead of HCO_3^-, over pericellular channels as part of the pH gradient which adapted the model for azooxanthellate coral growth as in the case of the investigated CWCs (fig. 2.24). Ca^{2+} supply was suspected to be derived directly from ambient seawater via ion channels or Ca-ATPase enzymes (e.g. Gagnon et al., 2012, Zoccola et al., 2004, 1999, Tambutté et al., 1996, Isa et al., 1980). A similar enzyme which specialises in Mg transport is known as well (Ip & Lim, 1991). Variations in ECF pH are attributed to the mineralisation of different structures (RAD and TD) of the CWC skeleton (Rollion-Bard & Blamart, 2015, Rollion-Bard et al., 2011, 2010, Holcomb et al., 2009).

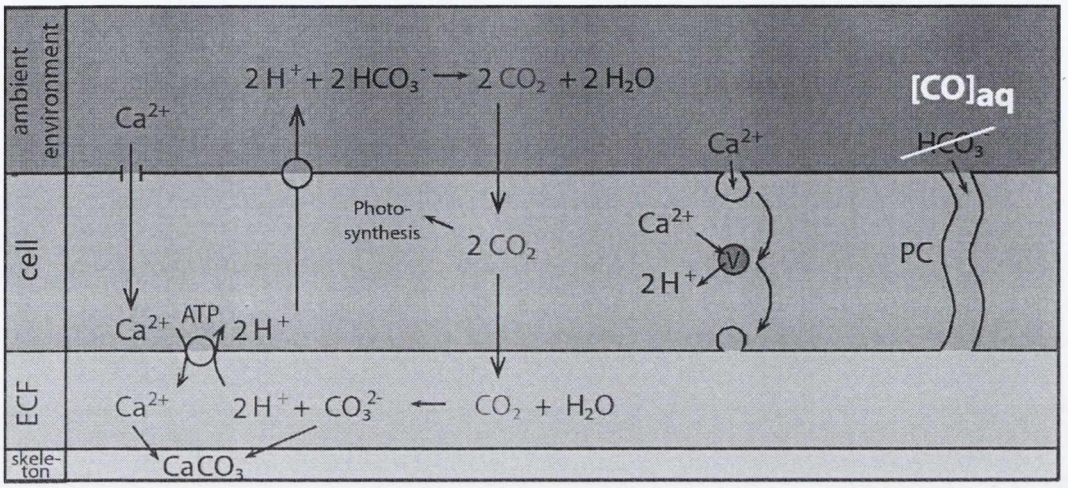


Figure 2.24: Model by McConnaughey et al. (1997) (modified): Exchange of Ca^{2+} and H^+ with the help of a Ca-ATPase drives ion exhange. Ca^{2+} can also be transported across the cell wall in vacuoles (V) while for HCO_3^- the use of pericellular channels (PC) is suggested. Adaptions suggested by Adkins et al. (2003) in white.

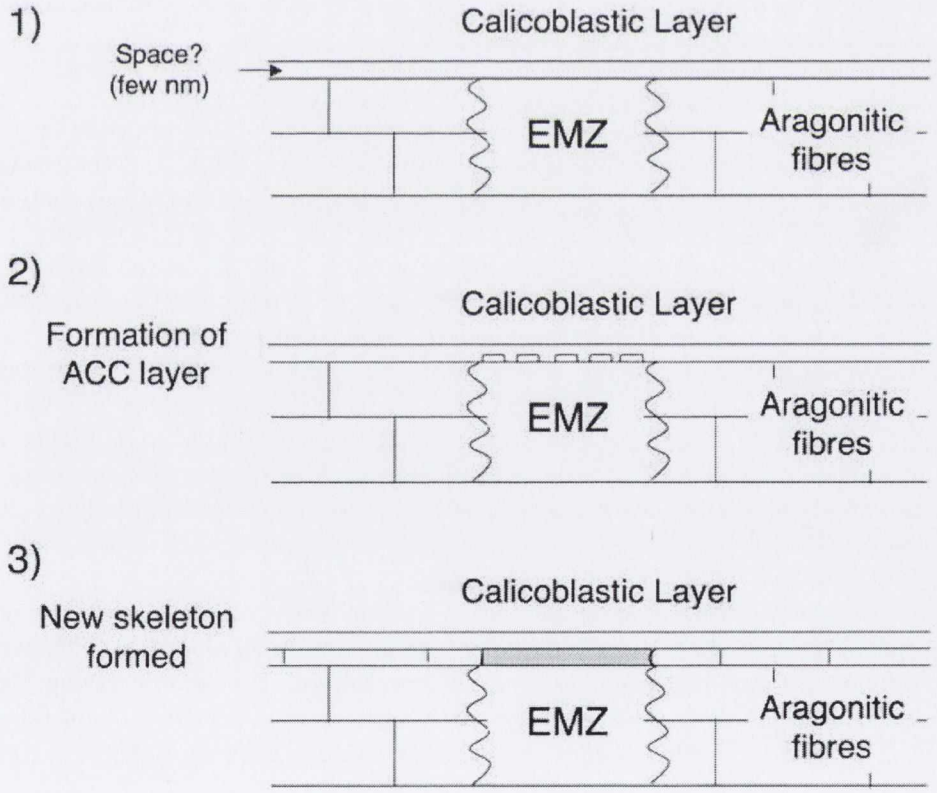


Figure 2.25: A proposed alternative to discussed calcification models (from Rollion-Bard et al., 2010). First the calicoblastic layer lifts to create a space on the aragonitic fibres. Step 2 then describes the involvement of ACC in the precipitation of fibres and EMZ. Finally ACC mineralises to form new skeletal layers.

An impact of precipitation rates on partition coefficients and a consequent modification of the crystallographic structure was suggested (Rollion-Bard & Blamart, 2015). A good example for such a growth rate dependent mechanisms is the 'surface entrapment model' (Gabitov et al., 2008, Watson, 1996). It states that high growth rates potentially increase the chance of incorporation of 'isotopically' enriched crystal surface layers independent of isotopic mass which could account for variations in elemental composition along growth (Gabitov et al., 2008). Higher precipitation rates also increase the number of lattice defects due to the connected decrease in density (typically RAD) (e.g. Montagna et al., 2014, van de Locht et al., 2013). The entrapment of trace and minor elements in lattice defects has been suggested as an alternative process to explain enrichment and variations in elemental concentrations (e.g. Montagna et al., 2014, Mitsuguchi et al., 2012. Modifications of the crystallographic structure can involve substitution mechanisms where different isotopic radii or charges decrease the probability of a simple substitution of Ca^{2+} by other elements (Speer, 1983). Rollion-Bard & Blamart (2015) discussed zones with RAD-like compositions as former RADs which have been incorporated into fibres during thickening.

The RF is currently one of the most popular mechanisms to explain elemental variations (Rollion-Bard & Blamart, 2015, Montagna et al., 2014). RF is based on the existence of an ECF as a semi-closed or closed reservoir (e.g. Rollion-Bard & Blamart, 2015, Montagna et al., 2014). The fluid is assumed to initially have a composition similar to ambient seawater (e.g. Rollion-Bard & Blamart, 2015, Montagna et al., 2014) and the fractionation may be described as

$$(Me/Ca)_{CWC} = D_{Me} * (Me/Ca)_0 * F^{(D_{Me}-1)}, \tag{2.1}$$

where D_{Me} is the partition coefficient between the aragonitic CWC and the seawater for an element Me, F is the fraction of Ca in the fluid relative to the initial content of Ca, and $(Me/Ca)_0$ is the initial Me/Ca ratio of the fluid, $(Me/Ca)_{CWC}$ is the ratio incorporated into the coral skeleton (e.g. Gagnon et al., 2007). In the model these elements with a partition coefficient $D_{Me} > 1$ (e.g. Sr or Ba) will be preferentially incorporated into the structure, consequently the fluid will be gradually depleted of these elements (e.g. Gagnon et al., 2007). With progressive carbonate precipitation the elements with a partition coefficient $D_{Me} < 1$ (e.g. Mg) which are initially discriminated against at starting conditions are then incorporated at a higher rate after the fluid was depleted of the preferred elements; this process continues until the fluid is replenished and the cycle starts again (e.g. Rollion-Bard & Blamart, 2015, Gagnon et al., 2013).

An alternative was suggested in the form of a model based on McConnaughey et al. (1997) and Cohen & McConnaughey (2003) with the addition of an organic-rich carrier phase or ACC as a possible precursor phase in aragonite precipitation carrying higher elemental concentrations (e.g. in Mg) (fig. 2.25) (Politi et al., 2010, Rollion-Bard et al., 2010, Meibom et al., 2004, Addadi et al., 2003, Weiner & Dove, 2003).

Over the last decades the location of biomineralisation has been suggested to lie in the soft tissue itself as well as in the secreted mucus. A thin layer of mucus between the skeleton and its overlying soft tissue was hypothesised to be an origin of initial mineral crystallisations (Reitner, 2005). The study revealed comparable protein compositions for the mucus excreted on the epidermal surface and the one building

up the layer between skeleton and tissue (Reitner, 2005). These findings invite an evaluation of mucus as one potential contributor to the ECF but were, as far as visible from published data, never investigated further.

2.4 Biogeochemistry

2.4.1 Analytical Techniques - State-of-the-Art

Stable Isotope Ratios

Standard analysis of stable oxygen and carbon isotope ratios is commonly performed by Multi-Collector Isotope-Ratio Mass Spectrometry (MC-IRMS) (e.g. Marali et al., 2013) or Secondary Ion Mass Spectrometry (SIMS) (e.g. Rollion-Bard et al., 2010) while stable boron isotope ratios so far were measured using either Thermal Ionization Mass Spectrometry (TIMS) (e.g. McCulloch et al., 2012), SIMS (e.g. Rollion-Bard et al., 2010) or ion microprobe (e.g. Rollion-Bard et al., 2011). The use of Laser Ablation Inductively Coupled Plasma Mass Spectrometry (LA-ICP-MS) to acquire $\delta^{11}B$ ratios in coral carbonates is still being tested (Kaczmarek et al., 2015, Fietzke et al., 2010). Sampling is usually performed as a series of spots along growth (e.g. Rollion-Bard et al., 2010) or as a series of microdrill lines parallel to growth layers (e.g. Marali et al., 2013).

Trace and Minor Element Compositions

Table 2.9: Different techniques used for trace and minor element composition analysis including examples of studies:

Technique	Study (example)
Inductively Coupled Plasma Optical Emission Spectrometty (ICP-OES)	Dietzel et al., 2004
Secondary Ion Mass Spectrometry (SIMS) and NanoSIMS	Gaetani et al., 2011 Rollion-Bard & Blamart, 2015
Multi-Collector Inductively Coupled Plasma Mass Spectrometry (MC-ICP-MS)	Robinson et al., 2006
Laser Ablation Quadrupole Inductively Coupled Plasma Mass Spectrometry (LA-Q-ICP-MS)	Montagna et al., 2014

2.4.2 Stable Oxygen and Carbon Isotope Ratios

Several studies have analysed light stable isotope ratios along one of the growth directions in the corallite wall or in septa of aragonitic CWCs in order to detect fractionation effects and their relation to environmental parameters (López Correa et al., 2010, Adkins et al., 2003, Rollion-Bard et al., 2003, Spiro et al., 2000, Freiwald, 1998, Mortensen & Rapp, 1998, Mikkelsen et al., 1982). Due to technical limitations caused by the necessary minimum sample weight most studies are, however, restricted to a relatively low resolution. While early studies applied spot sampling (ca. 1 mm ø) along linear growth (e.g. Freiwald, 1998, Mortensen & Rapp, 1998), more recent

studies use 2-3 mm long lines of circa 100 μm width parallel to the external wall surface oriented along growth layers to cover variations along radial growth (e.g. Marali et al., 2013, López Correa et al., 2010).

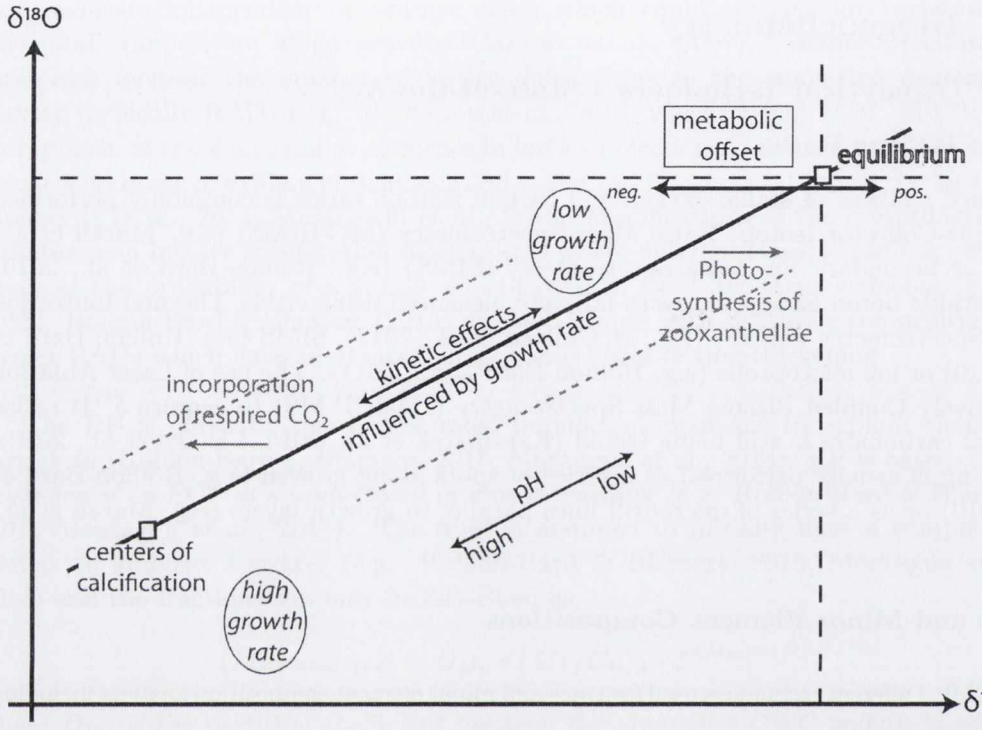


Figure 2.26: A linear regression of $\delta^{13}C/\delta^{18}O$ ratios reveals kinetic effects while deviations from the correlation can be interpreted as metabolic effects (modified after Adkins et al., 2003, McConnaughey et al., 1997, Emiliani et al., 1978). The linear regression of $\delta^{13}C/\delta^{18}O$ shows kinetic fractionation relative to the equilibrium with seawater and metabolic fractionation in the form of deviations from the line.

Different growth phases can show different fractionation effects affected by metabolic activity and variations in growth rate identifiable at higher resolution (e.g. McConnaughey, 1989a, 1989b). With increasing growth rate, the effects of kinetic fractionation on the light stable isotope composition of the skeleton seem to increase (López Correa et al., 2010, Rollion-Bard et al., 2010, Juillet-Leclerc et al., 2009, Blamart et al., 2007, Adkins et al., 2003, Rollion-Bard et al., 2003, McConnaughey et al., 1997, McConnaughey, 1989a, 1989b, Emiliani et al., 1978) (fig. 2.26). Indeed, EMZs within the skeleton of *L. pertusa* are known to exhibit high fractionation effects in connection with high growth rates typical of initial calcification phases which are reflected in low $\delta^{13}C/\delta^{18}O$ (Cohen & Gaetani, 2010, Rollion-Bard et al., 2010, 2009, 2003, Cohen et al., 2006, Blamart et al., 2005, Cuif & Dauphin, 2005a) (fig. 2.26). Increasing availability of food supply is one possible factor causing increased growth rates (Roberts et al., 2009b). When looking at other phylla, Putten et al. (2000), for example, found minima in $\delta_{13}C_{shell}$ in calcitic bivalves during spring peak primary production coinciding with Chl α maxima. No similar study is yet available for CWCs.

'Lines Technique' for Temperature Reconstruction

The reconstruction of ambient water parameters, like temperatures, salinities or pH is one aim of research in environmental sciences. Stable oxygen isotope ratios were discussed in connection with coral growth and environmental reconstruction (López Correa et al., 2010, Rollion-Bard et al., 2010, Gagnon et al., 2007, Blamart et al., 2007, 2005, Adkins et al., 2003, Rollion-Bard et al., 2003, Cuif & Dauphin, 1998, Emiliani et al., 1978). This is, however, complicated by species-specific fractionation effects. In 2000 Smith et al. introduced the so-called 'lines technique' in an attempt to overcome this obstacle and to use stable oxygen and carbon isotope ratio trends for temperature reconstructions (eq. 2.2 and 2.3) (fig. 2.27). Smith et al. (2000) provided two possible equations for the approach, based on boundary conditions depending on the available information on ambient water parameters: for $\delta^{13}C_{CWC} = \delta^{13}C_{water}$ (eq. 2.2) and for unknown water geochemistry $\delta^{13}C_{water} = \delta^{18}O_{water} = 0$ (eq. 2.3). $\delta^{18}O_{CWC}$ marks the intercept of the $\delta^{13}C/\delta^{18}O$ regression line with the y-axis.

$$\delta^{18}O_{CWC} - \delta^{18}O_{water} = (-0.25 \pm 0.01) * T(°C) + (4.97 \pm 0.24) \quad (2.2)$$

$$\delta^{18}O_{CWC} = (-0.22 \pm 0.01) * T(°C) + (4.51 \pm 0.35) \quad (2.3)$$

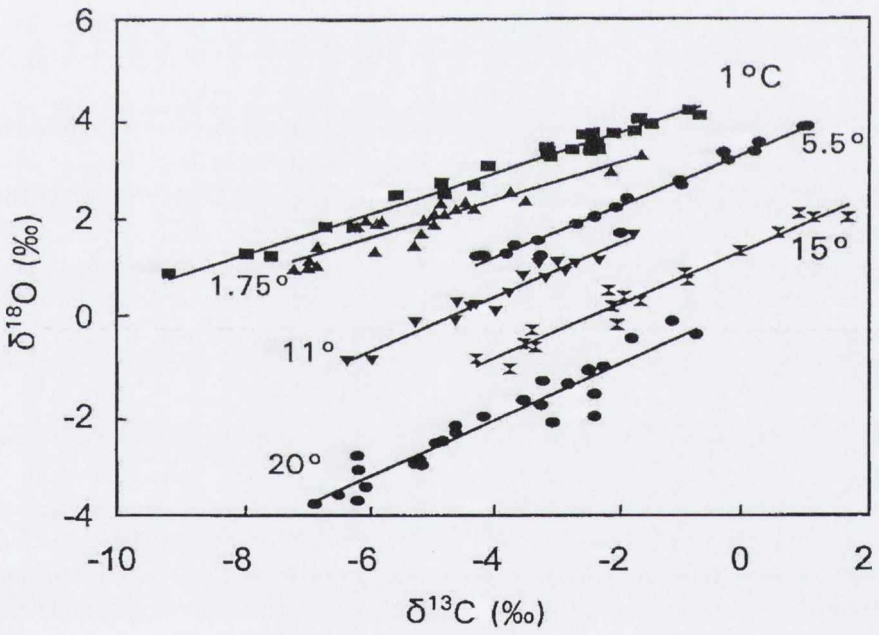


Figure 2.27: Different regression lines for six solitary corals from different temperature regimes (Smith et al., 2000).

This technique is applicable only under the premise that the data points can be plotted onto a statistically robust regression line (Smith et al., 2000). Deviations from the regression line between $\delta^{18}O$ and $\delta^{13}C$ can be indications of the existence and magnitude of metabolic effects (McConnaughey et al., 1997, McConnaughey, 1989a, 1989b). The approach was tested on a number of coral species, both tropical and cold-water, with varying results (Marali et al., 2013, Heikoop et al., 2000, Smith et al., 2000, Spiro et al., 2000). Different slopes in the plotted correlations between stable carbon ($\delta^{13}C$) and oxygen ($\delta^{18}O$) isotope ratios were also discussed in connection with

different geographical regions, and consequently different water masses and temperature regimes, and results from several locations were published (Spiro et al., 2000, Mortensen & Rapp, 1998, Mikkelsen et al., 1982). One problem still remaining, however, might be the existence of species-specific variations, especially where different species are used together in the same reconstruction model. In addition to tropical species a number of CWCs (e.g. *L. pertusa* and *D. dianthus*) are commonly used for the model (e.g. Marali et al., 2013, Smith et al., 2000). The cold-water corals *M. oculata*, *S. variabilis* or *E. rostrata* have not yet received much attention in this field.

2.4.3 Stable Boron Isotope Ratios

Stable boron isotope ratios in coral carbonates have been discussed in the light of seawater-pH reconstruction for some time (e.g. Trotter et al., 2011, Blamart et al., 2007). On one hand, boron uptake (B/Ca) is said to be controlled by temperature while δ^{11}B is seen in connection with pH variations within the seawater (including some species-specific biological fractionation) (Rollion-Bard et al., 2011, Trotter et al., 2011, Klochko et al., 2009, 2006, Blamart et al., 2007, Pagini et al., 2005, Zeebe, 2005).

Boron is found in two species in the ocean: borate ($B(OH)_4^-$) and boric acid ($B(OH)_3$), where borate is often assumed to be the species incorporated into CWC aragonite from an internal calcifying fluid (Wall et al., 2015, Anagnostou et al., 2012, McCulloch et al., 2012, Allison et al., 2010, Klochko et al., 2009, Pagini et al., 2005). The main discussion point evolves around the question whether both of the boron species are incorporated into the coral skeleton and at what ratio (Rollion-Bard et al., 2011, Trotter et al., 2011). High Field Magic Angle Spinning Nuclear Magnetic Resonance (^{11}B MAS NMR) suggested that the presence of both species in different proportions is related to microstructure (Rollion-Bard et al., 2011). The approaches for the reconstruction of ambient pH are complicated by differences in δ^{11}B within different microstructural units (EMZs and fibres) which was attributed to different incorporation ratios of the two boron species (Rollion-Bard et al., 2011, Blamart et al., 2007).

The ability to adjust the internal pH is attributed to both, shallow water corals and CWCs, but is still under investigation (e.g. Trotter et al., 2011, Blamart et al., 2007). Additionally a stronger correlation with seawater aragonite saturation state (Ω) than with pH was suggested (McCulloch et al. 2012). The proposed IpHRAC (Internal pH regulation abiotic calcification) model argues for a powerful pH_{cf} regulation mechanism (pH_{cf} = pH of the calcifying fluid) (McCulloch et al., 2012). A gradient between internal pH and external seawater pH was reported by many studies and the increase in internal pH ranges between 0.5 and >1 pH units (measured and reconstructed) depending on the region of the skeleton and the calcifying species (e.g. Raddatz et al., 2014, Anagnostou et al., 2012, Rollion-Bard et al., 2011, Trotter et al., 2011, Blamart et al., 2007, Al-Horani et al., 2003). Whether reconstructed pH variations in the skeleton are in agreement with common calcification models is still discussed (e.g. Anagnostou et al., 2012, McCulloch et al., 2012, Rollion-Bard et al., 2011, Blamart et al., 2007). So far, two relationships between internal and external pH were suggested.

$$\Delta pH = -(0.75 \pm 0.12) * pH_{SW} + (6.88 \pm 0.93) \tag{2.4}$$

$$\Delta pH = -0.71 * pH_{SW} + 6.43 \tag{2.5}$$

The equation (ΔpH) marks the difference between internal and external pH. Equation 2.4 was reported by Anagnostou et al. (2012), equation 2.5 by McCulloch et al. (2012). The calculation of the internal pH would allow for a correction necessary for a more accurate paleo-pH reconstruction (e.g. Anagnostou et al., 2012). Existing research in connection with pH reconstruction so far shows that a correction at least for a biologically-driven, species-specific pH regulation mechanism is necessary for this approach (e.g. Anagnostou et al., 2012).

2.4.4 Trace and Minor Element Concentrations

When it comes to the distribution of magnesium (Mg) in relation to microstructures in CWCs, researchers agree on high concentration in RAD and lower concentrations in fibres (Rollion-Bard & Blamart, 2015, Montagna et al., 2014, Raddatz et al., 2013, Case et al., 2010, Gagnon et al., 2007, Cohen et al., 2006). This is associated with decreased $\delta^{18}O$ and $\delta^{13}C$ in Mg-rich areas (Sinclair et al., 2006). The mechanism behind this phenomena, on the other hand, is still not clear. One common hypothesis suggests higher concentrations of Mg-rich organic material in areas of high growth rates as remnants of an organic precursor phase (Rollion-Bard & Blamart, 2015, Montagna et al., 2014, Cuif et al., 2003). ACC is rich in Mg, therefore, ACC as a precursor phase of RADs could account for the association with microstructures (Case et al., 2010, Politi et al., 2010, Meibom et al., 2004). The difference in ionic radius between Mg^{2+} and Ca^{2+} renders a direct substitution between both ions difficult (Montagna et al., 2014). Alternative explanations for Mg incorporation were discussed in Montagna et al. (2014) and Rollion-Bard et al. (2015) and included, apart from the above described model suggestions, the possible adsorption of Mg^{2+} into crystallographic discontinuities or lattice defects. Crystallographic discontinuities and lattice defects are more abundant when mineralisation takes place at a higher rate (Montagna et al., 2014, van de Locht et al., 2013). Then again where a possible correlation between Mg and temperature is considered based on the Rayleigh fractionation model, a substitution of Mg^{2+} for Ca^{2+} in CWCs has to be a prerequisite (Gaetani et al. 2011).

Earlier attempts of employing Mg/Ca for environmental reconstruction of ambient seawater temperatures produced ambiguous results (Gaetani & Cohen, 2006, Shirai et al., 2005) leading to investigations into new approaches in the form of Rayleigh-based multi-elemental coral thermometry (e.g. Gaetani et al., 2011) or Li/Mg ratios (Rollion-Bard & Blamart, 2015, Montagna et al., 2014, Hathorne et al., 2013a, Raddatz et al., 2013, Case et al., 2010). Lithium is positively correlated with Mg, and consequently associated with microstructures while the ratio between Li and Mg is suggested to be correlated with ambient temperatures (e.g. Montagna et al., 2014, Case et al., 2010). However, the application of Li/Mg for the reconstruction of ambient temperatures is still being evaluated (e.g. Rollion-Bard & Blamart, 2015, Rollion-Bard et al., 2009). Montero-Serrano et al. (2013) studied variations in Li/Mg ratios along the growth of a *M. oculata* colony from the Bay of Biscay together with radiocarbon dating and neodymium isotope ratios (εNd) to connect the observations to past oceanography. They used early approaches (Montagna et al., 2008) and received temperatures and variations in accordance with live observations and available data from the last 30 years (Montero-Serrano et al., 2013, De Mol et al., 2011).

A detailed discussion of Li incorporation mechanisms into coral microstructure and connection with ambient water temperatures was given in earlier publications (Montagna et al., 2014 (eq. 2.6), Hathorne et al., 2013a (eq. 2.7), Raddatz et al., 2013 (eq. 2.8), Case et al., 2010 (eq. 2.9), Rollion-Bard et al., 2009). So far the observed correlation between Li/Mg ratios and temperature led to several equations in terms of reconstruction (fig. 2.28):

$$Li/Mg(mmol/mol) = 5.41e^{(-0.049*T(°C))} \tag{2.6}$$

$$Li/Mg(mmol/mol) = 5.16e^{(-0.0492*T(°C))} \tag{2.7}$$

$$Mg/Li(mol/mmol) = (0.015 \pm 0.002) * T(°C) + (0.174 \pm 0.018) \tag{2.8}$$

$$Mg/Li(mol/mmol) = (0.009 \pm 0.0008) * T(°C) + (0.19 \pm 0.006) \tag{2.9}$$

The different equations were based on different coral samples: eq. 2.6 was based on CWCs (including *L. pertusa* and *M. oculata*) and tropical corals and included the results from Case et al. (2010), eq. 2.7 was based on tropical corals and CWCs from two earlier studies (Raddatz et al., 2013, Case et al., 2010), eq. 2.8 was based on *L. pertusa*, eq. 2.9 was based on CWCs (including *L. pertusa*, *D. dianthus*, *E. rostrata*, *E. profunda*).

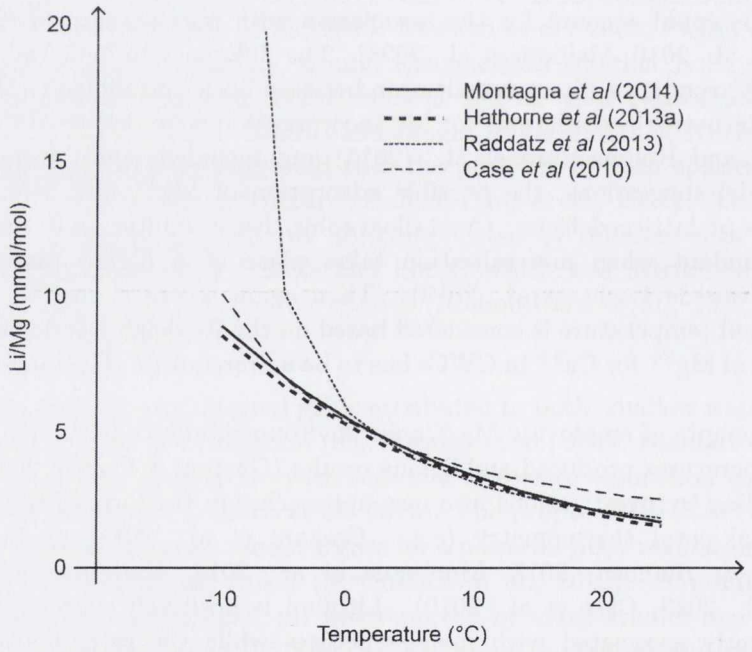


Figure 2.28: Different studies produced different Li/Mg (mmol/mol) correlations with temperature. The regression lines are similar for the temperature range of deep sea scleractinian occurrence. Differences might be attributed to a species effect.

Magnesium displays pronounced antithetical behaviour with uranium (U) in CWCs (Anagnostou et al., 2011, Robinson et al., 2006, Sinclair et al., 2006, Montagna et al., 2005, Shirai et al., 2005). Furthermore, an association between microstructures and U concentrations was reported with low U concentrations in EMZs (Anagnostou et al., 2011, Robinson et al., 2006, Sinclair et al., 2006, Shirai et al., 2005). Particularly high U concentrations were observed along septal edges (Robinson et al., 2006). Low U/Ca

ratios in bivalves were found in connection with organic-rich layers (Gillikin & Dehairs, 2013). The mechanisms behind the incorporation of U in CWCs are still fairly unknown.

U^{4+} and U^{6+} have a similar ionic radius as Ca^{2+} but differ in charge while the radius of UO^{2+} (uranyl) is larger than Ca^{2+} (Anagnostou et al., 2011, Shen & Dunbar, 1995). The orthorhombic and non-planar structure of CO_3^{2-}, however, allows for larger ion substitution (De Villiers, 1971). Possible mechanisms for U substitution influenced by biological activity were compiled by Shen & Dunbar (1995):

(1) UO_2^{2+} replaces Ca^{2+}: $CaCO_3 + UO_2^{2+} \rightleftharpoons UO_2CO_3 + Ca^{2+}$ [ii]

(2) $[CaCO_3]_{coral} + UO_2(CO_3)^{2-} \rightleftharpoons [CaUO_2(CO_3)^2]_{coral} + CO_3^{2-}$ [iii]

(3) $[CaCO_3]_{coral} + UO_2CO_3 \rightleftharpoons [UO_2CO_3]_{coral} + CaCO_3$ (entire group replaced)

An inverse correlation between U and carbonate ion concentrations suggests a possible connection to pH (DeCarlo et al., 2015, Raddatz et al., 2013, McCulloch et al., 2012, Anagnostou et al., 2011, Inoue et al., 2011). Latest approaches of using U/Ca ratios as a pH proxy argued that avoiding CoCs and using bulk samples from the fibrous region of the CWC skeletons allow for an accurate reconstruction of palaeo-pH, undisturbed by internal variations (Raddatz et al., 2014). Raddatz et al. (2014) even presented two equations for a possible pH reconstruction from CWC carbonates, derived from a wider area (between Norway and the Mediterranean Sea) (eq. 2.10) and only from the North Atlantic (eq. 2.11).

$$U/Ca = (-1.72 \pm 0.32) * pH + (15.43 \pm 2.65) \tag{2.10}$$

$$U/Ca = (-1.82 \pm 0.32) * pH + (16.18 \pm 2.56) \tag{2.11}$$

Consequently a higher pH should be correlated to lower U concentrations (e.g. Rollion-Bard et al., 2010). This would then be the case for EMZs where $\delta^{11}B$ analysis suggested a higher pH and where ^{11}B concentrations are higher (Rollion-Bard et al., 2010).

Variations in ^{238}U in the open ocean were found to be conservative relative to variations in salinity in the ambient water masses (eq. 2.12) (Owens et al., 2011, Pates & Muir, 2007, Schmidt, 2006, Delanghe et al., 2002, Chen et al., 1986, Ku et al., 1977). Anomalies found for some regions were discussed connected to the contact with organic rich sediment or remote removal processes (Owens et al., 2011, Delanghe et al., 2002). The global ocean correlation between ^{238}U and salinity was established as by Owens et al. (2011):

$$^{238}U(ng/g) = (0.1 \pm 0.006) * salinity + (0.326 \pm 0.206) \tag{2.12}$$

It has to be mentioned that Raddatz et al. (2014) observed a positive correlation between U/Ca in *L. pertusa* and seawater salinity for NE Atlantic sites but attributed this to the correlation between salinity and pH in the seawater.

[ii] referenced as Christ et al., 1955

[iii] referenced as Swart & Hubbard, 1982

The Sr/Ca ratio measured in tropical corals was originally suspected to be inversely correlated with sea surface temperature (SST) but variabilities were found and connected to symbiont activity or growth rate which causes problems with SST reconstruction (Cohen & Sohn, 2004, Meibom et al., 2003, Cohen et al., 2002, Cohen et al., 2001, De Villiers et al., 1995). A possible temperature correlation is still under review for CWCs (Raddatz et al., 2013, Cohen et al., 2006). Partly Sr/Ca and Mg/Ca appear inversely correlated which would suggest a relation with microstructural units but such a correlation is being discussed (Mouchi et al., 2014, Gagnon et al., 2013, Raddatz et al., 2013, Holcomb et al., 2009, LaVigne et al., 2008, Gagnon et al., 2007, Cohen et al., 2006, Gaetani & Cohen, 2006, Shirai et al., 2005). A new method suggested $\delta^{86/88}$Sr to be a better paleo-temperature proxy (also tested on *L. pertusa*) or to be correlated to the isotopic composition of seawater (Raddatz et al., 2013, Rüggeberg et al., 2008). Both Sr/Ca and $\delta^{86/88}$Sr show a sensitivity to the aragonite saturation state (Gagnon et al., 2013). A quantitative temperature reconstruction most likely requires a multi-element approach to isolate and remove 'vital effects' beforehand (Gaetani et al., 2011). Alternatively a quantitative temperature reconstruction with respect to growth rate was proposed (Saenger et al., 2008).

Potential Nutrient Proxies

Commonly used nutrient proxies in marine environments include barium (Ba), cadmium (Cd), iron (Fe) and manganese (Mn). Earlier results on Ba/Ca compositions in tropical coral skeletons, while first interpreted as temperature related, later turned out to be connected to upwelling events (Lea et al., 1989). With upwelling water masses comes an increased input of nutrients which results in higher Ba/Ca signals (Pretet et al., 2014, Lea et al., 1989). Even though CWCs were found in depths providing different contextual settings with regard to upwelling mechanisms, the correlation between nutrient influx and Ba/Ca should still hold. CWC habitats are commonly found in regions with high primary production in surface waters which provides fast sinking particles to the deep (e.g. Roberts et al., 2009b).

The suggested connection was found in different species, for example, in the form of a nonlinear relationship between skeletal Ba/Ca peaks in invertebrates and Chl α in spring blooms during primary production (Putten et al., 2000, Stecher et al., 1996). Different models were put forward to describe the relation between Ba levels in the coral skeleton and in ambient seawater (Anagnostou et al., 2011, LaVigne et al., 2011). Nevertheless, experimental approaches also suggested that Ba holds potential as a palaeotemperature proxy, but only under the premise whereby the composition of the solution is known (Dietzel et al., 2004). Putten et al. (2000) found a combination of temperature control and seasonal physiological effects or changes in the composition of the organic matrix as a driver of variations in minor/trace element content in general. However, for Ba/Ca variations a coupling with microstructural variations is still unclear and could be species-specific. While Kunioka et al. (2006) did not find a match with the distribution of organic material in otoliths; Holcomb et al. (2009) found high Ba/Ca values in granular aggregates which commonly contain higher organic fractions and are found in EMZs.

Cd and Mn are commonly discussed in connection with upwelling events and ocean stratification as well as aeolian fluxes and have been successfully applied in investigations of El Niño-Southern Oscillation (ENSO) variability (Pretet et al., 2014, Carriquiry & Villaescusa, 2010, Matthews et al., 2008, Shen & Boyle, 1988, Shen et al., 1987). Mn, however, appears to reflect seasonal cycles in a more pronounced fashion than Cd which is correlated with nutrients (P, N) (Delaney et al., 1993, Shen & Boyle, 1988). Distribution coefficients of Cd and Mn seem to be species-specific in tropical corals (Carriquiry & Villaescusa, 2010). Pretet et al. (2014) found an inverse relationship between Cd concentrations and salinity which was not found in Ba. This is in contradiction to earlier findings where Cd incorporation is independent from growth rates, metabolic activity, temperature and salinity (Matthews et al., 2008).

The connection between Fe content in the surface waters and Chl α production, especially in High Nitrate Low Chlorophyll (HNLC) waters has been established over many studies in different parts of the Pacific and Atlantic Ocean (Le Moigne et al., 2014, Achterberg et al., 2013, Baker & Croot, 2010, Duggen et al., 2010, 2007, Hamme et al., 2010, Langmann et al., 2010, Croot et al., 2005, Boyd et al., 2004). Fe was proven to be a limiting factor for primary production but at the same time to have a fertilising effect when its input is increased (Le Moigne et al., 2014, Ryan-Keogh et al., 2013, Baker & Croot, 2010, Hamme et al., 2010, Langmann et al., 2010, Blain et al., 2008, Duggen et al., 2007, Boyd et al., 2004). A limitation of Fe input is less effective where the surface waters are depleted in macronutrients (after the bloom) (Ryan-Keogh et al., 2013) but also causes incomplete utilisation of such macronutrients which consequently sink and become available in deeper regions (Le Moigne et al., 2014). Twining et al. (2014) found a faster release of macronutrients P and S as well as micronutrients Zn and Ni in comparison with Si (macronutrient) and Fe (micronutrient) within the uppermost 200 m of the water column. The process of Fe fertilisation of phytoplankton blooms and the consequent removal of a large part of the available macronutrients in these zones shows a seasonal amplitude (Le Moigne et al., 2014, Painter et al., 2014, Ryan-Keogh et al., 2013, Nielsdóttir et al., 2009, Blain et al., 2008, Boyd et al., 2005).

In the North Atlantic the seasonal modes appear to have shifted between the 1980s, where there was a clear double peak to be seen, to the 2000s where spring blooms show a significantly stronger signal (Martinez et al., 2011). Le Moigne et al. (2014) list possible sources for Fe input into the oceans ranging from mixing fluxes to atmospheric deposition. One possible non-seasonal source for Fe are volcanic eruptions (e.g. Le Moigne et al., 2014, Hamme et al., 2010, Langmann et al., 2010). Studies conducted directly after the eruption of the Icelandic volcano Hekla in 2000 (Frogner et al., 2001) and after the eruption of Eyjafjallajökull (Iceland) in 2010 (Achterberg et al., 2013, Henson et al., 2013) discovered a stronger phytoplankton bloom in the area. Such events might be short-lived and rather cause an extended phytoplankton growth season (Henson et al., 2013, Duggen et al., 2007) but still have potential to be detected in biomineralisation patterns in the area. The rapidly sinking ash particles transport the adsorbed P, Fe, Mn and Si to the area of the surface ocean water where these macronutrients and 'bioactive' trace elements are released and become available to primary production (Henson et al., 2013, Frogner et al., 2001). During this process the elements Fe and Mn react in high concentration (Frogner et al., 2001).

In connection with spring phytoplankton blooms Fones et al. (2004) also found a pale green/beige fluff layer on top of the deep Atlantic sediment which displayed moderate maxima for the trace elements Zn, Cu, Ni, Cd, Fe, Mn and Co but a larger maxima for Cd. This discovery can be compared with biomineralisation patterns from areas with pronounced 'fluff' layers or nepheloid layers.

Part II

Material and Methods

Chapter 3

Material

3.1 Scleractinian Samples

The cold-water corals available for discussion in this thesis were collected during four research cruises onboard the RV Celtic Explorer between 2011 and 2014. Observations and specimen collection (table 3.1) took place over the course of 33 dives of Remotely Operated Vehicle (ROV) *Holland I* (Marine Institute) between several hundreds and almost 3,000 m depth along the complex canyon system of the Whittard Canyon and the Porcupine Bank. Each dive was documented as a separate event even when it was aborted and repeated. The listed events refer to the dives which resulted in successful CWC collection (octocorals and hexacorals) (table 4.1).

The selection of samples for geochemical analysis was conducted on the basis of the following criteria: (1) availability; (2) presence of *E. norvegica* tubes; (3) location. The study started in September 2011 at which point only one sample of *L. pertusa* was available from the earlier research cruise CE11006. Therefore, this sample was the basis for the first study (Chapter 7). During research cruise CE12006 in April 2012 additional samples (*M. oculata* and *D. dianthus*) became available and were included for a comparison of stable isotope ratios in different species (Chapter 6). During the research cruise CE13008 in June 2013 the collection of the CWCs was extended (Chapters 8 and 9). From this supplementary material a selection of *L. pertusa* and *M. oculata* specimens with presence of *E. norvegica* tubes from different canyons was added to the study to extend the insight into calcification patterns and regional differences. Finally research cruise CE14009 in June 2014 added insight into the variety of different habitat types in the Whittard Canyon (with less focus on sample collection). Additionally a series of *M. oculata* samples from different water masses and seasons differentiated by ambient temperature is included in the analysis. For this transect own material available from the Whittard Canyon and Porcupine Bank was supplemented by one *M. oculata* sample from the Mediterranean Sea (Santa Maria di Leuca) (785-789 m) collected at 39°33.1'N and 18°32.0'E in Februar 2001 (kindly provided by M. Lopéz Correa, Friedrich-Alexander-Universität, Erlangen-Nürnberg), one *M. oculata* retrieved south of Iceland (Hafadjup) during cruise ICECTD-12 in June 2012 (kindly provided by M. Lopéz Correa, Friedrich-Alexander-Universität, Erlangen-Nürnberg with permission from N. Frank, Laboratoire des Sciences du Climat et de l'Environnement (LSCE), Gif-sur-Yvette) and one *M. oculata* from the Indian Ocean collected in July 1986 (kindly provided by M. Lopéz Correa, Friedrich-Alexander-Universität, Erlangen-Nürnberg).

Table 3.1: Samples collected from the Porcupine Bank and Whittard Canyon during different research cruises between 2011 and 2013. Samples selected for geochemical analysis in bold.

BDV	Species	*E. norvegica* presence	event	depth
Porcupine Bank (CE13008)				
1009	*M. oculata*	+	7	750 m
1029	*L. pertusa*	+	7	760 m
1033	*L. pertusa*	+	7	670 m
1036	*L. pertusa*	+	7	757 m
1051	*M. oculata*	+	7	756 m
1088	*D. dianthus*	-	11	760 m
1154	*S. variabilis*	-	15	1300 m
1221	*E. rostrata*	-	26	1400 m
1224	*S. variabilis*	+	26	1400 m
1226	*S. variabilis*	+	26	1400 m
1233	*S. variabilis*	+	26	1400 m
1234	*E. rostrata*	-	26	1390 m
1239	*S. variabilis*	+	26	1390 m
1247	*S. variabilis*	+	26	1390 m
1351	*S. variabilis*	-	32	1460 m
1352	*D. dianthus*	-	32	1460 m
1353	*S. variabilis*	-	32	1465 m
1355	*S. variabilis*	-	32	1465 m
1361	*S. variabilis*	+	36	1400 m
1372	*S. variabilis*	+	36	1330 m
Whittard Canyon (CE11006)				
n/a	*L. pertusa*	-	12	1290m
Whittard Canyon (CE12006)				
458	*D. dianthus*	-	12	750 m
458	*D. dianthus*	-	12	750 m
458	*D. dianthus*	-	12	750 m
458	*D. dianthus*	-	12	750 m
459	*M. oculata*	+	12	750 m
459	*M. oculata*	+	12	750 m
Whittard Canyon (CE13008)				
1446	*L. pertusa*	+	39	700 m
1447	*L. pertusa*	+	39	700 m
1450	*L. pertusa*	-	39	700 m
1452	*M. oculata*	-	39	700 m
1453	*D. dianthus*	-	39	700 m
1526	*D. dianthus*	-	52	700 m
1527	*L. pertusa*	-	52	700 m
1534	*L. pertusa*	-	62	1100 m
1535	*D. dianthus*	-	62	1100 m
1540	*L. pertusa*	+	62	1100 m
1587	*L. pertusa*	+	76	650 m
1589	*D. dianthus*	-	76	675 m
1590	*M. oculata*	+	76	765 m

Chapter 4

Methods

A variety of methods was applied to analyse the available material. Habitat analysis was conducted on the basis of video footage and connected CTD data. Further-on mass spectrometry in connection with different sampling strategies (microdrill, laser ablation) was used to investigate geochemical signals in different scleractinian species with regard to isotopic composition and its variations.

4.1 Field Operations

A part of this project was the participation in a number of research cruises led by NUI Galway carried out under the Sea Change strategy with the support of the Marine Institute and the marine research subprogramme of the National Development Plan 2007-2013. The research vessel Celtic Explorer is equipped with a Remotely Operated Vehicle (ROV) with a direct video feed in operation and a robotic arm for sample collection. During the ROV dives (table 4.1) the samples for collection and analysis are selected in collaboration with the ROV pilots while a number of transects for environmental description and quantification are conducted (mostly during CE14009). The ROV *Holland I* from the Marine Institute is standard fitted with 2 manipulators with grabbers, a slurp sampler (1-3 chamber sample containers), 2 bioboxes (alternative with additional deviders) and a sediment corer box (6 cores). The ROV is also equipped with 8 Pal composite video channels, 1 HD TV channel, 1 near sit, 1 b/w, 1 œ 14-366 colour zoom, 1 œ 14-208 Digital stills, 2 œ 14-502a HDTV inspection camera, 1 Pegasus+ colour camera, 2 aurora colour tooling camera, 1 mini tooling camera with integrated ring light.[1]

[1] `www.marine.ie`; last accessed Jan 8, 2016.

Table 4.1: A total of 33 ROV dives was undertaken to collect environmental data.

Cruise	Event	Date	Length (hh:mm)	Latitude	Longitude	Depth (m)
CE11006	12	Apr 25, 2011	5:10	48.83879°	11.0473°	1,380
CE12006	12	Apr 16, 2012	10:30	48.7607°	10.4608°	750
CE12006	64	Apr 22, 2012	9:20	48.7014°	10.5697°	1,335
CE13008	7	Jun 2, 2013	9:00	53.9738°	12.6227°	763
CE13008	11	Jun 3, 2013	0:10	54.0118°	12.6368°	1,480
CE13008	14	Jun 4, 2013	5:00	54.0572°	12.5531°	1,202
CE13008	15	Jun 4, 2013	6:30	54.0560°	12.5548°	1,401
CE13008	26	Jun 5, 2013	1:00	54.0599°	12.5493°	1,320
CE13008	27	Jun 5, 2013	6:30	54.0599°	12.5493°	1,320
CE13008	32	Jun 7, 2013	11:30	54.0537°	12.5963°	1,579
CE13008	36	Jun 7, 2013	18:30	54.0552°	12.5457°	1,361
CE13008	39	Jun 9, 2013	13:40	49.0098°	10.9488°	666
CE13008	45	Jun 11, 2013	10:00	49.0101°	10.9449°	654
CE13008	52	Jun 12, 2013	12:15	48.8856°	10.9229°	780
CE13008	62	Jun 13, 2013	13:45	48.6440°	10.4758°	1,360
CE13008	76	Jun 15, 2013	8:35	48.7632°	10.4599°	745
CE13008	85	Jun 17, 2013	20:30	48.6258°	10.7069°	2,560
CE13008	89	Jun 18, 2013	12:20	48.6563°	10.4124°	1,031
CE13008	91	Jun 19, 2013	15:10	48.6375°	10.6839°	2,400
CE14009	5	Jun 9, 2014	8:00	48.6663°	9.94527°	700
CE14009	7	Jun 10, 2014	14:15	48.7021°	10.5532°	1,500
CE14009	9	Jun 11, 2014	10:00	48.7089°	10.5607°	1,130
CE14009	12	Jun 11, 2014	18:40	48.6353°	10.4974°	1,500
CE14009	15	Jun 12, 2014	4:45	48.4671°	10.3979°	2,665
CE14009	17	Jun 13, 2014	7:10	48.4670°	10.3993°	2,710
CE14009	19	Jun 13, 2014	16:15	48.4673°	10.4004°	2,680
CE14009	25	Jun 14, 2014	6:10	48.4673°	10.3994°	2,669
CE14009	27	Jun 15, 2014	20:10	48.5865°	10.7710°	2,800
CE14009	29	Jun 16, 2014	4:00	48.7046°	10.5582°	1,348
CE14009	31	Jun 17, 2014	10:00	48.4872°	10.3967°	1,774
CE14009	33	Jun 18, 2014	2:45	48.7215°	10.3787°	746
CE14009	40	Jun 18, 2014	13:50	48.7379°	10.3718°	700
CE14009	45	Jun 19, 2014	3:00	48.8847°	10.5120°	605

4.2 Video Transects and Habitat Classification

While grab and box core samples only give a temporally and spatially limited impression of the local environment, ROV tracks provide a broader overview of underlying terrain while the ROV navigates. This allows for a sense of geographical scale and environmental characteristics of the habitats. The ROV video footage from research cruises CE13008 in June 2013 and CE14009 in June 2014 was used for the habitat classification with focus on ROV dives in canyon areas in relation with the investigated scleractinian species (table 4.1). The colonial scleractinians were unsuitable for a coral count strategy based on individual specimens but could be used for an estimation of coral coverage in relative terms. The coral coverage analysis for investigated areas is in progress in the form of a MSc thesis at NUIG (Felim O'Toole). A qualitative approach was chosen for CWC occurrence and habitat description since only a part of the CE14009 dives was set at a more or less constant speed and straight flight path, the camera (HD) view was generally pointed forewards and slightly downwards, and many of the dives were interrupted for sample collection and detail views. A qualitative

overview over habitat type and topography in connection with scleractinian occurrence ('absence/presence') was most suitable for a discussion of associated environmental parameters (habitat, temperature, density, etc) and a quantitative approach would have been beyond the scope of the thesis.

Canyon morphology and sedimentology were combined to give a conceptional description of different coral habitats within the canyons. The initial identification of CWC species was conducted through visual analysis of morphological features via video feed supported by an inspection of the collected specimens where available. Each of the selected dives was analysed for geomorphological features (vertical wall, ridge), sedimentological patterns (ripple fields, erosional structures) and CWC occurrence (live coral, coral rubble) with focus on scleractinians. Where changes in the environment or CWC cover were observed the time periods on the video was noted; the four defined categories (water column [descent and ascent], no coral evidence, coral rubble, live coral) were then coded into the complimentary sonardyne data and displayed in different colours on maps in *ArcGIS* version 10.0 (esri). In addition to this the depth of CWC occurrences was connected to available Conductivity-Temperature-Depth (CTD) data from the area to compare ambient water parameters.

4.3 Sample Preparation

Collected specimens were mechanically cleaned and air-dried onboard, transported to the laboratories at Trinity College Dublin (TCD) where they were submerged in a 5% H_2O_2 bath for 2-5 hours and cleaned mechanically with a soft brush to remove rests of organic material. To exclude the possibility of diagenetic alterations the material from different areas of corallites and polychaete tubes was analysed using X-ray defraction (XRD) to confirm its aragonitic composition. Selected CWC sections for further analysis were mounted in epoxy resin and cut along the longitudinal axis of the corallite wall using a *Buehler IsoMet 1000* precision saw. The surface destined for geochemical analysis was polished, and where possible the opposite half of the sample section was used to produce a thin section.

4.4 Microscopy

A thin section of the cross section was produced in the laboratories of the Friedrich-Alexander-Universität (Erlangen-Nürnberg) and at Trinity College Dublin (table 4.2). A variation of the orientation of cross sections relative to the investigated structure was chosen (fig. 4.1).

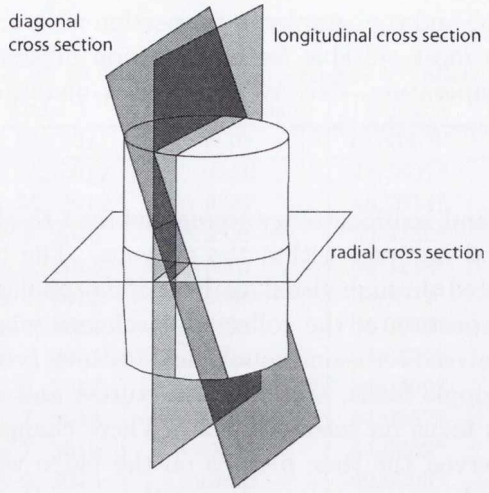


Figure 4.1: The cross section was selected with regard to different orientations relative to the corallite/tube growth.

Table 4.2: Thin sections for different chapters with varying orientations (fig. 4.1) of cuts through corallite and polychaete tube.

Sample	Species	Orientation Corallite	Orientation Tube
459-M1	*M. oculata*	longitudinal	
459-M1-E	*M. oculata* w/ *E. norvegica*	±longitudinal	radial
459-M2-E	*M. oculata* w/ *E. norvegica*	diagonal	diagonal
L1	*L. pertusa*	longitudinal	
1009	*M. oculata*	longitudinal	
1009-E	*M. oculata* w/ *E. norvegica*	mostly radial	radial
1036-E	*L. pertusa* w/ *E. norvegica*	longitudinal	diagonal
1447-E	*L. pertusa* w/ *E. norvegica*	radial	longitudinal
1587-E	*L. pertusa* w/ *E. norvegica*	radial	radial

4.5 Sampling Strategies for Geochemical Analysis

4.5.1 Surface Sampling

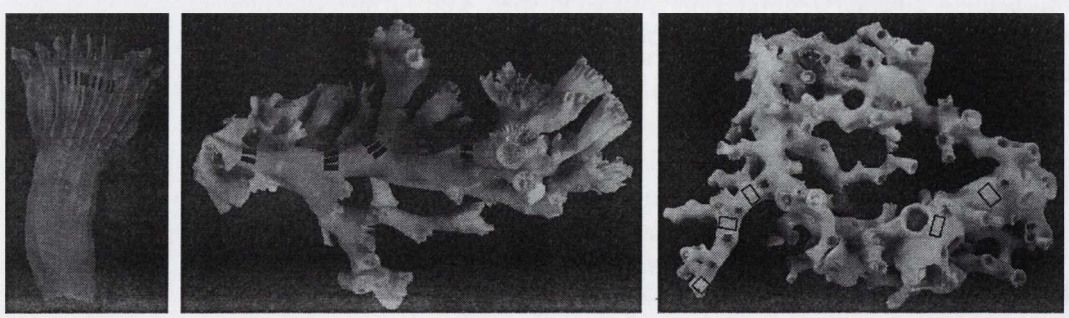


Figure 4.2: For a reconstruction of ambient temperatures samples from the most recent skeletal precipitates (CWC surface) were ablated from three species: *D. dianthus, L. pertusa, M.oculata* (left to right).

For the comparison of different CWC species in Chapter 6 the surface samples were ablated from the outermost thin layer using a hand-held drill (fig. 4.2). In the case

of *D. dianthus* the samples were ablated over an area of ca. 3-5 mm length in the upper corallite area between the costae. Areas of potential overgrowth, bioerosion, and contamination were avoided. *L. pertusa* is sampled in sets of 3 parallel lines, and *M. oculata* was sampled over a square area of 3-5 mm^2 (due to thinner wall sections) along coral branches and polychaete tubes (fig. 4.2).

4.5.2 Microdrill Bulk Sampling

To increase the resolution for evaluation of stable isotope composition, material was collected from 400-500 μm long and circa 500 μm long sections of each of the layers separately in *L. pertusa* L1 (CE11006) (fig. 4.3).

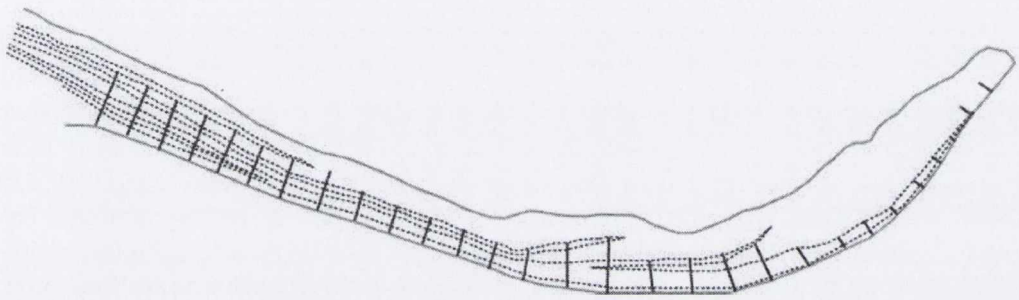


Figure 4.3: To increase the resolution for stable isotope analysis the individual layers were divided into segments of 400-500 μm length and sampled by microdrill separately for each layer.

4.5.3 Microdrill Line Sampling

Samples for stable isotope ratio analysis from *M. oculata* branches in Chapters 8 and 9 were also drilled using a *Leica GZ6 New Wave* micromill. The lines were positioned in series of 2-2.5 mm long and 300 μm deep lines parallel to visible growth layers providing a cross section through radial growth (fig. 4.4). After sampling by microdrill the cross sections were repolished to provide a smooth surface for laser ablation (accuracy and precision increase with stable focus).

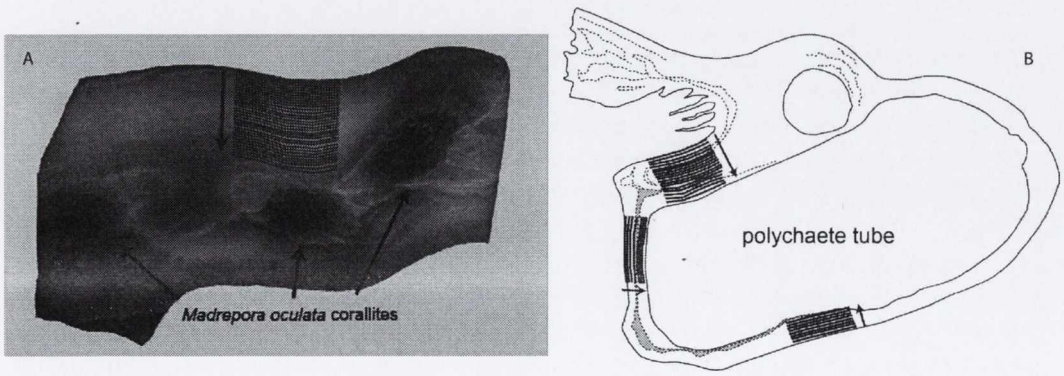


Figure 4.4: Positions of microdrill lines parallel to the sample surface and with respect to microstructural layers in the skeleton across *M. oculata* branches (A) and neighbouring *E. norvegica* tubes (B).

4.5.4 Laser Ablation *in-situ* Sampling

All ICP-MS analysis of trace and minor element compositions was performed in direct connection with laser ablation for *in-situ* analysis. The polished sample sections were ablated with an excimer UV laser (*Photon Machines analyte excite*), 193nm ATLex 300si powered with <4 ns pulse length. The software *Chromium 2.1* (Photon Machines Inc,) was used to define laser ablation lines with a square-shaped aperture between 12 and 47 μm width. Individual lines were placed in direct contact or parallel to each other with a separation of 60-100 μm where larger areas were covered without expected strong variations. To generally ensure minimum ablation depth and maximum sample preservation the laser fluence was kept relatively low (3.31-4.31 J/cm^2) (details table 4.5) (setup for the technique in our laboratory was also discussed in detail in Ubide et al., 2015). The scan speed was generally set to half of the aperture size for experiments (with the exception of first tests). A repetition rate of 20 Hz was chosen for preablation and reduced to 10 Hz for ablation. A pause of 20-25 s after preablation and 30 s after each of the ablation lines allowed for washout of previously ablated material to avoid contamination. Two standard lines were positioned before and after the sample and one additional line was included after every eight sample ablation lines. The standard NIST silicate glasses NIST610, 612 and 613 were ablated and measured using the same parameters as the sample. The silicate glasses are naturally harder and denser than the aragonitic samples, therefore, ablation depth was generally higher in samples. Absolute depth was not measured.

4.6 Analysis

4.6.1 Gas Chromatograph Isotope Ratio Mass Spectrometry (GC-IRMS)

The carbonate powder obtained from drilling was collected in vials, reacted with phosphoric acid (103%) at 70°C and analysed. The first samples (*L. pertusa* L1 sampling steps 9-30) were analysed on a *Thermo MAT-252* gas chromatography isotope-ratio mass spectrometer (GC-IRMS) at the UFZ Helmholtz Centre for Environmental Research (Halle, Germany) and the rest of this sample (*L. pertusa* L1 sampling steps 1-8) was analysed on a *Thermo DeltaPlus* continuous flow IRMS (CF-IRMS) at the Geochemistry Laboratories at Trinity College Dublin (TCD).

For this technique the phosphoric acid is reacted with the carbonates to produce CO_2 gas. The gas is mixed with helium (He) and transported into the mass spectrometer. The stream of CO_2 molecules is charged positively in the ion source box, accelerated and intensified with electric lenses to be led through a magnetic field. Here different masses are collected in separate so-called Faraday cups where the intensity of the electric currents is measured and converted. The machine error is relatively large due to the small sample weight in first experiments, therefore, further stable isotope analysis is conducted using a *Gasbench II* on a *ThermoFinnigan Five Plus* IRMS with a *Kiel III* carbonate device in the laboratories of the FAU in Nürnberg/Erlangen for improved precision. The Kiel device functions as a gas trap to increase the amount of gas for analysis. Different laboratory standards are used to bracket the samples. The laboratory at the FAU calibrates the used *in-house* standards to international standards NBS-19 and LSVEC to check reproducibility and accuracy. Individual standard deviations (SD) of different analytical sessions are given (table 4.3).

Table 4.3: Laboratory standards bracketing stable isotope analysis (SIA) are calibrated to NBS19 and LSVEC for accuracy and reproducibility (FAU Erlangen-Nürnberg). MS = mass spectrometry.

MS session	Date	Lab	Standard Material	$\delta^{18}O$ (± 2 SD)	$\delta^{13}C$ (± 2 S.D.)
1	Mar, 2012	Halle	KH2	-3.86 ± 0.36‰	-47.39 ± 0.35‰
1	Mar, 2012	Halle	CO-9	-15.36 ± 0.17‰	0.69 ± 0.24‰
2	Jul, 2012	TCD	IAEA CO-1	± 1.30‰	± 0.06‰
2	Jul, 2012	TCD	Cranford Dolomite	-10.69 ± 0.46‰	-8.13 ± 0.09‰
3	Apr, 2013	FAU	Li_2CO_3	-15.89 ± 0.06‰	-12.80 ± 0.07‰
3	Apr, 2013	FAU	Sol2	0.13 ± 0.04‰	-5.76 ± 0.07‰
4	Apr, 2013	FAU	Erl5	-49.21 ± 0.06‰	-16.83 ± 0.04‰
4	Apr, 2013	FAU	Sol2	0.13 ± 0.03‰	-5.78 ± 0.06‰
5	Apr, 2013	FAU	Erl5	-49.20 ± 0.07‰	-16.83 ± 0.07‰
5	Apr, 2013	FAU	Sol2	0.13 ± 0.06‰	-5.78 ± 0.07‰
6	Oct, 2014	FAU	Erl5	-49.21 ± 0.06‰	-16.83 ± 0.06‰
6	Oct, 2014	FAU	Sol2	0.13 ± 0.04‰	-5.78 ± 0.06‰

4.6.2 Laser Ablation Quadropole Inductively Coupled Plasma Mass Spectrometry (LA-Q-ICP-MS)

Elemental analysis was performed on a quadrupole inductively-coupled plasma mass spectrometer *iCAP Q* (model s) (*Thermo Scientific*) at the laboratories at Trinity College Dublin. The international standards NIST610, NIST612 and NIST613 were included at regular intervals in all analysis using calcium (^{43}Ca) as the internal standard. For some experiments (Li/Mg in *M. oculata*) a second standard glass (NIST610) was added. All element concentrations were processed in *Iolite* version 2.5 (Paton et al., 2011) (details in section 4.7) and reported in ppm. At the time of analysis the coral standard JCp-1 which was still being certified was not officially available and our laboratory was not involved in characterisation of this new standard (Hathorne et al., 2013b). The so-far certified values (e.g. Sr/Ca and Mg/Ca) were based on solution ICP-MS and were still reported with significant laboratory bias (Hathorne et al., 2013b). Preliminary technical information for JCp-1 Coral (*Porites* sp.) is available from solution ICP-MS (Okai et al., 2002). The reported values here include Ba, Fe, Mg and Sr at concentrations typical in our samples. Currently a number of laboratories (including Trinity College Dublin (TCD)) are collaborating on certifying JCp-1 for laser ablation ICP-MS.

A set of lines was each measured as one continuous experiment using the *Qtegra2.2* software provided by *Thermo Scientic Inc.*. The number of analytes per experiment was kept to a minimum to allow for maximum dwell times (depending on concentration in the sample material). Individual dwell times varied between 5 and 50 ms in pulse mode whereby major elements like Ca and Sr were partly switched to analog mode to avoid signals beyond detection maximum.

Details on the technique were given in a number of publications which will be used for the following overview (e.g. Thomas, 2013, Steel & Henchman, 1998, Houk, 1986). After laser ablation the sample is transported to the ICP torch by a carrier gas (here: for earlier experiments a mixture of He and Ar, later only He, always with a small portion of N_2). Ar joins the gas mix in the ionisation source where a strong magnetic field generates the ionised gas. The sample ions are then transported through

the plasma vacuum between two cones (with a small orifice) to remove most of the Ar and reduce the pressure (expanding ion beam). The ion lens optics (positively charged) separates positively charged ions and focusses the resulting positively charged ion beam through the collision-reaction cell. In the quadrupole mass spectrometer the beam is filtered so only desired analyte ions of one specific mass-to-charge ratio (m/z) remain. The two sets of opposing rods create an electrostatic field in the space between. Here the principles of inertia and charge apply when the flight path of the trajectories of passing ions is guided into spirals so that only the specifed m/z reaches the detector. The field can be changed rapidly by changing the applied RF/DC voltages. The plasma mostly produces single charged particles (therefore, the focus can be on the mass). Elements with low ionisation efficiencies still allow for robust quantitative determinations while high ionisation efficiencies render quantitative determinations impractical. Doubly charged ions for most elements are negligible in cases of lowest second ionization potentials (e.g. Ba^{2+}) the share usually doesn't exceed 1-3% (Houk, 1986). Interference can be caused by isobars (isotopes of different elements with the same mass), polyatomic/molecular species and doubly charged species (e.g. $^{138}Ba^{2+} \leftrightarrow {}^{69}Ga^{+}$) (Thomas, 2013). The ICP-Q-MS system allows for minimisation of interferences e.g. by kinetic energy discrimination.

A set of shorter experiments were run first to determine the possible contamination factors and suitable analytes (table 4.4). Experiments 1 to 7 were performed to establish the most feasible ablation aperture size and speed to obtain a signal with minimized background distortion and at the same time well pronounced elemental pattern (appendix C). The results of the first set were then used to select the most promising elements to determine possible growth information and potential environmental signals (table 4.4). The setup machine parameters for all following experiments are given in tables 4.5 and 4.6.

Table 4.4: A series of laser ablation parameters and a selection of different trace and minor elements is tested prior to analysis to optimise results. For details on Signal-Noise-Ratios (SNRs) see Appendix D.3.

Exp.	Element	Dwelling Time	Spotsize in μm	Scan Speed in μm/s
1	^{25}Mg, ^{137}Ba, ^{88}Sr, ^{238}U	50 ms	8 / 15 / 30	4 / 6 / 10
2	^{7}Li, ^{11}B, ^{31}P, ^{232}Th	50 ms	8 / 15 / 30	4 / 6 / 10
3	^{51}V, ^{55}Mn, ^{57}Fe, ^{86}Sr	50 ms	8 / 15 / 30	4 / 6 / 10
4	^{230}Th, ^{232}Th, ^{234}U, ^{235}U, ^{238}U	50 ms	150	200 shots
5	^{25}Mg, ^{51}V, ^{57}Fe, ^{63}Cu, ^{238}U	50 ms	10	6
6	^{25}Mg, ^{66}Zn, ^{111}Cd, ^{137}Ba, ^{238}U	50 ms	10	6
7	^{25}Mg, ^{31}P ^{55}Mn, ^{238}U	50 ms	10	6

Table 4.5: Fluence, energy and gas flow details of the carrier gas throughout experiments.

			Gas Flow in ml/min		
Experiments	Fluence	Energy	He	Ar	N_2
12 - 16	3.31 J/cm^2	7 mJ	1000	850	6.0
17 - 23	3.31 J/cm^2	7 mJ	800	700	6.0
24 - 30	3.33 J/cm^2	7 mJ	800	700	7.0
31 - 37	3.31 J/cm^2	7 mJ	750	700	6.0
38 - 42	4.31 J/cm^2	7 mJ	750	700	6.0
43 - 46	3.31 J/cm^2	7 mJ	750	700	6.0
47 - 48	3.9 J/cm^2	5 mJ	650	0	6.0
49 - 51	3.9 J/cm^2	5 mJ	650	0	6.0
52 - 55	3.9 J/cm^2	5 mJ	650	0	6.0

Table 4.6: List of details of individual experiments using LA-ICP-MS. Dwelling times apply to all listed elements unless noted otherwise in brackets. Experiments 47-55 give different dwelling times for listed elements in order of listing.

Experiment	Date	Elements	Lines	Dwelling Time
12	May 15, 2013	^{25}Mg, ^{137}Ba, ^{88}Sr, ^{111}Cd, ^{238}U	40	50 ms
13	May 15, 2013	^{25}Mg, ^{137}Ba, ^{88}Sr, ^{111}Cd, ^{238}U	24	50 ms
14	May 16, 2013	^{25}Mg, ^{137}Ba, ^{88}Sr, ^{111}Cd, ^{238}U	30	50 ms
15	Sep 23, 2013	^{25}Mg, ^{137}Ba, ^{88}Sr, ^{111}Cd, ^{238}U	24	50 ms
16	Sep 23, 2013	^{25}Mg, ^{137}Ba, ^{88}Sr, ^{111}Cd, ^{238}U	40	50 ms
17	Nov 25, 2013	^{25}Mg, ^{137}Ba, ^{88}Sr, ^{111}Cd, ^{238}U	40	50 ms
18	Nov 25, 2013	^{25}Mg, ^{137}Ba, ^{88}Sr, ^{111}Cd, ^{238}U	48	50 ms
19	Nov 26, 2013	^{25}Mg, ^{137}Ba, ^{10}B, ^{11}B, ^{226}Ra	8	50 ms
20	Nov 26, 2013	^{25}Mg, ^{137}Ba, ^{10}B, ^{11}B, ^{238}U	14	50 ms
21	Nov 26, 2013	^{25}Mg, ^{137}Ba, ^{88}Sr, ^{111}Cd, ^{238}U	24	50 ms
22	Nov 26, 2013	^{25}Mg, ^{137}Ba, ^{88}Sr, ^{111}Cd, ^{238}U	24	50 ms
23	Nov 26, 2013	^{25}Mg, ^{137}Ba, ^{88}Sr, ^{111}Cd, ^{238}U	24	50 ms
24	Feb 18, 2014	^{25}Mg, ^{137}Ba, ^{88}Sr, ^{111}Cd, ^{238}U	24	50 ms
25	Feb 18, 2014	^{25}Mg, ^{137}Ba, ^{88}Sr, ^{11}B, ^{238}U	32	50 ms
26	Feb 18, 2014	^{25}Mg, ^{137}Ba, ^{88}Sr, ^{11}B, ^{238}U	25	50 ms
27	Feb 19, 2014	^{10}B, ^{11}B, ^{25}Mg, ^{137}Ba, ^{88}Sr, ^{238}U	24	50 ms / 25 ms (B)
28	Feb 19, 2014	^{10}B, ^{11}B, ^{25}Mg, ^{137}Ba, ^{88}Sr, ^{238}U	32	50 ms / 25 ms (B)
29	Feb 19, 2014	^{10}B, ^{11}B, ^{25}Mg, ^{137}Ba, ^{88}Sr, ^{238}U	24	50 ms / 25 ms (B)
30	Feb 19, 2014	^{10}B, ^{11}B, ^{25}Mg, ^{137}Ba, ^{88}Sr, ^{238}U	14	50 ms / 25 ms (B)
31	May 19, 2014	^{31}P, ^{57}Fe, ^{25}Mg, ^{137}Ba, ^{238}U	36	50 ms
32	May 19, 2014	^{48}Ti, ^{51}V, ^{55}Mn, ^{75}As, ^{85}Rb, ^{80}Y, ^{90}Zr, ^{111}Cd, ^{121}Sb	7	20 ms
33	May 19, 2014	^{7}Li, ^{23}Na, ^{25}Mg, ^{35}Cl, ^{238}U	8	50 ms, 70 ms (Li), 5 ms (Na)
34	May 19, 2014	^{25}Mg, ^{137}Ba, ^{88}Sr, ^{57}Fe, ^{238}U	23	50 ms
35	May 21, 2014	^{25}Mg, ^{137}Ba, ^{88}Sr, ^{57}Fe, ^{238}U	23	50 ms / 5 ms (Sr)
36	May 21, 2014	^{25}Mg, ^{137}Ba, ^{88}Sr, ^{57}Fe, ^{238}U	23	50 ms / 5 ms (Sr)

Experiment	Date	Elements	Lines	Dwelling Time
37	May 21, 2014	^{25}Mg, ^{137}Ba, ^{88}Sr, ^{7}Li, ^{238}U	44	50 ms / 5 ms (Sr)
38	May 22, 2014	^{25}Mg, ^{137}Ba, ^{88}Sr, ^{7}Li, ^{238}U	32	50 ms / 5 ms (Sr)
39	May 22, 2014	^{25}Mg, ^{137}Ba, ^{88}Sr, ^{7}Li, ^{238}U	44	50 ms / 5 ms (Sr)
40	May 23, 2014	^{25}Mg, ^{137}Ba, ^{88}Sr, ^{7}Li, ^{238}U	48	50 ms / 5 ms (Sr)
41	May 23, 2014	^{25}Mg, ^{137}Ba, ^{88}Sr, ^{7}Li, ^{238}U	45	50 ms / 5 ms (Sr)
42	May 23, 2014	^{25}Mg, ^{137}Ba, ^{88}Sr, ^{7}Li, ^{238}U	36	50 ms / 5 ms (Sr)
43	July 14, 2014	^{25}Mg, ^{137}Ba, ^{88}Sr, ^{7}Li, ^{238}U	36	50 ms / 5 ms (Sr)
44	July 14, 2014	^{25}Mg, ^{137}Ba, ^{88}Sr, ^{7}Li, ^{238}U	36	50 ms / 5 ms (Sr)
45	July 15, 2014	^{25}Mg, ^{137}Ba, ^{88}Sr, ^{7}Li, ^{238}U	30	50 ms / 5 ms (Sr)
46	July 15, 2014	^{25}Mg, ^{137}Ba, ^{88}Sr, ^{7}Li, ^{238}U	37	50 ms / 5 ms (Sr)
47	Oct 28, 2014	^{25}Mg, ^{7}Li, ^{238}U	10	7.5 ms / 8 ms / 50 ms
48	Oct 28, 2014	^{25}Mg, ^{7}Li, ^{238}U	10	gas ran out
49	Nov 27, 2014	^{25}Mg, ^{7}Li, ^{238}U	16	7.5 ms / 8 ms / 50 ms
50	Nov 27, 2014	^{25}Mg, ^{7}Li, ^{238}U	8	7.5 ms / 8 ms / 50 ms
51	Nov 27, 2014	^{25}Mg, ^{7}Li, ^{238}U	30	7.5 ms / 8 ms / 50 ms
52	Dec 1, 2014	^{25}Mg, ^{7}Li, ^{238}U	10	7.5 ms / 8 ms / 50 ms
53	Dec 1, 2014	^{25}Mg, ^{7}Li, ^{238}U	10	7.5 ms / 8 ms / 50 ms
54	Dec 1, 2014	^{11}B, ^{25}Mg, ^{137}Ba, ^{238}U	40	50 ms
55	Dec 1, 2014	^{11}B, ^{25}Mg, ^{137}Ba, ^{238}U	42	50 ms

4.7 Data Processing

The ICP-MS data, including x-y coordinates from the laser log file, was imported into *Cellspace* in the software *Iolite* version 2.5 in the *IGOR Pro 6.35* environment. The Trace_Element_IS data reduction scheme (DRS) was selected to integrate different concentrations of the internal standard calcium ^{43}Ca in sample and standard. The Ca content in the standards was adopted from literature (Jochum et al., 2011) while a concentration of 40.04% was assumed for the coral carbonates (according to averaged carbonate compositions). The DRS subtracted baseline integrations (background noise corrections) and linked the results from analysis with the published contents (table 4.7) of different elements in the standard to convert the counts per second into a concentration (in ppm) for each element in the sample. The programme corrected the results following the equations by Longerich et al. (1996):

$$\sigma_{indiv} = \sqrt{\sum_{i=1}^{n_b} \frac{\left(\overline{X} - X_i\right)^2}{n_b - 1}} \tag{4.1}$$

where σ_{indiv} is the standard deviation of individual determinations per population, n_b is the number of background determinations, while X are individual measurements.

$$\sigma_{R_{net}} \approx \sqrt{\frac{2}{n}}\sigma_{indiv} \tag{4.2}$$

$$S = \frac{R_{IS_{CWC}}}{C_{IS_{CWC}}} \left[\frac{R_{AN_{STD}}}{C_{AN_{STD}}} \frac{R_{IS_{STD}}}{C_{IS_{STD}}}\right] \tag{4.3}$$

$$C_{AN_{CWC}} = \frac{R_{AN_{CWC}}}{S} \tag{4.4}$$

$$LOD = \frac{3\sigma_{indiv}}{S} \sqrt{\frac{1}{n_b} + \frac{1}{n_a}} \tag{4.5}$$

Where R_{net} marks the difference between the count rate of the selected ablation and the count rate for the background, $\sigma_{R_{net}}$ is the standard deviation of the net count rate, S equals the normalised sensitivity, $R_{AN_{CWC}}$ and $R_{AN_{STD}}$ are the count rates of the analyte in the CWC and the standard material (STD) respectively (in cps), $R_{IS_{CWC}}$ and $R_{IS_{STD}}$ reflect the count rates of the internal standard (^{43}Ca) in the CWC and the standard material (STD) respectively (in cps). The same labels are used for the concentrations: $C_{AN_{CWC}}$, $C_{AN_{STD}}$, $C_{IS_{CWC}}$ and $C_{IS_{STD}}$ for concentration of analyte in CWC and standard material (STD) respectively, and of interal standard (^{43}Ca) in CWC and standard material (STD) respectively. LOD refers to the Limits of Detection. n_a is the number of ablation intervals which are integrated.

Table 4.7: Accepted elemental concentrations in standard glass NIST612 (Jochum et al., 2011) and NIST610 (Paton et al., 2011 and references there).

Element	NIST612	NIST610
boron (B)	34.3 ppm	356 ± 14 ppm
barium (Ba)	39.3 ppm	435 ± 46 ppm
cadmium (Cd)	28.1 ppm	259 ± 10 ppm
iron (Fe)	51.0 ppm	458 ± 9 ppm
lithium (Li)	40.2 ppm	485 ± 44 ppm
magnesium (Mg)	68.0 ppm	465 ± 54 ppm
strontium (Sr)	78.4 ppm	515.5 ± 0.5 ppm
uranium (U)	37.38 ppm	461.5 ± 1.1 ppm
$^{11}B/^{10}B$	4.048	4.049

Longerich et al. (1990) discussed different calibration strategies for solution ICP-MS. External calibration which compares the signal intensity of a standard and a sample can be applied for laser ablation ICP-MS as well (table 4.7). The process does, however, not correct for matrix effects (Longerich et al., 1990). The internal standardisation in the case of laser ablation has to be varied from the solution based one (Longerich et al., 1990). Laser ablation does not allow for the inclusion of a controlled peak in one element. For the measured aragonite ^{43}Ca acts as the defined internal standard. Longerich et al. (1990) suggested a combination of calibration strategies to solve drift, interference and matrix effects, whereas matrix effects are harder to correct where laser ablation is applied to an aragonitic samples and a NIST glass. Matrix effects are concentration dependent (Longerich et al., 1990) which is a problem here since elemental concentrations in the NIST glasses are higher than the ones in the carbonate. The mass of the internal standard should be close to that of the analysed element (Longerich et al., 1990). On the other hand, matrix effects are mass dependent and decrease with increasing mass (Longerich et al., 1990) which works in favour of ^{137}Ba and ^{238}U analysis.

The isotopes used in the study were partly chosen with regard to their low potential for interferences. ^{238}U and ^{137}Ba, for example, are known for low interference with other elements (Hirata, 2004, May & Wiedmeyer, 1998, Allison, 1996) (table 4.8).

Interference of xenon (^{129}Xe, ^{131}Xe) with barium measurements was reported for several Ba isotopes, especially ^{136}Ba, but uncertainties tested to be within 1% (Gagnon et al., 2013). ^{137}Ba seems to be free of such interferences (Hirata, 2004, May & Wiedmeyer, 1998).

Table 4.8: A summary of polyatomic interferences in ICP-MS (May & Wiedmeyer, 1998).

Isotope	Abundance	Interference
^{11}B	80.09%	^{12}C
^{137}Ba	11.23%	–
^{111}Cd	12.8%	$^{95}Mo^{16}O^+$, $^{94}Zr^{16}O^1H^+$, $^{39}K_2{}^{16}O_2{}^1H^+$
^{56}Fe	91.66%	$^{40}Ar^{16}O^+$, $^{40}Ca^{16}O^+$, $^{40}Ar^{15}N^1H^+$, $^{38}Ar^{18}O^+$, $^{38}Ar^{17}O^1H^+$, $^{37}Cl^{18}O^1H^+$
^{25}Mg	10.13%	$^{12}C_2{}^1H^+$
^{88}Sr	82.58%	–
^{238}U	99.27%	–

Iolite does not differentiate between different isotopes of an element but since we

assume natural abundance of isotopes in both, standard material and CWCs, the data correction should not be affected. When it comes to absolute data, additional factors like possible interferences with other elements during data acquisition have to be considered. Ratios between the isotopes of the same element (e.g. $^{11}B/^{10}B$) as well as of different elements (e.g. $^{7}Li/^{25}Mg$) are best calculated from baseline corrected data. For this purpose a plug-in created by Dr. D. Chew (TCD) was altered to add different ratios from intermediate channels (before standard correction) to the output.

Although the reported variations refer to elemental variations rather than single isotopes in the following chapter the results will be reported with reference to the measured isotope to avoid confusion in comparison with other studies and to allow reconstruction.

To include background signals in the error discussion the detected noise will be compared to the sample signal using signal-noise-ratios (SNRs) (appendix D.3). Since no guidelines for the interpretation of SNRs are available the following categories (table 4.9) were set up for all following discussions:

Table 4.9: Signal-Noise-Ratio categories here for further discussions.

Category	Interpretation	SNR value
I	Signal not reliably distinguishable from background	<10
II	Signal has to be treated with care	10 to <100
III	Signal clearly distinguishable from background	100 to >100
IV	Background can be neglected	>1000

Part III

Results and Discussion

Chapter 5

CWC Habitats along the Irish Shelf

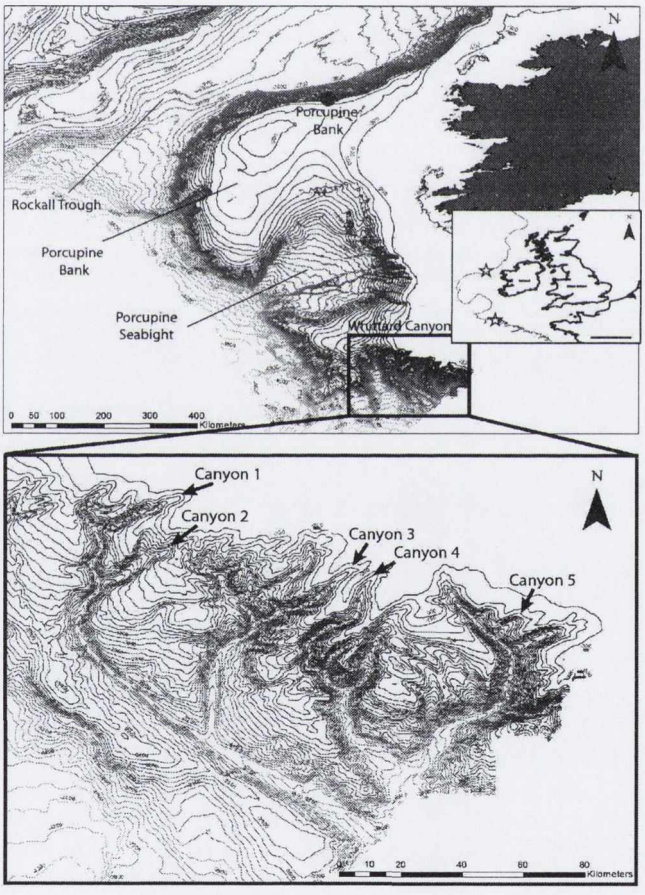


Figure 5.1: Overview over the different canyons investigated on the Porcupine Bank (PB) (circle) and in the Whittard Canyon (WC) system (box) investigated during the ROV dives in 2011, 2012, 2013 and 2014. The studied canyons in the WC were numbered 1 to 5 (from W to E).

In the years 2011, 2012, 2013 and 2014 four research cruises (CE11006, CE12006, CE13008, CE14009) onboard of the RV Celtic Explorer led to the Whittard Canyon (WC), approximately 300 nautical miles south of Ireland, and to an unnamed canyon system on the Porcupine Bank facing the Rockall Seabight (which will be referred to as Porcupine Bank (PB) here) (fig. 5.1 and table 5.1). To allow for the interpretation of geochemical signals detected in the CWC skeletons different habitats, geomorphology, biodiversity and CWC morphology must be understood and considered. Research cruise CE11006 in April 2011 was interrupted by technical problems and during research cruise CE12006 in April 2012 weather conditions only allowed for two dives including the investigation of a vertical wall area described in Johnson et al. (2013). The last two years finally allowed for extensive ROV dives to explore the canyons. The video footage from the ROV dives in 2013 and 2014 was used for the following habitat definitions. The observed coral occurrence was compared to ambient water parameters (temperature, salinity, density, fluorescence) collected close to the dive sites via Conductivity-Temperature-Depth (CTD) casts. The focus lies on similarities and variations between different locations, temporal and spatial variability of water profiles (as far as available) and possible limiting factors of coral occurrence. The footage extends the insight into habitat variability and preferences and will provide additional information for further discussions in the following chapters.

Table 5.1: List of selected dives for habitat description and coral occurrence analysis. CE13008 events 7 to 36 are located in the PB canyon. All other dives refer to the WC.

Cruise	Event	Date	Length (hh:mm)	Latitude	Longitude	Depth
CE12006	12	Apr 16, 2012	10:30	48.7607°N	10.4608°W	750 m
CE13008	7	Jun 2, 2013	9:00	53.9738°N	12.6227°W	763 m
CE13008	11	Jun 3, 2013	10:00	54.0118°N	12.6368°W	1,480 m
CE13008	14	Jun 4, 2013	3:00	54.0572°N	12.5531°W	1,202 m
CE13008	15	Jun 4, 2013	6:30	54.0560°N	12.5548°W	1,401 m
CE13008	26	Jun 5, 2013	2:00	54.0599°N	12.5493°W	1,320 m
CE13008	27	Jun 5, 2013	6:30	54.0599°N	12.5493°W	1,320 m
CE13008	32	Jun 7, 2013	10:30	54.0537°N	12.5963°W	1,579 m
CE13008	36	Jun 7, 2013	12:30	54.0552°N	12.5457°W	1,361 m
CE13008	39	Jun 9, 2013	13:40	49.0098°N	10.9488°W	666 m
CE13008	52	Jun 12, 2013	12:15	48.8856°N	10.9229°W	780 m
CE13008	62	Jun 13, 2013	13:45	48.6440°N	10.4758°W	1,360 m
CE13008	76	Jun 15, 2013	8:35	48.7632°N	10.4599°W	745 m
CE14009	5	Jun 9, 2014	8:00	48.6663°N	9.94527°W	700 m
CE14009	7	Jun 10, 2014	14:15	48.7021°N	10.5532°W	1,500 m
CE14009	9	Jun 11, 2014	10:00	48.7089°N	10.5607°W	1,130 m
CE14009	12	Jun 11, 2014	18:40	48.6353°N	10.4974°W	1,500 m
CE14009	25	Jun 14, 2014	6:10	48.4673°N	10.3994°W	2,669 m
CE14009	31	Jun 17, 2014	10:00	48.4872°N	10.3967°W	1,774 m

5.1 Introduction to Canyon Habitats

5.1.1 Porcupine Bank

In June 2013 the Porcupine Bank canyon was investigated during eight ROV dives from a depth of around 750 m down to 1,500 m complemented by a series of CTD casts. During all of the dives, i.e. at all times of the day (and night), a high particle load was observed within the water column and the sandy parts of the canyon floor showed a green fluffy cover on top of the sediment in many locations. This phenomenon is likely connected to the presence of nepheloid layers (NLs) and being investigated separately by oceanographers at NUIG. For the studies on skeletal composition in scleractinians of these areas it is important to consider particle influx from deeper ocean floor areas by the so-called nepheloid layers.

In higher regions (around 700-800 m) of the PB canyon we found extensive *M. oculata* and *L. pertusa* assemblages mostly on rocky surfaces of the canyon floor. Along the seafloor at that depth larger boulders offered a solid basis for settling of many sessile organisms including the stony corals. No vertical canyon walls were encountered during the dives. The tube worm *E. norvegica* was a common symbiont found among the branches of *M. oculata* and *L. pertusa*. The cliffs were more often settled by thinner branched *L. pertusa* and *M. oculata* compared to the thick branches found on the canyon floor. Pieces of dead *L. pertusa* formed patches of hard grounds.

The deeper regions showed the most pronounced changes in the occurrence of scleractinians. The species *M. oculata* and *L. pertusa* had completely disappeared around 1,400 m depth and gave space to *S. variabilis* which was accompanied by *E. rostrata*. The exact transition was not observed and no information is available about whether it is a sudden or a gentle transition process with areas where co-occurrence of all species is expected. *E. rostrata* and *S. variabilis* were often found growing in close contact (see Appendix A.5) and partly even formed extensive structures which then provided valuable habitats for many other species in the deep (e.g. fig. 2.12).

5.1.2 Whittard Canyon

The vertical wall investigated during CE12006 showed *M. oculata* and *D. dianthus* in co-occurrence with soft corals and bivalves (Johnson et al., 2013). CE13008 recovered scleractinian samples from four neighbouring canyons (canyons 1 to 4) together with extensive video footage from the ROV dives (fig. 5.2). All analysed 2013 dives were located in the upper areas of the different canyon arms close to the shelf (fig. 5.2). Before and/or after each dive a CTD cast was deployed in the area which provided additional information on water parameters of the site around that time. During CE14009 the ROV dives followed the same strategy but focused on deeper regions in canyons 3 and 4 to intensify the biodiscovery here, and explored canyon 5.

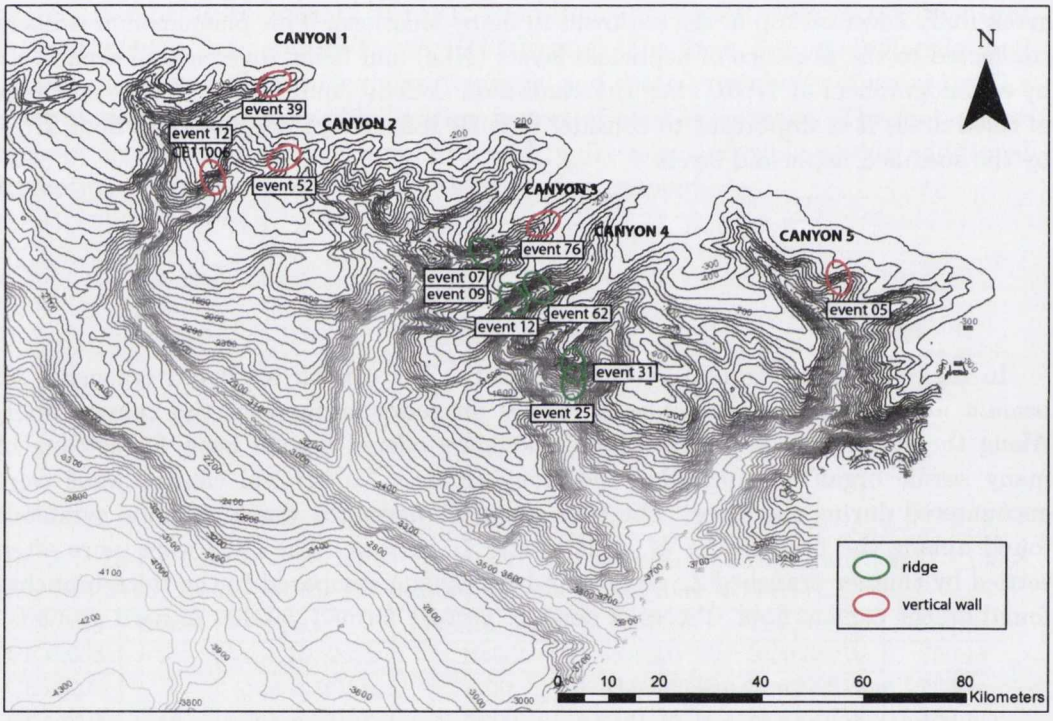


Figure 5.2: The map shows the distribution of ROV dive sites in scleractinian habitats within the five investigated canyons in the Whittard Canyon system and distinguishes between the two main habitats (ridge, vertical wall).

Canyon 1 (CE13008, event 39)

The canyon floor at 700-720 m was covered with coral rubble as substrate for live scleractinians on soft sediment (fig. 5.3). *L. pertusa* colonies here built thin as well as thick branched colonies, and occurred in mixed colonies of white and orange bushes. The foot of the wall consisted of flater erosional steps in the yellowish bedrock where *L. pertusa* and *M. oculata* are present. Around 650 m depth the underside of overhangs was settled by *Acesta excavata*, soft coral and mostly orange *L. pertusa* and *D. dianthus*. *Madrepora oculata* became more abundant around 610 m and took over as the dominating colonial CWC together with the solitary *D. dianthus*, especially in steeper areas. During the whole dive a high particle load was observed in the water column.

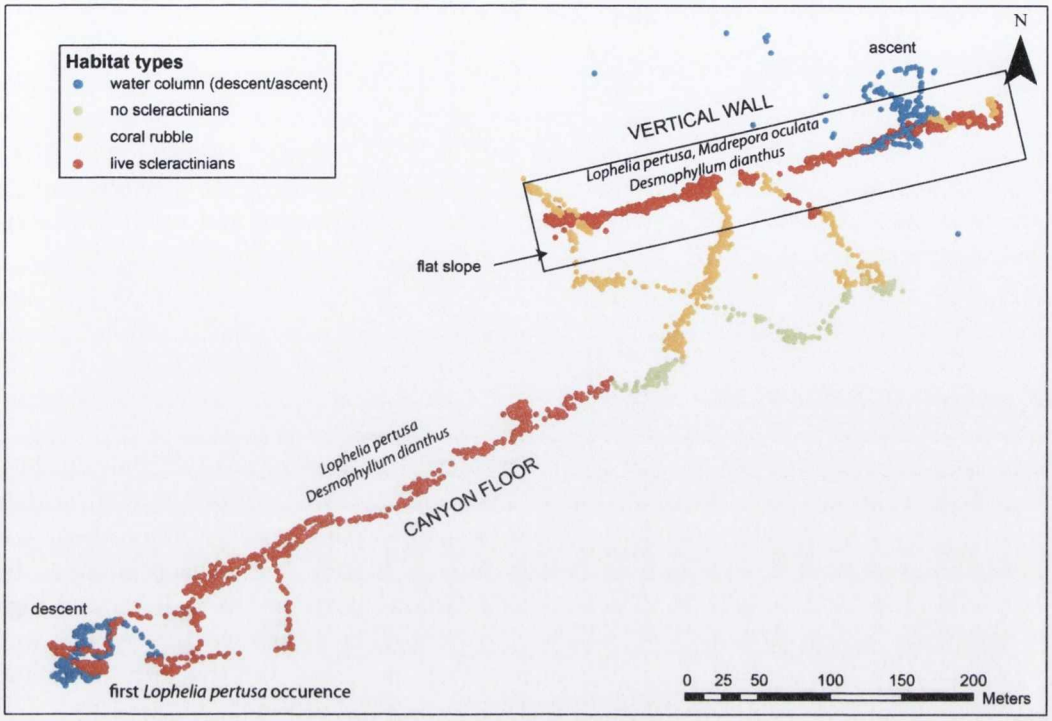


Figure 5.3: ROV dive track (event 39) from the canyon floor to the vertical wall. The box marks the ENE-WSW orientation of the vertical wall facing SSE which starts at 650 m depth.

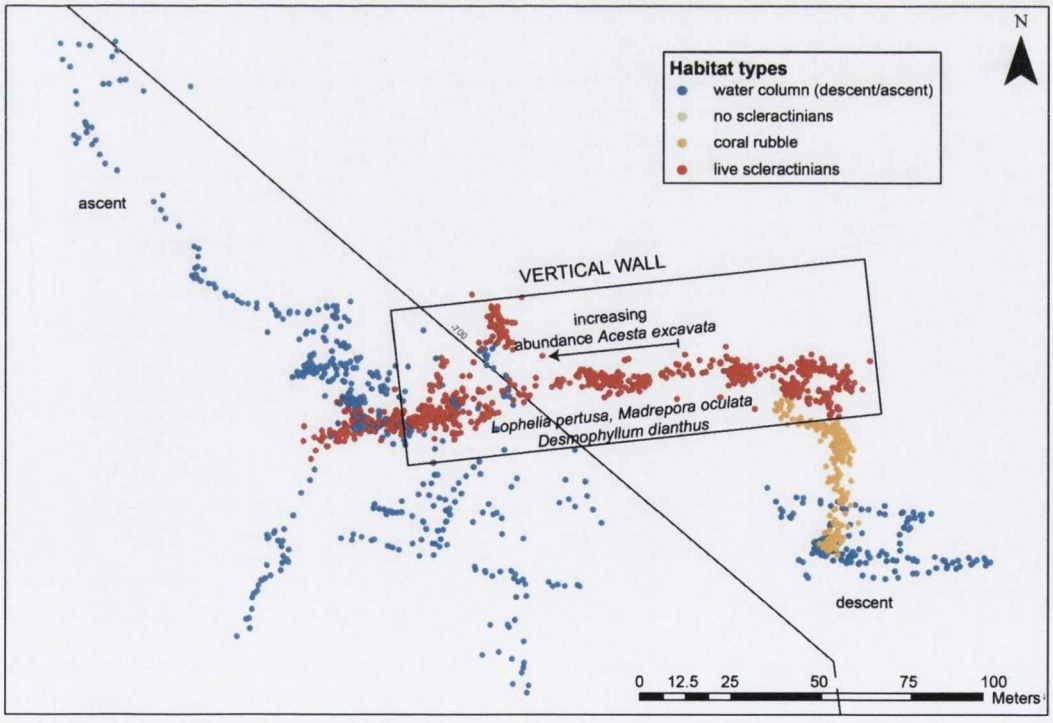


Figure 5.4: ROV dive track (event 52) leads from the canyon floor to the vertical wall and follows it horizontally crossing the 700 m isobath. The box marks the orientation of the SSE facing vertical wall.

Canyon 2 (CE13008, event 52)

This dive (fig. 5.4) was located in the same canyon as an earlier dive during cruise CE11006 in 2011 which provided *L. pertusa* sample L1 (Chapter 7). The wall was of similar sedimentological appearance as canyon 1. The lower wall was covered by patches of *Acesta excavata*, *Neopycnodonte zibrowii*, *L. pertusa*, *M. oculata* and *D. dianthus*. At 730 m the top of the wall was marked by anemones and small *L. pertusa* and *M. oculata* patches.

Canyon 3 (CE13008, event 76)

The dive location was opposite of event 12 during research cruise CE12006 in 2012 (fig. 5.5). Around 760 m depth we found small colonies of *L. pertusa* and *M. oculata* with single echinoids. The underside of overhangs was populated by *A. excavata* and *D. dianthus* around 750 m and further up (approximately 715 m) accompanied by *L. pertusa*, *M. oculata* and *N. zibrowii* shells. Higher parts of the wall showed high diversity and abundance of CWCs and *A. excavata*. The sight onto the vertical wall was mostly obscured by large shrimp swarms. The top of this wall was located around 630 m depth, covered by soft sediment and with low coral diversity.

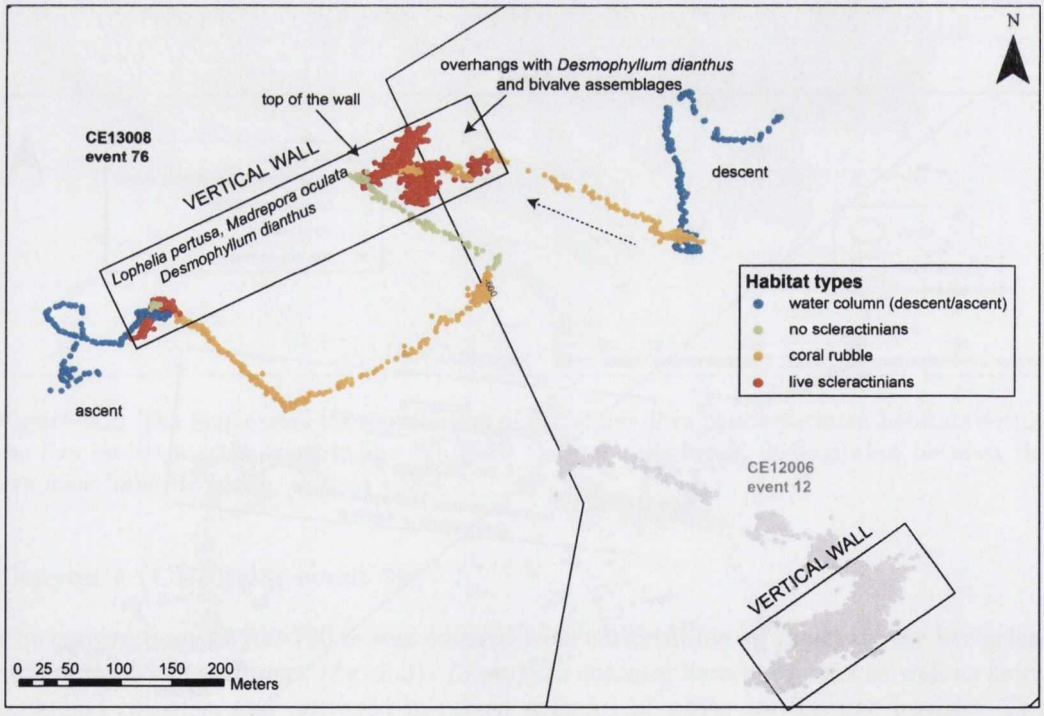


Figure 5.5: ROV track (event 76) followed a path from coral rubble to a vertical wall. The boxes indicate the horizontal extension and orientation of the investigated vertical wall section. SE of event 76 the map shows the location of event 12 during research cruise CE12006 along the opposite wall (in gray). A detailed description of the biodiversity here was published by Johnson et al. (2013). The wall (CE13008) faces SSE while the earlier explored one (CE12006) faces NNW.

Canyon 3 (CE14009, events 7 and 9)

Dive 7 started at a depth around 1,410 m on the silty-sandy canyon floor (fig. 5.6). White *L. pertusa* specimens had generally thicker developed branches than orange specimen. *E. norvegica* was still common amongst *L. pertusa* and *M. oculata* at 1,159 m where large colonies of *S. variabilis* grew on a ridge. The colony size increased around 1,140 m depth. The surface morphology (with large CWC accumulations) made it difficult to identify on a species level but both species *L. pertusa* and *S. variabilis* appeared to be present. *L. pertusa* appeared swollen giving it a *Solenosmilia*-like appearance but the branch morphology allowed for differentiation. Scleractinians prevailed to 949 m with deserted patches in between. The highest diversity was found along the ridge. Large, mostly dead, *S. variabilis* colonies were habitat to a large number of brisingid starfishes.

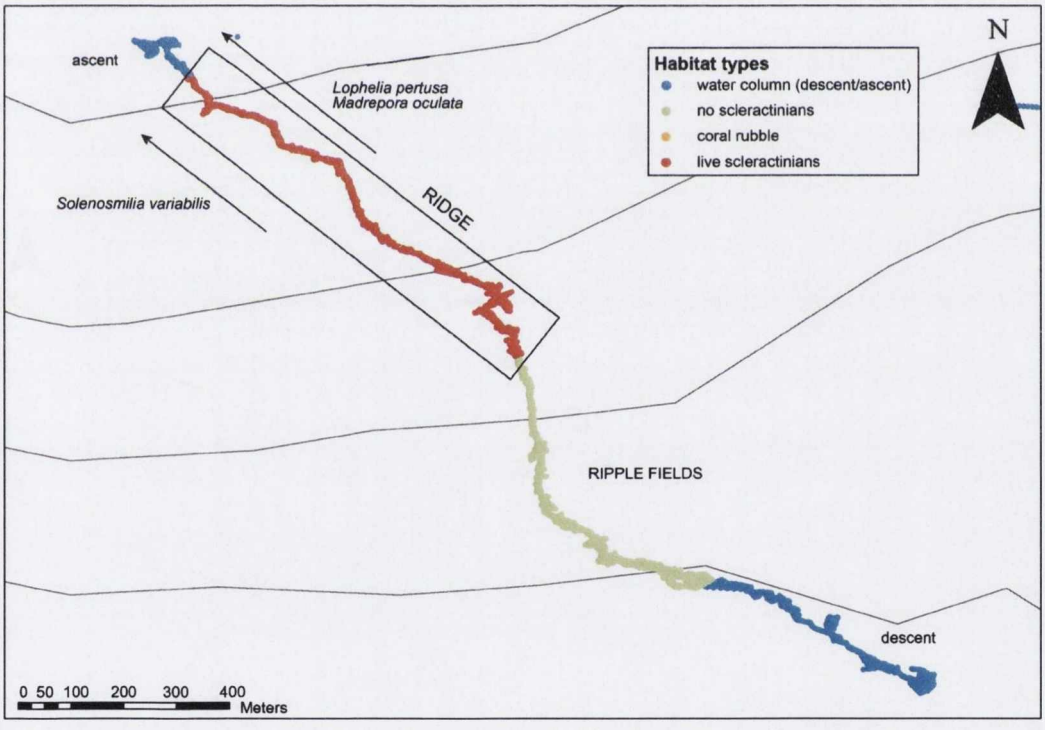


Figure 5.6: ROV dive track (event 7) from canyon floor to the ridge and along it. The box marks the orientation and location of the ridge with variations in CWC occurrence.

Event 9 repeated the top part of event 7 along the ridge starting at 1,129 m and climbed to about 930 m along the ridge (fig. 5.7). The environment observations supported these of event 7 with the difference that *S. variabilis* was absent.

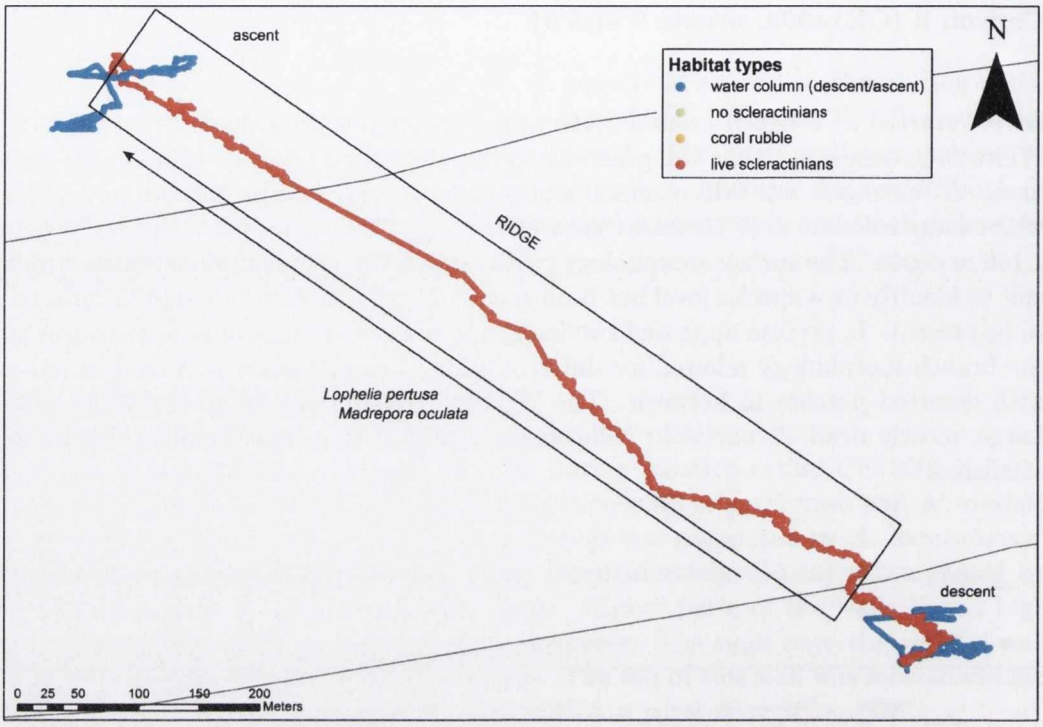


Figure 5.7: ROV dive track (event 9) along the ridge described for fig. 5.6. The box indicates the longitudinal orientation of the ridge.

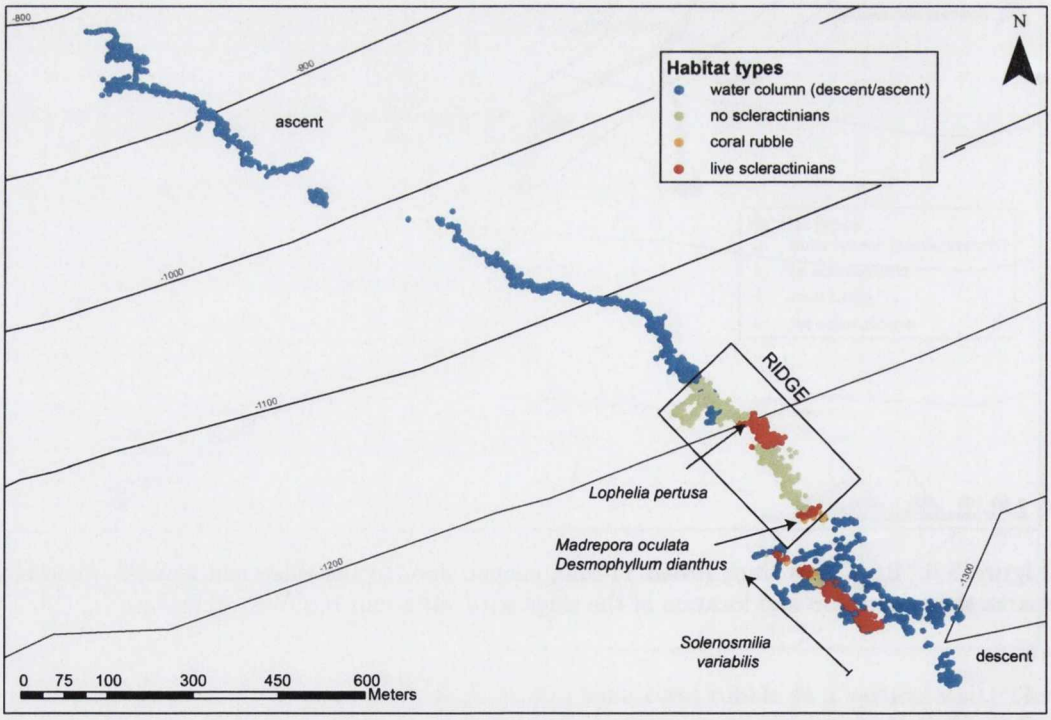


Figure 5.8: The ROV dive of event 62 followed a ridge upslope. The box marks the location and orientation of the ridge. It most likely continues further on. The onset of *L. pertusa* and *M. oculata* occurrence with *D. dianthus* is marked with arrows. Before the onset of *L. pertusa* occurrence *S. variabilis* was identified in deeper areas.

Canyon 4 (CE13008, event 62)

Canyon 4 was explored from around 1,420 m depth during the ROV dive of event 62 (fig. 5.8). Around 1,260 m *M. oculata* and *D. dianthus* were found after *S. variabilis* occurrence in deeper parts along the ridge. The video footage made identification of the thicker branched scleractinians difficult, and no sampling was possible (*L. pertusa* or *S. variabilis*). Around 1,130 m *L. pertusa* and *M. oculata* could be identified here together with tubes of the polychaete *E. norvegica*. From around 1,160 m on a high particle load in the water could be seen, partly moved by currents.

Canyon 4 (CE14009, event 12)

The dive started at approximately 1,365 m depth on a silty-sandy floor (fig. 5.9). The deepest parts were mostly settled by small *L. pertusa* colonies in sheltered erosional depressions on vertical surfaces. This area was also the deepest confirmed location (1,343 m) where live *L. pertusa* was found during our cruises. Thin-branched specimens of *L. pertusa* were found in erosional depressions on the open wall with live branches growing downwards from dead colony parts. Around 1,260 m a clear (and the only here directly observed) co-occurrence of *L. pertusa* and *S. variabilis* (whereby *S. variabilis* was only represented by one single colony) was seen. Around 1,010 m depth the dive reached a ridge with *L. pertusa* and *M. oculata* colonies in symbiosis with *E. norvegica*. The assemblages continued with short interruptions up to 905 m depth.

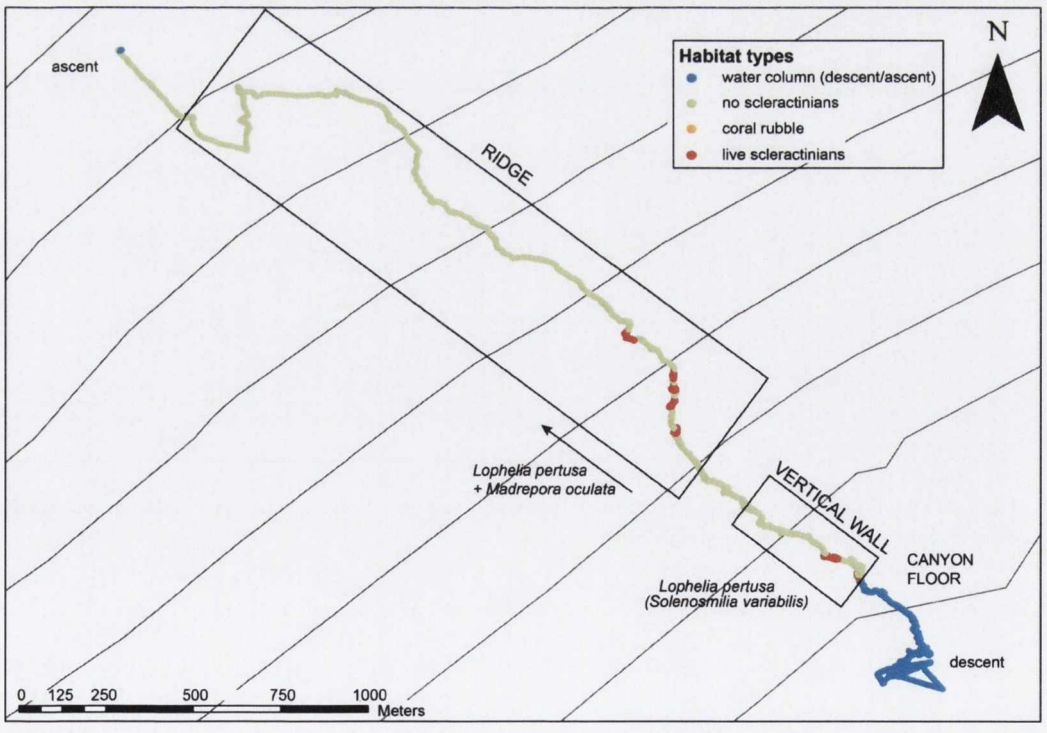


Figure 5.9: ROV dive track (event 12) from the canyon floor up the wall and along the ridge. Vertical wall and ridge showed *L. pertusa* predominance. Both boxes indicate the orientations of ridge and wall incline. The wall faces SE.

Canyon 4 (CE14009, event 25)

The dive started at 2,670 m depth on the soft sediment of the canyon floor. First indications of live *S. variabilis* with brisingids were found at a depth of 1,790 m on topographic highs. A single specimen of *E. rostrata* was detected at 1,730 m depth. Over the next approximately 200 m depth CWC cover and the colony size increased along the ridge. The occurrence of large *S. variabilis* colonies was interrupted by sponge gardens in topographic lows along the ridge.

Canyon 4 (CE14009, event 31)

Starting the dive at 1,770 m depth *S. variabilis* colonies were encountered on the canyon floor before disappearing again between 1,777 and 1,745 m and reappearing on a ridge structure (fig. 5.10). The fine sediment was covered with *S. variabilis* colonies of increasing size, mostly dead with a high abundance of large brisingid starfish. Where the path of the dive appeared to diverge to the ridge flanks the coral cover decreased. *S. variabilis* colonies reached more than 1 m in width and ca. 0.5 m in height.

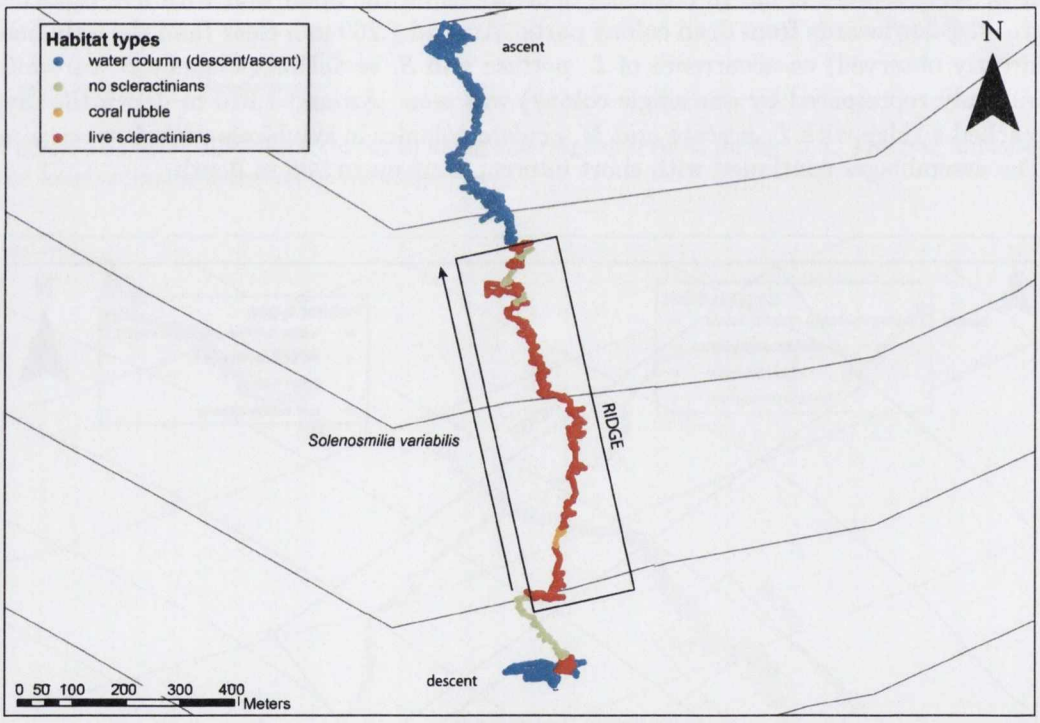


Figure 5.10: ROV dive track (event 31) from the canyon floor to a ridge with *S. variabilis* colonies. The ridge climbs to the NNW.

Canyon 5 (CE14009, event 5)

At the foot of the vertical canyon wall around 602 m depth the sandy floor was covered with dead CWCs and bivalve shells but showed no sign of live corals (fig. 5.11). The lower wall showed live *M. oculata* with visible *E. norvegica* tubes growing on the rubble with long-spined echinoids grazing here. The next approximately 30 m upwards along the wall revealed sparse CWC cover before the wall steepens and *L. pertusa* (white and orange) and *M. oculata* (orange) appeared in single bushy colonies. *D. dianthus*

joined the assemblage between 560 m and 530 m depth and became more abundant under overhangs together with the bivalve *A. excavata* (dominates the environment here). Around 520 m depth a flatter part was covered by rubble with *M. oculata* in colonies with *E. norvegica* tubes. The occurrence of *M. oculata* and further-on *L. pertusa* stabilised by *E. norvegica* tubes increased. Another short stretch of vertical wall led to the sand covered top at ca. 450 m.

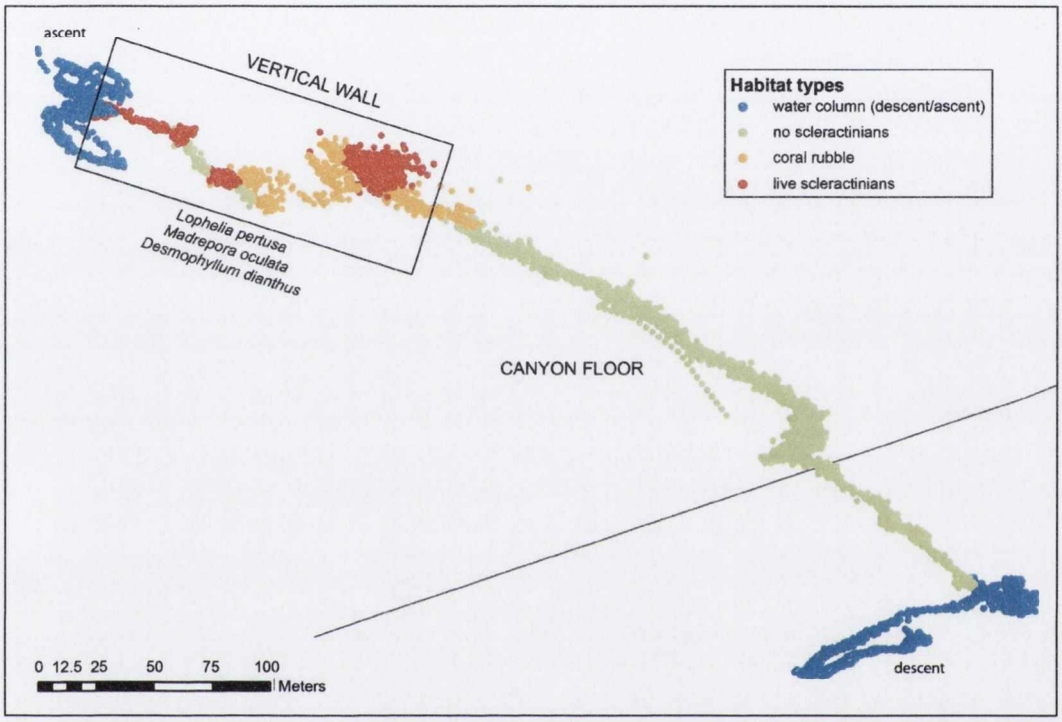


Figure 5.11: ROV dive track (event 5) climbing from canyon floor to the wall which faces SE.

5.1.3 CTD Data and Scleractinian Occurrences

All ROV dive sites in the canyons (fig. 5.12) were accompanied by CTD casts around the same location which highlighted a strong association between the occurrence of scleractinians and deeper peaks in fluorescence (table 5.2). Fluorescence reflected Chl α concentrations in the water column which pointed to increased nutrient flux possibly in connection with internal currents (fig. 5.13 to 5.22). The two CTD profiles at the site of event 39 also showed variations in the peak intensities with 18 hours time difference between CTDs which could be connected to different stages of tidal forcing (fig. 5.15 and 5.16). Since the water parameters were all collected in late spring/early summer they did not provide information on seasonal variations.

Table 5.2: List of selected CTD casts close to discussed ROV dive sites and in connection with CWC occurrence.

Cruise	CTD	Date	Time	Latitude	Longitude	Depth
CE13008	2	Jun 2, 2013	10:30	53.98622°N	12.61000°W	761 m
CE13008	5	Jun 3, 2013	03:50	54.01241°N	12.63288°W	1,445 m
CE13008	6	Jun 3, 2013	21:00	54.04713°N	12.63652°W	1,800 m
CE13008	15	Jun 6, 2013	07:45	54.14318°N	12.59468°W	2,400 m
CE13008	17	Jun 6, 2013	20:25	54.05298°N	12.59567°W	1,500 m
CE13008	20	Jun 9, 2013	03:44	49.00975°N	10.94879°W	660 m
CE13008	21	Jun 10, 2013	09:07	49.00985°N	10.94879°W	660 m
CE13008	30	Jun 12, 2013	n/a	48.88582°N	10.92280°W	738 m
CE13008	39	Jun 13, 2013	11:55	48.64408°N	10.47577°W	1,360 m
CE13008	52	Jun 16, 2013	01:45	48.76307°N	10.45987°W	741 m
CE14009	3	Jun 9, 2014	17:17	48.66650°N	09.94518°W	687 m
CE14009	4	Jun 10, 2014	07:20	48.70220°N	10.55320°W	1,486 m
CE14009	7	Jun 11, 2014	15:09	48.63160°N	10.49370°W	1,495 m
CE14009	17	Jun 15, 2014	18:45	48.58660°N	10.77100°W	2,796 m

Canyon 1 showed CWC cover on the canyon floor and alternating dominance of *L. pertusa* and *M. oculata* along the investigated stretch of vertical wall (fig. 5.15). Canyon 2 exhibited CWC coverage along the wall without any clear dominance of either of the two colonial CWCs. Canyon 3 was covered by four dives: CE12006 event 12 and CE13008 event 76 in upper reaches and CE14009 events 7 and 9 in deeper parts. *L. pertusa* and *M. oculata* occurrence was found from 620 m to below 1,100 m with indications of *S. variabilis* on deeper parts of a ridge. All occurrences were associated with regions of increased fluorescence and located below the salinity peak. Canyon 4 was studied in four dives: CE13008 event 62, CE14009 events 12, 25 and 31. The canyon region further up showed a ridge with *L. pertusa* above 1,150 m and *S. variabilis* below 1,150 m. Further down *L. pertusa* occurrence extended to 1,350 m (deepest observed occurrence during the described dives) while *S. variabilis* extended from 1,350 m to below 1,950 m, mostly along ridges (fig. 5.12). The salinity peak between 700 and 1,000 m/1,100 m, possibly connected to the presence of Mediterranean Outflow Water (MOW), lay above observed scleractinian existence. In canyon 5 we found a wall of *L. pertusa* and *M. oculata* within an increase of salinity, possibly connected to the MOW.

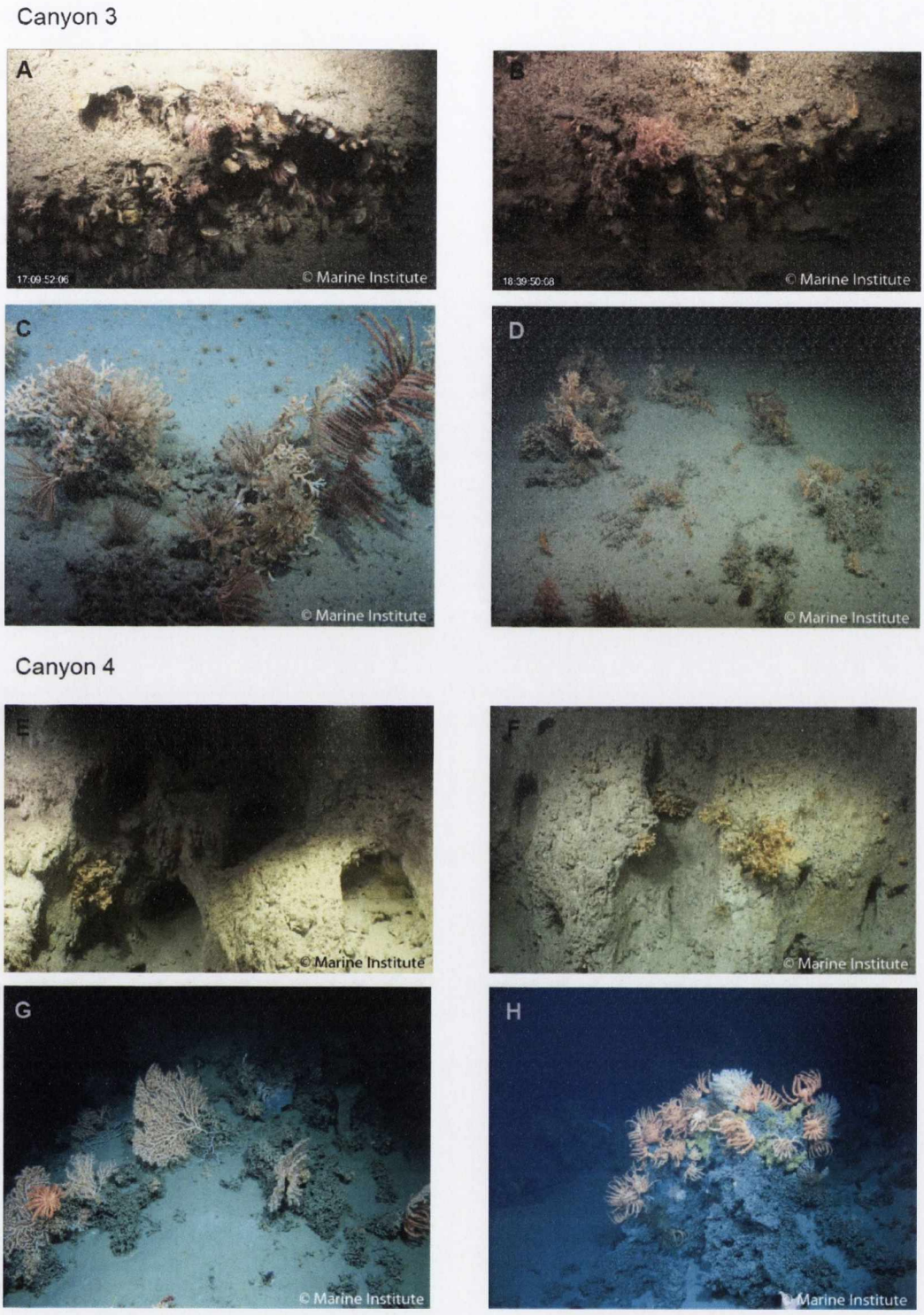


Figure 5.12: The two most prominent scleractinian habitats in the Whittard Canyon with examples from canyon 3 and 4: vertical walls (upper part canyon 3) and ridges (lower part canyon 3 and 4). A and B) Scleractinians, bivalves and soft corals under overhangs on a vertical wall. C and D) Sandy ridge with smaller scleractinians (*L. pertusa*). E and F) Vertical wall with erosional depressions around 1,350 m depth with *L. pertusa* growing in sheltered areas. G and H) Ridge with large colonies of mostly dead *S. variabilis* with soft corals and large numbers of brisingid starfish on top. For copyright information see Acknowledgements.

Porcupine Bank

Upper canyon

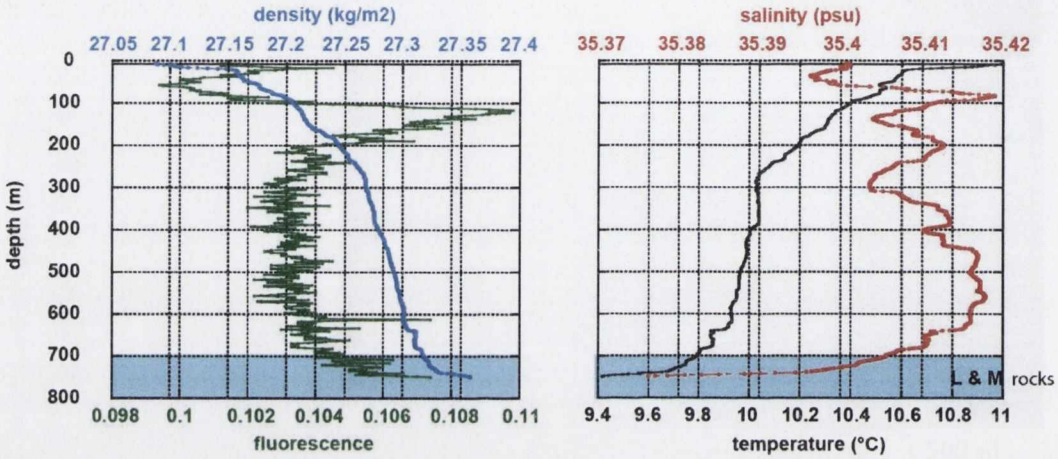


Figure 5.13: CTD cast 2 close to the location of ROV dive 7 (CE13008) showed a correlation between the occurrence of *L. pertusa* (L) and *M. oculata* (M) (green box) on rocks and wall parts and the increase in fluorescence and density. The CTD cast ended before the maximum depth of the dive was reached.

Lower canyon

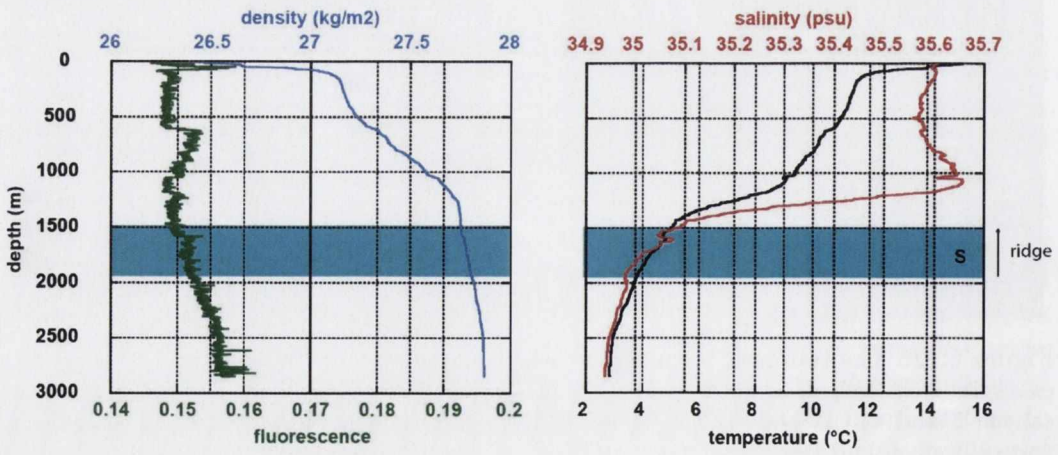


Figure 5.14: CTD cast 17 in the lower reaches of PB indicates the environmental parameters of *S. variabilis* occurrence along the ridge (green box).

Whittard Canyon

Canyon 1

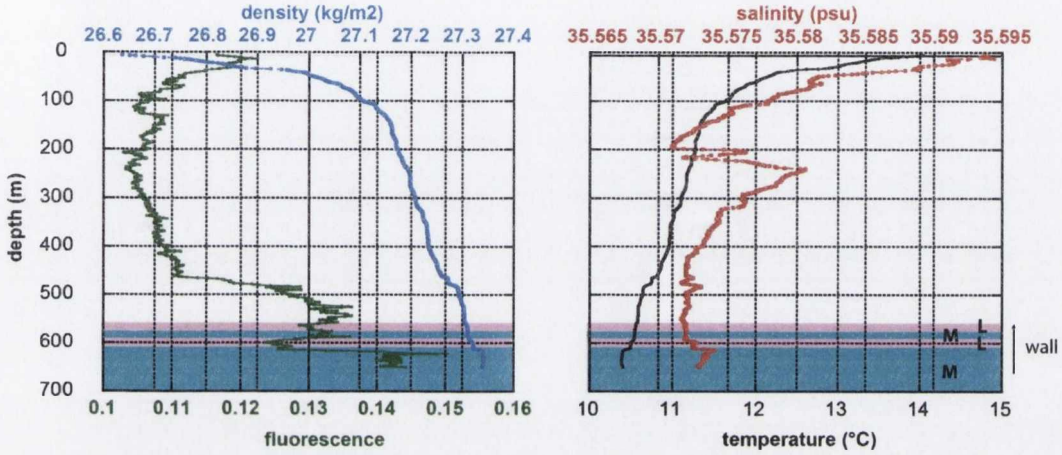


Figure 5.15: CTD cast 20 (at 3:44 am) reflected water parameters at the location of ROV dive 39. *L. pertusa* and *M. oculata* alternated in dominating the CWC occurrences on the wall below 550 m coincided with the increase in fluorescence below 500 m.

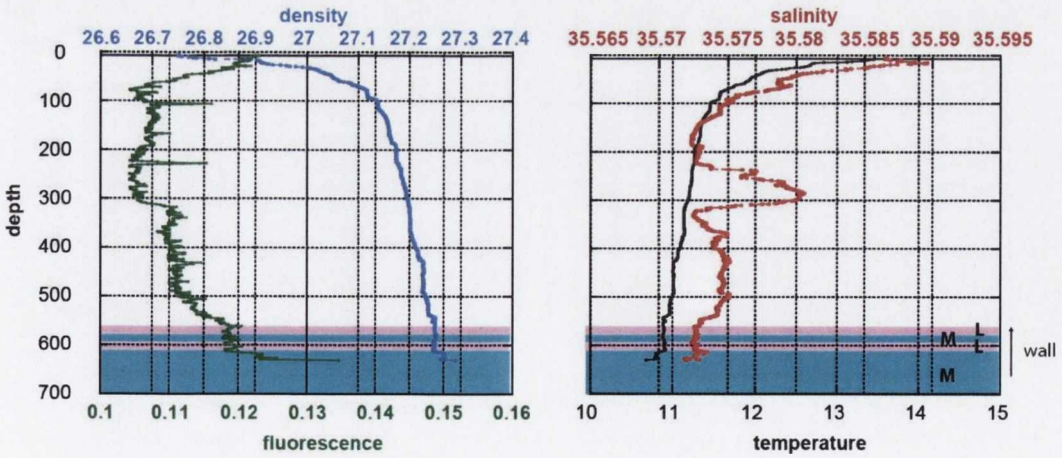


Figure 5.16: CTD cast 21 was taken at the same location but 18 hours after cast 20 (fig. 5.15). The water column showed clear variations in fluorescence between both CTDs. This points to tidal influences on fluorescence peaks.

Canyon 2

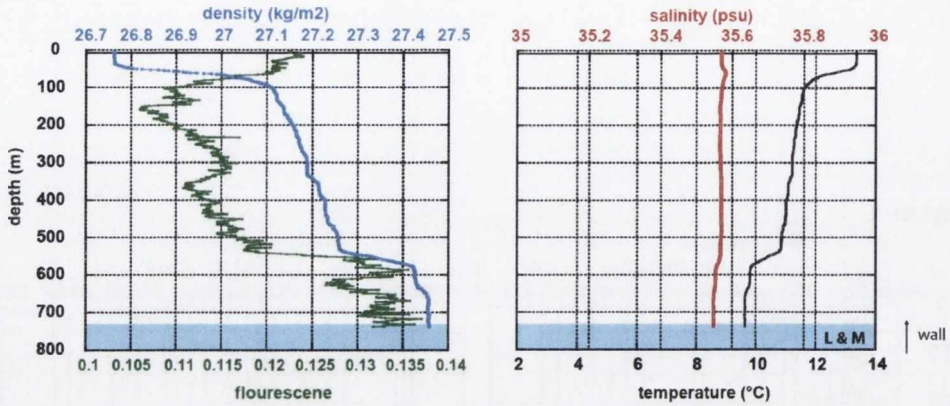


Figure 5.17: The dive ended before the lower limit of CTD cast 30 close to ROV event 52. The increase in fluorescence appeared to prevail below 750 m and in relation with CWC occurrence (*L. pertusa* (L) and *M. oculata* (M)).

Canyon 3

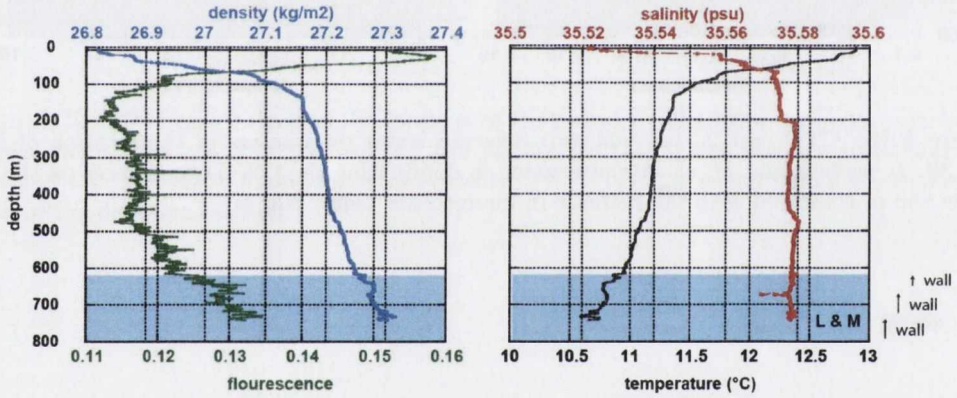


Figure 5.18: *L. pertusa* (L) and *M. oculata* (M) occurred in correlation with a visible increase in fluorescence in CTD cast 52 along the vertical wall (event 76).

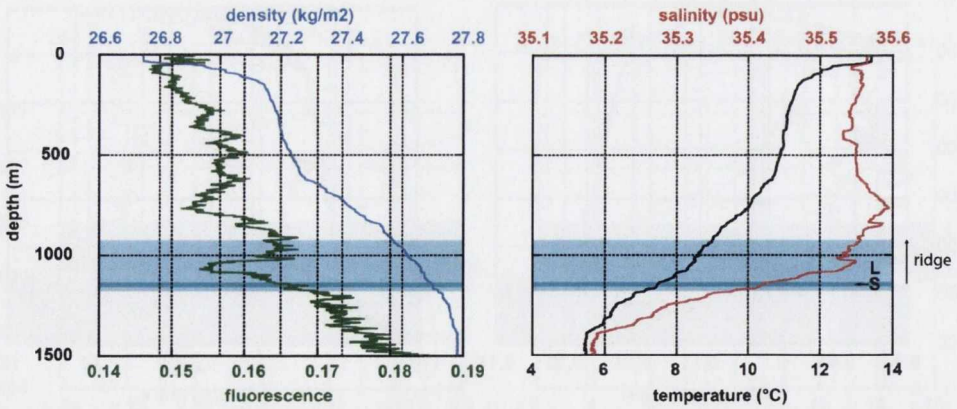


Figure 5.19: The CWC occurrence observed during ROV dives 7 and 9 was mostly correlated with peaks in fluorescence in CTD cast 04 (CE14009). The upper peak also appeared to be connected to the temporal increase in salinity (MOW connected). L = *L. pertusa*, S = *S. variabilis*.

Canyon 4

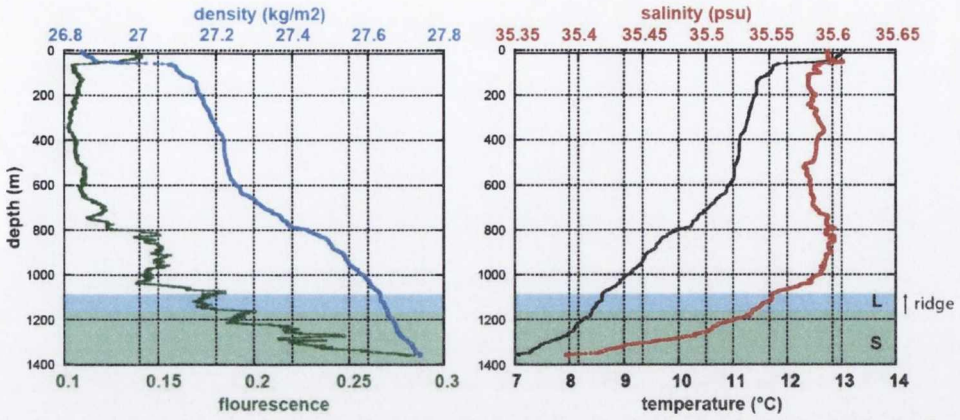


Figure 5.20: CWC occurrence along ROV dive 62 (CE13008) fell below the peak in salinity and fluorescence between 800 and 1,000 m (CTD cast 39) (which possibly indicated MOW influence). The dive itself showed *L. pertusa* (L) above 1,200 m depth (in blue) and *S. variabilis* (S) (in green) below this correlated with deeper peak in fluorescence.

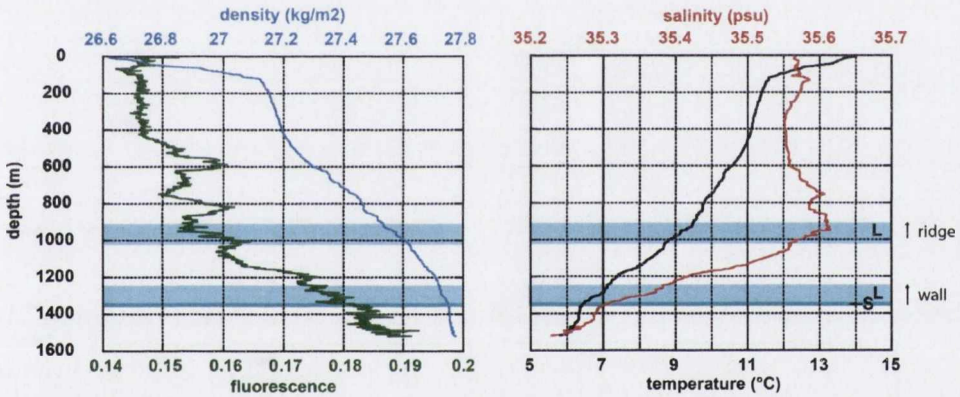


Figure 5.21: ROV dive 12 (CTD cast 07, CE14009) shows *L. pertusa* (L) occurrence between 900 and 1,000 m and between 1,250 and 1,350 m correlated with fluorescence peaks before *S. variabilis* occurred and possibly took over as the dominant species below 1,340 m.

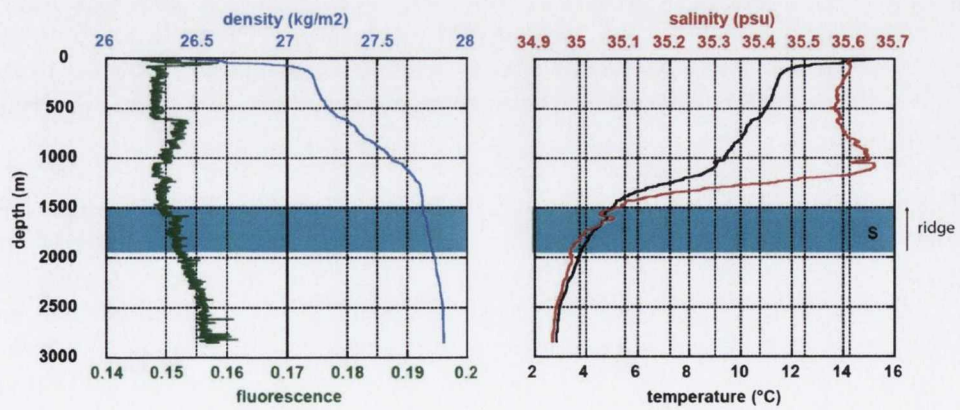


Figure 5.22: The deeper ROV dives 25 and 31 revealed a ridge with *S. variabilis* (S) occurrence observed between 1,500 and almost 2,000 m depth. The scleractinian occurrence was found in the area of the increase in fluorescence (CTD cast 17).

Canyon 5

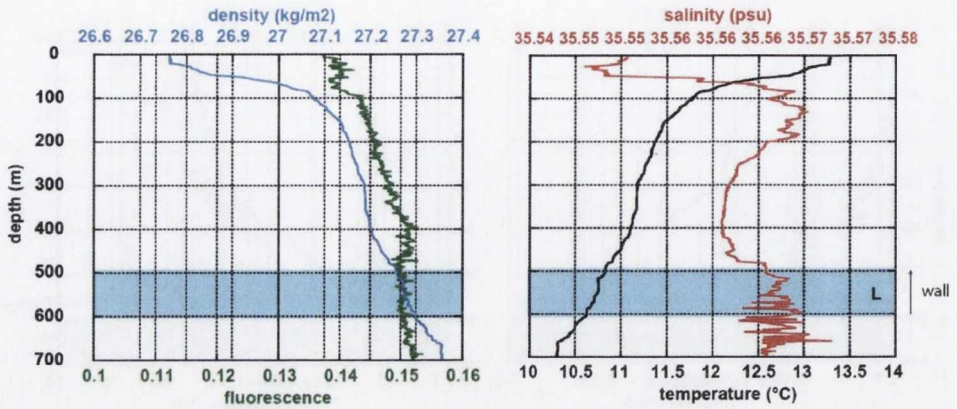


Figure 5.23: ROV dive 5 showed *L. pertusa* along a vertical wall between 500 and 600 m depth. No significant peak in fluorescence was seen at these depths but salinities here showed an increase and strong variations for this area in CTD cast 03.

5.2 Discussion

5.2.1 Environmental Parameters and Scleractinian Occurrence

Within the limits of our observations during the research cruises the occurrence of *L. pertusa* (and *M. oculata*) in WC and PB was connected to a temperature range between 6.5 and 11°C, a salinity range between 35.31 and 35.61 psu, a density range between 27.25 and 27.75 kg/m^3, and fluorescence between 0.104 and 0.2 (table 5.3). The occurrence of *S. variabilis* in both areas was connected to temperatures from 8.7 to below 3.8°C, salinities between 34.98 and 35.41 psu, densities above 27.0 kg/m^3, and fluorescence between 0.11 and beyond 0.18 (table 5.4). *E. rostrata* was found with *S. variabilis* in habitats with temperatures below 5°C, salinities below 35 psu and water densities above 27.7 kg/m^2. Fluorescence ranges above 0.11 were observed for this species.

The occurrence of *L. pertusa* mostly lay within the known tolerance range of temperature and salinity in northern waters but was in some cases in the Whittard Canyon also found below and above the density range defined for the species' occurrence in the N Atlantic (27.35-27.65 kg/m^3) (Järnegren & Kulli, 2014). *D. dianthus* was found in assemblages with *S. variabilis* as well as *L. pertusa* and *M. oculata*, therefore, we can assume that *D. dianthus* has a wider tolerance range. The two CTD profiles available for scleractininan habitats in canyon 1 (fig. 5.15 and 5.16) also showed daily fluctuations in temperatures around 0.5°C and in density around 0.1 kg/m^2 while salinity appeared more stable.

The most consistent environmental signal which accompanied the coral occurrence was the increase in fluorescence. Peaks in fluorescence mostly started around a pronounced peak in salinity (where available) but further peaks followed in deeper areas with increased peak strength towards the canyon floor. The occurrence of all species seemed to be ruled by fluorescence peaks (connected to nutrient input) in the Whittard Canyon. The fluorescence peaks appeared to be canyon-specific events which could only partly be related to the MOW but might be influenced by internal currents and tidal forces. The deeper peak might be related to benthic nepheloid layers (BNLs) which had been reported down to below 2,500 m depth (Wilson et al., 2015). The upper peak in fluorescence may be related to the existence of Intermediate Nepheloid Layers (INLs) (Wilson et al., 2015).

The temperature and salinity ranges for *L. pertusa* and *S. variabilis* overlapped partly but *L. pertusa* was generally found in higher temperatures and salinities (fig. 5.24). Since densities were influenced by temperature and salinity together they seemed to be a dominant limiting factor in scleractinian occurrences as suggested before (e.g. Dullo et al, 2008). The transition from *L. pertusa* dominance to *S. variabilis* dominance appeared to lie in densities between 27.5 and 27.8 kg/m^3 with co-occurrence of both species found here. Although the scleractinian occurrence seemed connected to peaks in fluorescence no upper limit of fluorescence ranges could be established here.

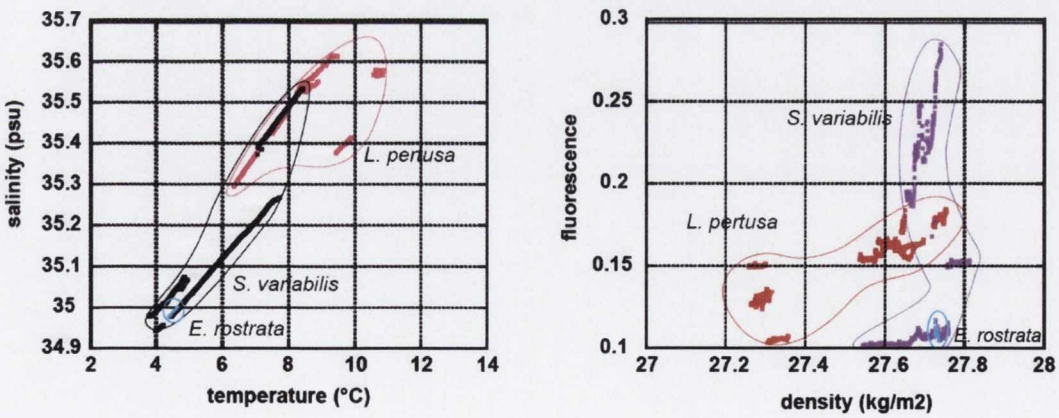


Figure 5.24: Generally *L. pertusa* was found in higher temperatures and salinities than *S. variabilis*. The peaks in fluorescence were higher in the area of *S. variabilis* occurrences. *S. variabilis* seemed to be connected to a defined density envelop ranging between 27.5 and 27.8 kg/m^2

Table 5.3: Range of water parameters in areas of CWC occurrence in our study area. ROV events off Porcupine Bank and in the Whittard Canyon:

Research Cruise	Event	Canyon	Depth (m)	Species	T (°C)	Salinity (psu)	Density (kg/m^3)	Fluorescence
CE13008	7	-	700-800	*L. pertusa/M. oculata*	<9.4-9.75	<35.38-35.405	27.32-27.36	0.104->0.107
CE13008	7	-	>1,400	*S. variabilis/E. rostrata*	<5	<35	>27.7	>0.11
CE13008	39	1	610-720	*L. pertusa/M. oculata*	10.5-0.9	35.572-35.575	27.25-27.35	0.115-0.135
CE13008	52	2	<730	*L. pertusa/M. oculata*	~9.6	35.54	27.45	0.132-0.137
CE13008	76	3	630-760	*L. pertusa/M. oculata*	10.6-10.95	35.57-35.58	27.25-27.31	0.125-0.135
CE14009	7	3	<1,300	*L. pertusa/M. oculata*	7.4-8.9	35.41-35.55	27.59-27.70	0.154-0.166
CE14009	7	3	>1,300	*S. variabilis*	7.43	35.41	27.70	0.166
CE14009	9	3	950-1,177	*L. pertusa/M. oculata*	<9.1	<35.55	>27.55	0.168
CE14009	9	3	1,150-1,159	*S. variabilis*	~8.7	~35.4	~27.7	~0.165
CE13008	62	4	930-1,129	*L. pertusa/M. oculata*	~8.5	35.53-35.55	27.64-27.65	0.17-0.2
CE14009	12	4	906-1,343	*L. pertusa/M. oculata*	6.5-9.5	35.31-35.61	27.53-27.75	0.154-0.181
CE14009	12	4	1,265, 1,343-1,365	*S. variabilis*	6.4-7.1	35.30-35.38	27.72-27.75	0.176-0.183
CE14009	25	4	1,505-1,950	*S. variabilis*	3.8-5.0	34.98-35.08	27.76-27.81	0.149-0.152
CE14009	31	4	1,600-1,772	*S. variabilis*	<7.2	<35.4	>27.71	<0.183
CE14009	5	5	460-602	*L. pertusa/M. oculata*	10.6-10.8	35.57	27.26-27.36	0.150-0.152

Table 5.4: Within the scope of the study the scleractinians in focus were found within the following ranges:

Species	Depth (m)	T (°C)	Salinity (psu)	Density (kg/m^3)	Fluorescence
Lophelia pertusa	460-1,343 m	6.50-10.95	35.31-35.61	27.25-27.75	0.104-0.200
Madrepora oculata	460-1,343 m	6.50-10.95	35.31-35.61	27.25-27.75	0.104-0.200
Solenosmilia variabilis	1,150-1,950	3.80-8.70	34.90-35.41	27.70-27.81	0.110-0.183
Enallopsammia rostrata	>1,400	<5.00	<35.00	>27.70	>0.110

5.2.2 Testing Existing Habitat Predictions

Many studies on bathymetry focused on physical features of the bottom morphology. Without multibeam data our results could not be compared to these studies. It was, however, possible to use the observations from all ROV dives of the last three years (table 4.1) to compare the Presence/Absence of *L. pertusa* in the Whittard Canyon to published model projections for this species and location (Rengstorf et al., 2013) (fig. 5.25).

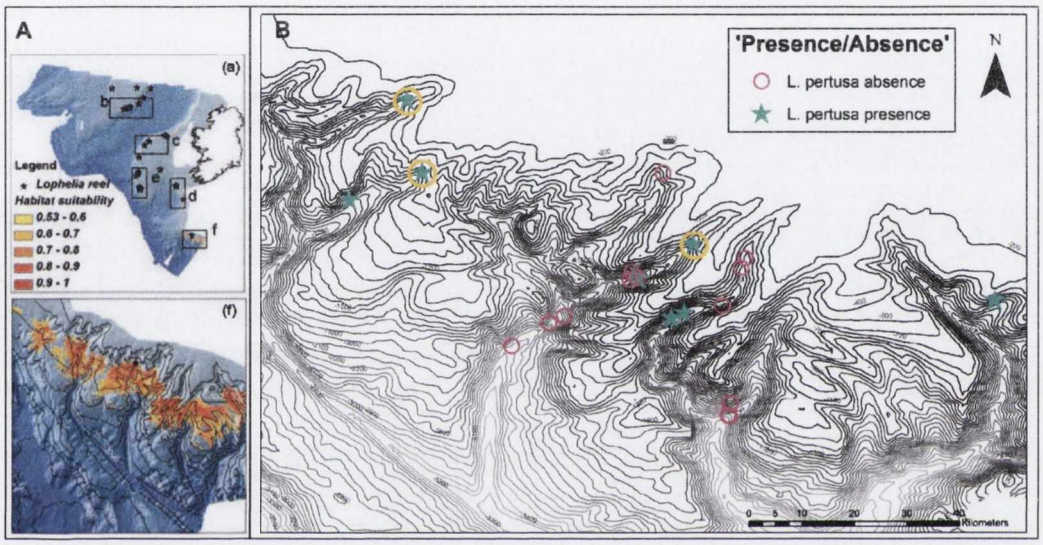


Figure 5.25: Rengstorf et al. (2013) produced a habitat prediction for the species *L. pertusa* in the Whittard Canyon (A). The studied ROV dives within the Whittard Canyon showed the overlap with and deviations from these predictions; green stars and pink circles mark previously discussed findings. The uppermost reaches of the canyons with their rich vertical wall habitats lay beyond model predictions (yellow circles) (B).

The example of predictive modelling for *L. pertusa* occurrence in the Whittard Canyon was based on seabed slope, temperature and bottom shear stress as the most important variables (Rengstorf et al., 2013). In comparison with our observations during the ROV dives the presence and absence of *L. pertusa* partly diverted from these predictions along the upper reaches of the canyons where the vertical walls were more abundant. The predicted upper limit of 9.9°C (Rengstorf et al., 2013) lay below the observed limit and appeared to be an underestimate. The vertical walls might substitute the optimal bottom conditions by providing a way of reaching higher currents with particle load and higher temperature. This is one example of the difficulty of detailed habitat predictions due to the complexity of CWC adaptations and interaction with different environmental parameters. The discussed model by Rengstorf et al. (2013) was, like many other models, based on factors like bathymetry which could not be discussed since no comparable high-resolution data was available for the presented data. In addition, CTD casts suggested that the peak in fluorescence connected with the CWC occurrences was an important variable. The model predictions (Rengstorf et al., 2013) did not consider this parameter. Future models should include fluorescence peaks, possibly in connection with intermediate and benthic nepheloid layers.

5.2.3 Habitat Geomorphology

The vertical wall habitat was well classified for this area before (Johnson et al., 2013, Huvenne et al., 2011). The first ROV dive in 2012 only revealed *M. oculata* and *D. dianthus* which was probably coincidental due to the limited area that could be covered during individual ROV dives. Further dives in 2013 gave evidence to *L. pertusa* and *M. oculata* occurrences along the walls and underneath ledges without any significant habitat preference of either species. Since *D. dianthus* was identified at all depths and in co-occurrence with all colonial scleractinians this species will be neglected in further discussions. Vertical walls as CWC habitats in assemblages with bivalves appeared to be typical for the upper reaches of the canyons above 800 m depth. All dives showed current movement with high particle load along the wall. The canyon floor below the wall was typically covered with coral rubble which is scarcely settled by small colonies and solitary scleractinians. The settling sediment on the floor appeared to make this habitat less favourable for suspension feeders.

The ridges observed deeper down in the canyons were so far not described for the WC. Since no multibeam bathymetric data was collected during the cruises no further information on the overall geomorphological context was possible. In other environments (e.g. Porcupine Seabight) similar ridges were described in ripple-field-like arrangements (Foubert et al, 2011). The ridge appeared to consist of dune-like sediment accumulations but scleractinians found along the ridges commonly required hard substrate for settlement. Therefore, it could be assumed that the buried dead coral colonies form part of the core. The morphology of the feature plus the location within the canyons ruled an interpretation as a carbonate mound out. The ridges were located perpendicular to the canyon currents up the canyon wall. Sediment waves had been described from the neighbouring Porcupine Seabight (e.g. Foubert et al., 2011) but appeared to be smaller in scale than the here observed structures.

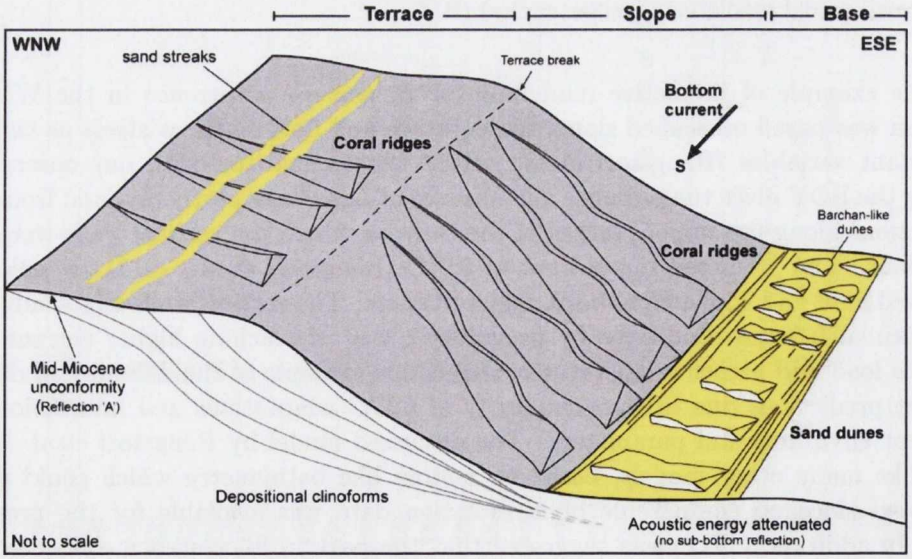


Figure 5.26: Main features of deep sea coral ridges (Correa et al., 2012).

Coral ridges were classified on a terrace in the W Atlantic in connection with unidirectional currents (Correa et al., 2012). Here sand dunes and waveform coral ridges were differentiated by the orientation of their steep sides in relation to the current direction and sediment dynamics (Correa et al., 2012) (fig. 5.26). In the WC internal currents were most likely bidirectional possibly due to tidal influence. The full extent and morphology of wave sides and information on sediment particle size were unknown in the reported case, therefore, a differentiation using these criteria was not possible. The same applied to information on the internal structure. Without further data (e.g. multibeam bathymetry, drill cores) no clear interpretation regarding the origin of the ridge formation was possible. However, the development of large coral structures along the ridge (and partly along less steep sides) of the waveforms indicated a comparable structure as described by Correa et al. (2012) but has to be verified. Further dives in the area should take a closer look at the composition of the structures.

Chapter 6

Comparative Study on Interspecies Differences in the Geochemistry of Scleractinians

One chosen approach to investigate CWCs as environmental recorders was light stable isotope ratio analysis (oxygen and carbon). While *L. pertusa* was included in different studies on $\delta^{18}O$ and $\delta^{13}C$ (e.g. Mortensen & Rapp, 1998, Mikkelsen et al., 1982), and *D. dianthus* was even part of studies on ambient temperature reconstruction (Smith et al., 2000), *M. oculata* is relatively unexplored in this context. Therefore, as a first step, a comparative study was launched to highlight the potential of three available scleractinian species from the Whittard Canyon (fig. 6.1) for temperature reconstruction using the 'lines technique' (Smith et al., 2000). This chapter provides a first evaluation of this approach and the basis for the selection of species for further analysis.

6.1 $\delta^{13}C$ and $\delta^{18}O$ Correlation

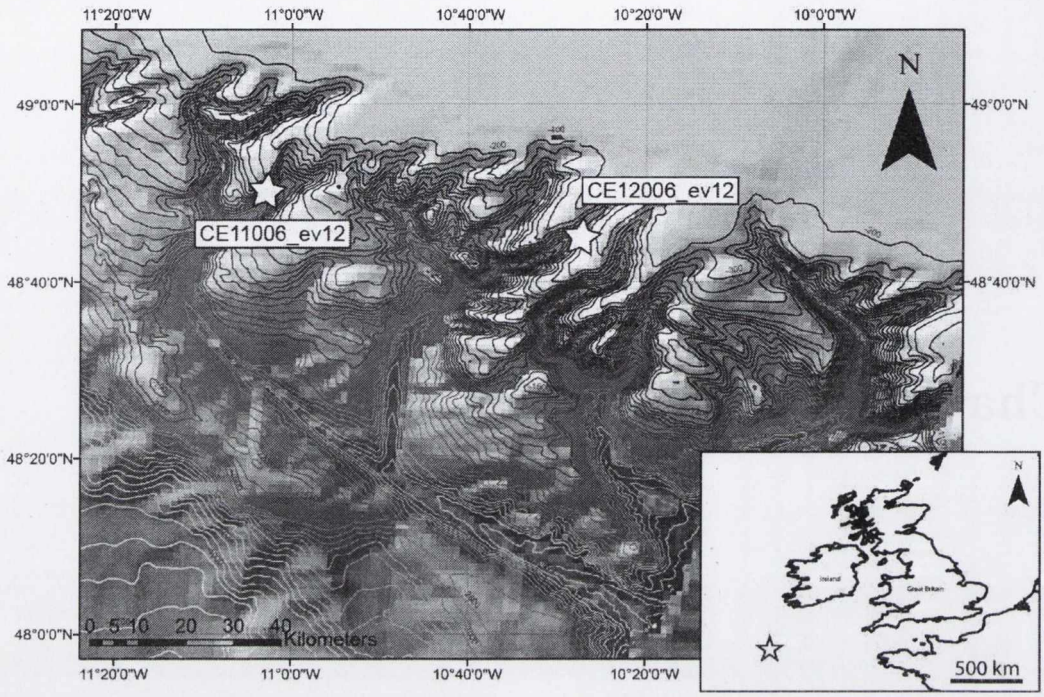


Figure 6.1: Different species were sampled from the Whittard Canyon during two research cruises: *Lophelia pertusa* at CE11006 event 12, *Madrepora oculata* and *Desmophyllum dianthus* at CE12006 event 12.

A selection of three CWC species from vertical walls in two canyons in the Whittard canyon complex were sampled for stable isotope analysis (fig. 6.1). The samples were ablated with a hand-held drill from the CWC surface, i.e. the latest precipitates. Minima, maxima and averages of $\delta^{18}O$ and $\delta^{13}C$ were listed in table 6.1.

Table 6.1: Stable isotope ratio maxima and minima together with average stable isotope ratios in different species from the Whittard Canyon. M = *M. oculata*; L = *L. pertusa*; D = *D. dianthus*.

	Species	$\delta^{18}O_{max}$	$\delta^{18}O_{min}$	$\delta^{13}C_{max}$	$\delta^{13}C_{min}$	$\delta^{18}O_{mean}$	$\delta^{13}C_{mean}$	n
459-M1	M	1.66‰	-0.95‰	-2.11‰	-7.04‰	0.14‰	-5.41‰	21
459-M2	M	2.30‰	-0.61‰	-0.53‰	-7.37‰	0.60‰	-4.85‰	22
458-C1	D	2.53‰	0.29‰	0.11‰	-4.46‰	1.64‰	-1.90‰	23
458-C2	D	2.61‰	-0.47‰	1.26‰	-4.98‰	1.25‰	-1.56‰	22
458-C3	D	2.83‰	-0.66‰	0.43‰	-8.36‰	1.46‰	-2.35‰	24
458-C4	D	1.63‰	0.3‰	-1.69‰	-5.01‰	0.88‰	-3.40‰	21
L1	L	2.88‰	0.59‰	-0.09‰	-5.64‰	1.76‰	-2.75‰	20

The results from both *M. oculata* and *L. pertusa* specimens showed a good fit to a $\delta^{13}C/\delta^{18}O$ regression line and, therefore, a high correlation between both stable isotope ratios throughout the recent growth phase (fig. 6.2 and 6.3). Of the four *D. dianthus* specimens only two displayed a comparable fit and correlation (fig. 6.4). The other two showed a less significant fit to the regression line (R^2 below 0.7). While

both *M. oculata* datasets overlapped and the intercept with the y-axis as well as the slope lay close, only two out of four *D. dianthus* specimens (C1 and C3) plotted on comparable regression lines (fig. 6.3).

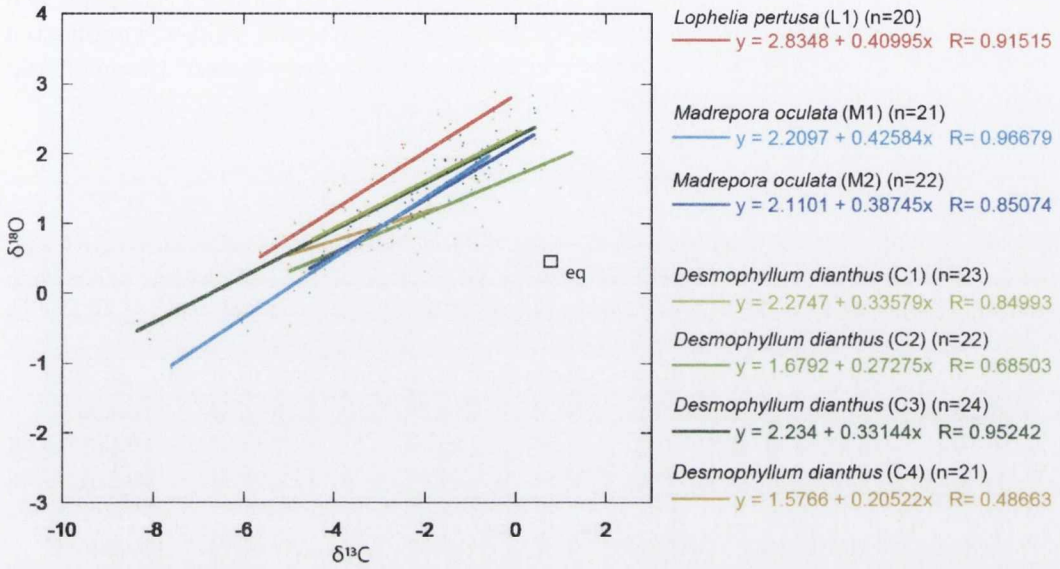


Figure 6.2: A selection of different species from the Whittard Canyon shows inter- and intraspecies variations in geochemistry. The samples were collected from the outermost layers (equivalent with most recent growth). The box marks ambient water composition.

6.2 Discussion

According to the 'lines technique' the intercept of the regression line with the y-axis can be used to reconstruct ambient seawater temperatures (table 6.2) (Smith et al., 2000). Smith et al. (2000) published two possible equations for the approach. One option for the case that $\delta^{13}C_{CWC} = \delta^{13}C_{water}$ (eq. 6.1), the second for the case that the geochemical composition of the surrounding water is unknown and $\delta^{13}C_{water} = \delta^{18}O_{water} = 0$ is assumed (eq. 6.2). Neither option fully applied in our study, as $\delta^{13}C$ of the ambient water in the area lay above cero ($\delta^{13}C_{water} \approx 0.76‰$). However, even with a different equation the variations in intercepts between specimens and species led to high variations in reconstructed temperatures (compare table 6.2).

$$\delta^{18}O_{CWC} - \delta^{18}O_{water} = (-0.25 \pm 0.01) * T(°C) + (4.97 \pm 0.24) \quad (6.1)$$

$$\delta^{18}O_{CWC} = (-0.22 \pm 0.01) * T(°C) + (4.51 \pm 0.35) \quad (6.2)$$

All species from the Whittard Canyon showed a positive offset from equilibrium with seawater stable isotope ratios the highest offset was found for *L. pertusa* while it was slightly smaller for *M. oculata* (fig. 6.3). However, *D. dianthus*, although more variable, came closer to equilibrium in all four samples (fig. 6.3). The original research on a temperature reconstruction approach was conducted on solitary CWCs and tropical corals (Smith et al., 2000). The approach was continued on solitary corals with varying regression lines (Marali et al., 2013). None of the published regression lines fitted our data in general and in the case of *D. dianthus* as a solitary species in particular (fig. 6.4). The two best fit regression lines for *D. dianthus* specimens

(C1 and C3) were closest to the published slopes. All of the data (our results and literature) pointed to a high variability within *D. dianthus* and among CWCs from the same environment. This made an absolute temperature reconstruction without knowledge about species-specific offsets (due to 'vital effects') impossible. To date no study on a quantification of species-specific fractionation effects is available and it is unclear if such an effect can be quantified (among other things complicated by inter-species variability). A relative negative correlation between intercept and ambient temperature appeared to exist (table 6.2).

Table 6.2: $\delta^{18}O/\delta^{13}C$ regression line parameters (intercept and slope) and reconstructed temperatures for different species from the Whittard Canyon using both equations (see reference in brackets) (Smith et al., 2000). The measured temperature at the sampling depth is 10.190°C, $\delta^{18}O_{water} = 0.45‰$, $\delta^{13}C_{water} \approx 0.76‰$.

	Species	Intercept	Slope	$\delta^{13}C_{CWC}$	T_{recon} [6.1]	T_{recon} [6.2]
459-M1	*M. oculata*	2.21‰	0.43	-5.41‰	12.841°C	10.456°C
459-M2	*M. oculata*	2.11‰	0.39	-4.85‰	13.240°C	10.909°C
458-C1	*D. dianthus*	2.27‰	0.34	-1.90‰	12.581°C	10.161°C
458-C2	*D. dianthus*	1.68‰	0.27	-1.56‰	14.963°C	12.867°C
458-C3	*D. dianthus*	2.23‰	0.33	-2.35‰	12.744°C	10.346°C
458-C4	*D. dianthus*	1.58‰	0.21	-3.40‰	15.374°C	13.334°C
L1	*L. pertusa*	2.83‰	0.41	-2.75‰	10.341°C	7.615°C

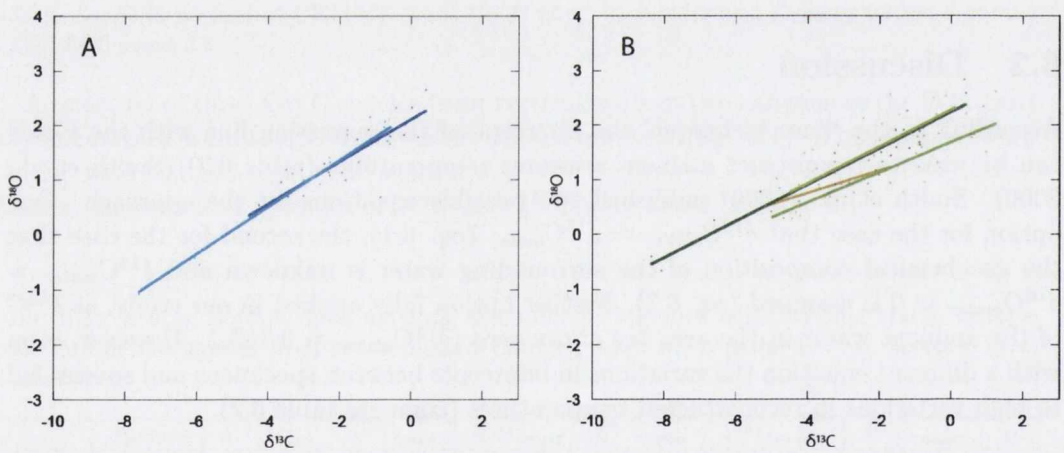


Figure 6.3: Two *M. oculata* specimen (A) and four *D. dianthus* specimen (B) from the Whittard Canyon in comparison.

Therefore, using the 'lines technique' as it is, to retrieve information about ambient seawater temperature seems insufficient. An improvement might be achieved by integrating measured $\delta^{13}C$ values since the carbon isotope ratios are influenced by metabolic activity and are known for species-specific fractionation effects (e.g. McConnaughey, 1989a, 1989b). This requires, however, a much larger dataset. It is possible that a well-established equation for specific species increases accuracy and precision. The following chapter will focuses on *M. oculata* from different temperature regimes to test the potential of this species.

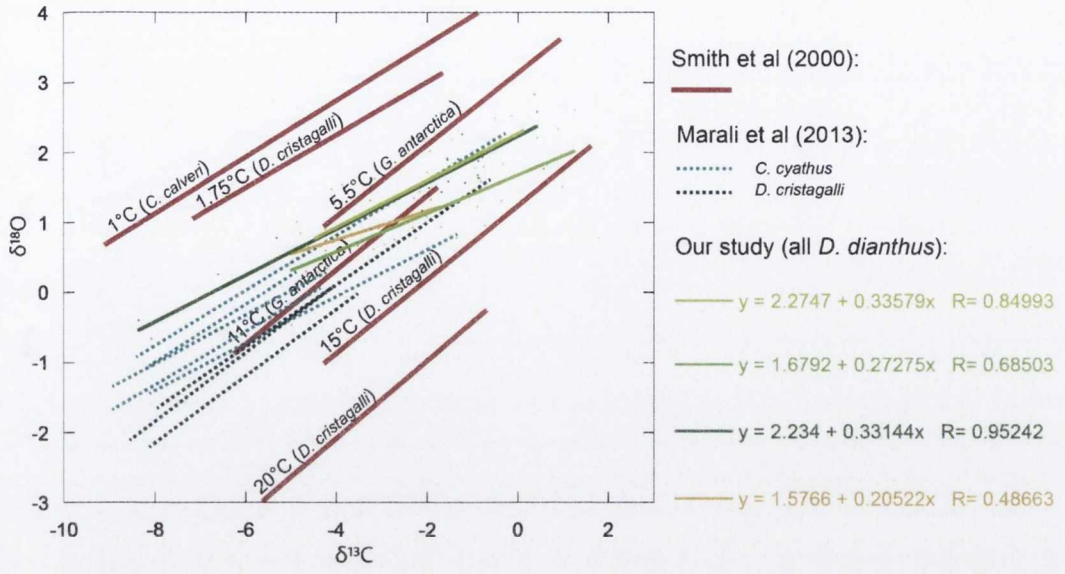


Figure 6.4: The comparison of regression lines produced from *D. dianthus* (in older publications labelled as *D. cristagalli*) samples from the Whittard Canyon to those from two earlier studies showed strong variations in slopes with partly low fits.

The applied sampling technique, using surface samples, was originally suggested by Smith et al. (2000) to improve the approach by focusing on most recent calcifications. Nevertheless, it could also cause deviations and potentially include more contaminations as *D. dianthus*, for example, exhibited a high degree of sponge infestations and other bioerosion which might not be visible from the surface but still influence geochemical signals. On the other hand, since sponge infestations were usually found within older layers, this surface sampling technique held a higher potential to avoid such contaminations but cannot completely rule them out. Published studies on solitary corals reported the exclusion of bioeroded areas and possibly data rejection. Without more knowledge about biomineralisation processes, however, outlier rejection can change correlation parameters like the intercept significantly. The fact that the here presented data included all measurements might account for the fact that higher variations in regression lines and lower degrees of correlation for different specimens were found.

This would consequently reduce the precision compared to earlier studies. Outlier rejection could increase precision and clean up results which could be one reason for the difference to published data. Outlier rejection would be misleading and was, therefore, not performed. As a result two of the regression lines for *D. dianthus* showed a poor fit ($R^2 < 0.7$) and clear variations in slopes.

Chapter 7

Case Study: *Lophelia pertusa*

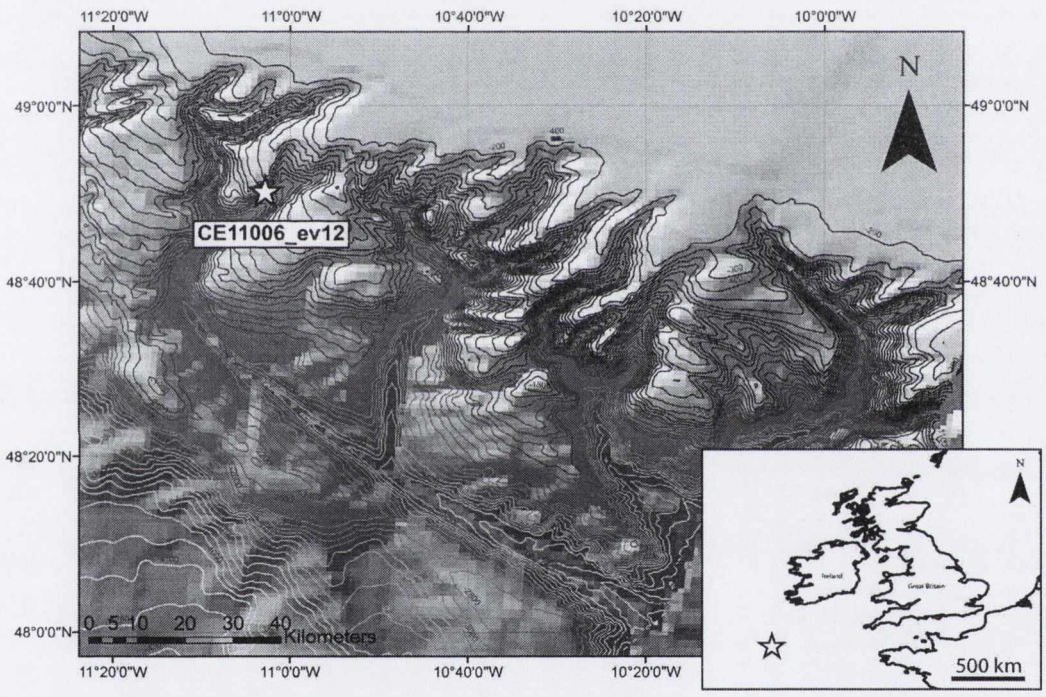


Figure 7.1: Location of *L. pertusa* sampling location in a canyon in the western part of the Whittard Canyon system (research cruise CE11006 in 2011).

The scleractinian species *L. pertusa* had been in the focus of many studies before but so far the exact mechanisms of biomineralisation are still discussed. Most investigations were based on bulk samples along individual directions of growth without producing a complete image of geochemical variations along growth (e.g. Raddatz et al., 2014, Lopéz Correa et al., 2010). The following chapter attempts to increase the resolution of geochemical variations along growth of a sample from the Whittard Canyon (fig. 7.1) using different sampling techniques (microdrill sampling and laser ablation), discuss the application and test the potential of different isotopes in this context. The results are to highlight small scale variations and provide additional information for a discussion of existing proposed biomineralisation models.

7.1 Patterns in Coral Growth

7.1.1 Microstructures

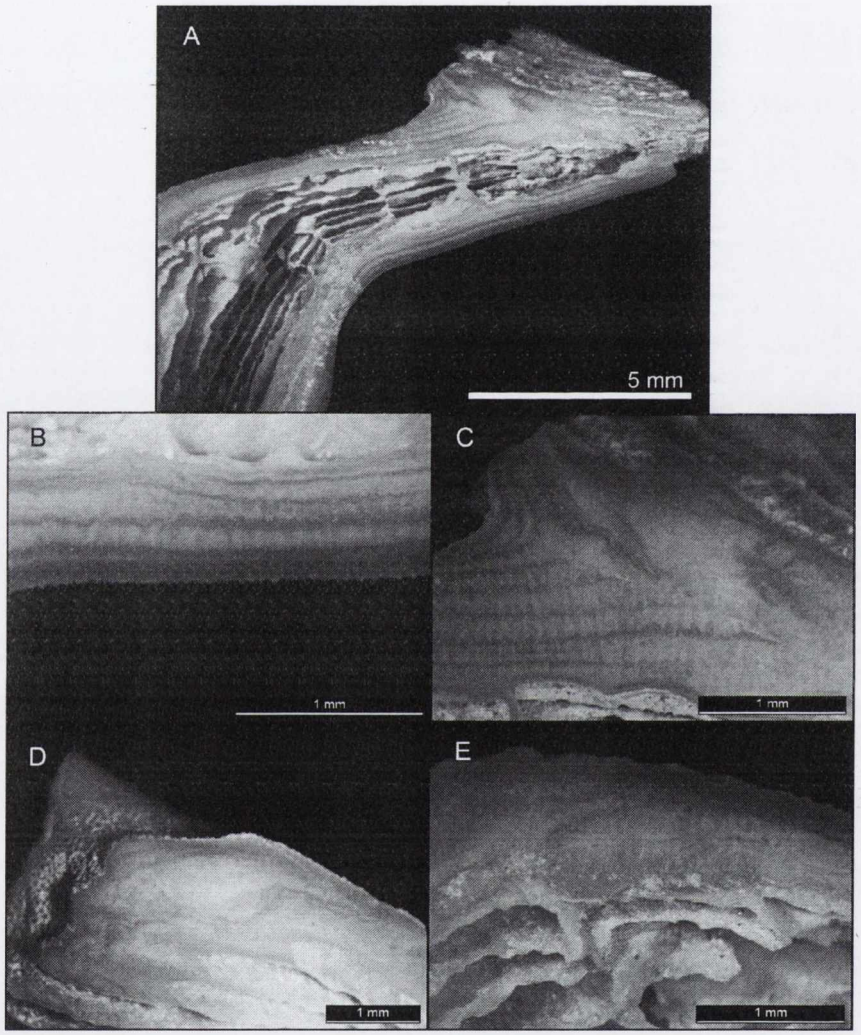


Figure 7.2: Under reflected light: A) Alternating layers along *Lophelia pertusa* skeletal growth. B)+C) White layers display increment-like structures. D)+E) Stepwise bending layers within the top part of corallite, in context with septal growth and onset of new corallites (E) (compare fig. 2.22).

The thick section of the *L. pertusa* L1 sample displayed 'increments' in the white layers under reflected light (fig. 7.2 (B)). Under transmitted light a network of thin lines was visible running through the white layers perpendicular to the orientation of layers (fig. 7.3 (A)). The thin lines were easier visible in the beige layers under transmitted light (appeared translucent here) while white layers make their detection harder as they commonly appear dark (brown). Combining transmitted and reflected light imagery the network of lines seemed to consistently cover the whole theca.

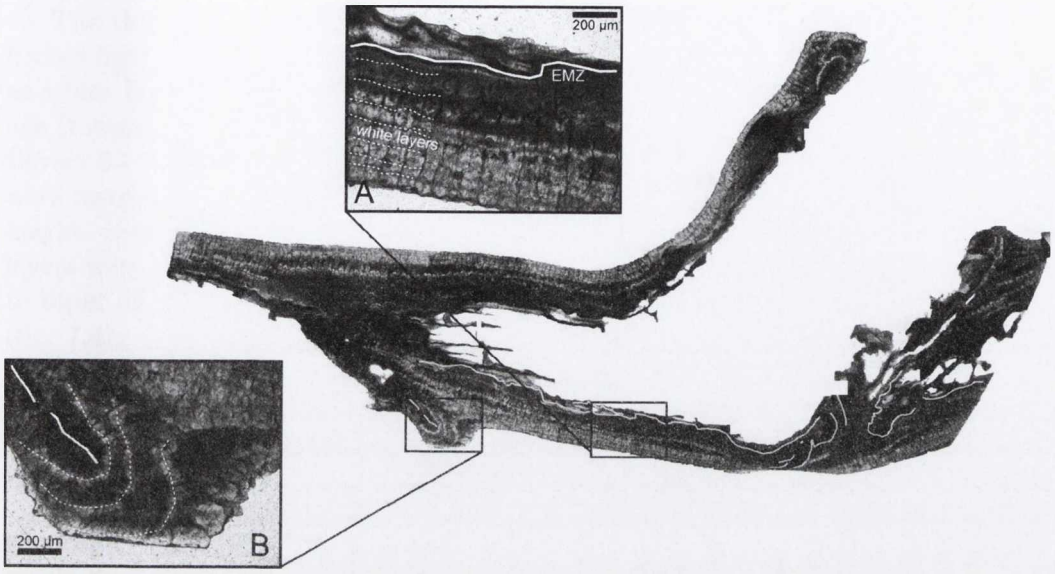


Figure 7.3: Under transmitted light: A) Alternating layers across the *Lophelia pertusa* wall. Fibre bundles were partly visible within the translucent layers. Dotted lines represent 7 white layers, solid lines indicate EMZ position. B) The tip of the theca displayed bending white and beige layers as well as segmented EMZs indicate stepwise growth in length.

7.1.2 δ^{18}O and δ^{13}C Analysis along *L. pertusa* Growth

The bulk samples, extracted over 400-500 μm long intervals of individual layers (see 'Methods' and compare fig. 7.4 and 7.5), showed δ^{18}O ranging from -2.4‰ to 2.7‰, while δ^{13}C varied between -8.4‰ and -2.3‰ (table 7.1). Both stable isotope ratios showed a distinct peak around the middle part of each layer, which was more pronounced in the stable carbon isotope signal (>2‰), and additionally a small peak towards the end of longer layers (fig. 7.4). The δ^{13}C peaks of the innermost layers were consistently found in the same area within the layers (fig. 7.4). The two most recently precipitated layers (= outermost layers) generally revealed higher stable isotope ratios which increased gradually along the linear growth axis and formed a wider peak.

Table 7.1: *L. pertusa* L1: stable isotope maximum, minimum, mean and standard deviation (SD) per layer.

Layer	$\delta^{18}O_{max}$	$\delta^{18}O_{min}$	$\delta^{13}C_{max}$	$\delta^{13}C_{min}$	$\delta^{18}O_{mean}$	SD	$\delta^{13}C_{mean}$	SD
1	2.65	-1.35	-2.33	-5.88	0.69	0.98	-4.08	1.15
2	1.79	-2.43	-4.67	-7.58	0.06	1.12	-6.51	0.99
3	2.05	-1.31	-3.59	-7.35	0.21	1.15	-6.18	1.36
4	1.09	-2.10	-5.24	-8.37	-0.69	0.97	-6.98	0.92
5	0.00	-1.70	-5.23	-7.77	-0.88	0.59	-6.61	0.91
6	0.36	-2.13	-5.07	-8.24	-0.58	0.79	-7.12	0.73
7	-0.35	-1.86	-6.83	-7.63	-0.90	0.59	-7.40	0.31

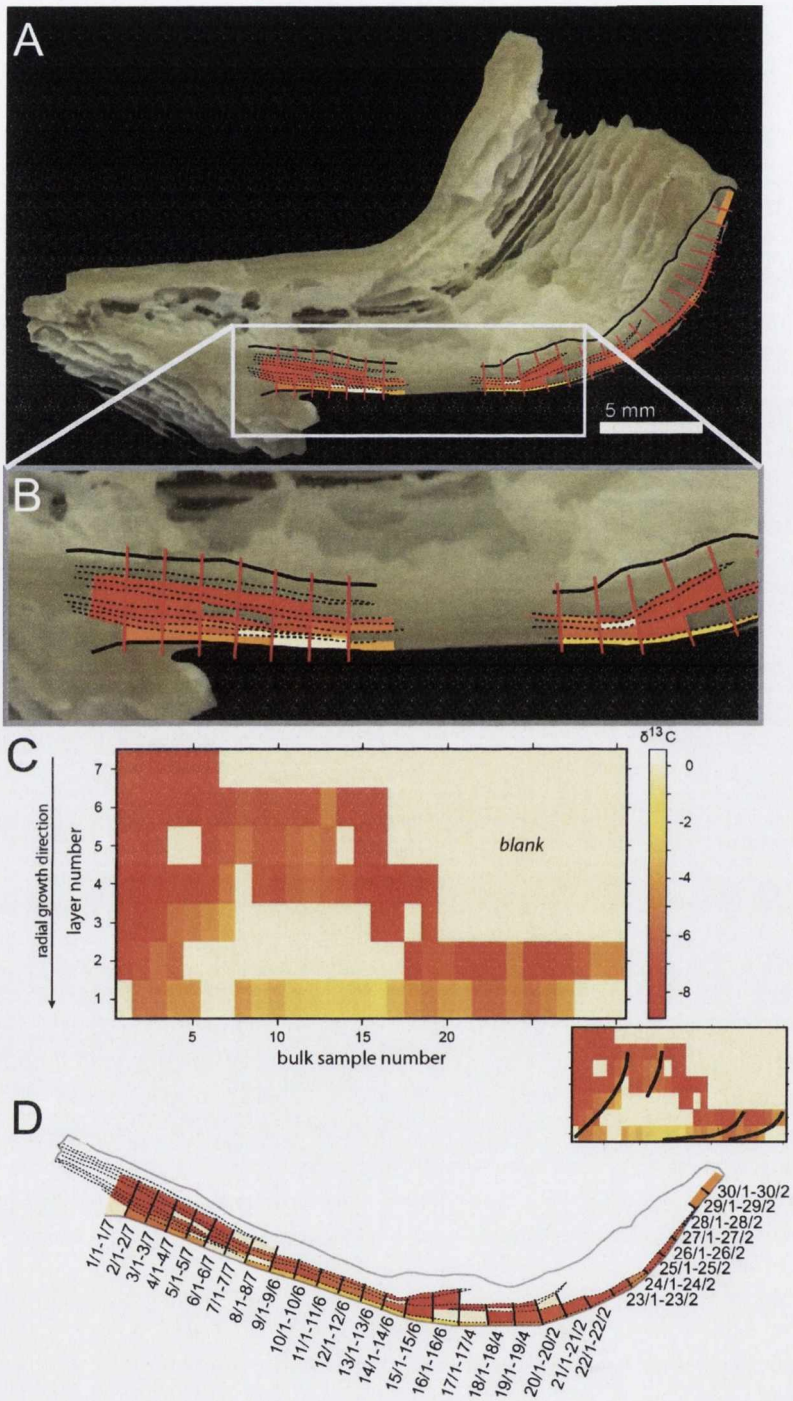


Figure 7.4: A) The full theca was separated into 30 sections (ca. 450 μm steps) (red lines) which were sampled in bulk separately for each layer using a microdrill. Here parts of the data are overlain to show the association with sketched layers. B) Zoom shows alternating white and beige layers and parts of the $\delta^{13}C$ data. C) Stable carbon isotope ratios display variations in radial (y-axis) and longitudinal (x-axis) growth. Diagonal trend with a peak in ratios stretches across layers. D) The full data set in combination with a sketch of the visible layers. Stable isotope ratios are reflected in the gradient colours. Labels refer to 'bulk sample number/layer'. Layers from outermost (layer 1) inwards (to layer 7). White areas mark gaps in data.

The thin section displayed seven (partly eight) dark layers (= white layers in reflected light) following the EMZs, not all of which were actually visible macroscopically as white layers under reflected light since the thickness of the layers decreased with age (towards external wall). The ones which were formed during earlier growth phases (layers 3 - 7) could not be detected over the whole length of the analysed sample but were restricted to the lower half. This is consistent with a gradual increase in corallite height. New layers thicken and lengthen the skeleton in *L. pertusa*. Some of the white layers were hard to detect in the middle part of the corallite wall since they appeared to taper off where the growth direction changed around the onset of the new corallite (fig. 7.4).

Although the reduction of sample weight lowers accuracy, precision and reproducibility, the standard deviation still lay below the range of variations seen over the whole corallite wall and could be discussed in relative context with visible microstructural variations. All layers showed a more or less pronounced transient peak in stable isotope ratios around the middle part of the corallite. When stable isotope ratios were transformed into heat colours a possible pattern could be detected (fig. 7.4 and 7.5). This was better visible in $\delta^{13}C$ variations (fig. 7.4).

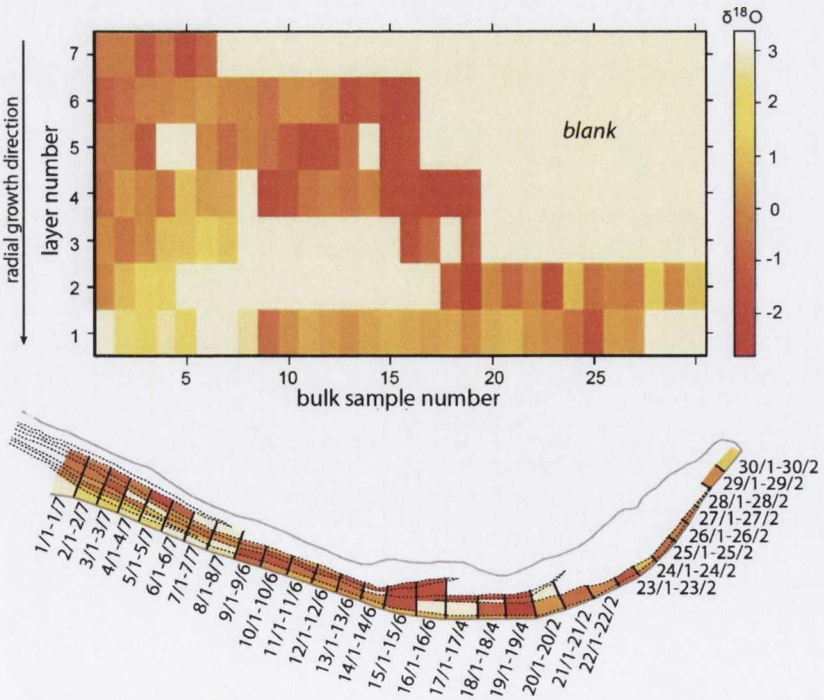


Figure 7.5: Stable oxygen isotope ratios. Sampling, gradients and labelling as in fig. 7.4. The trend towards peak ratios again runs diagonally across layers (in yellow colours).

7.1.3 Mapping of Elemental Patterns over the Full Length of the *Lophelia pertusa* Corallite

Laser ablation settings (see 'Methods') produced a high resolution map of variatons along growth. The results from laser ablation are not discussed as absolute values but rather as relative variations of elemental concentration based on selected isotope within the skeleton due to the lack of matrix matched standards. After data reduction in *Iolite* (version 2.5) (Paton et al., 2011) the averages from different experiments were compiled and the standard deviation of the mean was calculated (table 7.2 and 7.3). Since the bracketing standard glass NIST612 comprised different elemental concentrations than the sample, the standard deviation (SD) was converted into the relative standard deviation of the mean (RSD) (table 7.2).

The SNR values were very low for Mg, Ca, Ba and U, and neglectable for Sr (see appendix D.1). The signal measured for Cd was not distinguishable from the background noise. Relative uncertainty associated with measurements in the homogenous standard materials (table 7.2 and 7.4) were clearly lower than those measured in samples (table 7.3 and 7.5).

Table 7.2: Elemental concentrations NIST612 standard; averages and SD of the mean in ppm and as RSD.

	Average	SD (2σ) of the Mean	RSD	n
^{238}U	37.39 ppm	0.21 ppm	0.55%	8171
^{25}Mg	77.02 ppm	0.61 ppm	0.79%	8171
^{137}Ba	39.70 ppm	0.14 ppm	0.36%	8171

Table 7.3: Elemental concentrations in *L. pertusa* along coral growth from line averages; averages and SD of the mean in ppm and RSD.

	Average	SD (2σ) of the Mean	RSD	n
^{238}U	3.09 ppm	0.25 ppm	16.24%	160 lines
^{25}Mg	1004.00 ppm	163.00 ppm	8.03%	160 lines
^{137}Ba	13.28 ppm	2.27 ppm	17.10%	160 lines

Table 7.4: Elemental concentrations NIST612 standard for the additional experiment including boron concentrations; averages and SD of the mean in ppm and as RSD for the additional experiment on ^{11}B.

	Average	SD (2σ) of the mean	RSD	n
^{238}U	37.42 ppm	0.64 ppm	1.7%	4 lines
^{25}Mg	68.30 ppm	2.40 ppm	3.5%	4 lines
^{11}B	34.10 ppm	1.30 ppm	3.8%	4 lines

Table 7.5: Boron concentrations in *L. pertusa* along coral growth from line averages; averages and SD of the mean in ppm and RSD.

	Average	SD (2σ) of the Mean	RSD	n
^{238}U	2.92 ppm	0.22 ppm	7.6%	14 lines
^{25}Mg	817.00 ppm	48.00 ppm	5.9%	14 lines
^{11}B	71.00 ppm	6.40 ppm	9.0%	14 lines

The distributions in ^{238}U and ^{25}Mg formed consistent patterns when data from individual ablation lines was uploaded into *Cellspace*. The image displayed alternating bands of high and low ^{238}U concentrations parallel to visible layers and correlated with these. This correlation (in thickness and dispersal) was best seen in comparison with microstructural layers under transmitted light. When comparing the distribution patterns in elemental composition, the general trend towards antithetical behaviour of ^{238}U and ^{25}Mg was most prominent (fig. 7.6). The distribution pattern of ^{238}U presented clear and pronounced banding which matched the visible layers in the carbonate structure (fig. 7.7). The thickness and dispersal of ^{238}U bands were best correlated with translucent layers visible in the thin section. In addition, clear accumulations of ^{238}U could be seen along the outer rim of the corallite wall. Younger precipitates (towards the outer theca) displayed reduced band thickness, i.e. calcification phases with distinct elemental compositions appeared shorter. Bands of high ^{238}U composition seemed to become more dominant as the thickness of low ^{238}U bands decreased.

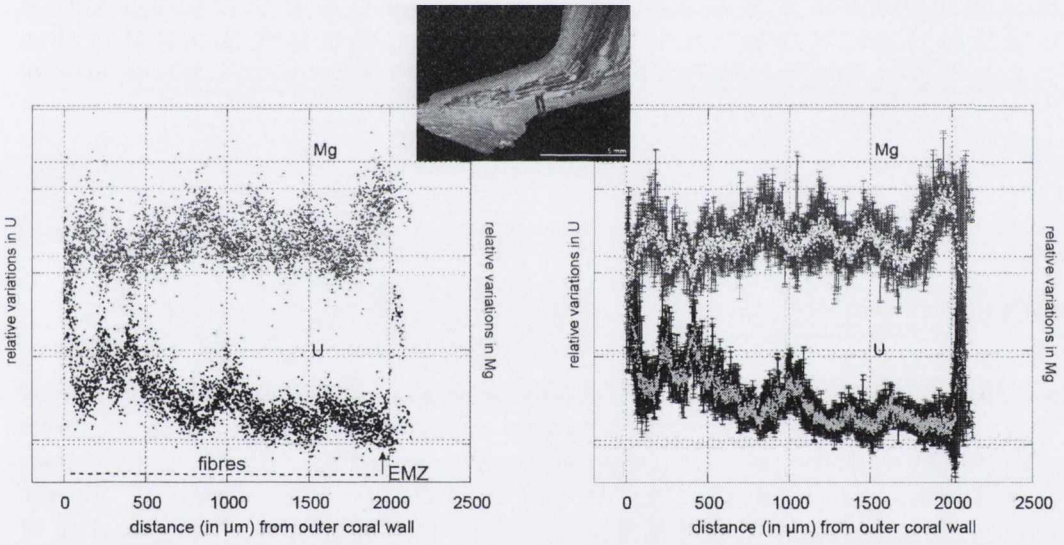


Figure 7.6: Overlaying five consecutive ablation lines (34 to 38) from the early phase of linear growth (gray box on image) shows the general trend towards correlation of ^{25}Mg and ^{238}U (left). The variations are smoothed out by calculating moving averages of every five data points (right). The standard deviation for each of the averages is shown in its error bar.

Generally areas of higher concentrations showed more pronounced and detailed patterns in the distribution in ^{25}Mg and ^{238}U. Areas of lower ^{238}U concentrations (innermost part of the corallite wall) were complimented by additional details displayed in high ^{25}Mg concentrations in the same area. The same applied to areas of high ^{238}U and low ^{25}Mg. Towards the upper part of the theca the ^{238}U and ^{25}Mg bands fanned out and curved inwards in association with the presence of white layers (compare fig. 7.7).

Older regions along the inner part of the wall which were consistent with early growth phases including the areas that were referred to as 'Early Mineralization Zones' (EMZ) generally showed high ^{25}Mg values peaking directly along the suggested

EMZs. The visible white layers in microstructure were also accompanied by high ^{25}Mg concentrations, forming bands that extended beyond the tapering off of the visible (white) microstructural layers. Further up along the linear growth axis (towards the corallite opening) the white layers in microstructure tapered off and with them also any pronounced bands of high ^{25}Mg concentrations. The upper third of the corallite wall coincided with the onset of a budding event and the growth of a new corallite (fig. 7.7). Here the ^{25}Mg values generally increased with growth in length but stayed below the maximum ^{25}Mg concentrations.

The lower two thirds of the sampled corallite wall (consistent with earlier growth) showed lower concentrations in ^{238}U which increased during later growth stages. The upper wall region within the first curving of the layers showed low ^{238}U contents in the inner corallite part. With age the curving high ^{238}U bands lay closer together. The area along the inner region of the wall showed high values where septa connected to the wall. Here the ablation extended into a layer of the attached septum. The outer half of the wall displayed the distinct ^{238}U bands which coincided most clearly with beige areas of the skeleton. ^{238}U analysis revealed seven bands of low ^{238}U concentration in corallite 1 and five bands in corallite 2 (fig. 7.7). These bands appeared in close succession along the radial growth but were clearly distinguishable in the area of curvature (reflecting linear growth; as shown in fig. 7.7).

Barium (^{137}Ba)

The Ba pattern was more irregular (fig. 7.7) than the clear bands evidenced by ^{238}U and ^{25}Mg distribution. The largest continuous areas of high Ba were located along the early shorter growth layer (inner lower third) and along the curvature of layers (center). Where there were Ba peaks running over a number of ablation lines their orientation was consistent with microstructures (white and beige layers). Within the area of curved layers the bands of higher Ba concentrations followed the direction of the layers. Patterns in Ba also curved towards the corallite cavern along the upper wall of corallite 1, i.e. they changed the orientation from parallel to diagonal in correlation with the corallite layers. Within the following wall section of corallite 2 the orientation of the bands was more or less parallel to the outer wall again (fig. 7.7).

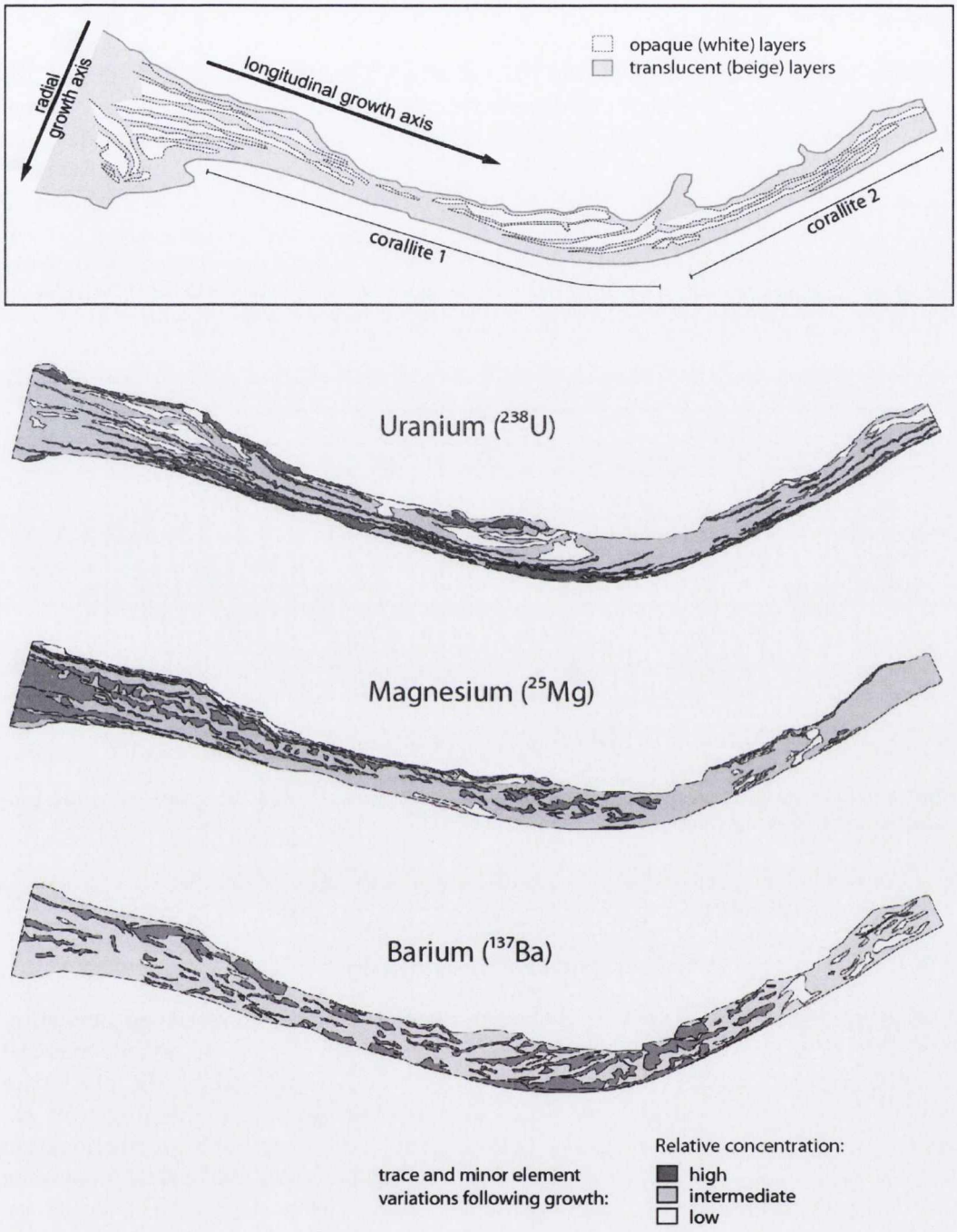


Figure 7.7: Visible layering in *L. pertusa* sample L1 (white and beige layers). The categories for trace and minor element concentrations were defined using the average concentrations with 2 SD intervals (intermediate concentrations: 5-95%). High concentrations lie above mean averages plus 2 SD, low concentrations lie below mean averages minus 2 SD. The variations in ^{238}U, ^{25}Mg and ^{137}Ba showed pronounced correlation especially around the central area.

Boron (^{11}B)

Analysis of boron concentrations along the growth axes in the area of layer curving was included in a short experiment to complete the dataset and allow for further discussion. ^{11}B appeared strongly associated with microstructural layers which was easier detected along the curvature (Appendix fig. E.3). ^{11}B and ^{238}U also showed high covariance in the general trend. The stable boron ratios ($^{11}B/^{10}B$), on the other hand, revealed no correlation with growth features (Appendix fig. E.3). Since the SNR suggested to treat any boron measurements with care, the absence of an association with microstructures was a preliminary result. The RSD for ^{11}B in the standard was 3.8% while variations in the sample were 9% (fig. 7.8 and Appendix fig. E.3; table 7.3 and 7.4).

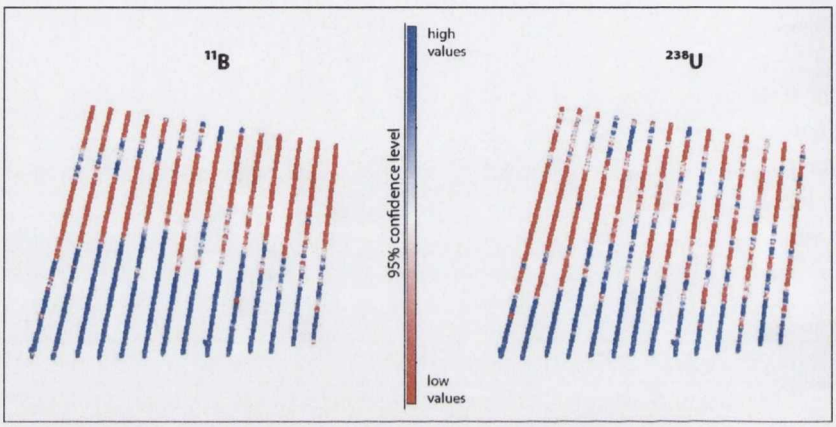


Figure 7.8: Stable boron isotope ratios along ablation lines showed little variations, no pronounced pattern or correlation with microstructures.

7.2 Discussion

7.2.1 Magnesium Incorporation Mechanisms

Magnesium incorporation into coral skeletons has generally been discussed in connection with a number of possible mechanisms: (1) enclosure of traces of organic material into the aragonite lattice (Rollion-Bard et al., 2010); (2) enclosure of Mg into lattice defects during periods of high, or accelerated, growth rates (e.g. Montagna et al., 2014); (3) surface entrapment (e.g. Gabitov et al., 2008); (4) Rayleigh fractionation (e.g. Gagnon et al., 2013); (5) active pH up-regulation in the Extracytoplasmic Calcifying Fluid (ECF) (e.g. McConnaughey et al., 1997). Options (1) to (3) are dependent on precipitation rates. A dependency of Mg incorporation on salinity was ruled out by a number of studies (e.g. Pretet et al., 2014).

If magnesium was incorporated directly from the ambient seawater or from nutrient input, variations in Mg bands would co-vary with surrounding environmental conditions. This hypothesis would suggest a covariance between Mg levels in the skeleton and ambient Chl α levels if Mg was derived from Chl α. The increase in growth rate indicated by the thicker layers would then be an additional effect of the increased energy input during these phases. In this case high Mg concentrations would be correlated with high primary production and incorporated directly into the skeleton during such phases. As a nutrient proxy, Ba would then be positively correlated with

peaks in Mg (e.g. Lea et al., 1989). We cannot find such a clear correlation in our data where only earlier growth shows an co-occurrence of ^{25}Mg and ^{137}Ba peaks. This is possibly an ontogenic effect with earlier growth phases driven by nutrient input (detailed discussion in the following sections) i.e. only early phases would be consistent with an external trigger.

If magnesium incorporation is not directly correlated with environmental variations in Mg input but with biologically driven growth rate variations a different hypothesis is possible. A higher growth rate is accompanied by an increase in the occurrence of lattice defects (e.g. van der Locht et al., 2013). Due to its radius Mg^{2+} is more likely to be incorporated into lattice defects than to be substituted for Ca^{2+} (e.g. Montagna et al., 2014). Therefore, an increase in growth rate would also cause peaks in Mg in correlation with the higher abundance of lattice defects. At the same time the probability increases that a possible Mg-rich precursor phase (organic material or amorphous calcium carbonate (ACC)) left unconverted organic rests within the crystal lattice (e.g. Rollion-Bard et al., 2010). The same is valid for surface entrapment where high growth rate results in the incorporation of enriched layers on the corallite surface which would have been dissolved under lower growth rate conditions (Gabitov et al., 2008, Watson et al., 1996). All these growth rate effects can account for increased Mg-incorporation but are also applicable for other trace and minor elements. For example, organic material is also relatively rich in U (Amiel et al., 1973). So in this case a positive correlation with ^{238}U should be seen which is not the case for the internal variations. The entrapment into defects is more probable for small ions like Mg^{2+} than for U. Surface enrichment (Gabitov et al., 2008) would account for high elemental concentrations in all elements and would again result in a positive correlation between ^{25}Mg and ^{238}U. This phenomenon is only seen along some of the external surfaces of the skeleton. The drivers of growth rate variations are not relevant for these models.

A pH-/alkalinity regulating mechanism on the other hand provides an explanation for variations in trace and minor element compositions and a connection with growth rate variations. The process itself is either driven by physical factors like $2H^{+}$ - Ca^{2+} exchange through ion channels or vacuoles or by enzymes like a Ca-ATPase (e.g. Adkins et al., 2003, Zoccola et al., 1999, McConnaughey et al., 1997) (fig. 2.24). An active up-regulation of the internal pH in a hypothetical ECF would simultaneously increase the growth rate and its effects like lattice effects. A Mg-ATPase might be activated in connection with this and contribute to Mg incorporation during phases when the pH is high enough to facilitate fast skeletal growth without increased energy consumption due to ongoing pH up-regulation. This, however, suggests an incremential process which starts when a threshold pH is reached (Gagnon et al., 2013).

7.2.2 Uranium Incorporation into the Skeleton

Uranium is most likely derived from ambient seawater and is found in three sites within the corals: (1) in the organic material with a concentration between 40 and 70 ppm; (2) adsorbed to the surface layer with a negligible concentration of 40 to 60 ppb; and (3) in the aragonitic skeletal lattice with a concentration around 3 ppm (Amiel et al., 1973). The relation between U and growth rate, i.e. intraskeletal variations of growth rate, is ambiguous (Raddatz et al., 2014, Inoue et al., 2011). Different studies found an inverse correlation between U concentration and pH as well as carbonate ion

concentration (Raddatz et al., 2014, Anagnostou et al., 2011, Inoue et al., 2011). On the other hand, ^{238}U concentrations are correlated with ambient salinity in the open ocean (Owens et al., 2011, Pates & Muir, 2007, Schmidt et al., 2006, Delanghe et al., 2002, Chen et al., 1986, Ku et al. 1977). Since ^{238}U concentrations in seawater appear conservative, salinities can be used to estimate ^{238}U (Owens et al., 2011).

If U in the coral aragonite derived from traces of organic material in the lattice we would see a positive correlation between ^{238}U and ^{25}Mg since the organic material contains higher concentrations of both. Our results, however, show a well pronounced antithetical trend between ^{25}Mg and ^{238}U in accordance with other studies (e.g. Anagnostou et al., 2011, Robinson et al., 2006, Montagna et al., 2005) (fig. 7.6). Therefore, this explanation cannot account for the observed variations in ^{238}U or ^{25}Mg.

If the observed variations in ^{238}U in *L. pertusa* were purely connected to variations in salinity in the ambient water masses the equation by Owens et al. (2011) would provide comparable relative variations in ^{238}U concentrations in skeletons and water column. *L. pertusa* in the Whittard Canyon is mostly found in the upper and lower reaches of the Mediterranean Outflow Water (MOW) which is found between 700 and 1,100 m depth here and can be identified by higher salinities (Wilson et al., 2015). The usual MOW salinity of >35.6 psu, however, shows signs of dilution in the canyons (Wilson et al., 2015). Water profiles obtained for the uppermost 2,000 m in the Whittard Canyon show salinities between ~35 and ~35.8 psu across different water masses (Wilson et al., 2015, Johnson et al., 2013, Huvenne et al., 2011). These salinity variations of ~0.8 psu should be consistent with ^{238}U variations of ~0.08 $\mu g/g$ in the seawater (following the equation by Owens et al., 2011). This accounts for a relative variation around 2.5% across the full salinity range, for less around the depth range of the *L. pertusa* occurrence (even if seasonal shifts in the reaches of the different water masses are assumed). Therefore, an external ^{238}U variation driven by the variability in ambient salinity cannot account for the 16.24% relative variations observed in ^{238}U in *L. pertusa*. Consequently some other process has to be involved. It has to be mentioned that Raddatz et al. (2014) observed a positive correlation between *L. pertusa* U/Ca and seawater salinity for NE Atlantic sites but attributed this to the correlation between salinity and pH in the seawater.

The inverse correlation between U/Ca and pH (Raddatz et al., 2014, Inoue et al., 2011) has to be considered as well. Commonly pH is reconstructed using $\delta^{11}B$ signatures in the coral skeleton. Boron is found in two species in the ocean: borate ($B(OH)_4^-$) and boric acid ($B(OH)_3$), where borate is assumed to be the species incorporated into CWC aragonite from an internal calcifying fluid (Wall et al., 2015, Anagnostou et al., 2012, McCulloch et al., 2012, Allison et al., 2010, Klochko et al., 2009, Pagini et al., 2005). In addition, a biologically driven up-regulation of the pH in this internal ECF, e.g. by Ca-ATPase, is generally accepted (e.g. McCulloch et al., 2012). An increase between internal pH and external seawater pH was reported by many studies and ranges between 0.5 and >1 pH units (measured and reconstructed) depending on the region of the skeleton and the calcifying species (e.g. Raddatz et al., 2014, Anagnostou et al., 2012, Rollion-Bard et al., 2011, Trotter et al., 2011, Blamart et al., 2007, Al-Horani et al., 2003). Whether reconstructed pH variations in the skeleton are in agreement with common calcification models is still being discussed (e.g. Anagnostou et al., 2012, McCulloch et al., 2012, Rollion-Bard et al., 2011, Blamart et al., 2007).

Another complication to a pH reconstruction from stable boron isotope ratios arises from findings of portions of boric acid (up to 50%) in the aragonite in association with the distribution of microstructural units and hence possibly related to growth rate (Rollion-Bard et al., 2011, Klochko et al., 2009). The difference between internal and external pH (ΔpH) was lain down in different equations:

$$\Delta pH = -(0.75 \pm 0.12) * pH_{SW} + (6.88 \pm 0.93)^{\text{i}}$$

$$\Delta pH = -0.71 * pH_{SW} + 6.43^{\text{ii}}$$

From a calculation of the internal pH it was possible to apply corrections allowing a paleo-pH reconstruction (e.g. Anagnostou et al., 2012). Nevertheless, all results in connection with pH reconstruction so far showed that a correction at least for a biologically driven pH regulation which is species-specific is necessary to reconstruct the environmental parameters.

With the difficulties arising from the δ^{11}B-pH relationship in mind, U/Ca can be discussed in this context. So far the influence of growth rate on the incorporation of U was neglected or simplified (Raddatz et al., 2014, Inoue et al., 2011). A popular model for CWC calcification suggested the biologically controlled up-regulation of the pH in an internal fluid (ECF) from which calcium carbonates are precipitated (Adkins et al., 2003, McConnaughey et al., 1997, McConnaughey, 1989a, 1989b). This up-regulation is possibly driven by the enzyme Ca-ATPase and was connected to increased energy costs (10% per 0.1 pH units) (e.g. McCulloch et al., 2012). A high pH is beneficial for high precipitation rates. If the process of pH up-regulation was episodic, phases of lowered internal pH after phases of high growth rates would lead to an increased activity of the Ca-ATPase (redirecting additional energy from growth to Ca-ATPase activity). Depending on the ambient pH U exists in different species: at pH 4-5 increased values of $UO_2(CO_3)^0$, at pH 5-6 higher $UO_2(CO_3)_2^{2-}$ values persist, and a higher pH is dominated by $UO_2(CO_3)_3^{4-}$ (Djogić et al., 1986). The former two are speculated to be preferred to be incorporated into CWCs (Raddatz et al., 2014). Consequently a temporarily lowered internal pH could provide the preferentially incorporated U species and, therefore, account for an enrichment in ^{238}U along bands along growth.

In consequence a pH- and alkalinity-driven ECF provides the basis for growth rate variations. These then in turn provides variations in density and lattice defects. The same growth rate variations also provide surface entrapment possibilities with higher pH connected to different species of U. This results in variations in incorporation preference of U species. The thinning of layers towards the outer wall suggests biologically driven processes which overprint the signal.

7.2.3 Connecting Growth Rate to Geochemical Patterns

The variations in layer thickness possibly arise, in part, from different angles of the cut relative to the layer position (diagonal cuts increase the surface area). However the corallite often points away from the branch, therefore, curving sideways during the growth. This causes layers along the concave wall to experience some spatial

[i] Anagnostou et al., 2012
[ii] McCulloch et al., 2012

restriction which results in much thinner and less well developed layers compared to those on the unrestricted convex wall. Therefore, interpretations were based on the association of microstructure and geochemical composition where variations in elemental compositions were used to fill gaps in visible microstructure.

The microstructural layers give evidence of phases of radial growth while stepwise growth in length is captured in the individual curvature of the layers. CWC growth studies suggested that the growth in length takes place at a higher rate than radial growth (e.g. Mortensen & Rapp, 1998). *L. pertusa* was shown to continuously precipitate new aragonite crystals along the inner wall (mainly building septa), the outer wall (to thicken the wall), and in length visible as a 'curvature' of the (microstructural) layers away from the outer wall (e.g. Lartaud et al., 2013). Apparent bands of high/low ^{238}U or ^{25}Mg concentrations seem well associated with the orientation of these microstructures. The magnitude of average variability in U content, around 3 ppm, is consistent with previous observations in tropical corals (see Shen and Dunbar, 1995, Min et al., 1995). The matrix effect should be low in the case of ^{238}U due to its high mass (Longerich et al., 1990). This suggests that there should be a common denominator in skeletal precipitation patterns in corals from both habitats regardless of the obvious difference in environments, and that zooxanthellae activity has a minimal or even no influence on U incorporation. Therefore, the geochemical compositions and variations within the skeleton support a discussion on the basis of growth rate variations. Our findings generally show a strong antithetical behaviour of ^{25}Mg and ^{238}U that is consistent with findings by earlier studies (Robinson et al., 2006, Gagnon et al., 2007, Sinclair et al., 2006). The areas of increased frequency in high ^{238}U and low ^{25}Mg bands along the outer wall coincide with high $\delta^{18}O$ and $\delta^{13}C$ values, which are interpreted as periods of low growth rate (e.g. Rollion-Bard et al., 2003). These observations support a discussion on a hypothetical correlation between growth rates and ^{25}Mg and ^{238}U concentrations.

The lack of stronger pronounced ^{238}U bands in the lower and along the inner part of the wall can be interpreted in the sense of higher growth rate during the early life stages (Gass & Robers, 2011, Maier et al., 2009). The bands of ^{238}U enrichment correlate with models of radially decreasing growth and microstructural layers, including variations in growth rate, i.e. layer thickness, and seem to be more pronounced towards the outer regions of the corallite wall. To current knowledge the growth rate decreases with coral age (e.g. Adkins et al., 2003). This again should also reduce the influence of fractionation effects on carbonate precipitation which is consistent with our stable isotope results (increased $\delta^{18}O$ and $\delta^{13}C$ towards the outer edge). Whether these areas of high ^{238}U content are linked to interruptions in growth and how long such possible interruptions might have lasted cannot be concluded from the patterns.

Experiments showed that increasing ^{25}Mg contents were connected to a higher aragonite precipitation rate (Dietzel et al., 2004). ^{25}Mg is known for its strong association with coral microstructure with high concentrations in areas of higher growth rates (e.g. Gagnon et al., 2007, Cohen et al., 2006). These results are consistent with our observations and an interpretation in terms of growth rate. In contrast to existing studies the data presented here shows a continuous picture of these correlations with the microstructure throughout CWC growth including curvature and complex connections between consecutive corallites.

At first sight, stable isotope ratios show an episodic $\delta^{13}C$ increase per layer around the middle part of the corallite. In conjunction with the trace element maps it becomes clear, however, that this 'peak' is more likely the result of microstructural layers following the growth pattern seen most clearly in ^{25}Mg and ^{238}U distributions. When looking at visible white macrolayers along the transect used for laser ablation it is obvious that alternating layers might not be visible everywhere even when thin sections show their continued existence. The lower resolution in stable isotope analysis is most probably caused by a certain lack in accuracy (as high sample weight is necessary) when following the layers. Around the upper end of the lower corallite the calcified layers curve towards the interior (see fig. 7.7) and the stable isotope ratios increase which is consistent with lower growth rates.

Earlier studies discussed the influence of environmental parameters (mainly temperature, pH, salinity) on the incorporation of elements into coral skeletons based on the Rayleigh fractionation (e.g. Montagna et al., 2014, Rollion-Bard et al., 2010, 2009). Here the strong association between microstructure and ^{25}Mg and ^{238}U compositions together with constantly decreasing layer thicknesses and band distances appear to be mostly controlled by biological factors. Therefore, rather than external physical effects like temperature or salinity, a biological control in connection with metabolic activity and growth rates possibly combined with fluctuations in nutrient availability is suggested for ^{25}Mg and ^{238}U incorporation into CWC skeletons. A clear differentiation between external and internal drivers of variations in elemental composition is not yet possible based on the available information.

7.2.4 Nutrient Availability and Geochemical Signals

The sampling location lies within the lower reaches of the Mediterranean Ocean Water (MOW) but since the main source of nutrients in the heterotrophic systems of deep sea canyons usually comprises sinking primary production from the surface layers of the water column the water mass itself is unlikely the direct source of nutrients (Roberts et al., 2009a). Peak availability of particulates from surface productivity should, therefore, show a connection to periods of enhanced growth revealed by the geochemical composition of the CWCs. The availability of particulates deeper in the water column is delayed relative to the occurrence of surface primary production maxima by the time it takes them to sink. Depending on the size, shape and density of the sinking particles, and the depth and oceanography of the site, the speed can reach up to >1,000 m per day (Lo Bue et al., 2014, Siegel & Deuser, 1997, Asper, 1987, Fowler & Knauer, 1986, Shanks & Trent, 1980). The delay of a few weeks (at maximum) in any case, therefore, might not be significant in terms of seasonal signal. Within the Whittard Canyon area currently no indication exists for more than one peak in surface productivity per year. Satellite images give evidence to a front of high Chl α passing over the canyons between April and July.[iii] However, nepheloid layers were observed in the studied canyons on a regular basis and are potential contributors of POM and nutrients (e.g. Wilson et al., 2015). During all of our ROV dives over the last years the particle load in the canyon currents was relatively high between April and June.

[iii] `http://neo.sci.gsfc.nasa.gov/view.php?datasetId=MY1DMM_CHLORA`; last accessed Jan 8, 2016.

Khripounoff et al. (2014) found significant particle flow in bottom currents in a canyon in the Bay of Biscay to be associated with large peaks in carbon fluxes at the end of winter. Along the Brittany continental slope these fluxes proved insufficient as a sole energy supply for CWCs, especially during summer and autumn (due to reduced bottom currents), which suggested the necessity for additional nutrient supply from other sources like zooplankton to meet the CWC's energy demand (Khripounoff et al., 2014). Using nutrient proxies to connect growth layers to seasonality in food availability can provide additional insight into precipitation patterns and consequently use such a signal as a potential marker horizon for accurately determining the growth rate (fig. 7.9).

Within the reproduction cycles of the corals the phase of spawning at the start of the year is less energy consuming than gametogenesis in late summer and autumn (Waller & Tyler, 2005). Phytoplankton bloom in spring and the potential increase in particle flux in late summer might cover the increased energy demand for gametogenesis while a higher particle flux in benthic layers around the start of the year might enable to meet the energy demand caused by spawning activities. In total the annual budget should provide highest energy availability for coral growth and skeletal precipitations during spring and early summer (before gametogenesis reaches a peak).

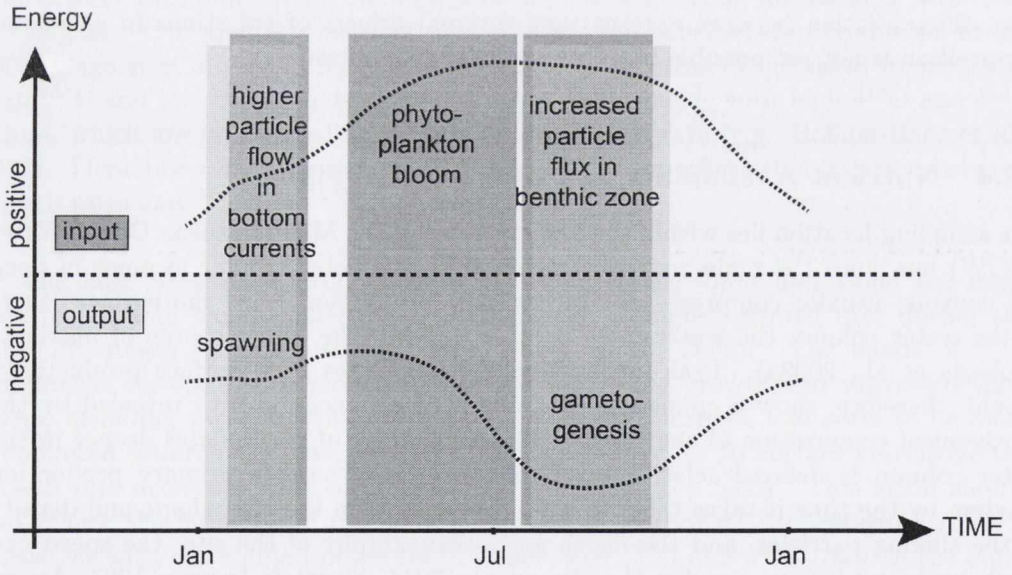


Figure 7.9: Parameters which possibly influence the energy budget of the corals over the course of the year (combination of different studies). Reproduction processes cause increased energy demand while increased nutrient input provides additional energy availability (e.g. Khripounoff et al., 2014, Brooke & Järnegren, 2013, Waller & Tyler, 2005). Therefore, spring is the time where most energy is available outside of reproductive cycles.

Barium (Ba) was shown to be a reliable nutrient proxy in corals (Lea et al., 1989). Anagnostou et al. (2011) reported a lack in correlation between bottom current particle influx and Ba variations which would mean that currents might not add to the Ba signal in the skeletons. After initial tests including different known nutrient proxies, ^{137}Ba was chosen here as the most promising element since concentrations were

sufficiently high (above background), showed low interferences, and appeared to be correlated with microstructures. Areas of higher ^{137}Ba could, therefore, be discussed in terms of increased nutrient input. While some isotopes of Ba showed analytical interference with other elements (like cerium and lanthanum), ^{137}Ba appeared to be relatively free of such effects (Hirata, 2004). Therefore, we are confident that the here selected ^{137}Ba provided good insight into relative Ba variations along growth. In addition to this, tests on other scleractinian samples (own results) fell within comparable ^{137}Ba ranges.

While phases of early growth mostly display a positive correlation between ^{137}Ba and ^{25}Mg, this trend appears inverted further along (radial) growth. Some studies reported a positive correlation between ^{25}Mg and ^{137}Ba, therefore, variations in such a correlation might point to biological effects.

A positive correlation between ^{25}Mg and ^{137}Ba possibly points to higher growth rates in connection with higher energy input from nutrients and its availability for growth. A situation like this could be expected in phases without gametogenesis, most likely early growth takes place in such phases. The correlation between ^{238}U and ^{137}Ba could then point to phases of high nutrient intake covering the energy demand of metabolic processes like gametogenesis. This geochemical pattern could point to phases of increased particle flux in benthic zones in autumn (e.g. Khripounoff et al., 2014).

The interrupted bands of high ^{137}Ba showed six to seven 'events' of higher ^{137}Ba associated with microstructural layer orientation in corallite 1 with varying correlation to ^{25}Mg and/or ^{238}U. In addition, approximately three phases of increased ^{137}Ba incorporation were found in corallite 2, especially around each onset of layers. The positive correlation of ^{25}Mg and ^{137}Ba was possibly connected to variations in growth rate and external signal. In that case it would also account for annual layering (spring).

7.2.5 Growth Information Extracted from an Individual *L. pertusa* Corallite

Based on a conceptional model whereby high/low ^{238}U and ^{25}Mg concentrations are indicative of variations in growth rate, the number of possible growth phases, i.e. variations in growth rate (instead of one average rate) can be reconstructed. One phase was defined as starting with high ^{25}Mg and ending with high ^{238}U concentrations. The number of low ^{238}U bands found across the wall of the lower corallite (corallite 1) led to the conclusion that at least six of the seven observed phases of increased growth rate, followed by six phases of lower growth rate, had left an imprint during the life of the polyp before the budding event took place (table 7.6). The younger corallite (corallite 2) displayed an additional five phases of higher growth rate which appeared to have taken place after most of the growth of corallite 1 had occurred (table 7.6). Since both polyps were alive until collection it is probable that both were still actively growing and that what looks like a longer developed phase of low growth rate along the outer wall of corallite 1 might actually consist of several phases of generally decreased growth rate (typical for more advanced age). There was, however, no indication for additional phases found in bands of geochemical signatures.

Table 7.6: *L. pertusa* (CE11006): Thickness of high ^{25}Mg layers translated into growth lengths of the two corallites. These growth phases are separated by phases of presumed low growth rates (high ^{238}U concentrations) which amount to a contribution of < 50 μm in length in growth. In the case of corallite 2 the full length is not available.

	Growth Phase	Radial Growth	Linear Growth
corallite 1	initial	100 - 200 μm	> 10 mm
	2^{nd} phase	< 400 μm	2.5 mm
	3^{rd} phase	100 - 200 μm	500 μm
	4^{th} phase	100 - 250 μm	600 μm
	5^{th} phase	150 - 50 μm	600 - 650 μm
	6^{th} phase	< 50 μm	400 μm
	7^{th} phase	< 50 μm	300 μm
corallite 2	initial	< 200 μm	~ 4 mm
	2^{nd} phase	150 - 250 μm	~ 3 mm
	3^{rd} phase	< 200 μm	600 μm
	4^{th} phase	200 - 300 μm	> 800 μm
	further	< 50 μm	N/A

If we assume one annual phase of increased phytoplankton production in the surface layer of the ocean during late spring and a connection between increased nutrient input (from surface production) and phases of increased growth, then the length of growth for corallite 1 was more than seven years and that of corallite 2 was five years (table 7.6). Each of these growth phases was followed by a decrease in growth rate marked by the incorporation of higher ^{238}U concentrations which became more dominant with age. This was interpreted as a biologically driven effect. The decrease in growth rate reflected in a logarithmic decrease in layer thickness (fig. 7.10). The averaged measurements showed a very good fit ($R^2 > 0.95$) for both corallites. Assuming annual layering (as suggested e.g. by Mortensen & Rapp, 1998) we found a linear growth rate decreasing from > 10 mm/year to 0.3 mm/year (for corallite 1) and a decrease in radial extension from approximately 250 μm/year to < 50 μm/year (including areas of potential low growth rate). These variations in growth rate throughout corallite precipitation could account for some of the differences in published growth rates.

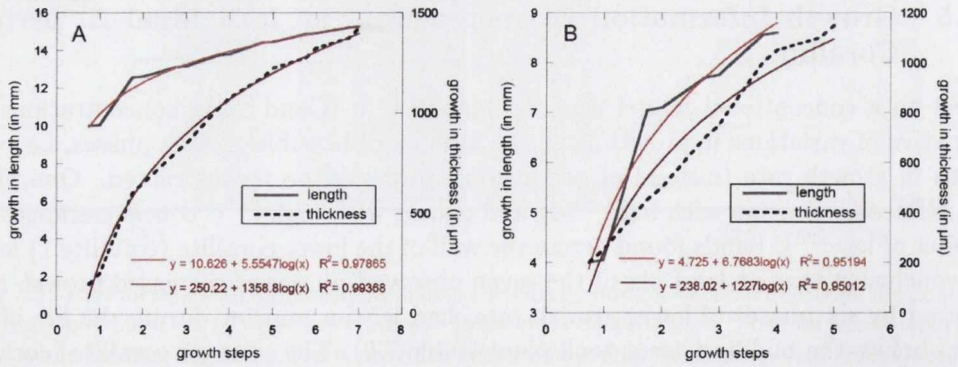


Figure 7.10: Plotting the averaged measurements between growth steps indicated by ^{238}U bands in connection with linear and radial extension (table 7.6) showed a logarithmic decrease in thickness during growth for both corallites. The shorter corallite displayed a poorer fit.

The number of phases per corallite and the development of layers is likely to be highly variable between locations and even between and within colonies. The relative decrease in phase length, however, might reveal a relationship and might provide a basis for environmental information in possible deviations from a (logarithmic) relation.

7.2.6 Reconstruction of Ambient Seawater pH

Raddatz et al. (2014) suggested equations for pH reconstruction from U/Ca ratios (eq. 2.10 and 2.11). Applied to our measurements of $^{238}U/^{43}Ca$ (assuming a constant Ca concentration which is highly unlikely) the internal pH fluctuations would amount to roughly $\Delta pH \approx 8$ (pH between 3 and 10). Reported measured internal pH variations of 0.3 pH units (Al-Horani et al., 2003) or $\delta^{11}B$-derived internal pH variations of ≈ 1 pH unit (Rollion-Bard et al., 2010) were far lower than our reconstructed variations would be.

Our data not only showed U variations between EMZ (or CoC) and fibres but also various cycles of U variations within the fibrous areas themselves. This led to the conclusion that avoiding the centres of calcification as suggested by Raddatz et al. (2014), or using bulk samples was not sufficient to exclude sampling areas of high U variance influenced by growth variations.

Traditionally pH variations in the coral skeletons were analysed using differences in stable boron isotope ratios ($\delta^{11}B$) between seawater and aragonite (Rollion-Bard et al., 2011). The boron content around 100 ppm measured in earlier studies on *L. pertusa* (e.g. Rollion-Bard et al., 2011) was consistent with our results. An area with clear layered patterns in ^{238}U around the top of the lower corallite showed a similar pattern in ^{11}B (fig. E.3). Uranium showed far more pronounced patterns in concentration and displayed several distinguishable layers which were not found as pronounced in the B signal although generally the patterns appeared to be positively correlated. The inverse correlation between U and pH, as well as the positive correlation between $\delta^{11}B$ and pH did not contradict a positive correlation between ^{11}B and ^{238}U since stable boron isotope ratios depend on the ratio between ^{11}B and ^{10}B. Rollion-Bard et al. (2010) reported a ^{11}B enrichment in fibres which was consistent with our observations of high ^{11}B and ^{238}U along the outermost growth where bands of high ^{238}U were close together. However, the pattern in ^{11}B also indicated variation in B within fibrous layers. $^{11}B/^{10}B$ derived from LA-ICP-MS analysis and used with care did not show any correlation with ^{11}B or ^{238}U patterns within the limits of precision (fig. E.3). The applied technique is still in a test phase and lacks the precision of other techniques (e.g. ^{11}B MAS NMR, see e.g. Kaczmarek et al., 2015, Rollion-Bard et al., 2010). It might, however, suffice for a look at relative patterns (Kaczmarek et al., 2015, Fietzke et al., 2010).

The argument was, therefore, that U is more suitable to provide insights into variations in growth rate and to infer the age of the corals from growth seasons, length/cyclicity of such seasons has yet to be established. Rollion-Bard et al. (2011) found lower pH factors in areas of higher growth rates in *L. pertusa* corresponding to lower pH. When using the raw data (in cps) to look at the $^{11}B/^{10}B$ ratios no apparent pattern with regard to microstructure or otherwise appears. Laser ablation ICP-MS with the applied data reduction does not yet provide the necessary precision to achieve absolute ratios which can be used for a calculation of $\delta^{11}B$ and pH using the equation provided by Rollion-Bard et al. (2011). Should variations in geochemical composition across fibrous layers be connected to variations in internal pH, this would lead to a modification of existing models of precipitation of structural units (RAD and TD). Rollion-Bard et al. (2011) only reported a different pH between EMZs and fibres, therefore, a higher resolution is necessary to check for further internal pH variations within fibres.

Chapter 8

Case Study: *Madrepora oculata* Skeletal Geochemistry

So far the scleractinian species *M. oculata* is underrepresented in detailed studies on coral growth and biogeochemistry. The species, however, is usually found together with the well-studied reef builder *L. pertusa* over wide areas of the NE Atlantic, and is even the most abundant reef builder in some CWC habitats in the Mediterranean Sea (e.g. Taviani et al., 2005). *L. pertusa* was found to show considerable metabolic effects which distort possible environmental records in the skeletal material (chapter 6 and 7). This chapter will, therefore, focus on the patterns of growth in *M. oculata* and the species' potential to act as a recorder of ambient temperatures in comparison to other species, especially the commonly used *L. pertusa*. Growth structures in *M. oculata* have never been studied in detail and no literature was found on this. This chapter provides detailed insight into individual corallite precipitation and colony growth and tests the use of *M. oculata* for future studies on environmental reconstruction. Methodology and discussion were based on literature review and on results presented in the previous chapters of this thesis.

For the first part focusing on microstructures a section of a *M. oculata* branch from the Whittard Canyon and from a Porcupine Bank colony were investigated for similarities and differences. The second part compared a set of *M. oculata* samples from popular locations in terms of temperature reconstruction using different approaches [lines technique (Smith et al., 2000), Li/Mg (e.g. Case et al., 2010)].

8.1 Patterns in Coral Growth

8.1.1 Microstructures

The stepwise theca lengthening was only visible along the upper corallite wall. The process was later covered by the pronounced thickening of the intercorallite area. Radial growth was generally produced by these branch thickening layers. Individual layers were clearer visible in sample 459-M1 with more opaque areas in the thin section (fig. 8.1). The thin sections of *M. oculata* samples showed a similar network of fine lines running across all layers to that found in *L. pertusa*. Under reflected light and magnification some of the *M. oculata* samples also showed increment-like interruptions along the white layers as seen in *L. pertusa* but were harder to detect in *M. oculata* since the white layers were usually thinner (fig. 8.1 and 8.2). In some *M. oculata* samples (e.g. MM) the resolution showed that these structures were clearly accompanied by fluctuation in Mg and U. Different cut orientation in *L. pertusa* L1 showed that the 'increments' were 2-dimensional structures that could have the appearance of the bee hives (fig. 7.2-E). Available observations on *M. oculata* suggested that the same is the case for this species.

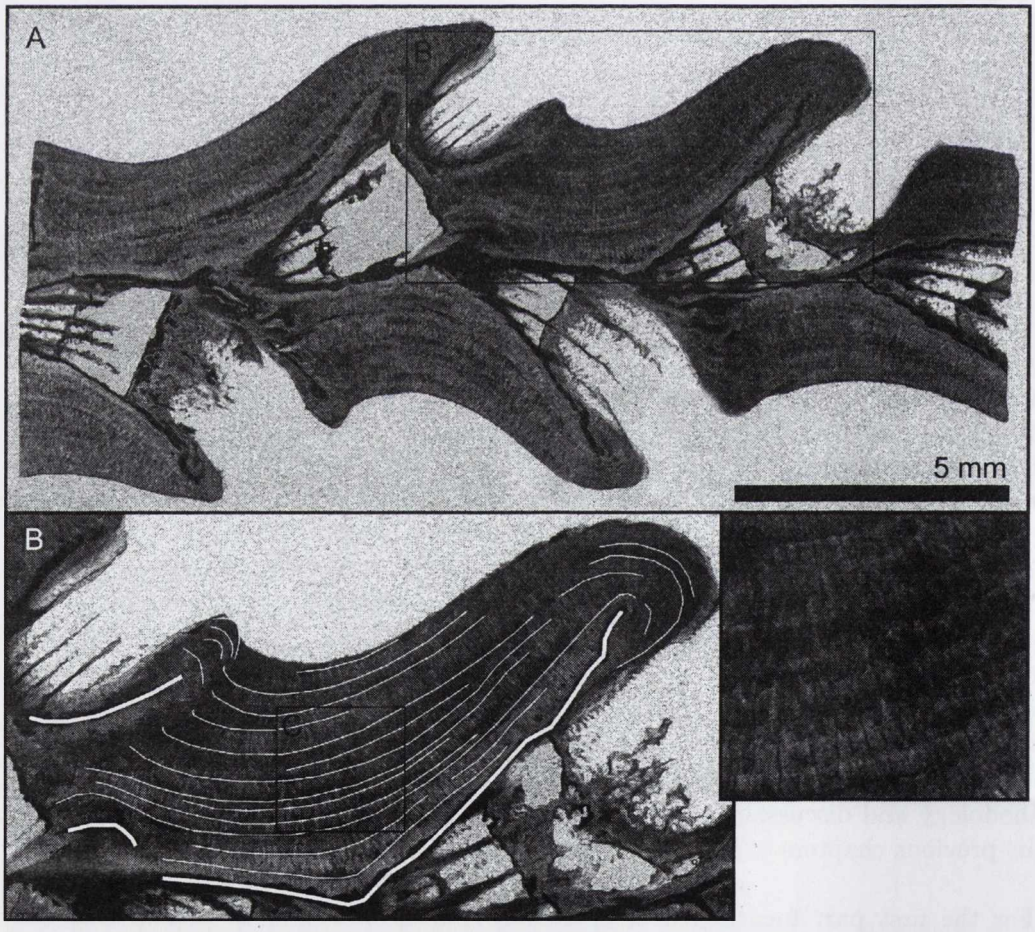


Figure 8.1: A) Microstructural layers in *Madrepora oculata* sample 459-M1 with connections between consecutive corallites. B) Solid lines show the location of EMZs from different corallites, dotted lines present the 14 microstructural layers. C) Thin lines cutting through well pronounced layers.

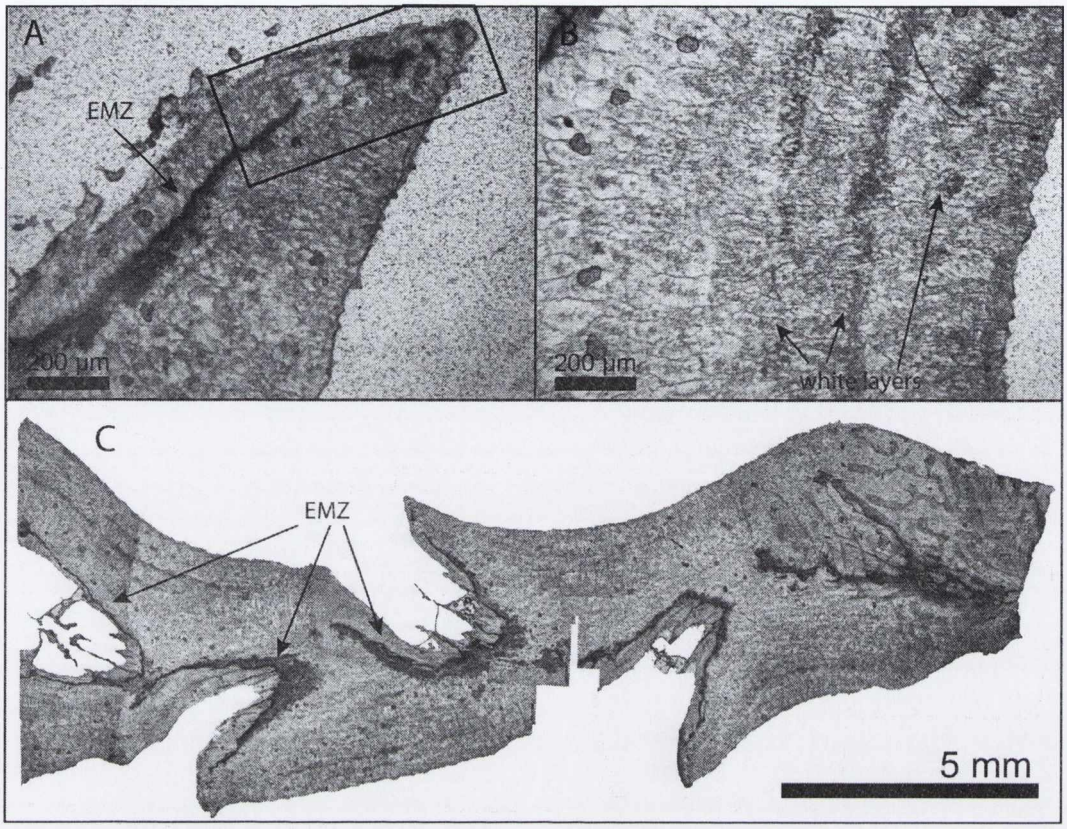


Figure 8.2: A)+B) Microstructural layers in *Madrepora oculata* sample 1009 (scale bar = 200 µm). A) The location of EMZs along the inner section of corallite wall show stepwise growth in length (box). B) A network of thin lines running across all layers (white layers appear dark in transmitted light) connect the different layers. C) The cross section through the branch shows the structural connections between consecutive corallites (image composed of photo mosaic, some partial images are missing as they were compromised).

8.1.2 Patterns in Trace and Minor Element Composition

Individual Corallite

^{25}Mg and ^{238}U were selected for laser ablation to check the correlation between structural layers and trace and minor element compositions in *M. oculata* on a finer scale, therefore, a section between two consecutive corallites[i] was covered with lines of laser ablation (table 8.1 and 8.2). The four experiment session for data aquisition (21-23 and 30) showed high SNR ratios for Ca, Mg, Ba and U, and SNR were only low for Cd measurements. The correlation between ^{238}U and ^{25}Mg and in association with microstructural layers was very good for the central thickening area and along the direct corallite wall of the lower corallite including the contact between both (fig. 8.3). Generally wall areas in direct contact with the cavity showed a similar pattern of growth in length and thickness as seen in *L. pertusa* (Chapter 7). The so-called Thickening Deposits (TD) seen along the direct contact with the cavity continued on in the space between two consecutive corallites where they are better developed. The thickening between the corallites did not show a decrease in layer thickness with progressing growth as observed in *L. pertusa*. Layer thickness displayed variations in thickness rather than a continuous decrease.

[i]the area between consecutive corallites was also known as 'coenosteum'

Table 8.1: Elemental concentrations in NIST612 standard during analysis along the individual 459-M1 corallite; averages and standard deviation (SD) of the mean in ppm and as RSD (%). The accuracy is given in relation to accepted values.

	Average	SD (2σ) of the Mean	RSD (%)	Accuracy	n
^{25}Mg	68.41 ppm	±1.80 ppm	2.64%	±0.41 ppm (0.61%)	24 lines
^{31}P	270.00 ppm	±830.00 ppm	310.00%	±223.40 ppm (479.40%)	8 lines
^{56}Fe	53.00 ppm	±26.00 ppm	49.00%	±2.00 ppm (3.92%)	8 lines
^{88}Sr	78.34 ppm	±0.97 ppm	1.24%	±0.06 ppm (0.08%)	16 lines
^{111}Cd	28.12 ppm	±0.33 ppm	1.16%	±0.02 ppm (0.07%)	16 lines
^{137}Ba	39.30 ppm	±0.49 ppm	1.25%	±0 ppm	24 lines
^{238}U	37.44 ppm	±0.51 ppm	1.35%	±0.06 ppm (0.16%)	24 lines

Table 8.2: Elemental concentrations along an individual *M. oculata* (459-M1) corallite; averages and standard deviation (SD) of the mean in ppm and as RSD (%).

	Average	SD (2σ) of the Mean	RSD (%)	n
^{25}Mg	728.69 ppm	±538.04 ppm	73.84%	101 lines
^{31}P	-300.00 ppm	±3100.00 ppm	-1200.00%	36 lines
^{56}Fe	800.00 ppm	±3900.00 ppm	520.00%	36 lines
^{88}Sr	9146.15 ppm	±3293.57 ppm	36.01%	65 lines
^{111}Cd	1.51 ppm	±13.29 ppm	880.24%	65 lines
^{137}Ba	32.59 ppm	±146.18 ppm	448.81%	101 lines
^{238}U	3.67 ppm	±0.51 ppm	1.35%	101 lines

Low ^{238}U concentrations were associated with the position of white microstructural layers and showed slight undulations (fig. 8.3). ^{238}U was generally inversely correlated with ^{25}Mg, especially when small-scale variability was smoothed out and underlying trends became more visible (fig. 8.3). While both, ^{238}U and ^{25}Mg, followed microstructural patterns, ^{137}Ba only showed rough indications of such a relationship. ^{137}Ba did not form continuous bands of high/low concentrations (fig. 8.3). ^{88}Sr showed some degree of covariation with ^{137}Ba and microstructures but strong technical interferences over parts of the analysed area led to the exclusion of strontium from detailed analysis. Potential deviation due to the rest of the gas carrying Sr (gas residue) into the chamber, appeared as if it mostly affects Sr, Ca and often Ba. ^{31}P appeared unsuitable for analysis due to the poor precision and accuracy (table 8.1). ^{57}Fe displayed no discernible pattern in concentrations (see Appendix E) and low SNRs. The ^{111}Cd signal was too low to be considered a true signal beyond background noise (table 8.2).

A well pronounced band of low ^{238}U following EMZs was found along the early growth phase and was surrounded by several phases of high ^{238}U concentrations before wall thickening sets in. The mechanism of branch thickening provided alternating thin bands of higher and lower ^{238}U concentrations whereby pronounced high ^{238}U concentrations were few and comparably thinner. The thickest bands of low ^{238}U concentrations were found during earliest growth and decreased towards the external wall section.

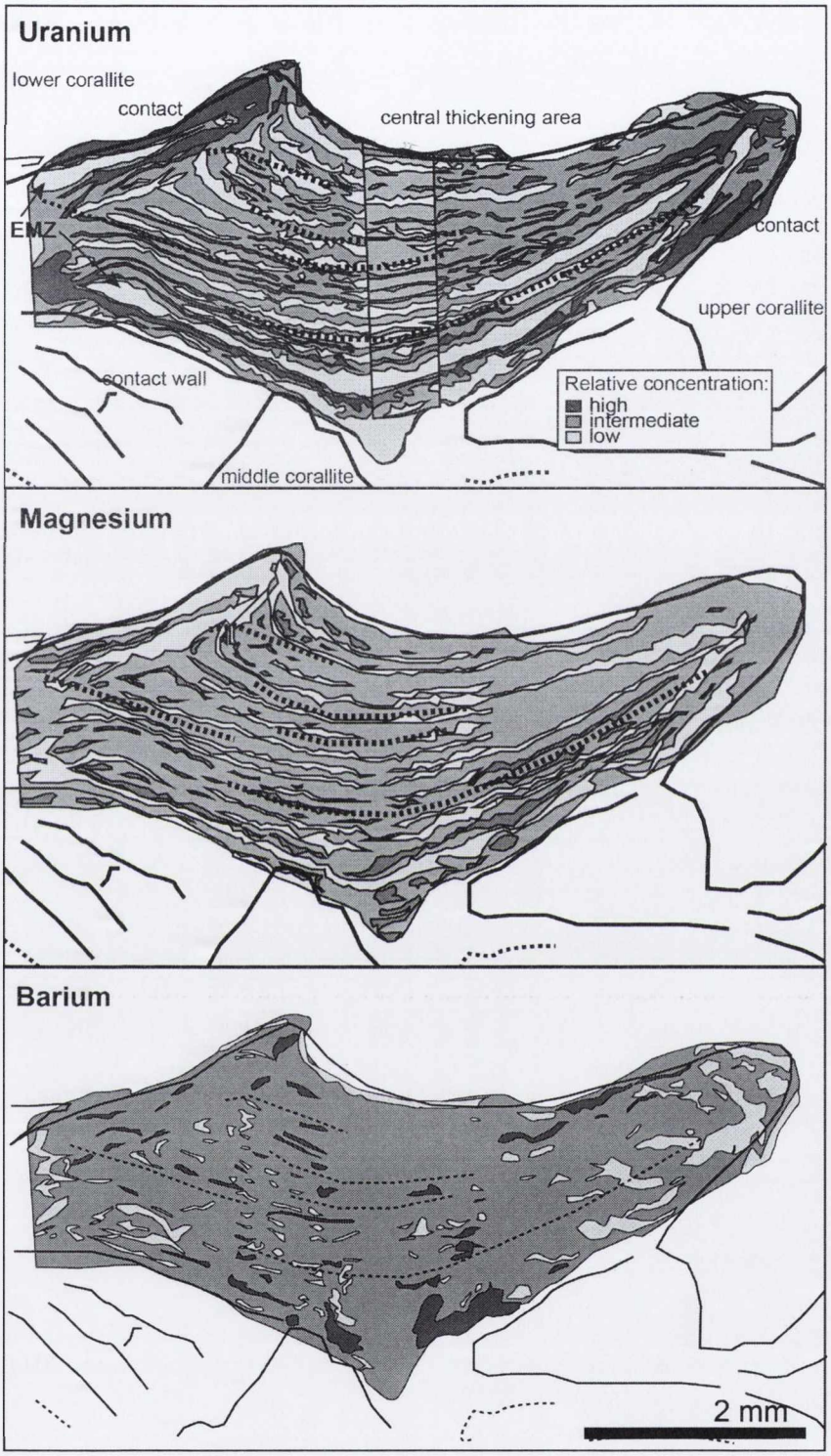


Figure 8.3: *Madrepora oculata* 459-M1: variations in elemental composition covering a complete section between three neighbouring corallites. Dotted lines represent macroscopically visible white growth layers. The box within uranium patterns overlaps with the results from a repetition of the experiment. The reproducibility is visible in the good fit.

8.1.3 Variations in Trace and Minor Element Compositions along Branches from Different Locations

To test reproducibility and investigate differences along branch calcification two *M. oculata* branch segments from different sampling locations (Whittard Canyon and Porcupine Bank) were analysed across Thickening Deposits (TD) using the same technique with laser ablation (see tables 8.3 to 8.6). The SNRs during analysis of sample 1009 and 459-M1 were high for Ca, Mg, Ba, U and Sr, while SNRs were below 10 for Fe and Li (see Appendix D.4 for details). Consequently Li and Fe results have to be viewed with extreme care.

Whittard Canyon

Table 8.3: Elemental concentrations NIST612 standard during analysis along the branch of sample 459-M1; averages and standard deviation (SD) of the mean in ppm and as RSD (%). The accuracy is given in relation to accepted values.

	Average	SD (2σ) of the Mean	RSD (%)	Accuracy	n
^{7}Li	40.19 ppm	±0.27 ppm	0.67%	±0.01 ppm (0%)	23 lines
^{25}Mg	70.27 ppm	±6.33 ppm	9.01%	±2.27 ppm (3.34%)	23 lines
^{88}Sr	79.10 ppm	±3.46 ppm	4.37%	±0.70 ppm (0.89%)	23 lines
^{137}Ba	39.30 ppm	±0.28 ppm	0.71%	±0 ppm	23 lines
^{238}U	37.39 ppm	±0.46 ppm	1.24%	±0.01 ppm (0.03%)	23 lines

Table 8.4: Elemental concentrations along different consecutive *M. oculata* corallites of sample 459-M1; averages and standard deviation (SD) of the mean in ppm and as RSD (%).

	Average	SD (2σ) of the Mean	RSD (%)	n
^{7}Li	0.80 ppm	±0.08 ppm	11.32%	82 lines
^{25}Mg	766.98 ppm	±32.54 ppm	4.24%	82 lines
^{88}Sr	7888.78 ppm	±373.82 ppm	4.74%	82 lines
^{137}Ba	12.32 ppm	±0.77 ppm	6.26%	82 lines
^{238}U	3.32 ppm	±0.15 ppm	4.43%	82 lines

Porcupine Bank

Table 8.5: Elemental concentrations NIST612 standard during analysis along the branch of sample 1009; averages and standard deviation (SD) of the mean in ppm and as RSD (%). The accuracy is given in relation to accepted values.

	Average	SD (2σ) of the Mean	RSD (%)	Accuracy	n
^{7}Li	40.23 ppm	±0.42 ppm	1.00%	±0.03 ppm (0.07%)	8 lines
^{25}Mg	69.05 ppm	±5.50 ppm	7.97%	±1.05 ppm (1.54%)	24 lines
^{56}Fe	54.51 ppm	±15.15 ppm	28.00%	±3.51 (6.88%)	16 lines
^{88}Sr	79.26 ppm	±3.51 ppm	4.43%	±0.86 ppm (1.10%)	24 lines
^{137}Ba	39.30 ppm	±0.30 ppm	0.77%	±0 ppm	24 lines
^{238}U	37.42 ppm	±0.94 ppm	2.52%	±0.04 ppm (0.11%)	24 lines

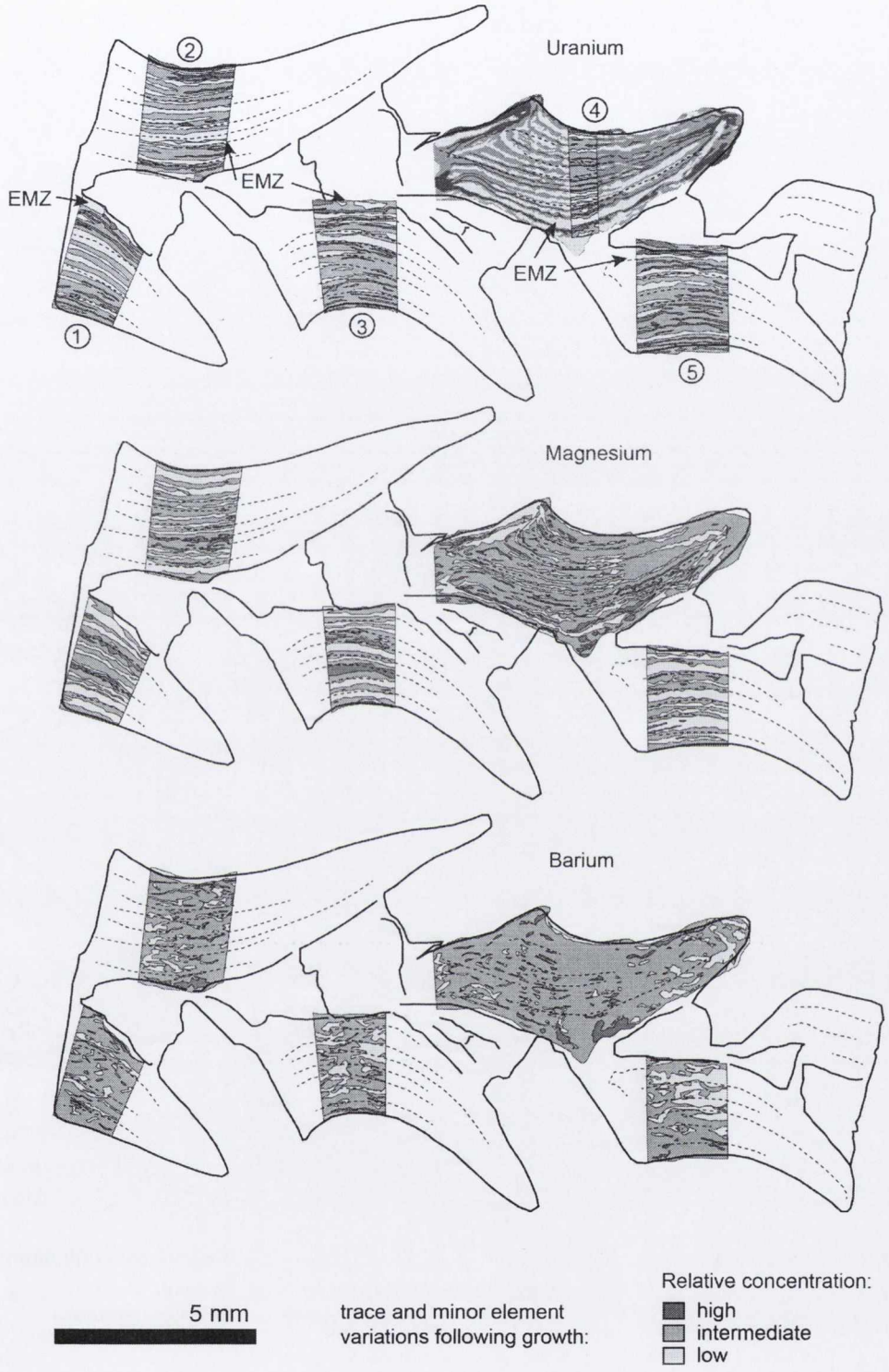


Figure 8.4: *Madrepora oculata* branch 459-M1 from the Whittard Canyon: variations in different elemental compositions along branch growth including the repeated analysis of the fully covered corallite (fig. 8.3).

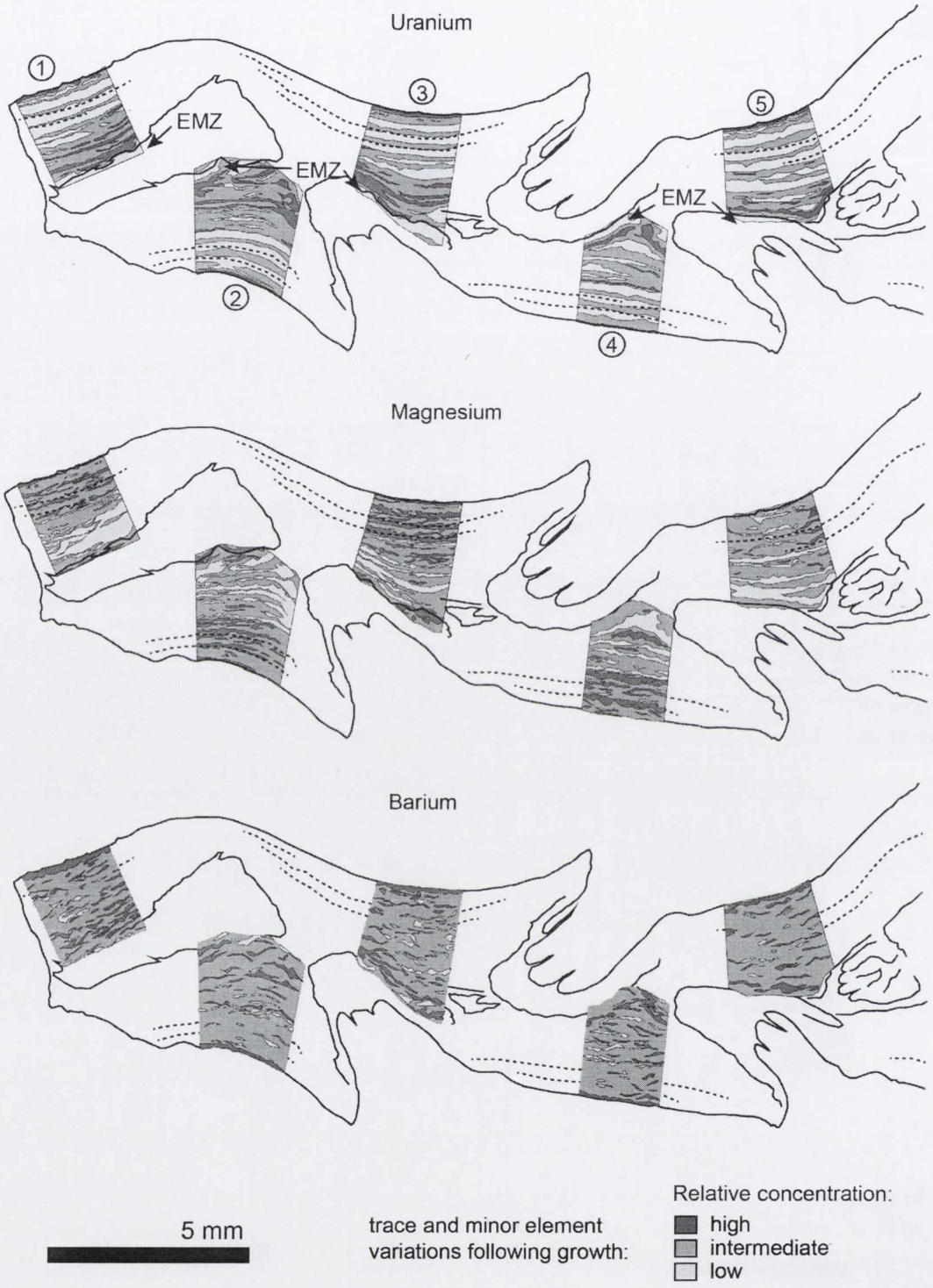


Figure 8.5: *Madrepora oculata* 1009 from the Porcupine Bank: variations in different elemental compositions along branch growth. The positive correlation between different elemental compositions along outermost bands points to a possible surface entrapment.

Table 8.6: Elemental concentrations in different *M. oculata* corallites along the branch of sample 1009 from the Porcupine Bank; averages and standard deviation (SD) of the mean in ppm and as RSD (%).

	Average	SD (2σ) of the Mean	RSD (%)	n
^{7}Li	0.86 ppm	±0.18 ppm	21.00%	44 lines
^{25}Mg	734.66 ppm	±68.35 ppm	9.30%	113 lines
^{56}Fe	145.33 ppm	±38.62 ppm	27.00%	69 lines
^{88}Sr	8556.90 ppm	±216.51 ppm	2.53%	113 lines
^{137}Ba	11.12 ppm	±1.09 ppm	9.83%	113 lines
^{238}U	3.24 ppm	±0.18 ppm	5.56%	113 lines

The branch of *M. oculata* sample 459-M1 (fig. 8.4) displayed a higher amount of small scale variations in the form of thin ^{238}U bands. As seen in section 8.1.2, a thicker band of low ^{238}U was located along the EMZ, and after a short phase of higher ^{238}U concentrations a second band correlated with a white microstructural layer. The number of high ^{238}U concentrations bands varied between segments but lay around 11 and 14. The branch appeared to have formed during a long series of shorter layer formation sequences.

M. oculata branch 1009 from the Porcupine Bank (fig. 8.5) showed clearly discernible bands of high and low ^{238}U concentrations. All five corallite sections of the branch were build-up by two to five thinner/relative thin bands (more or less continuous) during early mineralisation followed by four to five low ^{238}U bands. The outermost three bands were of similar thickness, well-developed and of equal thickness. The latest growth phase exhibited a very thin band of low ^{238}U concentration followed by a thin band of high ^{238}U concentration along the external wall section.

8.1.4 Discussion - *M. oculata* Growth Patterns

Geochemical Patterns

As in Scanning Electron Microscopy (SEM) and transmitted light microscopy the features revealed by LA-ICP-MS were highly dependent on the angle between cross section surface and growth layers. But unlike microscopy the general pattern visible in trace and minor elements seemed not to be obscured by this angle.

The study on *L. pertusa* in Chapter 7 and the discussion therein suggested that the antithetical correlation of ^{25}Mg and ^{238}U was caused by a pH-/alkalinity driven biological regulatory system and this appeared to be the most likely underlying mechanism here as well. This hypothetical pH-/alkalinity pump (e.g. Rollion-Bard & Blamart, 2015, McConnaughey, 1989a, 1989b) has potential to consequently influence the growth rate which in turn then produced different degrees of lattice defects and conversion of potential precursor phases (organic material, ACC). Consequently, high ^{25}Mg contents were discussed in connection with high precipitation rates, areas of high ^{238}U incorporation with slow calcification. Areas of higher ^{137}Ba and some degree of positive correlation with ^{25}Mg could be evaluated in connection with environmental forcing (nutrient fluxes) (Lea et al., 1989). Other potential nutrient related proxies (P,

Cd, Fe) prove unsuitable for this technique or lack a clear association with ^{25}Mg, ^{238}U or microstructure (see also table 8.2 and 8.1). The hypothesis here was that differences in ^{137}Ba composition as a nutrient proxy in the branches could give information on differences in and between environments. Following, both locations (Whittard Canyon and Porcupine Bank) appeared to be driven by different nutrient fluxes. Oceanographic observations in the area of the Whittard Canyon (see Wilson et al., 2015) pointed to a current system with nepheloid layers in the canyons which might have provided a constant supply of nutrient influx to some degree, therefore, causing the absence of well-defined sequences of growth. Scleractinians in the canyons were always found in association with peaks in fluorescence (indicative for Chl α).

Modelling the Branch Formation in *M. oculata*

The wall thickening appeared to originate from several neighbouring corallites, seen in comparable patterns across all corallites. The repetition in geochemical pattern (^{238}U) supported a calcification model where a whole section of the branch was thickened more or less simultaneously. Most likely budding took place relatively continuously which could also explain the fact that earlier growth showed evidence of relatively low calcification rates when applying conventional models of isotope fractionation and geochemistry where low fractionation effects were interpreted as low precipitation rates (e.g. Mortensen & Rapp, 1998).

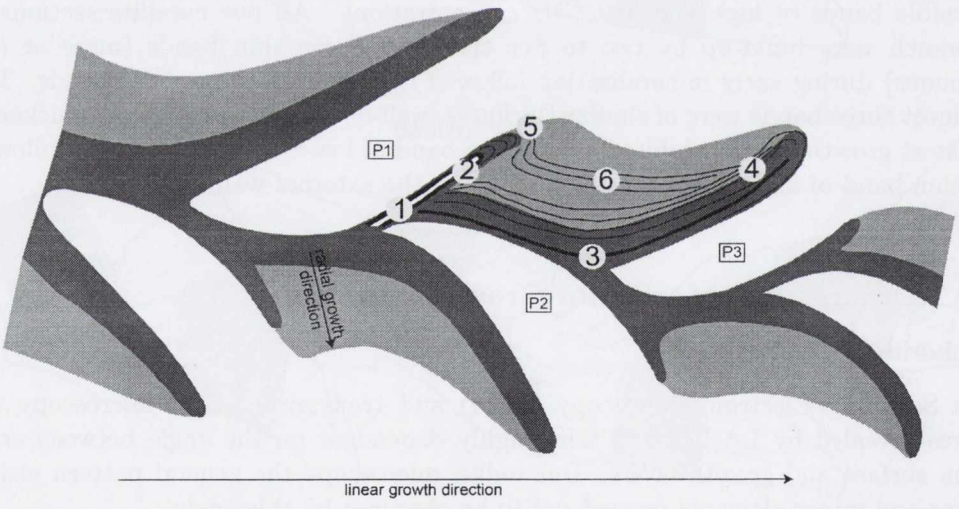


Figure 8.6: *Madrepora oculata* theca calcification model based on the covered section between consecutive corallites (section 8.1.2).

Table 8.7: Possible model of layer succession and involved processes along a *M. oculata* branch (fig. 8.6). Suggested steps 4 and 5 may occur simultaneously.

Step	Mineralisation Process	Dominant Geochemical Feature	Inferred Growth Rate
1	initial wall P1	high ^{25}Mg	high
2	thickening + lengthening P1	high ^{238}U	low
3	initial growth P2 + P3	high ^{25}Mg	high
4	thickening P2 + P3	high ^{238}U	low
5	longitudinal growth P1	high ^{238}U	low
6	thickening deposits intercorallite area	high ^{25}Mg and ^{238}U	high

The patterns in ^{25}Mg and ^{238}U and their association with microstructures were used in the following to establish a growth model and discuss possible variations in growth rate. The contact between three successive corallites (P1-P3 in fig. 8.6) provided a basis for modelling *M. oculata* growth. The branch section 459-M1 suggested a multi-stage calcification process (fig. 8.6) (table 8.7). Steps 1, 2 and 5 were connected to corallite P1 while steps 3 and 4 appeared to be related to the formation of corallites P2 and P3. Here no interruption in growth was visible in elemental concentrations or microstructure hence suggesting one event associated with early mineralisation phases of both corallites. The main thickening of the intercorallite area (coenosteum) (light grey in fig. 8.6) appeared to originate from P1 based on the bending of bands and partly discordant contact with the theca of P3. No information was available on whether these TD were precipitated under tissue cover or via mucus mineralisation.

According to observations by Orejas et al. (2008) *M. oculata* extends five corallites per year. This would suggest that the initial precipitates of all corallites were produced more or less at the simultaneously. Based on the visible layering in the *M. oculata* branch a possible model might be: Fast growth of the initial theca points to continuous linear extension with focus on budding and the formation of new corallites (not thickening). The process of thickening might follow later as a colony effect. Our observations suggest continuous CoCs for *M. oculata* as described for *L. pertusa* and *D. dianthus* (Cuif et al., 1999b).

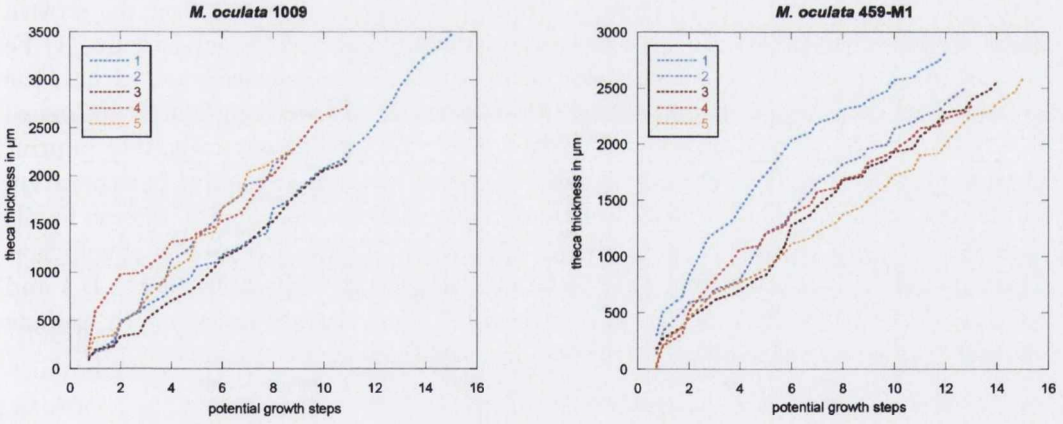


Figure 8.7: Layer thickness variations of individual *Madrepora oculata* corallites in the branches from different locations based on bands in ^{238}U and ^{25}Mg. Numbers refer to branch sections (see fig. 8.4 and 8.5 from left to right).

The highly reproducible geochemical pattern in TD between different corallites of sample 1009 pointed to a common calcification sequence which influenced the compositions in all corallites equally. The fact that analysis was run over several sessions should exclude technical causes for repeating patterns (accuracy/precision) (see Appendix E) i.e. re-occurring patterns in elemental concentrations could be reproduced beyond individual analytical sessions.

The thickness of the individual layers across corallite thickening did not show the clear decrease as seen in *L. pertusa* (fig. 8.7). Layers of high ^{238}U concentrations

in sample 1009 were found better developed (more massive) than in *L. pertusa* and appeared more concentrated during earlier growth phases rather than towards the outermost part of the corallite. This was possibly caused by an ontogenetic effect without excluding regional influence.

Nutrient fluxes

The canyon on the Porcupine Bank did not display pronounced peaks in fluorescence during our dives. It has to be said, though, that the area was only covered by one of the research cruises and the CTD data could only provide insight into a fraction of possible temporal variations in time. In the branch sample 1009 most corallites showed partial bands of high ^{137}Ba concentrations associated with early growth and a decrease in high ^{137}Ba bands towards the outer theca (younger deposits) and increase in the outer layers. Branch sample 459-M1 from the Whittard Canyon where nepheloid layers were found on a regular basis (Wilson et al., 2015) displayed less oriented variations and relatively patchy ^{137}Ba distributions.

Testing the Potential of Iron (Fe)

To determine the age of the corallite it would be helpful to detect useful marker horizons. Since volcanic eruptions are known to provide a temporary increase in iron to the marine surface primary production the value of this element as a 'marker horizon' in biomineralisation was tested. Iron (^{57}Fe) was included in analysis of the sample from the Porcupine Bank to check whether it was possible to detect a potential marker horizon in connection with recent volcanic eruptions (2011 Eyjafjallajökull eruption in Iceland). ^{57}Fe showed no detectable layer of increased concentrations over the growth of the analysed sample. This can be discussed in the light of different factors: (1) Fe is not a useful proxy to detect such peaks; (2) Fe is not being incorporated into the skeleton from external sources directly; (3) Fe concentrations are regulated by biological processes; (4) The impact of recent volcanic deposits was not strong enough to imprint on biomineralisation. Hypothesis (1) could be tested by analysing sulfur incorporation in this context. Hypothesis (4) would hold potential for palaeoreconstruction on fossils in connection with periods of more powerful eruptions. Possible eruptions of sufficient extent in the NE Atlantic region might be the Eldgjá (approximately 950 A.D.) and the Laki (1783-85) eruptions (Iceland). Generally more data is necessary to exclude volcanic eruptions as a marker horizon in coral skeletons

8.2 Testing Temperature Reconstruction Approaches

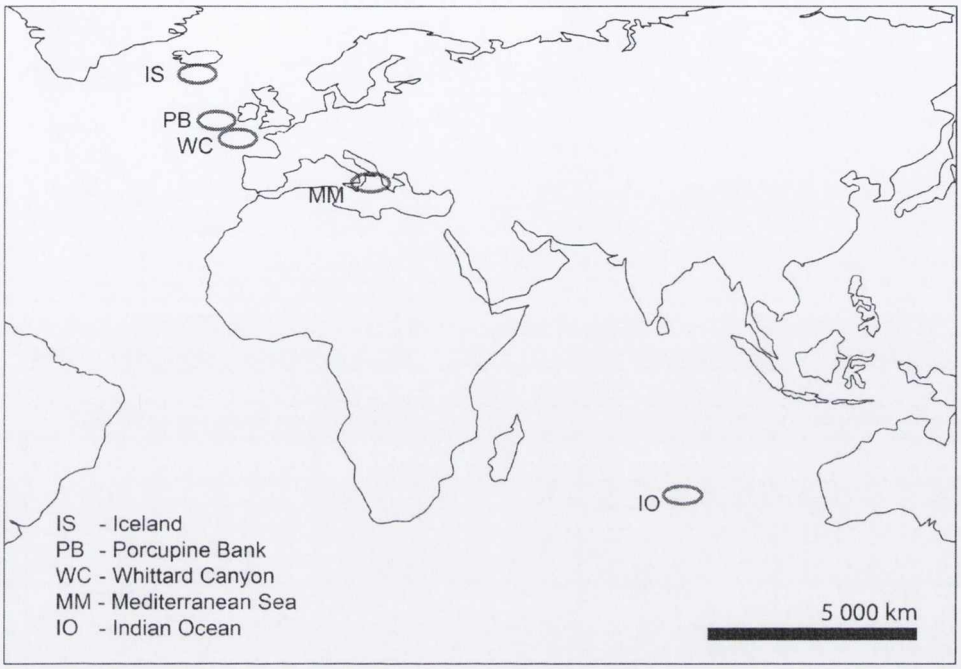


Figure 8.8: A set of *M. oculata* samples from different locations in the NE Atlantic, the Mediterranean Sea, and the Indian Ocean (legend gives samples names) were selected to support a generalised attempt at temperature reconstruction based on geochemical compositions.

8.2.1 Stable Oxygen and Carbon Isotope Ratios - 'Lines Technique'

A selection of *M. oculata* samples (appendix B) from different oceanographic settings (fig. 8.8) were analysed to test temperature reconstruction approaches. Approach one utilised stable isotope ratios for the so-called 'lines technique' (Smith et al., 2000) and the second approach looked into the use of Li/Mg ratios (e.g. Montagna et al., 2014, Raddatz et al, 2013, Case et al, 2010). Sampling for approach one was performed by microdrill lines following the microstructural layers. This strategy highlighted different growth periods with potentially varying growth rates and metabolic fractionation effects. In the case of the two specimens from the Whittard Canyon the samples were not only taken along a transect of the corallite wall but also along the contact with calcified *E. norvegica* tubes to compare fractionation effects between the areas. The results will be revisited in Chapter 9. Maxima, minima and average stable isotope ratios are given in table 8.8, fig. 8.9 and 8.10. Stable isotope ratios from all samples showed a good fit ($R^2 > 0.9$) onto linear regression lines (table 8.9 and fig. 8.11). The microdrill sampling strategy produced more data points in the lower reaches of the regression line (consistent with high growth rates) (fig. 8.9) than in the case of surface sampling (as applied in Chapter 6). High growth rates were generally discussed in connection with high fractionation effects and consequently increased ^{18}O and ^{13}C depletion. In the case of *L. pertusa* high growth rates were reported for early growth phases (e.g. Maier et al., 2009).

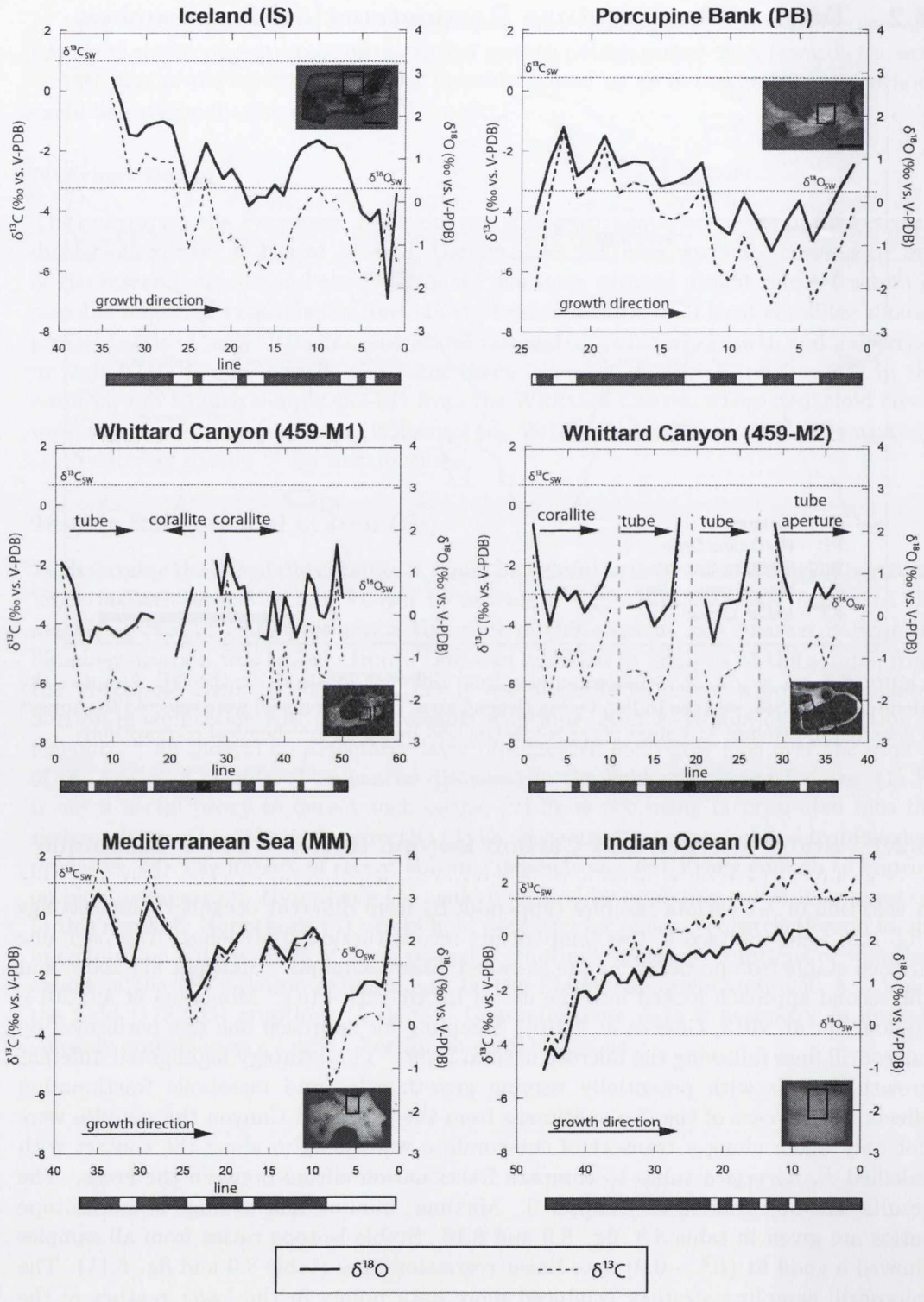


Figure 8.9: Stable isotope ratio variations along radial growth in *M. oculata* samples from different locations. The bars below individual graphs indicate the location of white and beige (in gray) layers as visible under reflected light. Black sections mark precipitation gaps between layers. Dotted horizontal lines indicate stable isotope ratios of the ambient seawater (table 8.9). Sampling areas along growth were included on photos (more detail in appendix C).

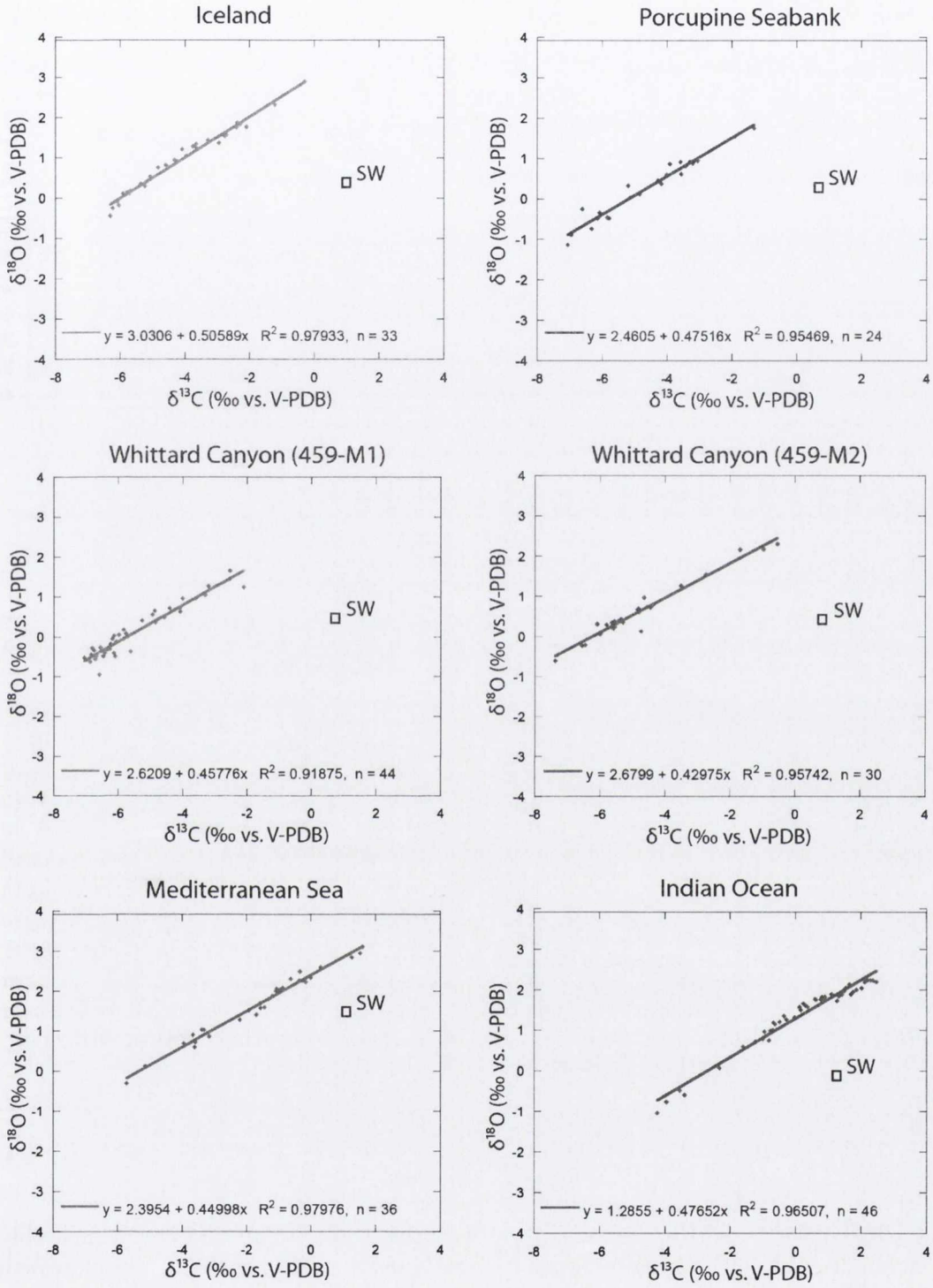


Figure 8.10: Stable isotope regression lines for *M. oculata* samples from different locations in comparison (without outlier rejection). One outlier was rejected in sample IS. The boxes mark the equilibrium with the ambient seawater.

Table 8.8: Stable isotope ratio maxima and minima together with the average for the different locations.
IS = Iceland (Hafadjup, 599 m)
PB = Porcupine Bank (53.97°N/-12.62°E, 700 m)
WC = Whittard Canyon (48.76°N/-10.46°E, 734 m)
MM = Mediterranean Sea (39.55°/18.53°E, 750-828 m)
IO = Indian Ocean (-37.68°N/77.52°E, ca. 700 m).

	Loc	$\delta^{18}O_{max}$	$\delta^{18}O_{min}$	$\delta^{13}C_{max}$	$\delta^{13}C_{min}$	$\delta^{18}O_{mean}$	$\delta^{13}C_{mean}$	n
IS	IS	2.90	-2.25	0.28	-6.30	0.83 ± 0.98	-4.16 ± 1.67	34
PB	PB	1.75	-1.14	-1.31	-7.06	0.31 ± 0.77	-4.53 ± 1.58	24
459-M1	WC	1.66	-0.95	-2.11	-7.04	0.14 ± 0.64	-5.41 ± 1.34	44
459-M2	WC	2.3	-0.61	-0.53	-7.37	0.60 ± 0.69	-4.85 ± 1.57	30
MM	MM	3.11	-0.3	1.6	-5.71	1.69 ± 0.80	-1.56 ± 1.75	37
IO	IO	2.24	-1.04	2.48	-4.23	1.38 ± 0.83	0.20 ± 1.70	46

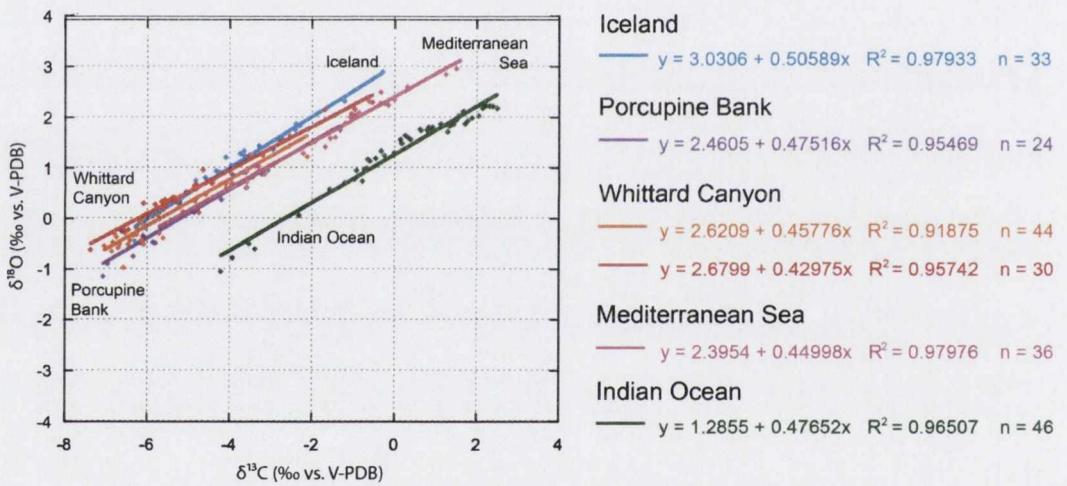


Figure 8.11: *Madrepora oculata* samples from different locations showed a clear relative correlation between different temperature regimes.

All *M. oculata* samples except for the one from the Indian Ocean exhibited comparably high δ^{18}O and δ^{13}C during early growth and a decrease during the course of growth (fig. 8.9). The one from the Indian Ocean started on minimum values which gradually increased over time with relatively small variation around 1‰ compared to the other samples where variations could reach up to 2-3‰. Generally stable isotope ratios in the samples from the Atlantic and Mediterranean Sea pointed to a phase of low growth rates during early growth. The sampled calcified polychaete tubes mostly displayed stable isotope ratios within the same range as corallite samples from the same specimen (fig. 8.9).

Table 8.9: *M. oculata*: Environmental parameters for the different sampling locations (own measurements and other sources), reconstructed temperatures (in °C) following the equations by Smith et al. (2000) and differences in reconstructed temperatures (ΔT).
IS = Iceland (599 m)
PB = Porcupine Bank (700 m)
WC = Whittard Canyon (734 m)
MM = Mediterranean Sea (750-828 m)
IO = Indian Ocean (≈ 700 m).

Loc	T_{meas}	Salinity	$\delta^{18}O_{SW}$	$\delta^{13}C_{SW}$	Intercept	eq. 6.1	eq. 6.2	ΔT
IS	5.96°C	35.07 psu	0.29‰	1.00‰	3.03‰	8.92°C	6.72°C	2.20°C
PB	10.31°C	35.40 psu	0.27‰	≈0.58‰	2.46‰	11.12°C	9.32°C	1.80°C
WC	0.19°C	35.58 psu	0.45‰	≈0.76‰	2.62‰	11.20°C	8.59°C	2.61°C
WC	10.19°C	35.58 psu	0.45‰	≈0.76‰	2.68‰	10.96°C	8.32°C	2.64°C
MM*	13.90°C	38.77 psu	1.46±0.11‰	1.10‰**	2.40‰	16.14°C	9.61°C	6.53°C
IO	≈ 2.50°C	≈ 34.00 psu	≈ -0.20‰***	≈1.30‰	1.27‰	14.02°C	14.75°C	0.73°C

* López Correa *et al.* (2010)
** Pierre *et al.* (1999)
*** Bigg & Rohling (2000), Schmidt *et al.* (1999).
all $\delta^{13}C_{SW}$ retrieved from CDIAC data base: http://cdiac.ornl.gov

8.2.2 Li/Mg Ratios

Another proposed tool for temperature reconstruction is the ratio between Li and Mg (e.g. Montagna et al., 2014). Therefore, the samples used for SIA (except for the sample from Iceland which was only available for SIA) were also analysed by LA-Q-ICP-MS over the central thickening area to compare patterns in ^{238}U, ^{25}Mg and ^{7}Li. The samples of *M. oculata* branches from the Whittard Canyon, Porcupine Bank, Mediterranean Sea and Indian Ocean were analysed for Li/Mg ratios by LA-Q-ICP-MS together with glass standards NIST610 and NIST612 to test suggested temperature reconstruction approaches (Rollion-Bard & Blamart, 2015, Montagna et al., 2014, Hathorne et al., 2013a, Raddatz et al., 2013, Case et al. 2010). Since elemental ratios like Li/Mg were more commonly measured using bulk solution ICP-MS (e.g. Hathorne et al., 2013a, Raddatz et al., 2013) a series of tests was run prior to analysis.

Variations with Aperture Size

An experiment testing different aperture sizes (and ablation speeds) was run on one of the samples (MM) to determine the most suitable setup (table 8.10 and fig. 8.12). Data reduction was performed in *Iolite* v2.5 (Paton et al., 2011) with NIST610 glass as the external standard.

Table 8.10: The table presents averages for different laser aperture sizes and scan speeds with 2 SD (standard deviation) as absolute (in ppm) and relative (in %) standard deviation. The ratios present results before (in cps) and after data reduction (in ppm) in *Iolite*.

Aperture Size	Ablation Speed	Li/Mg from cps (RSD)	Li/Mg from ppm (RSD)
12 μm	6 μm/s	0.01110 ± 0.00140 (12.0%)	0.000990 ± 0.000120 (12.0%)
24 μm	12 μm/s	0.01061 ± 0.00090 (8.5%)	0.000949 ± 0.000078 (8.2%)
47 μm	23 μm/s	0.01029 ± 0.00041 (4.0%)	0.000947 ± 0.000040 (4.2%)

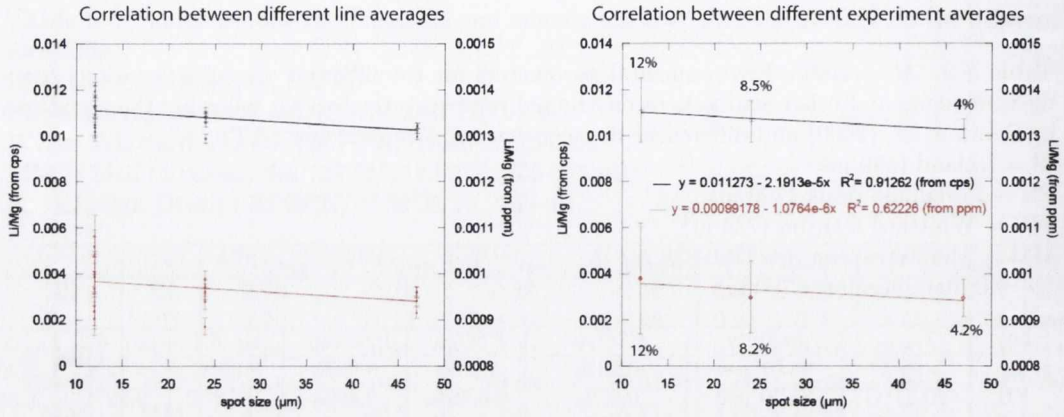


Figure 8.12: The averages per line (left) and per experiment (right) using raw data (from cps) (in black) and corrected values (from ^{7}Li and ^{25}Mg in ppm) (in red) for comparison of different parameters. The larger spot size showed larger variations in Li/Mg ratios for different lines and higher RSDs.

Comparison between Different Locations

For sample ablation a 47 μm square-shaped aperture with an ablation speed of 23 μm/s (at 10 Hz) after preablation with a 60 μm circle-shaped aperture at 350 μm/s (at 20 Hz) was chosen based on the aperture size tests (compare fig. 8.12). While ^{7}Li and ^{25}Mg concentrations showed variations related to the layered microstructures in the theca, the ratio between both elements appeared to smooth out microstructure related variations (fig. 8.13). The low SNR for ^{7}Li rendered a quantitative approach impossible; however, the fact that variations in ^{7}Li still seemed to be correlated to ^{25}Mg variations suggested a relative connection between both in accordance with published observations. The calculated ratio has to be used with care. The low accuracy and precision in ^{7}Li analysis make the temperature reconstruction approach difficult.

Averaged ^{7}Li/^{25}Mg ratios of individual *M. oculata* samples from different locations showed a relative correlation (tables 8.11 and fig. 8.14). The results showed higher ^{7}Li/^{25}Mg ratios for specimens taken from environments where lower ambient seawater temperatures (°C) were measured with a relative decrease in ratios with increasing temperatures (table 8.14). Only the two samples from the Porcupine Bank and Whittard Canyon which were collected from relatively similar temperature regimes appeared to show a positive correlation between temperature and ^{7}Li/^{25}Mg (in relation) (table 8.14). Precision, accuracy and SNRs were comparable for ^{7}Li and ^{25}Mg in samples from different locations. Accuracy was < 0.02 ppm, precision was below 0.5%, and SNR was between 7 and 10 for Li and between 882 and 1082 for Mg. Therefore, the low SNRs for Li appear to be the most likely source of error but relative variations between locations should hold since the error should be relatively similar for all samples. Salinities on the other hand showed a negative correlation with ^{7}Li/^{25}Mg ratios increasing with decreasing salinities for the NE Atlantic and Mediterranean Sea samples. This suggested that salinities might be a contributing factor which has to be considered when using ^{7}Li/^{25}Mg for environmental reconstruction. The measured ^{7}Li/^{25}Mg ratios were offset from the published equations (fig. 8.15).

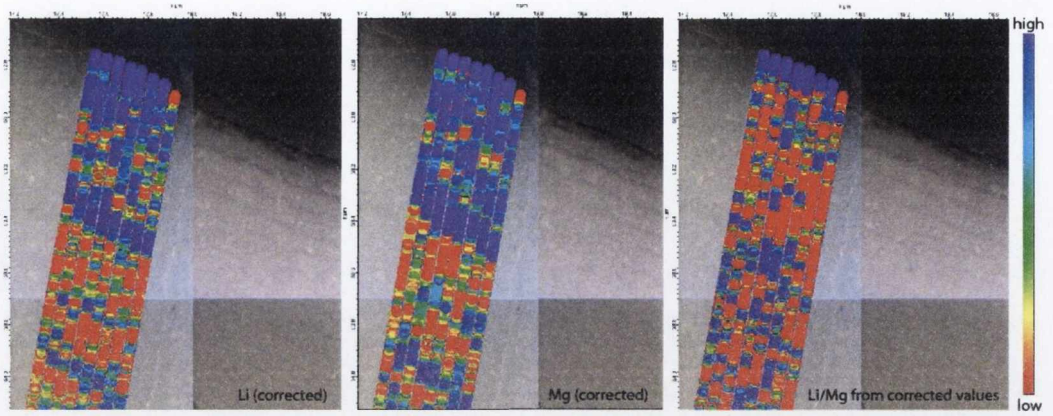


Figure 8.13: From left to right: Variations in ^{7}Li, ^{25}Mg and $^{7}Li/^{25}Mg$ ratios displayed in *Cellspace* (Paton et al., 2011) after processing the outer theca section. The range represents 2σ from averages (95% confidence interval). Small scale variations in ^{25}Mg and ^{7}Li during growth in relation to microstructure appeared positively correlated but mostly disappeared in $^{7}Li/^{25}Mg$ ratios. On the right to the laser ablation the impressions from microdrill lines are visible parallel to the theca surface for comparison of different resolutions.

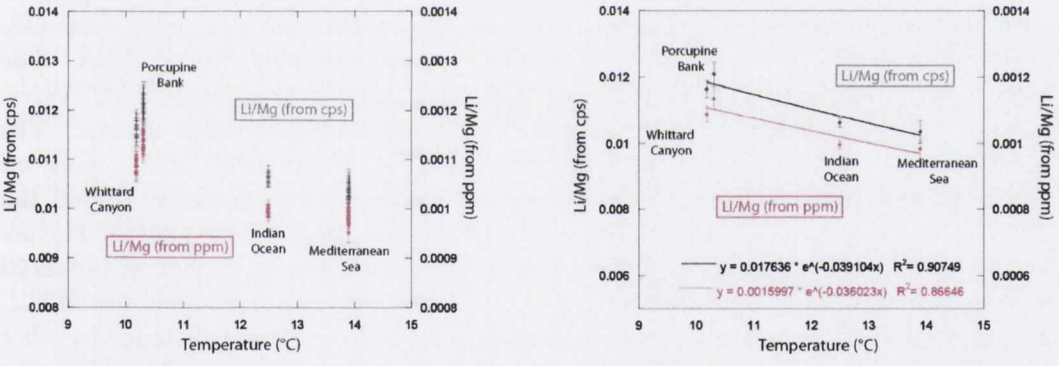


Figure 8.14: The $^{7}Li/^{25}Mg$ ratios from *M. oculata* samples from different locations showed a general trend for different temperature regimes. Left: Average per line. Right: Average per experiment. Gray data points represent ratios from raw data (^{7}Li and ^{25}Mg in cps), pink data points represent ratios from corrected data (^{7}Li and ^{25}Mg in ppm). The samples from the Whittard Canyon and Porcupine Bank originated from very similar temperature regimes but plotted inversely compared to the general trend. The sample from the Indian Ocean would fit the regression if the temperature was assumed to measure at least 12.5°C as suggested by the 'lines technique' correlation

Table 8.11: Averages of $^{7}Li/^{25}Mg$ ratios from different locations retrieved from raw data in cps and from corrected data in ppm. The ratios from raw data were approximately ten times higher than ratios calculated from the cps before data correction.

Loc	Depth (m)	T_{meas}	Salinity	$^{7}Li/^{25}Mg$ (from cps)	$^{7}Li/^{25}Mg$ (from ppm)
PB	700	10.31°C	35.40 psu	0.01209 ± 0.00035	0.001135 ± 0.000033
WC	734	10.19°C	35.58 psu	0.01163 ± 0.00026	0.001088 ± 0.000024
MM	750-828	13.90°C	38.77 psu	0.01035 ± 0.00034	0.000983 ± 0.000029
IO	≈ 700	≈ 12.50°C	≈34.00 psu	0.01062 ± 0.00014	0.000996 ± 0.000013

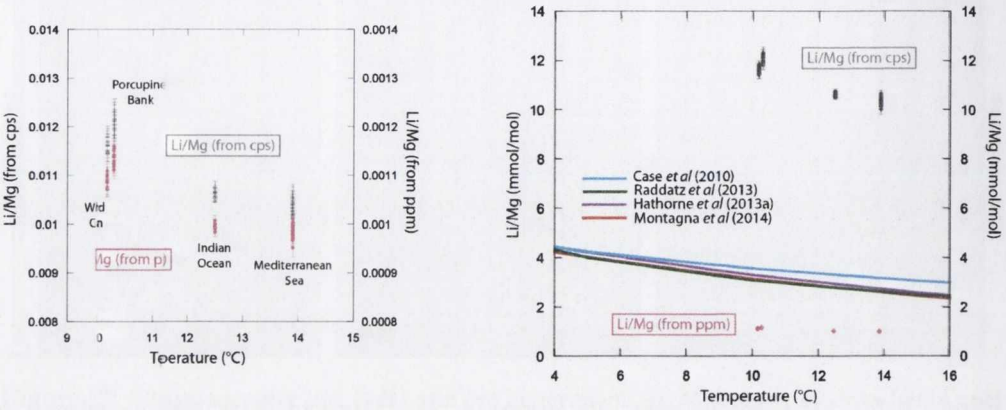


Figure 8.15: The $^{7}Li/^{25}Mg$ results presented in fig. 8.14 compared to trends published for different WC species (right).

8.2.3 Discussion - Temperature Reconstruction

Stable isotope analysis results showed a high degree of correlation between intercept with the y-axis and temperature regimes. Nevertheless there was an offset in relation with the suggested equations to reconstruct ambient temperatures which pointed to a species-specific effect. Slopes among all *M. oculata* samples were relatively similar (0.43-0.53) with a steeper slope (0.50) for the specimen from Iceland. The reconstructed temperatures lay closer to measured temperatures (table 8.9). Variations in intercepts might also be associated with differences in water masses. The Mediterranean Outflow Water (MOW) most probably did not reach the canyons off the Porcupine Bank while a diluted version of the MOW was detected around the depth of *M. oculata* occurrences in the Whittard Canyon (Wilson et al., 2015). Factors like this have to be considered for reconstruction approaches in regions of potential current variations. A correlation with salinity might also create relevant deviations. The regression line for the Indian Ocean sample showed the largest distance to other lines which points a stronger difference between this environment and the ones in the North Atlantic and Mediterranean Sea.

Generally all measured $^{7}Li/^{25}Mg$ values lay below the published Li/Mg data. The offset was clearly reduced after data reduction in *Iolite* (Paton et al., 2011) but Li/Mg ratios still produced unrealistically high temperatures in equations for a reconstruction of ambient temperatures (Montagna et al., 2014, Hathorne et al., 2013a, Raddatz et al., 2013, Case et al. 2010) (see eq. 2.6, 2.7, 2.8, 2.9). So far Li/Mg ratios were commonly analysed using solution ICP-MS on bulk samples with a specific coral standard (JCp-1) or individually composed solution standards (see table 8.12). The correlation between *Iolite* corrected results for the investigated (restricted) ranges produced a similar R^2 for the general ($R^2 = 0.8665$) as for the linear correlation ($R^2 = 0.8610$):

$$Li/Mg(mmol/mol) = 1.5997e^{(-0.036*T(^{\circ}C))} \tag{8.1}$$

$$Li/Mg(mmol/mol) = 1.4936 - 0.0378 * T(^{\circ}C) \tag{8.2}$$

Table 8.12: Analysis of Li/Mg in corals (CWCs and shallow water spemens)o far was performed with a variety of methods and standards. Laser ablation was usully incded as an additional test. Case et al. (2010) based the data reduction for laser ablaon sapling on a solution standard which introduced an analytical error caused by a matrix fect.
1 = cold-water corals, 2 = tropical corals.

Reference	Analytical Method	Standard Material	Marial
Montagna et al., 2014	solution ICP-MS	JCp-1	1 2
Montagna et al., 2014	LA ICP-MS	*in-house* coral std (Li) NIST614 (Mg)	1 2
Hathorne et al., 2013a	solution ICP-MS	mixed solution + JCp-1	*Pdes*
Raddatz et al., 2013	solution ICP-MS	JCp-1	*Loplia*
Case et al., 2010	solution ICP-MS	mixed solution	1 2
Case et al., 2010	LA ICP-MS	mixed solution	1 2

Since *M. oculata* was directly included in one of the studies al seval CWC species were tested, it can be ruled out that the significant offsetn Li/g was a species-specific effect. The offset between our results and publisld Li/g ratios could be caused by the selected approach i.e. analytical deviation: Lasc ablation was depending on the chosen parameters (see fig. 8.12) and a differnt apcure size, ablation speed or ablation rate might reduce or remove the offset. bre tes will be necessary to establish best suited parameters and to locate the sourc of deation for this method on the used machine. Another possible reason for theoffset :s in the available standards. Two NIST glasses were bracketing the samplefor anysis and were also included in between sample measurements. The Ca concitrati of both standards (^{43}Ca is the internal standard) lay around 8.2% and 8%, reective, which was not optimal for measurements of biogenic calcium carnatewith Ca concentrations around 40%. Most studies used mixed solution stancrds othe coral standard JCp-1. Solution standards are not matrix-matched and,herefe, cause possible bias. The coral standard JCp-1 was not officially availab at tl time of analysis but since standardisation of this standard is based on NIST0 anNIST612 (based on a plug-in by D. Chew), using the glasses should not accounr suchn offset.

The difference between published Li/Mg ratios in corals and th hereresented ^{7}Li/^{25}Mg ratios was possibly caused by the low mass of the msurecelements (especially ^{7}Li). The offset between samples which were not mtrix-ntched is higher for lighter isotopes (Longerich et al, 1990). Most publied rios were matrix-matched due to solution ICP-MS on bulk samples. Neverthss theLi/^{25}Mg ratios obtained from LA-ICP-MS showed a comparable relative crelatic for the available locations. ^{7}Li/^{25}Mg ratios for the NE Atlantic samples ad thene from the Mediterranean Sea displayed the same relative correlation ascan b seen in the δ^{13}C/δ^{18}O intercept. So far the decisive factor was suggeste to bambient temperature alone. We found a possible correlation with salinities r sanles from the NE Atlantic and Mediterranean Sea which might point to an adcionalfluence. This observation was inconclusive due to the limited amount of saples al due to the lack of environmental information for the Indian Ocean. More tes areecessary to prove or disprove a possible correlation. Internal variations inonneion with growth and growth rates have to be considered for Li/Mg ratios as wl. Roon-Bard & Blamart (2015) discussed different mineralisation models with respt to and Mg incorporation and found a temperature-controlled Rayleigh fractionion a unlikely mechanism for the variations. They came to conclude that precipitaon ra was the main influencing factor which was possibly indirectly affected by ambit temratures.

Chapter 9

Patterns in Coral Biomineralisation in Conrion with *E. norvegica* Tubes

Species interaction, especially in connection with carbonate pron, can provide additional insight into involved biomineralisation mechanismsolychaete *E. norvegica* was reported as a common symbiont and contributor tobility among scleractinian colonies which calcify the organic polychaete tubes integrating the symbiont into the coral structure (e.g. Roberts, 2005). Behavtudies on *L. pertusa* in connection with the polychaete were published in the d showed an impact on skeletal precipitation (e.g. Roberts, 2005, Mortensen, 20e impact on biomineralisation, however, has so far never been investigated in dere a series of *L. pertusa* and *M. oculata* branches with integrated *E. norvegic*showing different stages of calcification were analysed via microscopy and LAS along the contact between corallite and tube (table 9.1 and fig. 9.1). The aims at providing additional information on the tube calcification patterns aineralisation mechanisms of the CWCs.

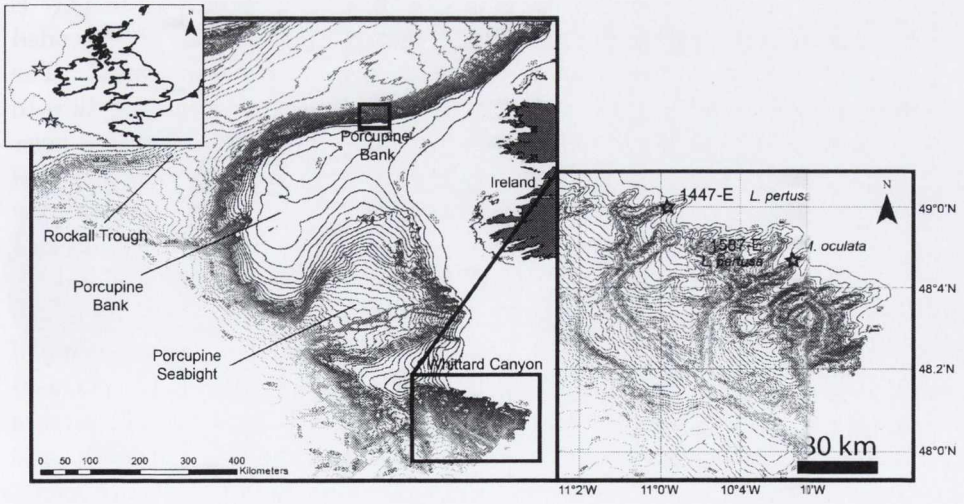


Figure 9.1: *E. norvegica* tubes are common among scleractinian coralsie Irish shelf. The analysed sample orginated from the Porcupine Bank and two weanches of the Whittard Canyon. Exact sample locations are listed in table 9.1.

Table 9.1: Coordinates (Lat/Long) and depth of different sampling locations for the two CWC species from two different locations.

Sample	Species	Location	Lat/Long	Depth	Cruise
459-M1-E	*M. oculata*	Whittard Canyon	48.7607°N/10.4608°W	750 m	CE12006
459-M2-E	*M. oculata*	Whittard Canyon	48.7607°N/10.4608°W	750 m	CE12006
1009-E	*M. oculata*	Porcupine Bank	53.9738°N/12.6227°W	760 m	CE13008
1033-E	*L. pertusa*	Porcupine Bank	53.9738°N/12.6227°W	670 m	CE13008
1036-E	*L. pertusa*	Porcupine Bank	53.9738°N/12.6227°W	757 m	CE13008
1447-E	*L. pertusa*	Whittard Canyon	49.0098°N/10.9488°W	700 m	CE13008
1587-E	*L. pertusa*	Whittard Canyon	48.7632°N/10.4599°W	650 m	CE13008

9.1 Patterns in Microstructure

The available thin sections presented different stages of polychaete tube calcification in cross sections through the corallite-tube contact. The *L. pertusa* sample 1447-E presented an early calcification stage in the form of a partial layer (fig. 9.2). It extended a few mm from the corallite and still left most of the organic tube uncovered. The precipitates showed white and beige fibrous sections that stretched from corallite to tube in varying thickness. The fibres were clearly organised in the thin corallite layer as well as in thicker tube layers. The thin corallite wall also showed first stages of wall layering. In comparison *M. oculata* sample 459-M2-E displayed a series of thin tube layers with organised fibre orientation and a closed tube opening in connection with corallite layers (fig. 9.3). The opening cover showed one partial layer underneath the organic layer that closed the tube in addition to the cover on the outside which connected corallite and tube in the diagonal cut. The fibre organisation and layering of corallite and tube wall were visible in the diagonal cut of sample 1036-E (*L. pertusa*) and stepwise cover of the tube (fig. 9.4). Another radial cross section of *L. pertusa* sample 1587-E through alternating white and beige layers continued seamlessly onto the tube covering layer (fig. 9.5). The inside of the tube again contained partial layers. All layers showed clear fibre orientation. The dark areas in tube layers might point to a lower degree of organisation. The radial cross section of *M. oculata* sample 459-M1-E showed a series of layers which were shared between tube and corallite with the exception of the innermost partial tube layer which only covered the tube (fig. 9.3).

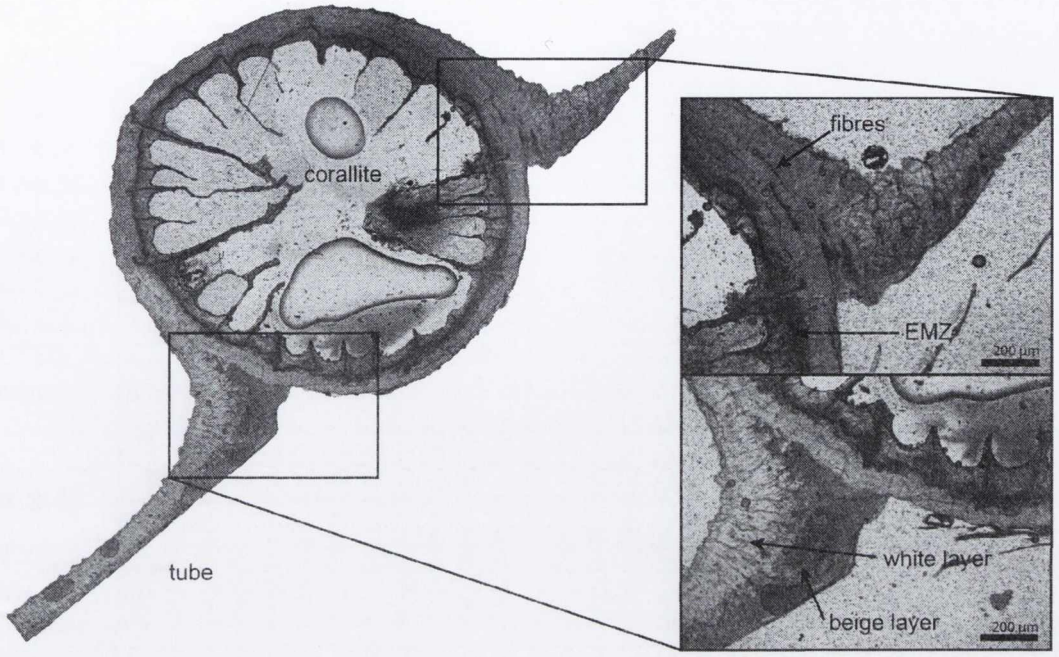


Figure 9.2: The thin section of sample 1447-E showed the contact between theca and tube calcification. The sample presented an early stage of tube precipitation with layers only covering parts of the tube. A) The initial layers showed a clear continuation onto the corallite layers. B) The tube precipitates showed an ordered structure in beige layers.

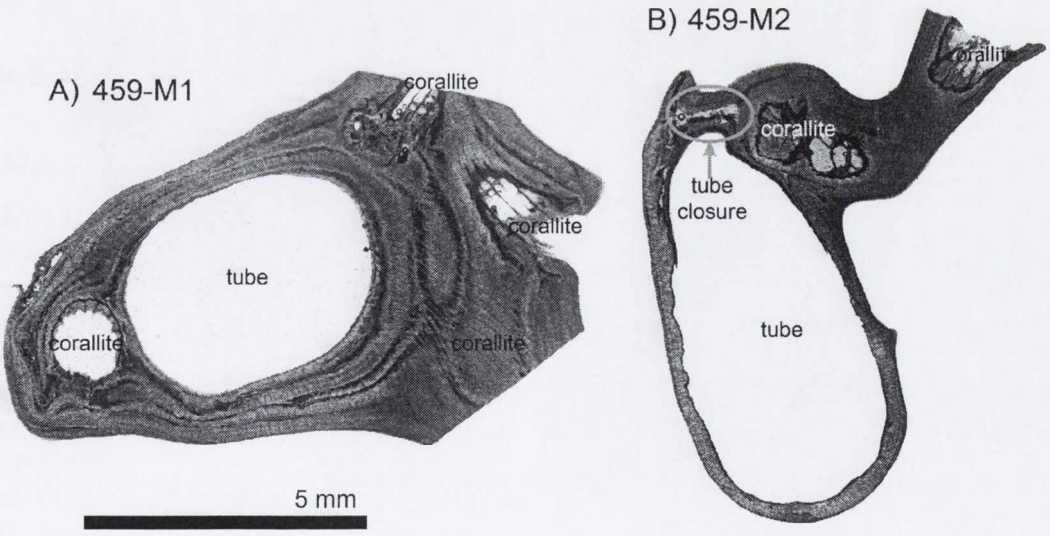


Figure 9.3: A) Thin section of sample 459-M2-E covers the area of a cross section close to the analysed one. The layering and fibre organisation along the tube was clearly visible. B) Thin section of sample 459-M1-E with connections between theca and tube thickening with organised fibres and alternating white and beige layers in both parts. Both showed a network of thin dark lines running across the corallite layers.

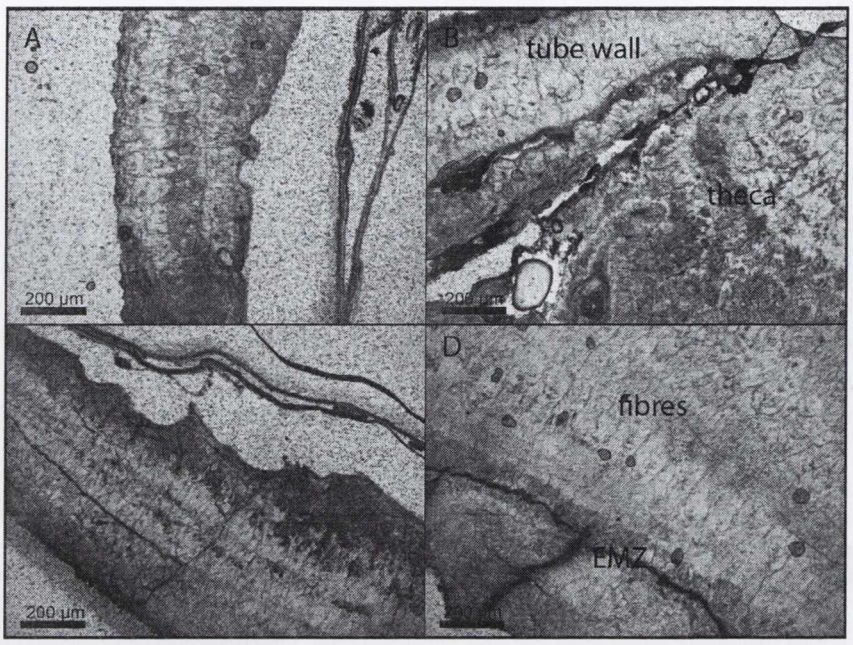


Figure 9.4: Thin section through sample 1036-E. Parts of the thin section were compromised during polishing, therefore, no mosaic was available. A+C) Tube precipitation showed white and beige layering and ordered fibrous structures visible in beige layers. B) Layering in corallite theca and tube at contact. D) Corallite calcification with EMZ and fibres.

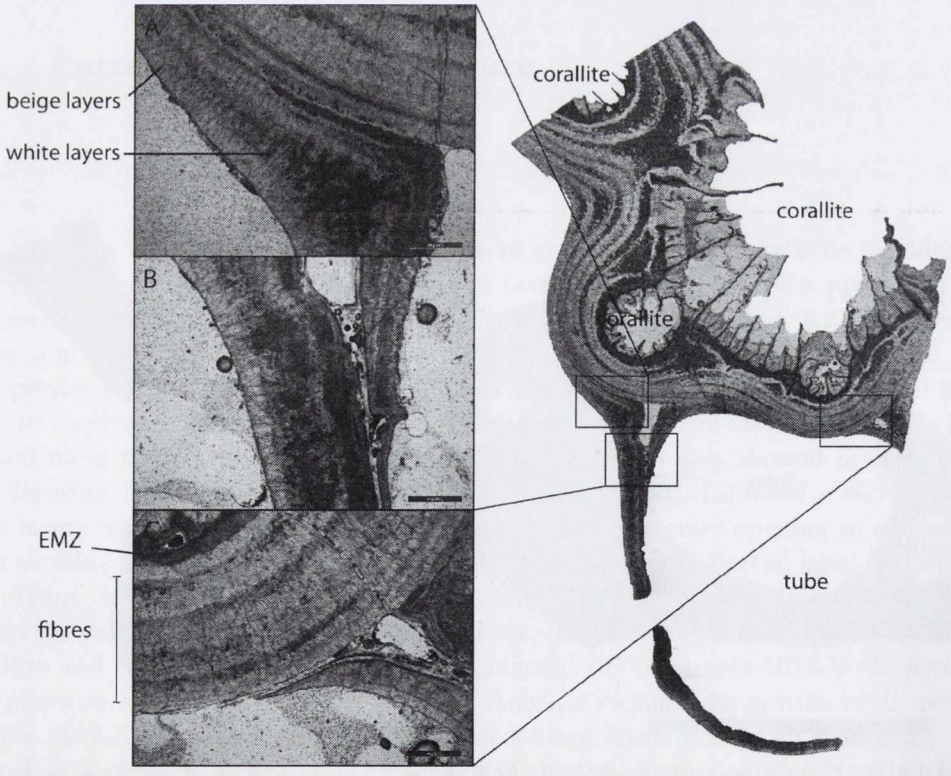


Figure 9.5: The thin section of 1587-E showed clear layering along theca and tube layering. A+C) show the contact between theca and tube with independent layers on the tube inside and continuing layers stretching from theca to the tube layers (A) including alternating white and beige layers. B) Tube layering.

9.2 Patterns in Geochemistry

The main range of absolute elemental compositions was quite similar in all samples. ^{25}Mg concentrations were found in the same range with the exception of *M. oculata* (1009) from Porcupine Bank which showed a lower average. While most samples revealed comparable ^{137}Ba contents, *L. pertusa* sample 1587-E from the Whittard Canyon displayed a lower relative range in variations. The same was true for ^{238}U in this sample. ^{238}U and ^{25}Mg were generally inversely correlated in all analysed cases and the patterns in ^{238}U displayed the clearer outlines. Therefore, the variations will be discussed based on patterns in ^{238}U compositions. ^{238}U variations were compared to ^{137}Ba and ^{11}B concentrations and stable oxygen and carbon isotope ratios in selected cases where they were available.

9.2.1 Stable Isotope Ratios in Connection with *E. norvegica* Tubes

The lower resolution of stable isotope analysis in samples 459-M1-E and 459-M2-E generally showed a positive correlation between high $\delta^{18}O$ and $\delta^{13}C$ and high ^{238}U bands (fig. 9.6 and 9.7). Sample 459-M1-E revealed a thin layer of high trace and minor element compositions along the inner tube wall during early tube calcification which were accompanied by relatively high $\delta^{18}O$ and $\delta^{13}C$ over the width of the first microdrill line. A possible contamination by epoxy resin cannot be excluded. The variations within the corallite wall were found associated with the pattern in the bands of elemental concentration as far as detectable despite the difference in resolution. Stable isotope variations in 459-M1-E showed strong differences in variation between the two analysed walls of the corallite. The wall in contact with the tube started with high values followed by a slight decrease and increase and showed a pronounced central part with low stable isotope ratios. The outer wall returned to high stable isotope ratios. Stable isotope ratios in the tube wall displayed the same range of stable isotope ratios and did not indicate additional fractionation effects.

9.2.2 Pattern in Trace and Minor Element Compositions in Calcified *Eunice norvegica* Tubes

Madrepora oculata

459-M1-E - Whittard Canyon The *Eunice* tube found with *M. oculata* sample 459-M1-E from the Whittard Canyon was analysed along a stretch of the tube and around the contact between the neighbouring corallite and the tube (tables 9.2, 9.3 and fig. 9.6, 9.8). SNRs are very high for Ca, Mg, Ba, Sr and U, below 100 fro B (less reliable but well beyond background) and too low for Cd (details in Appendix D.4). The bands of variations in ^{238}U concentrations were associated with layers in microstructure (fig. 9.3). The tube itself was surrounded by two growth layers of comparable thickness which directly overlay the originally organic tube. On the outside of these layers another four, considerably thinner layers with higher ^{238}U content revealed a discordant contact to the two underlying layers. Closer to the corallite ^{238}U concentrations were generally lower. The tube area in direct contact with the corallite also showed the two thicker layers of lower ^{238}U concentration which surrounded the tube. These were overlain by a sequence of seven thinner layers of higher ^{238}U concentration with discordant contact to the thick layers and which curved outwards towards the opening of the corallite suggesting these originated directly from the corallite.

^{11}B appeared positively correlated with ^{238}U. ^{137}Ba showed no consistent correlation with ^{238}U. Only along the innermost tube layers the bands of varying ^{137}Ba concentration seemed to be correlated with microstructural layers and also with ^{238}U. Outermost precipitations showed a less organised and more patchy appearance in the ^{137}Ba distribution.

Table 9.2: Elemental concentrations NIST612 standard during 459-M1-E analysis; averages and standard deviation of the mean in ppm and as RSD (%). The accuracy is given relative to accepted values.

	Average	SD (2σ) of the Mean	RSD (%)	Accuracy	n
^{11}B	34.32 ppm	0.73 ppm	3.01%	0.02 ppm (0%)	11 lines
^{25}Mg	68.39 ppm	1.98 ppm	2.89%	0.39 ppm (0.01%)	25 lines
^{88}Sr	78.42 ppm	0.48 ppm	0.62%	0.02 ppm (0.01%)	25 lines
^{111}Cd	28.09 ppm	0.21 ppm	0.74%	0.01 (0%)	6 lines
^{137}Ba	39.30 ppm	0.20 ppm	0.50%	0 ppm	25 lines
^{238}U	37.36 ppm	0.29 ppm	0.77%	0.02 ppm (0 %)	25 lines

Table 9.3: Elemental concentrations in *M. oculata* sample 459-M1-E and along the calcified polychaete tube; averages and standard deviation of the mean in ppm and as RSD (%).

	Average	SD (2σ) of the Mean	RSD (%)	n
^{11}B	101.26 ppm	32.99 ppm	32.58%	14 lines
^{25}Mg	1991.43 ppm	1629.52 ppm	81.83%	70 lines
^{88}Sr	7320.91 ppm	72.02 ppm	0.98%	70 lines
^{111}Cd	0.01 ppm	0.55 ppm	7800.00%	24 lines
^{137}Ba	25.14 ppm	23.37 ppm	92.96%	70 lines
^{238}U	3.42 ppm	0.30 ppm	8.88%	70 lines

459-M2-E - Whittard Canyon The tube sampled from *M. oculata* branch 459-M2-E from the Whittard Canyon in direct contact with two corallites in the cross section (tables 9.4, 9.5 and fig. 9.7, 9.9). During the analytical session Mg was the only element well beyond background levels, Ba and U were still sufficiently high, while SNRs for Li, Ca, and Sr were too low (details in Appendix D.4). The lower corallite shared its outermost layer with the tube without any visible interruption or shift in elemental composition or visible microlayers. The tube closure in contact with the upper corallite revealed no connection to the corallite layer. All layers in the corallite wall ran more or less parallel to the tube wall but appeared to have been precipitated before tube calcification started. None of the bands in ^{238}U concentrations suggested a direct connection between tube and corallite calcification. The tube closure showed a pronounced gap in calcification between the two visible layers. The tube closure displayed one inner layer which seemed to originate from the earlier event. The gap between both layers led to suspect the existence of an organic layer here. The internal layer was thickened by a second layer which showed a thin connection to the rim of the upper corallite on trace element maps suggesting an origin in this corallite without apparent link to the immediate corallite wall layers (fig. 9.3). The existence of the tube here apparently did not stimulate this corallite at the time of corallite formation.

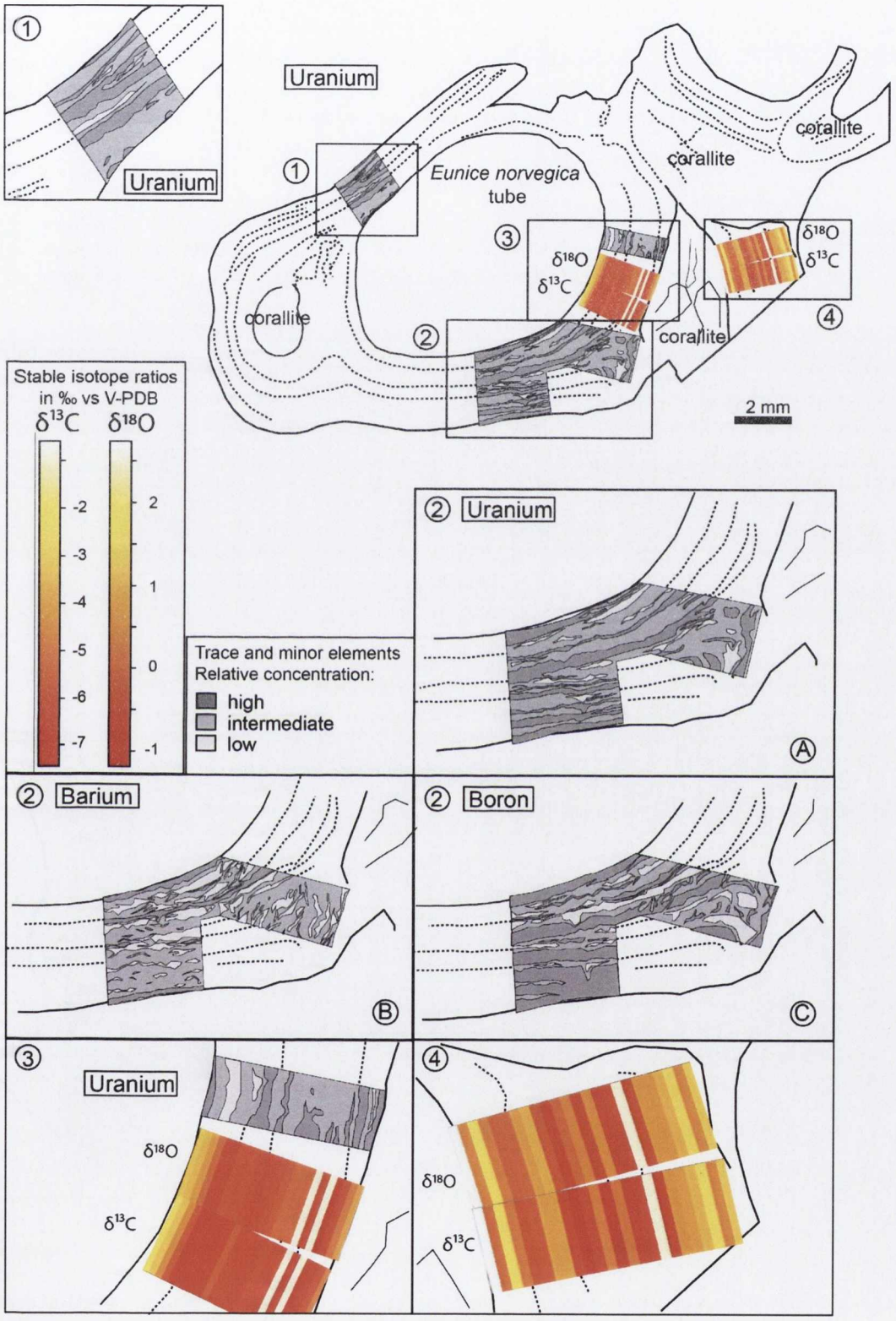


Figure 9.6: Complex microstructural layers and variations in elemental concentrations along the tube contact in *M. oculata* sample 459-M1-E. Stable oxygen and carbon isotope ratios across the wall were positively correlated and were displayed in heat colours. The tube represented a later stage in calcification. Thickening of the tube seemed to originate from different sources.

Table 9.4: Elemental concentrations of NIST612 standard during 459-M2-E analysis; averages and standard deviation of the mean in ppm and as RSD (%). The accuracy is given in relation to accepted values. Outlier rejection was applied to values beyond 2 SD.

	Average	SD (2σ) of the Mean	RSD (%)	Accuracy	n
^{7}Li	40.1 ppm	±4.1 ppm	10.0%	±0.10 ppm (0.25%)	7 lines
^{25}Mg	68.4 ppm	±3.8 ppm	5.6%	±0.40 ppm (0.01%)	7 lines
^{88}Sr	78.5 ppm	±1.3 ppm	1.7%	±0.10 ppm (0%)	6 lines
^{137}Ba	39.4 ppm	±1.6 ppm	4.0%	±0 ppm (0 %)	7 lines
^{238}U	37.4 ppm	±2.6 ppm	7.0%	±0.02 ppm (0 %)	7 lines

Table 9.5: Elemental concentrations in *M. oculata* and along the calcified polychaete tube (459-M2-E); averages and standard deviation of the mean in ppm and as RSD (%). Outlier rejection of 2 SD was applied.

	Average	SD (2σ) of the Mean	RSD (%)	n
^{7}Li	1.30 ppm	±3.70 ppm	280%	42 lines
^{25}Mg	3000.00 ppm	±9200.00 ppm	300%	43 lines
^{88}Sr	8280.00 ppm	±610.00 ppm	7%	43 lines
^{137}Ba	18.00 ppm	±32.00 ppm	180%	42 lines
^{238}U	3.08 ppm	±0.98 ppm	32%	44 lines

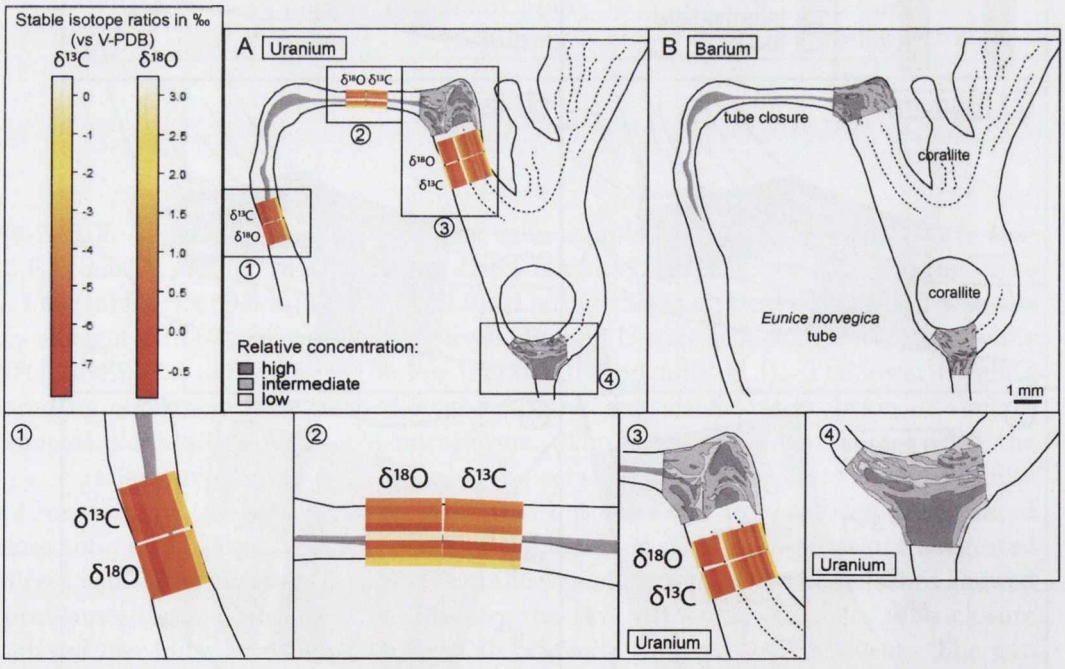


Figure 9.7: Microstructural layers and variations in elemental concentrations along the tube contact in *M. oculata* sample 459-M2-E. The investigated area of the tube represented an earlier stage in calcification including the tube closure.

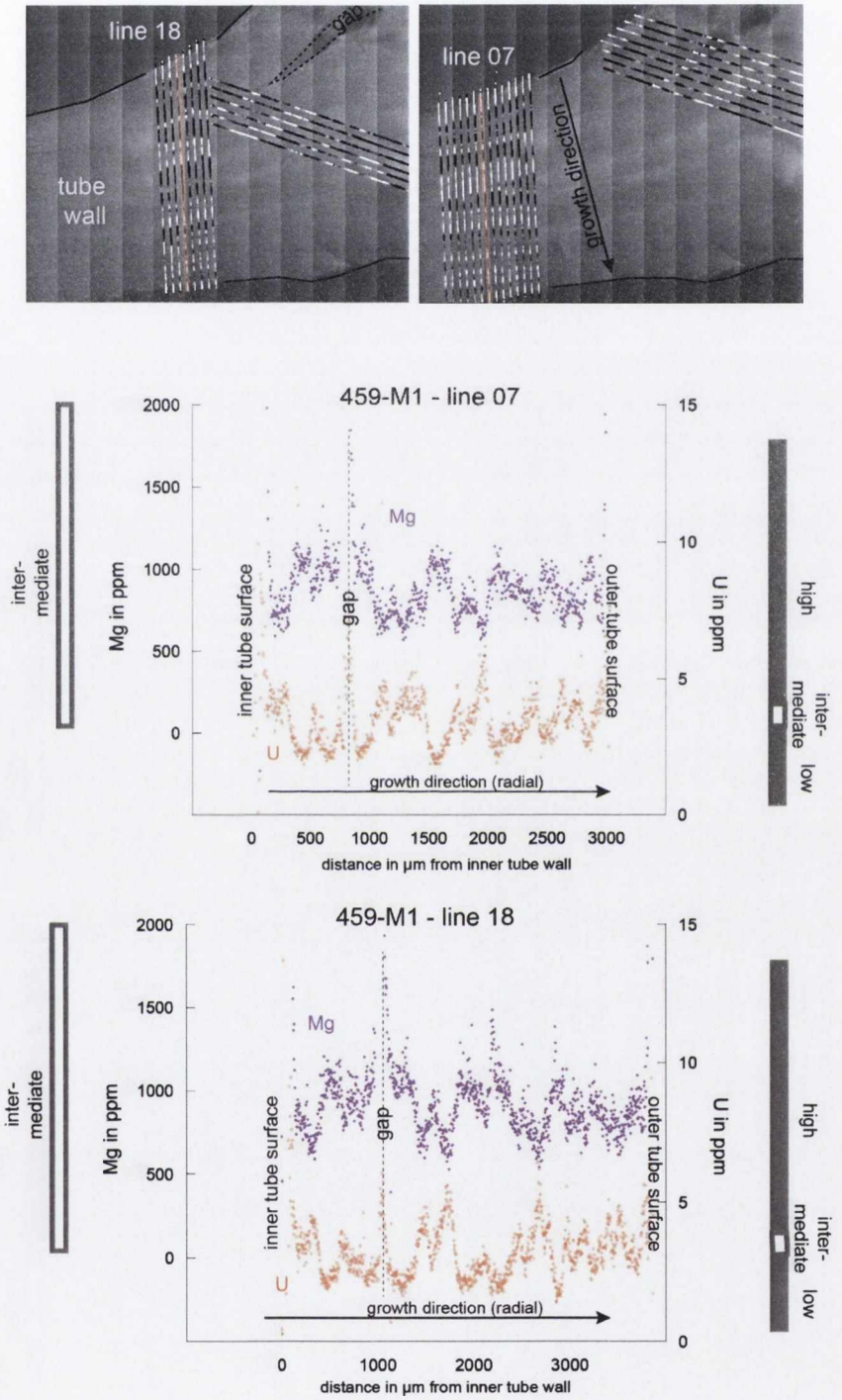


Figure 9.8: The cross section of *M. oculata* sample 459-M1-E consists of 36 laser ablation lines covering a series of tube layers close to the corallite contact (here U concentrations). Lines 07 and 18 show the variations in Mg and U in association with microstructural layers including an apparent gap in calcification in line 18. The y-axes give absolute values while bars show relative variations (95% confidence level).

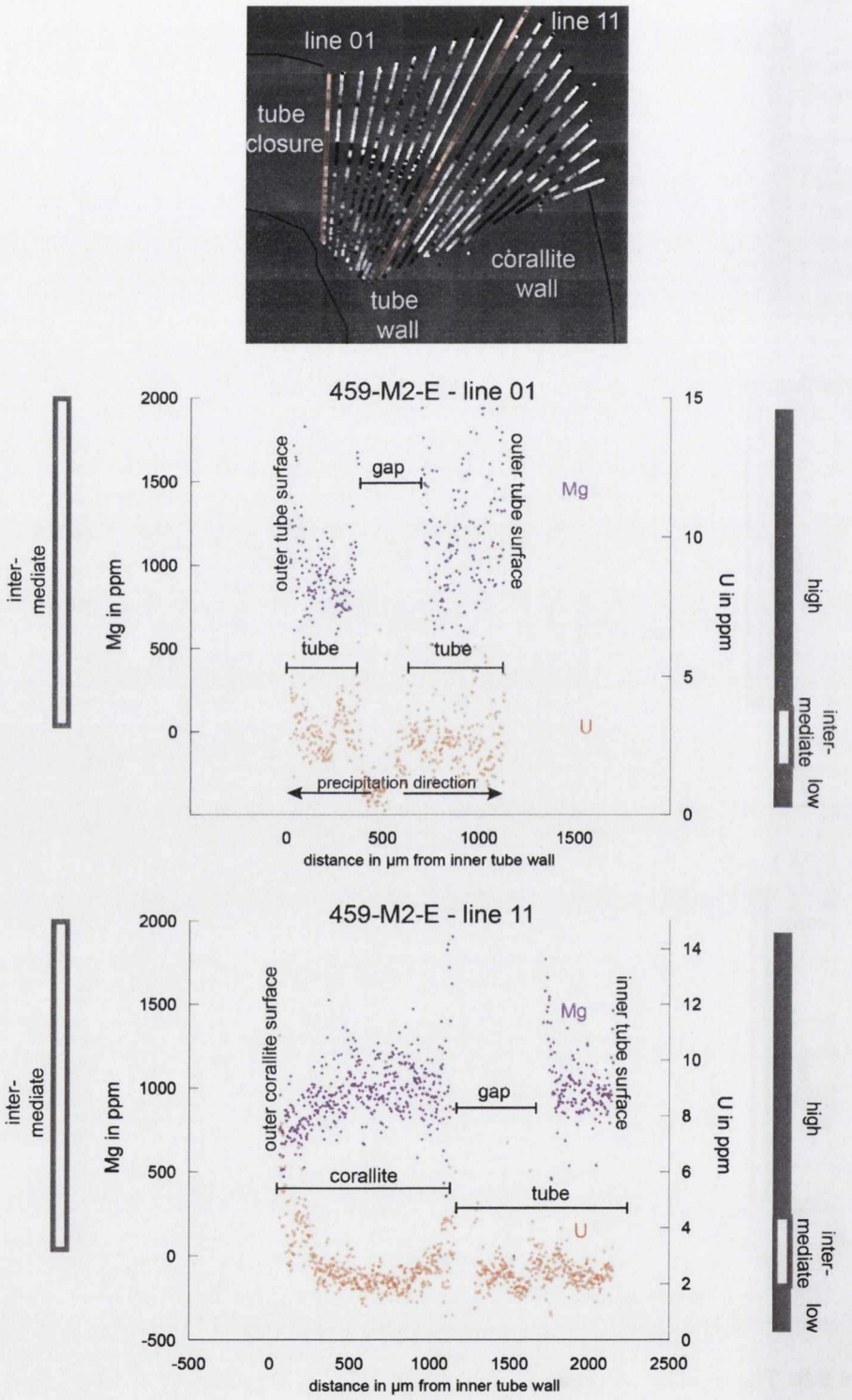


Figure 9.9: The cross section of *M. oculata* sample 459-M2-E was analysed in 21 laser ablation transects covering the contact between the double-layered tube closure and the top part of the neighbouring corallite ((here U concentrations). Line 01 gives insight into the tube closure layers while line 11 reaches from inner tube over a gap to the corallite layers.

1009 - Porcupine Bank The *M. oculata* sample 1009-E from the Porcupine Bank showed contacts between the tube and several neighbouring corallites (tables 9.6, 9.7 and fig. 9.10, 9.11). All SNRs except for Li were high. Li measurements have to be used with care (details on SNRs in Appendix D.4). Through the tube wall from inside to outside there were three narrow inner layers bordered by one central layer of low ^{238}U and continued by five varying, mostly more massive high ^{238}U layers. Apparently all layers originated from the corallite on the upper right (fig. 9.10). The tube wall away from contact with the corallites showed interruptions in growth and segmentation. The segments showed a connection to one or several neighbouring corallites. The segment on the lower left displayed a discordant contact between the inner and outer layers as well as tapering off of the outer layers and supported a model where different phases of precipitation occurred during independent events. The inner layers here could not be connected to one of the corallites directly. Here the inner layers contained low ^{238}U values, the central layers showed high ^{238}U bands. Four to five thin bands of decreasing ^{238}U content were followed by a thick band with low ^{238}U concentration. For sample 1009-E no thin section was available.

Table 9.6: Elemental concentrations of NIST612 standard during analysis of sample 1009-E; averages and standard deviation of the mean in ppm and as RSD (%). The accuracy is given in relation to accepted values.

	Average	SD (2σ) of the Mean	RSD (%)	Accuracy	n
^{7}Li	40.22 ppm	±0.53 ppm	1.32%	±0.02 ppm (0%)	18 lines
^{25}Mg	70.71 ppm	±5.17 ppm	7.31%	±2.71 ppm (3.99%)	18 lines
^{88}Sr	87.03 ppm	±7.32 ppm	9.03%	±8.63 ppm (11.01%)	18 lines
^{137}Ba	39.26 ppm	±0.52 ppm	1.32%	±0.04 ppm (0.10%)	18 lines
^{238}U	37.40 ppm	±0.76 ppm	2.04%	±0.02 ppm (0 %)	18 lines

Table 9.7: Elemental concentrations in *M. oculata* sample 1009-E and along the calcified polychaete tube; averages and standard deviation of the mean in ppm and as RSD (%).

	Average	SD (2σ) of the Mean	RSD (%)	n
^{7}Li	1.13 ppm	±1.47 ppm	130.73%	83 lines
^{25}Mg	839.82 ppm	±492.63 ppm	58.66%	83 lines
^{88}Sr	8238.82 ppm	±348.29 ppm	4.23%	83 lines
^{137}Ba	11.53 ppm	±5.42 ppm	46.98%	83 lines
^{238}U	3.36 ppm	±0.57 ppm	16.88%	83 lines

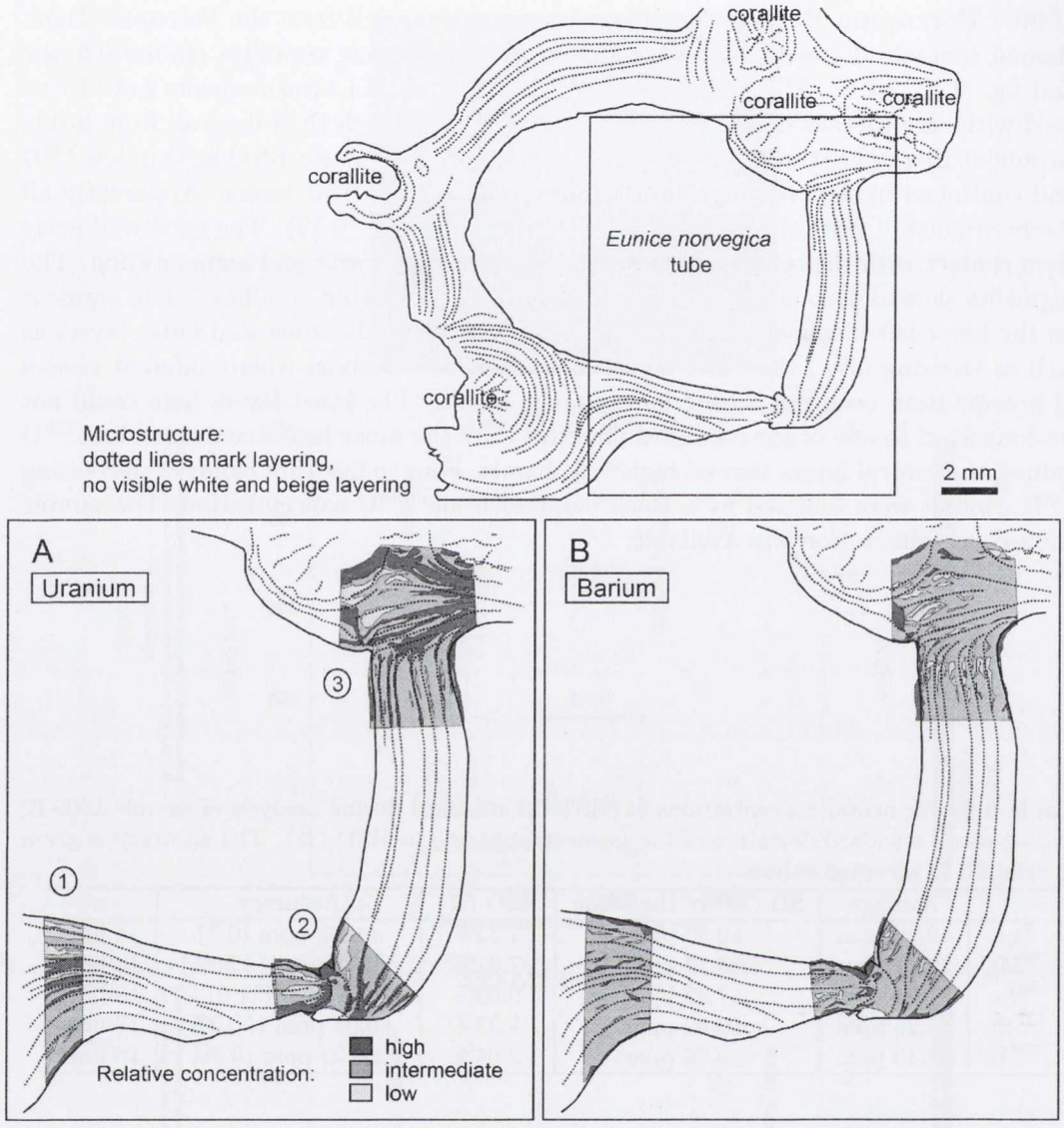


Figure 9.10: Microstructural layers and variations in elemental concentrations along the tube contact in *M. oculata* sample 1009-E. No distinct layer was surrounding the tube fully which suggested that branches existed before the tube calcification took place. Lower right tube calcification might originate from corallites on top right and lower left. The tube thickening showed a later stage with extensive layering. The discordance in layers of area A suggested two consecutive calcification events with several intervals each. Area 2 showed the union of two independently developed tube wall segments. The structure could have originated from partial tissue cover by different polyps. The contact at 3 showed the continuation of corallite layers in tube layers.

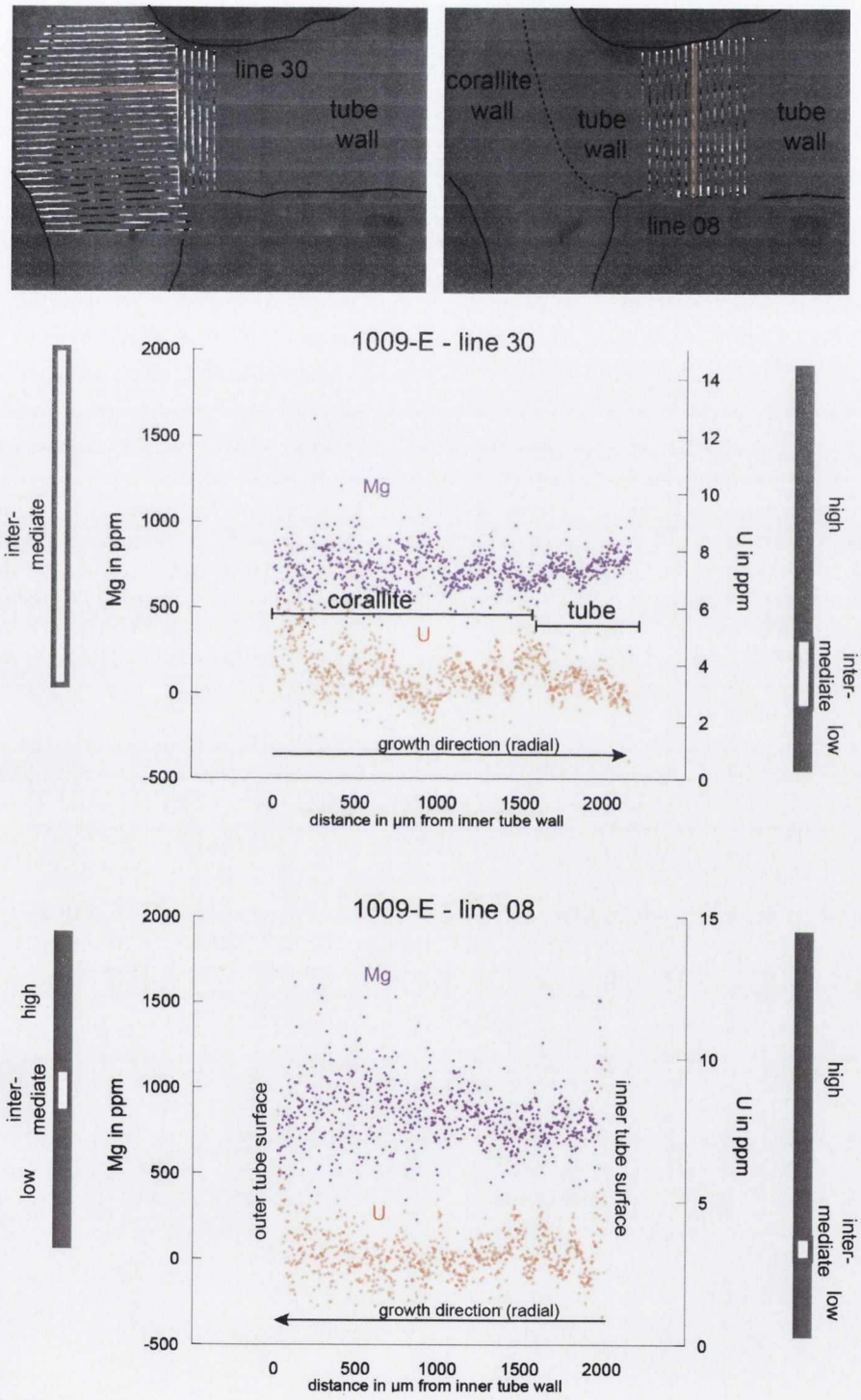


Figure 9.11: A set of 48 lines covers the cross section of *M. oculata* sample 1009-E (here U concentrations). Line 08 displays the microstructure associated variations in Mg and U. Line 30 stretches from corallite layers onto the bending tube layers. The y-axes give absolute values while bars show relative variations (95% confidence level). The banding was best pronounced within the inner tube layers. Corallite-associated layers showed a higher dispersal of concentrations and least pronounced banding in transect line 30.

Lophelia pertusa

1033-E - Porcupine Bank The thick walled *L. pertusa* corallite in sample 1033-E from the Porcupine Bank also showed a thick layer covering the tube (tables 9.8, 9.9 and fig. 9.12, 9.13). The experiment produced good SNRs for all elements except for Li (for details see Appendix D.4). The corallite displayed six relatively regular high-^{238}U bands alternating with high-^{25}Mg ones. The white layers correlated with low ^{238}U were thin and decreased in thickness towards the outer wall. Only the outermost two beige high-^{238}U layers continued onto the tube wall and covered a thick layer with lower ^{238}U concentrations which seemed to originate from the corallite wall. For sample 1033-E no thin section was available as not enough sample material was available.

Table 9.8: Elemental concentrations NIST612 standard during analysis of sample 1033-E; averages and standard deviation of the mean in ppm and as RSD (%). The accuracy is given in relation to accepted values.

	Average	SD (2σ) of the Mean	RSD (%)	Accuracy	n
^{7}Li	40.10 ppm	±0.70 ppm	1.8%	±0.10 ppm (0.02%)	8 lines
^{25}Mg	74.00 ppm	±19.00 ppm	26.0%	±6.00 ppm (8.82%)	8 lines
^{88}Sr	78.40 ppm	±4.50 ppm	5.7%	±0 ppm (0%)	8 lines
^{137}Ba	38.70 ppm	±3.00 ppm	7.6%	±1.32 ppm (3.36%)	8 lines
^{238}U	37.30 ppm	±1.20 ppm	3.2%	±0.08 ppm (0.21%)	8 lines

Table 9.9: Elemental concentrations in *L. pertusa* sample 1033-E and along the calcified polychaete tube; averages and standard deviation of the mean in ppm and as RSD (%).

	Average	SD (2σ) of the Mean	RSD (%)	n
^{7}Li	0.80 ppm	±1.20 ppm	150%	37 lines
^{25}Mg	930.00 ppm	±420.00 ppm	45%	37 lines
^{88}Sr	7680.00 ppm	±320.00 ppm	4%	37 lines
^{137}Ba	10.40 ppm	±3.10 ppm	29%	37 lines
^{238}U	3.06 ppm	±0.53 ppm	17%	37 lines

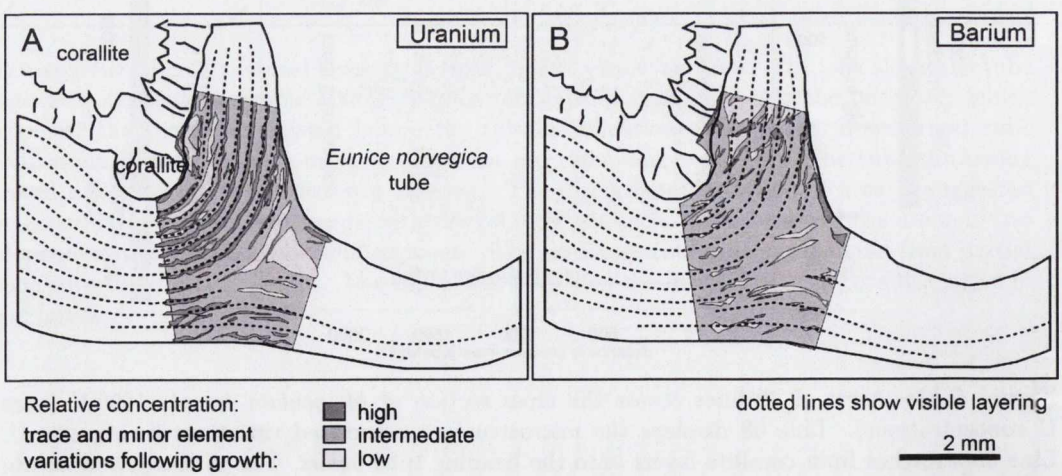


Figure 9.12: Microstructural layers and variations in elemental concentrations along the tube contact in *L. pertusa* sample 1033-E. The initial layer of tube mineralisation appeared more massive compared to others.

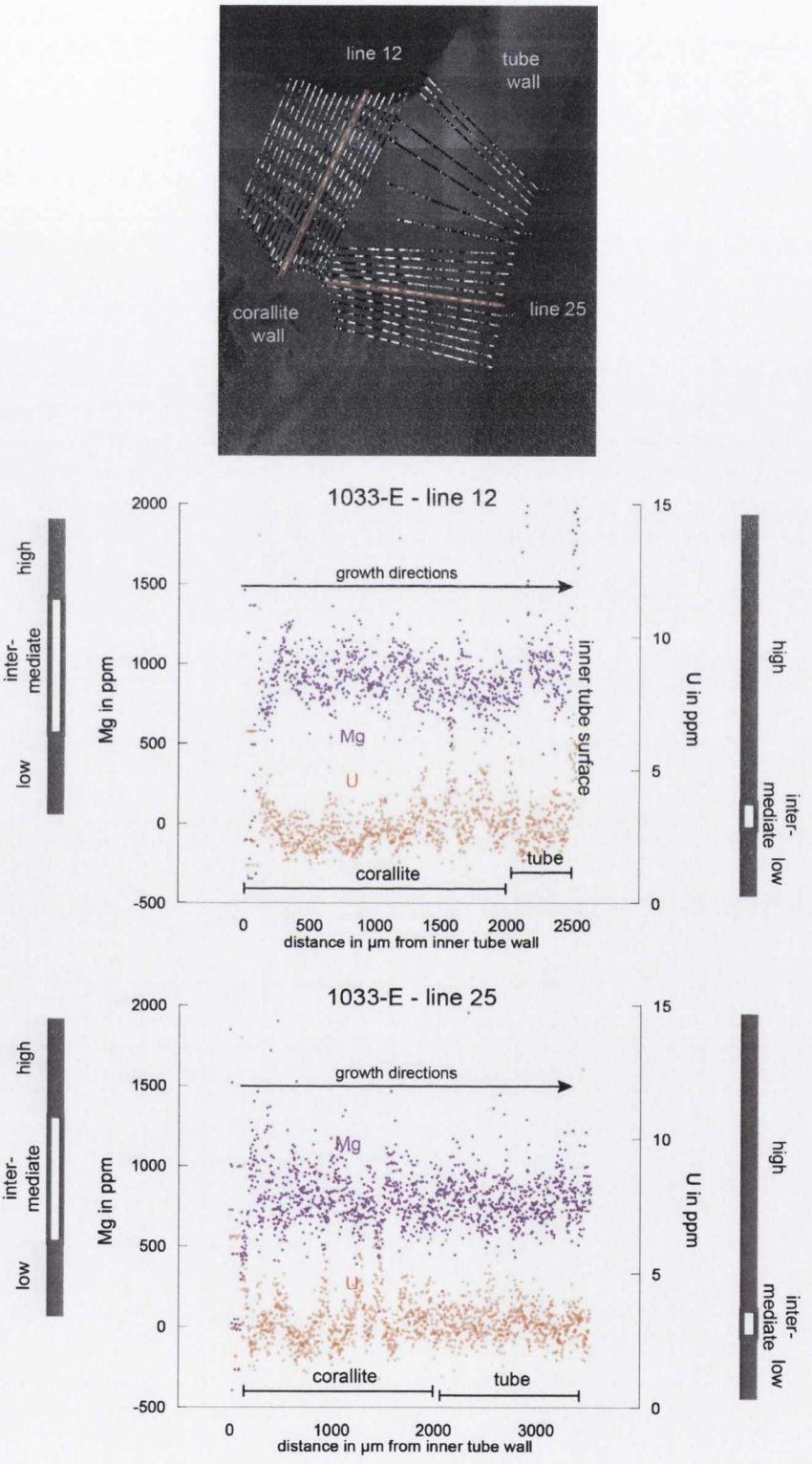


Figure 9.13: All 37 laser ablation lines were placed around the contact between corallite layers and tube layers in *L. pertusa* sample 1033-E (here showing U concentrations). The selected transects of line 12 and 25 present Mg and U variations of this contact on the inside and outside of the tube. The y-axes give absolute values while bars show relative variations (95% confidence level).

1036-E - Porcupine Bank Sample 1036-E originated from a *L. pertusa* colony collected from the Porcupine Bank canyon (tables 9.10, 9.11 and fig. 9.14, 9.15). With regards to SNRs all measurements except for Li were reliable (details in Appendix D.4). A cross section diagonally through the tube at the contact with the corallite gave insight into the contact. The visible layers within the tube wall were mostly white with dominantly low ^{238}U contents and these making up the corallite wall showed a strongly pronounced white center part with low ^{238}U concentration surrounded by a well-developed beige layer (possible double layer with high ^{238}U concentrations). Towards the inner corallite ^{238}U variations also retraced complex patterns in septa calcification. The white tube layers attached directly to the beige corallite layer. The tube itself displayed two low ^{238}U bands of increasing thickness along the contact. The layers covering the tube seemed to be originating from the corallite and suggested a stepwise calcification process (fig. 9.4). First layers only ran along the direct contact and displayed lower ^{238}U contents. With progressing calcification ^{238}U concentrations increased and layers stretched further.

Table 9.10: Elemental concentrations of NIST612 standard during analysis of sample 1036-E; averages and standard deviation of the mean in ppm and as RSD (%). The accuracy is given in relation to accepted values.

	Average	SD (2σ) of the Mean	RSD (%)	Accuracy	n
^{7}Li	40.20 ppm	±0.32 ppm	0.79%	±0 ppm	7 lines
^{25}Mg	71.00 ppm	±13.00 ppm	18.00%	±3.00 ppm (4.41%)	7 lines
^{88}Sr	80.00 ppm	±11.00 ppm	14.00%	±1.60 ppm (2.04%)	7 lines
^{137}Ba	39.30 ppm	±0.56 ppm	1.40%	±0 ppm	7 lines
^{238}U	37.40 ppm	±0.90 ppm	2.40%	±0.02 ppm (0%)	7 lines

Table 9.11: Elemental concentrations in *L. pertusa* sample 1036-E and along the calcified polychaete tube; averages and standard deviation of the mean in ppm and as RSD (%).

	Average	SD (2σ) of the Mean	RSD (%)	n
^{7}Li	0.80 ppm	±0.15 ppm	18.0%	20 lines
^{25}Mg	830.00 ppm	±310.00 ppm	37.0%	20 lines
^{88}Sr	7860.00 ppm	±190.00 ppm	2.4%	20 lines
^{137}Ba	11.40 ppm	±1.80 ppm	16.0%	20 lines
^{238}U	3.34 ppm	±0.32 ppm	9.6%	20 lines

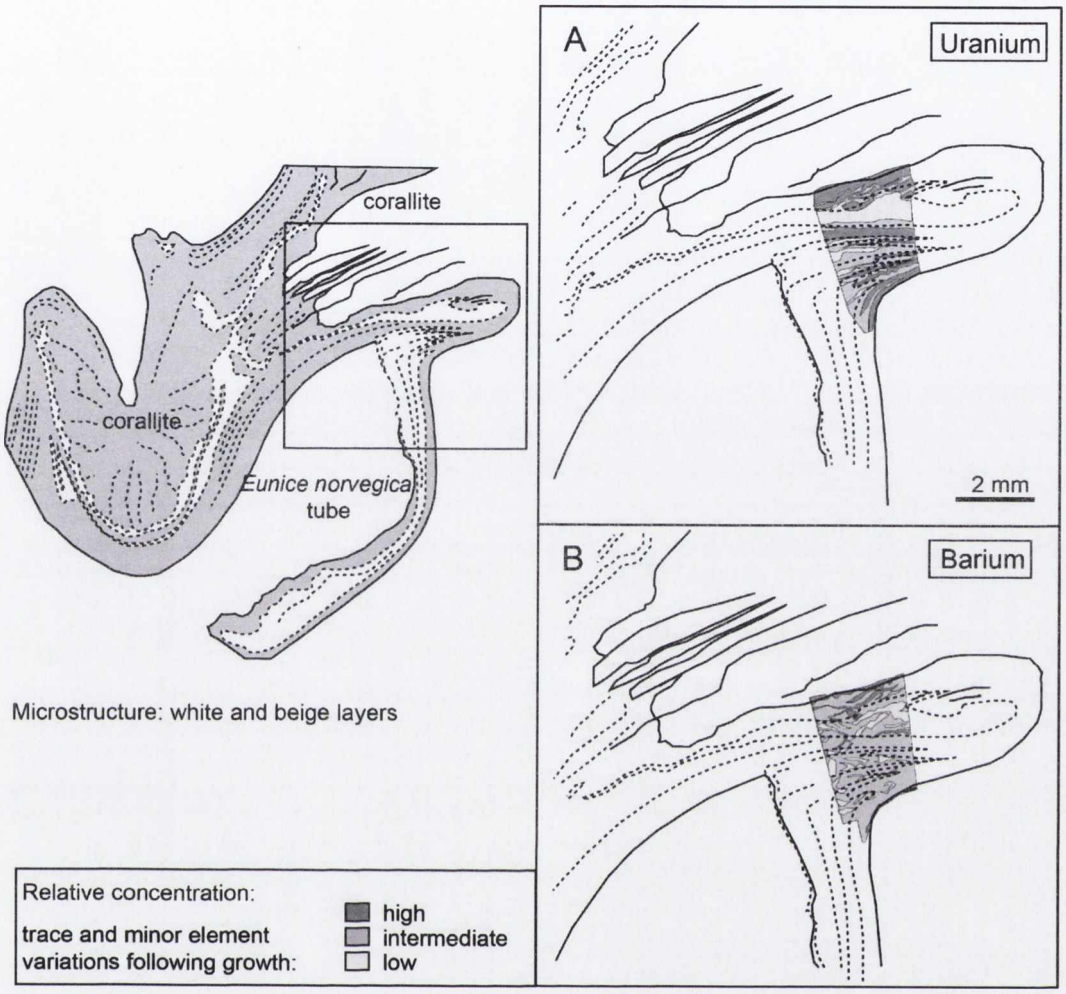


Figure 9.14: Microstructural layers and variations in elemental concentrations along the tube contact in *L. pertusa* sample 1036-E. The upper corallite was cut longitudially, while the attached tube showed a diagonal cross section. The tube displayed indications of a stepwise tube mineralisation process.

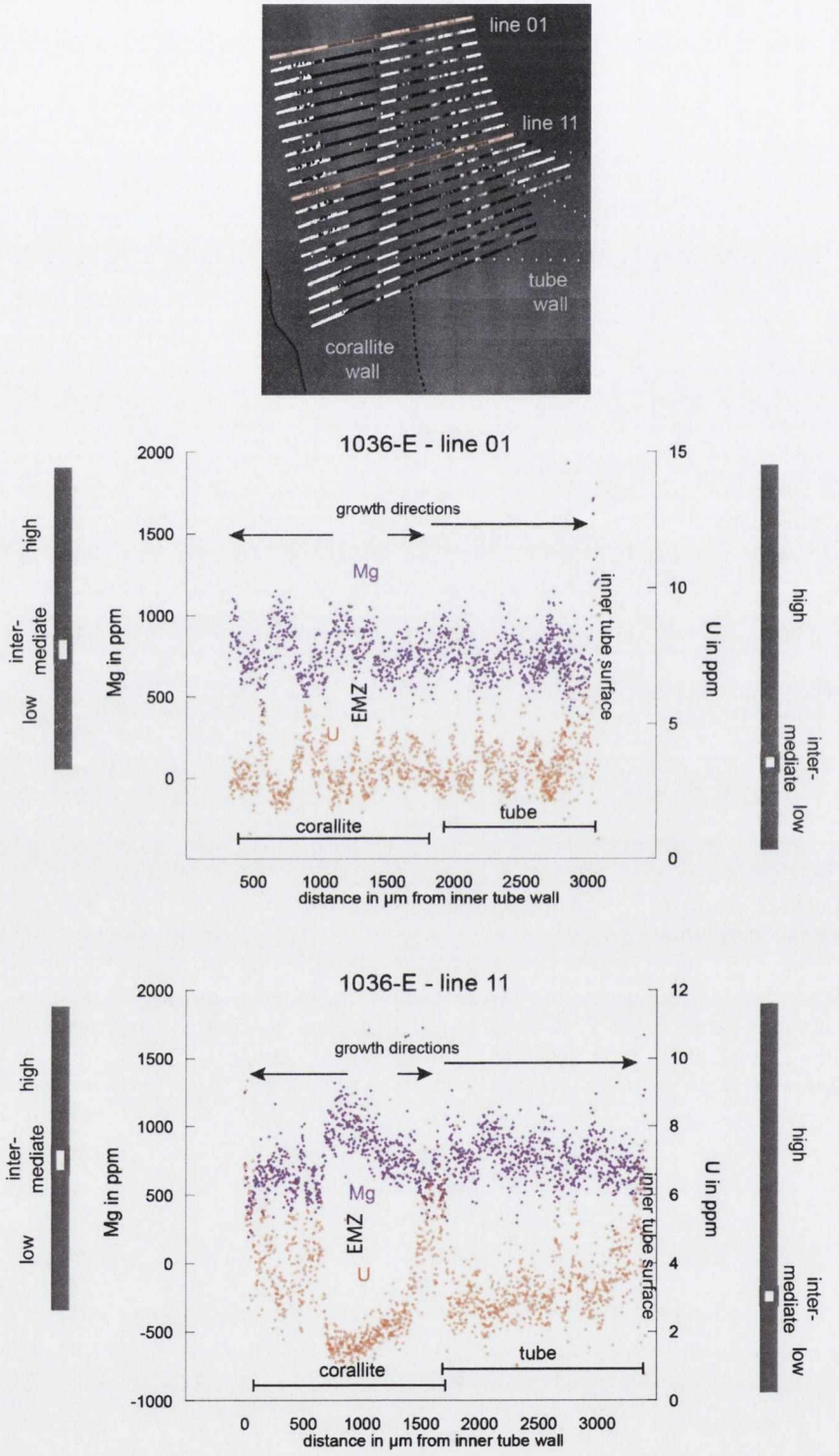


Figure 9.15: Absolute and relative variations in ^{25}Mg and ^{238}U in *L. pertusa* sample 1036-E follow from a transect through the longitudinal cross section of the corallite to the tube layers. Ablation line positioning and U concentrations shown on top.

1447-E - Whittard Canyon Sample 1447-E from the Whittard Canyon represented an early stage of the calcification process. The tube here was cut longitudinally (fig. 9.2). The innermost layer was more massive, the outer one thinner and unfinished. Calcifications covered the outside of the tube on top of the organic prototype. The corallite itself was built up of one to two layers of low ^{238}U accompanied by higher ^{25}Mg which was connected to EMZ and septa growth (typical during early growth stages) (tables 9.12, 9.13 and fig. 9.16, 9.17). While SNRs for B measurements were lower (below 100) compared to the other elements, B measurements were still more reliable than Li (in other experiments) (compare Appendix D.4).

Table 9.12: Measured elemental concentrations of NIST612 standard during analysis of sample 1447-E; averages and standard deviation of the mean in ppm and as RSD (%). The accuracy is given in relation to accepted values. Outlier rejection beyond 2 SD is applied.

	Average	SD (2σ) of the Mean	RSD (%)	Accuracy	n
^{11}B	34.31 ppm	±0.75 ppm	2.20%	±0.01 ppm (0%)	8 lines
^{25}Mg	67.94 ppm	±0.33 ppm	0.48%	±0.06 ppm (0.01%)	7 lines
^{137}Ba	39.37 ppm	±0.26 ppm	0.66%	±0.07 ppm (0.18%)	7 lines
^{238}U	37.47 ppm	±0.31 ppm	0.83%	±0.09 ppm (0.24%)	7 lines

Table 9.13: Elemental concentrations in *L. pertusa* sample 1447-E and along the calcified polychaete tube; averages and standard deviation of the mean in ppm and as RSD (%). Values beyond 2 SD were rejected as outliers.

	Average	SD (2σ) of the Mean	RSD (%)	n
^{11}B	84.00 ppm	±22.00 ppm	26%	39 lines
^{25}Mg	960.00 ppm	±300.00 ppm	32%	38 lines
^{137}Ba	11.30 ppm	±6.80 ppm	60%	38 lines
^{238}U	3.00 ppm	±0.72 ppm	24%	36 lines

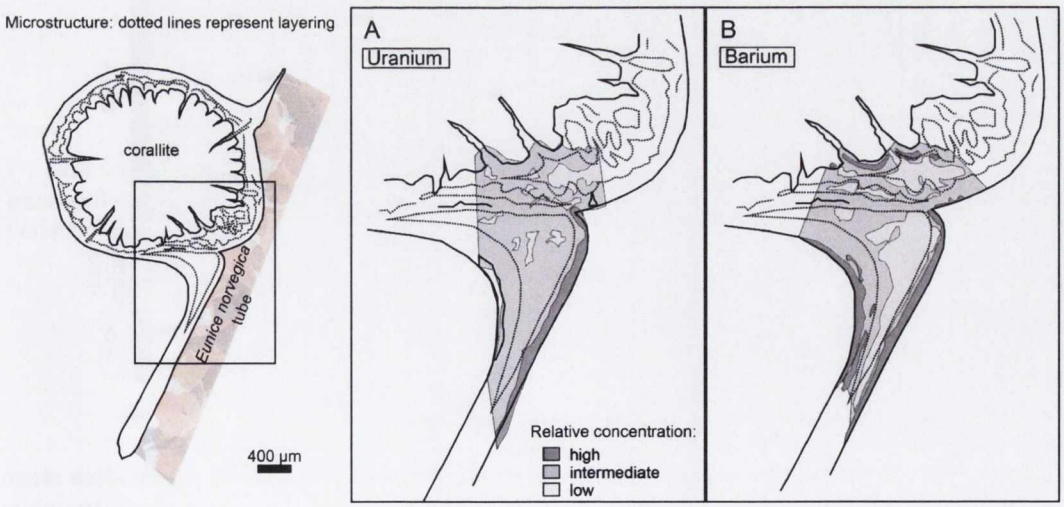


Figure 9.16: Microstructural layers and variations in elemental concentrations along the tube contact in *L. pertusa* sample 1447-E. The corallite was cut radially, the tube longitudinally. The sample represented an early stage in biomineralisation.

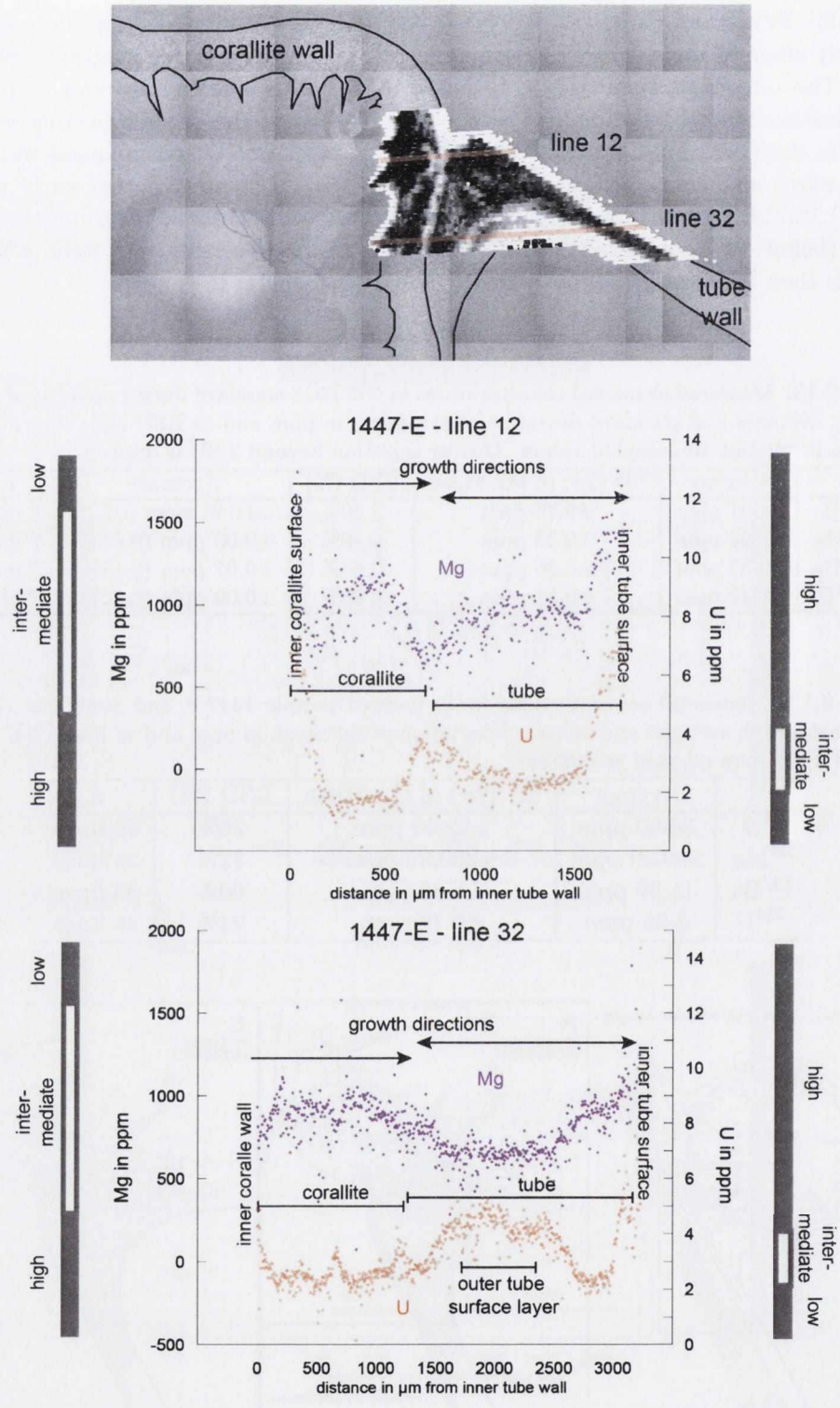


Figure 9.17: A set of 40 laser ablation lines cover the contact of an initial calcification stage (here U concentrations). Line 12 crosses through the inner part of the tube precipitates while line 32 is a cross section including the outermost tube layers. The y-axes give absolute values while bars show relative variations (95% confidence level).

1587-E - Whittard Canyon Sample 1587-E was collected from the Whittard Canyon (tables 9.14, 9.15 and fig. 9.18, 9.19). The measurements provided high SNRs for Ca, Mg, Ba, U, and sufficiently high for B (details listed in Appendix D.4). The cross section revealed four closely growing corallites which shared a set of white layers with low ^{238}U in the outermost layers (fig. 9.5). The outermost layers along the corallites were shared with the tube. The tube appeared to have experienced two phases of layer precipitation. A small fragment on the inside of the tube pointed to partial initial calcification of the tube.

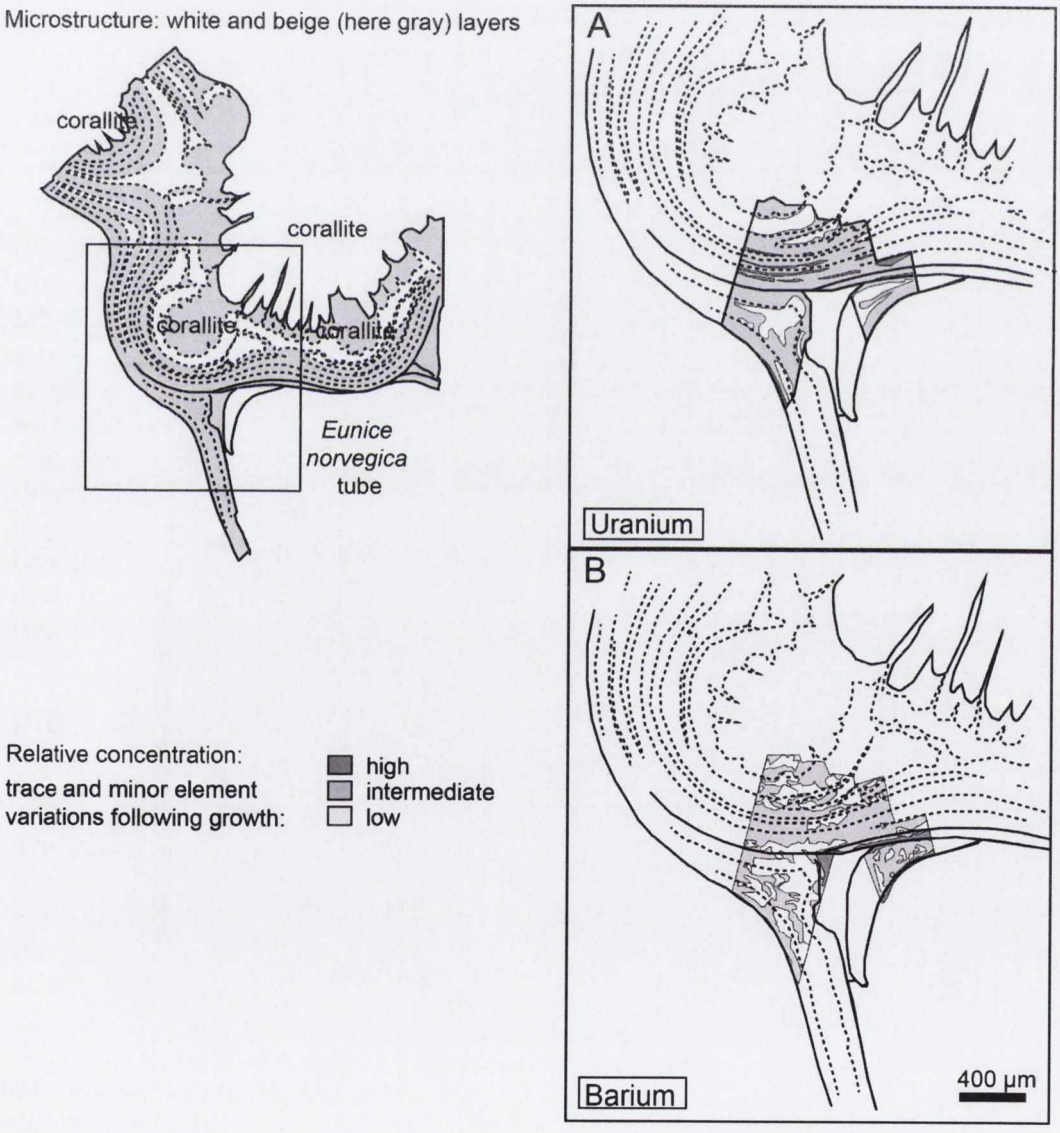


Figure 9.18: Microstructural layers and variations in elemental concentrations along the tube contact in *L. pertusa* sample 1587-E. The tube mineralisation in this case appeared to still be at an earlier stage.

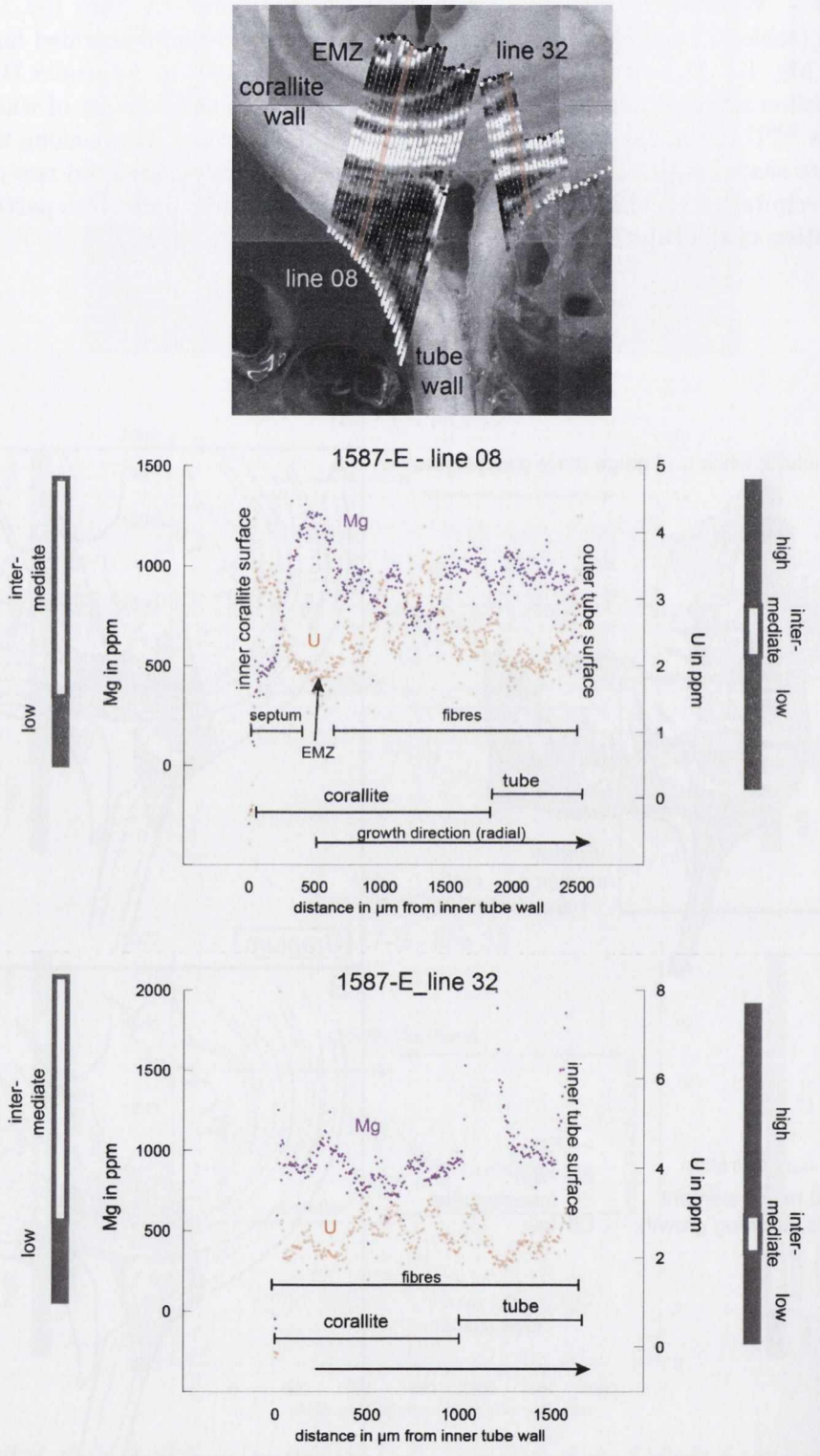


Figure 9.19: Sample 1587-E (*L. pertusa*) gives insight into well-developed corallite layers and the neighbouring tube precipitates (here U concentrations). Line 08 includes the main tube layers stretching directly from the corallite onto the tube. Line 32 includes a partial interior layer of the tube typically found in corners inside of the tube. The y-axes give absolute values while bars show relative variations (95% confidence level).

Table 9.14: Elemental concentrations NIST612 standard during analysis of sample 1587-E; averages and standard deviation of the mean in ppm and as RSD (%). The accuracy is given in relation to accepted values. Outlier rejection beyond 2 SD was applied.

	Average	SD (2σ) of the Mean	RSD %	Accuracy	n
^{11}B	32.60 ppm	±9.10 ppm	25.00%	±1.70 ppm (4.96%)	7 lines
^{25}Mg	68.20 ppm	±1.30 ppm	1.90%	±0.20 ppm (0.29%)	7 lines
^{137}Ba	39.30 ppm	±0.10 ppm	0.25%	±0 ppm (0%)	7 lines
^{238}U	37.80 ppm	±3.10 ppm	8.20%	±0.42 ppm (1.12%)	7 lines

Table 9.15: Elemental concentrations in *L. pertusa* sample 1587-E and along the calcified polychaete tube; averages and standard deviation of the mean in ppm and as RSD (%). Values beyond 2 SD were rejected as outliers.

	Average	SD (2σ) of the Mean	RSD (%)	n
^{11}B	86.00 ppm	±13.00 ppm	15%	38 lines
^{25}Mg	1250.00 ppm	±940.00 ppm	75%	37 lines
^{137}Ba	9.70 ppm	±3.70 ppm	39%	39 lines
^{238}U	2.48 ppm	±0.35 ppm	14%	39 lines

Generally the ^{137}Ba contents were higher along the borders of the layers. In 459-M1-E high ^{137}Ba contents were observed in the center of some layers positively correlated with high ^{25}Mg content bands which were only found in thicker layers. While 459-M2-E showed high ^{137}Ba in 'chaotic' areas around the corallite whose shape suggested a relation to septa growth, and while 1009-E showed no defined bands of high ^{137}Ba at all, in *L. pertusa* sample 1036-E high ^{137}Ba was found in areas of septa growth with bands tracing curved potential growth layers. In 1033-E a band of high ^{137}Ba contents showed along the outer rim of the corallite layers before the onset of the tube calcification. While in sample 1587-E high ^{137}Ba contents were found in areas of pronounced high ^{25}Mg bands, earlier growth stages in sample 1447-E did not show banding but ^{137}Ba generally appeared slightly higher along tube calcification. The most pronounced increases in ^{137}Ba were found along the contact between corallite and tube.

9.3 Discussion

9.3.1 Variations in Geochemical Composition

The following discussions were based on the assumptions that stable oxygen and carbon isotope ratios increase with decreasing growth rate and should be accompanied by low Mg and high U concentrations. In sample 459-M1-E and 459-M2-E (fig. 9.6 and 9.7) the composition of the innermost tube precipitates shows high δ^{13}C and δ^{18}O values. In 459-M1-E the inner and outer tube in contact with the environment or potential calcifying medium displays high concentrations of all measured trace and minor elements. While this appears consistent with the surface entrapment model (Gabitov et al., 2008, Watson et al., 1996) the same was not found in tube layers of sample 459-M2-E. Moreover this would not necessarily apply to stable isotope ratios unless a mass effect was connected to the entrapment model which had not been reported so far. Therefore, the results do neither provide support nor rejection of a surface entrapment hypothesis but could alternatively also point to traces of contamination along the surface.

9.3.2 Patterns in Geochemical Compositions and Implications

All *Eunice* results showed a connection between tube positioning and the form of layering. The observations on different samples suggested that calcification originated from a number of continuous precipitation events with stepwise cover and thickening of the tube and simultaneous thickening the neighbouring corallites. Assuming that the tube calcification process was driven by increased mucus secretion as suggested e.g. by Mortensen (2001), intervals of increased mucus contribution seemed to occur as a colony effect in *L. pertusa* and *M. oculata* since associated layers were shared among several corallites. The observations suggested an initial increase of mucus secretion at the direct contact between *Eunice* and the corals due to the irritation caused by the polychaete (Roberts, 2005, Mortensen, 2001). Consequently the mucus spreads over the 'affected' area, covering neighbouring corallites and possibly inspiring mucus production there as well. This would cause the appearance of a 'colony event'. A similar appearance should, therefore, be seen in connection with increased nutrient flow or sediment input (Larsson & Purser, 2011). CWC and polychaete both possibly take advantage of the same events like nutritional pulses since a shared food source was confirmed before (Larsson & Purser, 2011). One hyposthesis, therefore, could suggest that *E. norvegica* settlement follows an increase in nutritional input. A nutrient flux before *E. norvegica* involvement should show phases of increased calcification setting in before the tubes were included. Our data did not support a model like this. The tubes appeared to have already been positioned before the onset of an increase in carbonate precipitation.

Since none of the inspected areas showed indications of increased corallite thickening before the calcification of the attached tubes started, it is concluded that *Eunice* tubes were positioned before the mucus secretion increased. In addition it has to be mentioned that the layers which were shared between corallite and tube did not appear particularly thicker than earlier ones. Consequently the observations supported a model where *Eunice* settles among the coral branches (without apparent environmental incentive), and contributes to the activation of calcification. Where 'corners' were filled a centre of white precipitates was found within that layer. This appeared to be an effect of variations in mineralisation (rate) in such cases.

Despite slight variations between elemental ranges among samples the characterisation of tube calcification patterns was possible. The innermost layers directly overlying the *Eunice* tube were often built up of a thicker layer with high ^{25}Mg contents (partly rimmed by thin high ^{238}U areas). This phase was than overlain by 'sheets' with alternating high and low ^{238}U composition. These translucent layers always originated from one or several corallite openings and stretch around all neighbouring corallites (e.g. 1587-E and 1009-E). With increasing length of calcification the involved subset of layers thickened corallite and tube as one.

High ^{238}U values along the contact with the epoxy or in areas of interrupted growth pointed to contaminations not directly related to calcification patterns but more likely a direct effect of surface entrapment connected to carbonate precipitation in process (as suggested by e.g. Gabitov et al., 2008). The area might point to earlier stages of mineralisation or to unrelated accumulations along the surface. The same phenomenon was detected in areas of interrupted tube calcification (e.g. in 459-M1). The observations suggested that tube calcification was not necessarily

connected to a higher precipitation rate and did not appear to show significantly different fractionation effects (compare $\delta^{18}O$ and $\delta^{13}C$ in 459-M1-E and 459-M2-E). This supported aquarium experiments where no increase in metabolic activity in *L. pertusa* in connection with polychaete activity was detected (Mueller et al., 2013).

9.3.3 Implications for Biomineralisation Models

The available thin sections of the contact between tube and corallite calcification uniformly showed that the microstructure and fibre organisation along the shared layers displayed no change and was consistently correlated with ^{238}U and ^{25}Mg variations. This led to the hypothesis that both, corallite and tube, were calcified by the same process. The same patterns in microstructure, including the thin network of dark lines across fibrous areas, built up corallites without *E. norvegica* settlement in *L. pertusa* and *M. oculata*. These structures suggested that fibrous layers which encalcified the polychaete tubes and such thickening the corallite were of the same origin. It is well known from aquarium observations that the polychaete tubes are being encalcified by the mineralisation of coral mucus on the tube surface (Roberts, 2005, Mortenson, 2001). Reitner (2005) already published results pointing to mucus being the calcifying medium for corallite growth but so far models of coral calcification neglect to investigate this factor. Since the polyp epithelium in *L. pertusa* rarely extends over the growing edge of the corallite and doesn't cover larger portions of the external skeleton (Freiwald, 1998, Jensen & Frederiksen, 1992) the layering visible over the complete length of the corallites in the investigated species points to a mechanism independent of tissue cover. Freiwald (1998) reported a translucent film of mucus covering the skeleton parts which were not covered by tissue and this mucus film also being involved in the calcification process. A similar cover was described on polychaete tubes (Roberts, 2005, Mortensen, 2001). We found no differences in microstructure and geochemical patterns/composition between apparently mucus-mediated and calicoblastically controlled mineralisation which agreed with earlier studies on mineralisation (Freiwald, 1998). On the other hand, Freiwald (1998) reported a high degree of disorder in fibre bundles around the tube which was in direct contrast to our findings. All studied samples showed a comparable degree of fibre order in corallite and tube layers including the development of opaque and translucent layers.

Our findings strongly suggested mucus as the only or the main component of the calcifying medium (see fig. 9.20). A direct exchange with the ambient seawater was not excluded by this hypothesis. It can be speculated that the mucus was produced in a (semi-)closed space in contact with the ambient seawater between skeleton and soft tissue, and episodically released to cover wider parts of skeleton and tube. This would also allow for Ca-ATPase and other enzymes to influence the composition and regulate pH-/alkalinity. One possible hypothesis was that mucus is being produced by the tissue in contact with ambient seawater as the source of chemical components and at a starting pH. This, however, would then also imply changes in pH and alkalinity during the course of calcification in connection with changes in ^{238}U and ^{25}Mg during calcification i.e. a decrease of pH in the mucus with increasing mineralisation interval. The proposed replenishing of the reservoir with biologically driven increased pH values (or high alkalinities) would then simply be attributed to a new phase of mucus production. Generally some studies evolved around the composition of coral mucus but not in the light of the mucus acting as a calcifying medium (with the exception of Reitner, 2005).

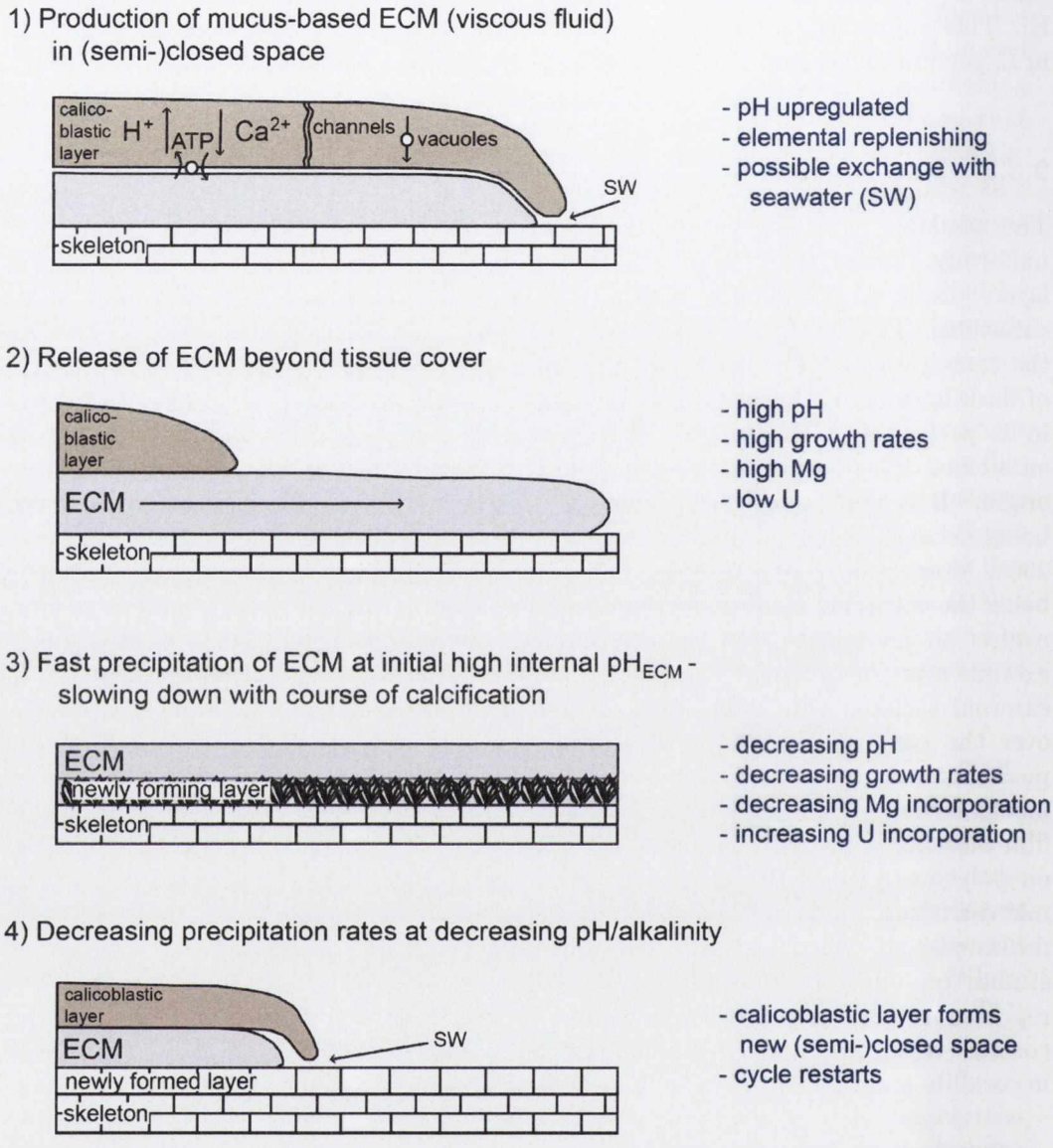


Figure 9.20: The presented adaption to existing models suggests a 4-step process of corallite layer calcification with mucus-like ectoplasmatic calcifying medium (ECM) production in a (semi-)closed space, release and stepwise mineralisation of the ECM (based on published models by Rollion-Bard et al., 2010, Adkins et al., 2003, McConnaughey et al., 1997, McConnaughey, 1989a, 1989b). Alternatively mineralisation might already start before the mucus is released. Step 4 is followed by the arrival of a new patch of mucus arriving.

One weakness of the proposed model (fig. 9.20) is the fact that the corals showed distinct surface features on the skeleton. In the case of *M. oculata* and *E. rostrata* these are ridges which wind around the calices and along the branch (fig. 9.21). For *L. pertusa*, *D. dianthus* and *S. variabilis* the surface structures comprise no ridges, only knobs. The pattern appeared quite regular and controlled but in the case of ridges could as well be connected to a flow pattern. Only in the case of *E. rostrata* a form of apparent tissue cover was found covering most of the skeleton (best seen on the backside where corallites are missing). However, many of the branching corals

including *L. pertusa*, *M. oculata* and *S. variabilis* display thickening and attachment structures which correlate with a mucus model (fig. 9.22, 9.23). Our detailed studies mainly focused on *L. pertusa* and *M. oculata* and further investigations will be necessary to see if there are different mechanisms in play for different species.

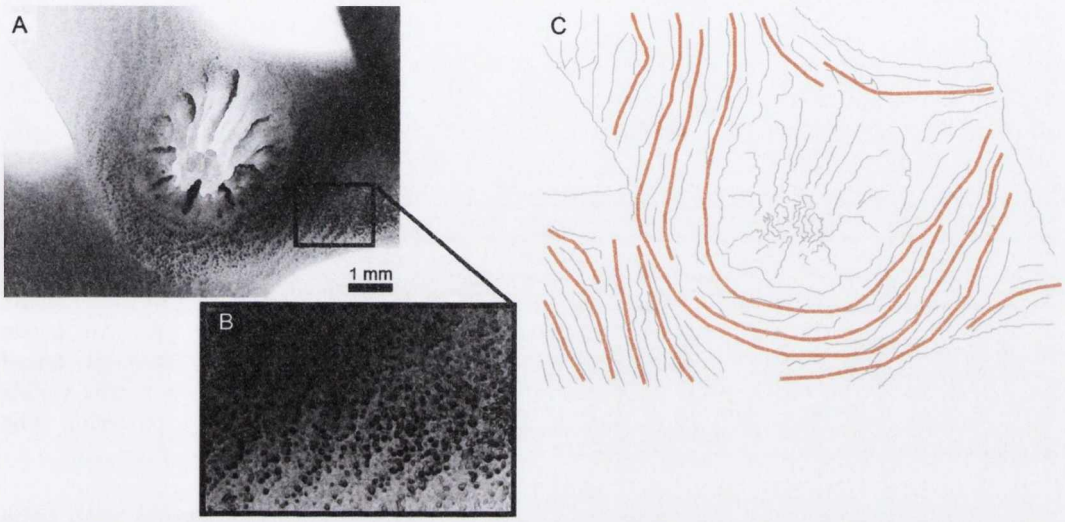


Figure 9.21: The surface of all *M. oculata* samples displayed distinct ridges across the granulated surface (A+B). The ridges surrounded the corallite opening and wound around to one side (to the back).

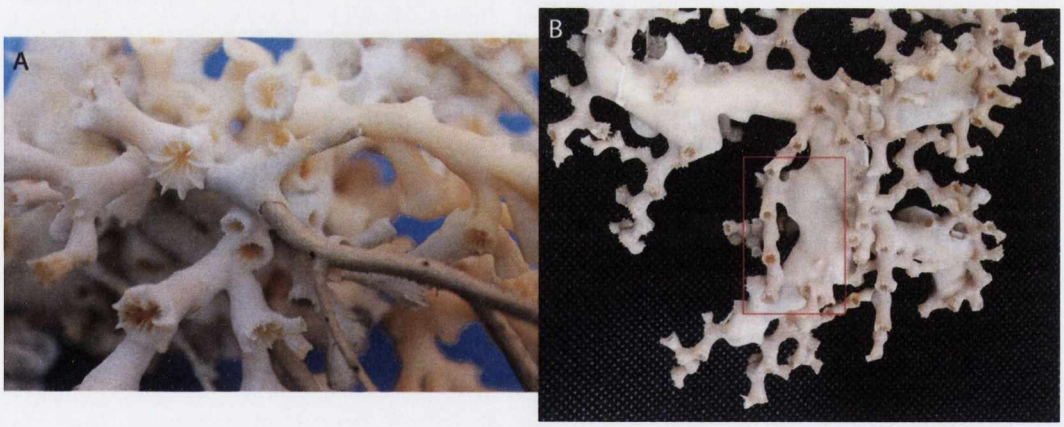


Figure 9.22: A) A branch of an octocoral was encalcified by *L. pertusa* over a distance away from the branch suggesting a mechanisms other than tissue cover. B) The connection between *M. oculata* branches and polychaete tubes without direct contact appeared to support mucus involvement (red box).

The existence and origin of thin 'lines' across the fibrous layers (see e.g. fig. 8.2) is still to be investigated but might be connected to some form of organic rests or nucleation sites during fibre mineralisation (Stolarski, 2003). On the other hand, a number of observations would be explained by the suggested model, such as the commonly observed variation in layer thickness (especially along *L. pertusa*), the reported latitudinal variations in stable isotope ratios in *L. pertusa* (Smith et al., 2002), and the ability of the corals to easily encrust small settling organisms like foraminifera or worm tubes. The lower viscosity of such a mucus layers would be able

to allow some degree of deformation being shaped by external factors without major disruptions in precipitation and could encrust settling organisms without disruption by possible defense mechanisms.



Figure 9.23: Partially and fully closed tube openings show the different stages of tube closure (from A to C) together with surface ridges. A) presents an unclosed tube with thin layers bending into the tube over its rim. All patterns are consistent with the ridges commonly found on the surface of all investigated *M. oculata* samples. In C) a change in colour was visible between earlier corallite calcifications and the lighter, apparently shared layers covering tube and several corallites.

Live observations of a higher level of corallite thickening in connection with tube presence where made in most investigated areas. Future research should be focused on the mechanisms involved in mucus secretion and mineralisation, especially with focus on pH and alkalinity changes in the mucus over the course of mineralisation. Understanding these processes would allow for more precise environmental reconstructions.

Part IV

Summary and Conclusion

The live observations during the research cruises on Porcupine Bank and in the Whittard Canyon show that the scleractinians are found within a wide range of environmental parameters. *L. pertusa* and *M. oculata* are generally found in depths above 1,300 m from which depth on *S. variabilis* and *E. rostrata* take over as the main reef builders. *D. dianthus* appears to be less restricted in depth and is found in assemblages with all of the other species. Compared to published temperature, salinity and density ranges it appears that *L. pertusa* might actually be able to survive conditions below the defined ranges in the NE Atlantic. Peaks in fluorescence appear to play a major role in scleractinian occurrences in deep sea environments.

Except for *E. rostrata* the other investigated species are found on the canyon floor and ridges as well as on vertical walls. Vertical walls appear to be mostly inhabited by *L. pertusa*, *M. oculata* and *D. dianthus* which might, however, be mostly due to the lower depth of the occurrence of such habitats. *E. rostrata* is only observed on the canyon floor with indications of single small colonies growing on deep sea ridges.

The polychaete *Eunice norvegica* is very common among *L. pertusa*, *M. oculata* and *S. variabilis* and is apparently not restricted to a specific depth. The tubes are found among scleractinian colonies along vertical walls as well as on the canyon floor or on ridges. Especially *S. variabilis* seems to react to the symbiont with extensively thickened branches which often appear 'swollen'.

The species *L. pertusa* and *M. oculata* show a number of similarities in geochemistry and microstructure. Trace and minor element compositions (^{238}U, ^{25}Mg, ^{137}Ba) for both species lie within similar ranges, ^{238}U and ^{25}Mg are generally inversely correlated in all samples and changes in concentrations are associated with microstructures. In all cases high ^{25}Mg values are found along EMZs. In thin sections both species reveal fine lines cutting across the fibrous layers. The same can be seen in layers which cover *E. norvegica* tubes. Early tube layers often show lower ^{238}U concentrations than later precipitations which thicken the tubes. Corallites and tubes display shared layers (visible in microstructure and geochemistry) in all species with origins traceable to different corallites. The layers are shared between different corallites as well as between tubes and corallites. The tube calcifications show additional precipitates especially during phases of initial calcification. In both species layers bend out from the calyx cavity. We find differences in the two scleractinian species mostly where consecutive corallites are involved. *L. pertusa* shows layers specific to individual corallites more clearly than *M. oculata*. The former covers its wall by a sequence of layers which progressively lengthen the corallite and curve towards the cavity at the top. Here only outermost layers (rich in ^{238}U) appear to continue onto the following corallite. In the case of *M. oculata* it is possible to detect stepwise lengthening only on the direct corallite wall where the calyx opening lies. Most of the thickening appears to be rather connected to a colony effect i.e. as a possible simultaneous mucus exudation from all/most polyps along a branch. Sample 1009 from the Porcupine Bank shows strongly pronounced repetition of layer sequences for consecutive corallites in the branch. Microstructures and especially geochemical patterns (in this case) show clear similarities along linear branch growth.

The biggest difference, however, can be seen in the majority of conventional light stable isotope ratios (δ^{13}C and δ^{18}O). While *L. pertusa* and *D. dianthus* are known to

show an increase in stable carbon and oxygen isotopic ratios with increasing age (towards the outer wall), *M. oculata* displays a general trend from high to low ratios. The only exceptions are low stable isotope ratios along the EMZ in all species. Therefore, while *L. pertusa* and *D. dianthus* interpreted to show a decrease in growth rate with increasing age reflected in reduced fractionation effects with time, *M. oculata* appears to start with a low growth rate and low fractionation effects and increases both with age. The latter might in some cases show a return to low growth rates in the longer term. The phenomenon has not been reported so far since no focus was put on the species yet.

Mortensen & Rapp (1998) interpreted thicker white layers as periods of stress. Since increased mucus excretion is discussed in connection with stress (Roberts, 2005, Mortensen, 2001, Freiwald, 1998) a mucus-related precipitation process could record deviations from 'normal' seasonality if 'normal' precipitation is not mucus-mediated.

The results suggest a modification of the calcification model where a layer of mucus is at least part of the so-called extracytoplasmic calcifying medium (ECM) or extracytoplasmic calcifying fluid (ECF). Mucus appears to be part of the calcification process with and without tissue cover. Studies on the symbiosis of *L. pertusa* and *E. norvegica* described the processes of encalcification of the polychaete tube (Roberts, 2005, Mortensen, 2001). The process includes stress-induced mucus secretion by the coral induced by the placement of the organic tube of the polychaete. Tissue cover is not necessarily a prerequisite here; the studies only report tissue involvement so far as to the positioning of the organic tube underneath the coenosarc (Mortensen, 2001). Reitner (2005) suggested the participation of mucus in corallite precipitation in the form of a layer between the tissue and the precipitated minerals. All this is in accordance with the results of the presented study. Our results indicate a possible influence of organic material on the precipitation of the fibrous layers leaving residue in the form of the thin lines crossing the layers (in accordance with the study of Stolarski, 2003). The continuation of layers from corallite to tube without any change in appearance seems to extend beyond suggested tissue cover. Differences in skeletal surface structures could point to species-specific variations in mucus viscosity.

The connection between environmental parameters and CWC biology cannot be clearly determined. From available studies so far at least the main period of gametogenesis appears to overlap with high primary production in the NE Atlantic in summer (e.g. Waller & Tyler, 2005). Spawning on the other hand might coincide with peaks in nepheloid layers along the shelf canyons around the end of winter (Khripounoff et al., 2014, Waller & Tyler, 2005). Gametogenesis is connected to a high energy demand which might be diverted from growth processes. Although spawning is probably less energy-consuming but might still have an effect on corallite growth, too. These details can possibly be connected to the episodes in growth we find in the analysed CWCs (compare Mouchi et al., 2014). Available information on the potential variations in annual energy budget suggest higher growth rate due to higher energy availability in spring.

Understanding the processes and the connections to the environments will promote predictions of CWC reactions to different changes in environments. Ocean acidification directly might be a factor but warming oceans and the implications for all areas (e.g. primary production) can have more unexplored consequences on reproductive cycles and reef health.

In summary the results here show that

(1) Live observations in upper areas of the canyons suggest density and fluorescence to be the most likely decisive factor for scleractinian occurrence. However, further investigations ask for a reevaluation of this since *L. pertusa* which seems to be most affected by limiting environmental parameters was found in greater depth beyond the published density envelop. These occurrences are all connected to the detection of strong internal currents (nepheloid layers) which probably provide an additional source of nutrition. Nutrition, therefore, might have a stronger influence on moving the range limits. In general, it appears that it is the combination of different factors rather than individual parameters alone which are decisive for the survival of corals.

(2) Environmentally the more or less constant presence of nepheloid layers might also prevent the formation of pronounced episodic bands which would provide a basis for the interpretation of nutrient proxies.

(3) *M. oculata* has potential for environmental reconstruction. Although no realistic absolute temperatures could be reconstructed following published approaches (using equations) we still find a relative correlation with temperature regimes assuming that temperatures in connection with specific currents are partly a decisive factor. A relative correlation between stable oxygen and carbon isotope ratios as well as for some Li/Mg ratios and temperature in samples from different environments is visible which suggests that $\delta^{13}C$ and $\delta^{18}O$ and Li/Mg are influenced by the same factors. The results also call for a more detailed study into combinations of environmental records (including temperature, salinity, pH) influencing growth rate and geochemistry. When considering different approaches of temperature reconstruction it appears that Li/Mg and $\delta^{13}C/\delta^{18}O$ might not only be correlated with temperature in *M. oculata*. More studies are necessary to identify decisive factors. Both approaches show a relative correlation which points to a common driver, most likely dominated by different water masses.

(4) Patterns of biomineralisation in microstructure and geochemistry are associated. This leads to the hypothesis that growth rate might execute a strong control on geochemical compositions and variations within. Generally the geochemical patterns (especially the antithetical behaviour of ^{238}U and ^{25}Mg) argue for a biologically controlled pH- and alkalinity regulation on the ECF within a (semi-)closed space. High ^{25}Mg concentrations consequently point to high growth rates at high pH and alkalinity while high ^{238}U concentrations suggest low pH or alkalinity conditions and low precipitation rates.

(5) The similarities in microstructure and geochemistry of corallite layers and tube precipitations point to a common source of calcifying medium. The layers thickening the corallite stretch onto the polychaete tube and thicken it as well without any visible interruption in microstructure or geochemistry. Considering the existing knowledge about mucus involvement in tube calcification this also suggests involvement of mucus in corallite precipitation. Since the composition and origin of the ECF (assuming carbonate precipitation takes place in a calcifying fluid as suggested by many models) are still speculative to some part, mucus might be a compositional part of the ECF if not a decisive factor. A (semi-)closed precipitation model with mucus

involvement in the calcification space is a possible hypothesis. Mucus as a carrier phase of elements or even as the boundary between external and internal environment might provide new modelling parameters. The *E. norvegica* tubes show continuous calcification layers extenting from corallites. Mucus involvement of course also points to a strong biological control and it contains a high percentage of organic components. The mucus production and mineralisation, as well as the isotopic composition of mucus and variations of it in connection with environmental parameters, has to be better understood for further discussions and to create a basis for identification of environmentally controlled patterns.

(6) From differences in patterns in ^{137}Ba concentration in branch samples 1009 and 459-M1 is seems that although the element cannot be used as an indicator of ambient ^{137}Ba variations in the area it might still hold potential to discuss local patterns in nutrient input. The formation of bands of high/low ^{137}Ba concentrations in the skeleton appears highly variable but the degree of organisation might be location-specific. It can be speculated that the clearer pronounced ^{137}Ba bands in sample 1009 are associated with more episodic nutrient input compared with the possible more or less continuous POM contribution from intermediate and benthic nepheloid layers in the Whittard Canyon.

The results of the presented thesis confirm the hypotheses that microstructure and geochemistry are indeed associated throughout growth, and that trace and minor element concentrations are therefore also associated with fractionation effect to a certain degree. The variations in uranium and magnesium could be associated to growth variations based on microstructure but barium as a nutrient proxy did hardly link with such signals. The collected data suggests that nepheloid layers might indeed have an impact on calcification patterns, especially variations in trace and minor element compositions, and that *M. oculata* branches are useful recorders of such environmental signals. The hypothesis that polychaete tube calcification is connected to higher metabolic activity which should reflect in δ^{13}C values has to be rejected at this point as no clear evidence was found to support this. The hypothesis that variations in light stable isotope ratios are associated with fractionation effects can neither be rejected nor confirmed based on the data at hand.

Part V

References

Achterberg, A.P., Moore, C.M., Henson, S.A., Steigenberger, S., Stohl, A., Eckhardt, S., Avendano, L.C., Cassidy, M., Hembury, D., Klar, J.K., Lucas, M.I., Macey, A.I., Marsay, C.M., Ryan-Keogh, T.J. (2013): Natural iron fertilization by the Eyjafjallajökull volcanic eruption, *Geophysical Research Letters* **40**: 921-926.

Addadi, L., Raz, S., Weiner, S. (2003): Taking Advantage of Disorder: Amorphous Calcium Carbonate and Its Roles in Biomineralization, *Advanced Materials* **15**(12): 959-970.

Adkins, J.F., Boyle, E.A., Curry, W.B., Lutringer, A. (2003): Stable isotopes in deep-sea corals and a new mechanism for 'vital effects', *Geochimica et Cosmochimica Acta* **67**(6): 1129-1143.

Adkins, J.F., Henderson, G.M., Wang, S.-L., O'Shea, S., Mokadem, F. (2004): Growth rates of the deep-sea scleractinia *Desmophyllum cristagalli* and *Enallopsammia rostrata*, *Earth and Planetary Science Letters* **227**: 481-490.

Allemand, D., Ferrier-Pagès, C., Furla, P., Houlbrèque, F., Puverel, S., Reynaud, S., Tambutté, E., Tambutté, S., Zoccola, D. (2004): Biomineralisation in reef-building corals: from molecular mechanisms to environmental control, *Comptes Rendus Palevol* **3**(6/7): 453-467.

Allison, N. (1996): Comparative determinations of trace and minor elements in coral aragonite by ion microprobe analysis, with preliminary results from Phuket, southern Thailand, *Geochimica et Cosmochimica Acta* **60**(18): 3457-3470.

Allison, N., Finch, A.A., EIMF (2010): δ^{11}B, Sr, Mg and B in a modern *Porites* coral: the relationship between calcification site pH and skeletal chemistry, *Geochimica et Cosmochimica Acta* **74**: 1790-1800.

Al-Horani, F.A., Al-Moghrabi, S.M., de Beer, D. (2003): Microsensor study of photosynthesis and calcification in the scleractinian coral, Galaxea fascicularis: active internal carbon cycle. *Journal of Experimental Marine Biology and Ecology* **288**: 1-15.

Althaus, F., Williams, A., Schlacher, T.A., Kloser, R.J., Green, M.A., Barker, B.A., Bax, N.J., Brodie, P., Schlacher-Hoenlinger, M.A. (2009): Impacts of bottom trawling on deep-coral ecosystems of seamounts are long-lasting, *Marine Ecology Progress Series* **397**: 279-294.

Amiel, A. J., Miller, D. S., Friedman, G. M. (1973): Incorporation of uranium in modern corals, *Sedimentology* **20**: 523-528.

Anagnostou, E., Huang, K.-F., You, C.-F., Sikes, E.L., Sherrell, R.M. (2012): Evaluation of boron isotope ratio as a pH proxy in the deep sea coral *Desmophyllum dianthus*: Evidence of physiological pH adjustment, *Earth and Planetary Science Letters* **349-350**: 251-260.

Anagnostou, E., Sherrell, R.M., Gagnon, A., LaVigne, M., Field, M.P., McDonough, W.F. (2011): Seawater nutrient and carbonate ion concentrations recorded

as P/Ca, Ba/Ca, and U/Ca in the deep-sea coral *Desmophyllum dianthus*, *Geochimica Cosmochimica Acta* **75**: 2529-2543.

Asper, V.L. (1987) Measuring the flux and sinking speed of marine snow aggregates, *Deep-Sea Research* **34**(1): 1-17.

Astraldi, M., Gasparini, G.P., Vetrano, A., Vignudelli, S. (2002): Hydrographic characteristics and interannual variability of water masses in the central Mediterranean: a sensitivity test for long-term changes in the Mediterranean Sea, *Deep-Sea Research I* **49**: 661-680.

Baker, A.R., Croot, P.L. (2010): Atmospheric and marine controls on aerosol iron solubility in seawater, *Marine Chemistry* **120**: 4-13.

Beaulieu, S.E. (2002): Accumulation and fate of phytodetritus on the sea floor, in R.N. Gibson, M. Barnes, R.J.A. Atkinson (eds): *Oceanography and Marine Biology: An Annual Review* **40**: CRC Press: 171-232.

Bell, N., Smith, J. (1999): Coral growing on North Sea oil rigs, *Nature* **402**: 601-602.

Beuck, L., Vertino, A., Stepina, E., Karolczak, M., Pfannkuche, O. (2007): Skeletal response of *Lophelia pertusa* (Scleractinia) to bioeroding sponge infestation visualised with micro-computed tomography, *Facies* **53**: 157-176.

Bigg, G.R., Rohling, E.J. (2000): An oxygen isotope data set for marine water, *Journal of Geophysical Research* **105**: 8527-8535.

Blamart, D., Rollion-Bard, C., Cuif, J.-P., Juillet-Leclerc, A., Lutringer, A., van Weering, T.C.E., Henriet, J.-P. (2005): C and O isotopes in a deep-sea coral (*Lophelia pertusa*) related to skeletal microstructure, in A. Freiwald, J.M. Roberts (eds): *Cold-water Corals and Ecosystems*, Berlin Heidelberg: Springer Verlag: 1005-1020.

Blamart, D., Rollion-Bard, C., Meibom, A., Cuif, J.-P., Juillet-Leclerc, A., Dauphin, Y. (2007): Correlation of boron isotopic composition with ultrastructure in the deep-sea coral *Lophelia pertusa*: implications for biomineralization and paleo-pH. *Geochemica Geophysics Geosystems* **9**: Q12001. doi: 12010.11029/12007GC001686.

Blain, S., Sarthou, G., Laan, P. (2008): Distribution of dissolved iron during the natural iron-fertilization experiment KEOPS (Kerguelen Plateau, Southern Ocean), *Deep-Sea Research II* **55**: 594-605.

Boerboom, C.M., Smith, J.E., Risk, M.J. (1998): Bioerosion and micritization in the deep sea coral *Desmophyllum cristagalli*, *Historical Biology* **13**: 53-60.

Boyd, P.W., Law, C.S., Wong, C.S., Nojiri, Y., Tsuda, A., Levasseur, M., Takeda, S., Rivkin, R., Harrison, P.J., Strzepek, R., Gower, J., McKay, R.M., Abraham, E., Arychuck, M., Barwell-Clarke, J., Crawford, W., Crawford, D., Hale, M., Harada, K., Johnson, K., Kiyosawa, H., Kudo, I., Marchetti, A., Miller, W., Needoba, J., Nishioka,

J., Ogawa, H., Page, J., Robert, M., Saito, H., Sastri, A., Sherry, N., Soutar, T., Sutherland, N., Taira, Y., Whitney, F., Wong, S.-K.E., Yoshimura, T. (2004): The decline and fate of an iron-induced subarctic phytoplankton bloom, *Nature* **428**: 549-553.

Braga-Henriques, A., Porteiro, F.M., Ribeiro, P.A., de Matos, V., Sampaio, Í., Ocaña, O., Santos, R.S. (2013): Diversity, distribution and spatial structure of the cold-water coral fauna of the Azores (NE Atlantic), *Biogeosciences* **10**: 4009-4036.

Brooke, S., Järnegren, J. (2013): Reproductive periodicity of the scleractinian coral *Lophelia pertusa* from the Trondheim Fjord, Norway, *Marine Biology* **160**: 139-153.

Brooke, S., Young, C.M. (2009): *In situ* measurement of survival and growth of *Lophelia pertusa* in the northern Gulf of Mexico, *Marine Ecology Progress Series* **397**: 153-161.

Bryan, W., Hill, D. (1941): Spherulites and allied structures, *Proceedings of the Royal Society Queensland* **52**: 41-53.

Buhl-Mortensen, L., Olafsdottir, S.H., Buhl-Mortensen, P., Burgos, J.M., Ragnarsson, S.A. (2014): Distribution of nine cold-water coral species (Scleractinia and Gorgonacea) in the cold temperate North Atlantic: effects of bathymetry and hydrography, *Hydrobiologia* **759**(1): 39-61.

Bythell, J.C., Wild, C. (2011): Biology and ecology of coral mucus release, *Journal of Experimental Marine Biology and Ecology* **408**: 88-93.

Cairns, SD, Kitahara, M.V. (2012): An illustrated key to the genera and subgenera of the Recent azooxanthellate Scleractinia (Cnidaria, Anthozoa), with an attached glossary, *ZooKeys* **227**: 1-47.

Carlier, A., Le Guilloux, E., Olu, K., Sarrazin, J., Mastrototaro, F., Taviani, M., Clavier, J. (2009): Trophic relationships in a deep Mediterranean cold-water coral bank (Santa Maria di Leuca, Ionian Sea), *Marine Ecology Progress Series* **397**: 125-137.

Carriquiry, J.D., Villaescusa, J.A. (2010): Coral Cd/Ca and Mn/Ca records of ENSO variability in the Gulf of California, *Climate of the Past* **6**: 401-410.

Case, D.H., Robinson, L.F., Auro, M.E., Gagnon, A.C. (2010): Environmental and biological controls on Mg and Li in deep-sea scleractinian corals, *Earth and Planetary Science Letters* **300**: 215-225.

Chen, J.H., Lawrence Edwards, R., Wasserburg, G.J. (1986): ^{238}U, ^{234} U and ^{232}Th in seawater, *Earth and Planetary Science Letters* **80**: 241-251.

Cheng, H., Adkins, J., Edwards, R.L., Boyle, E.A. (2000): U-Th dating of deep-sea corals, *Geochimica et Cosmochimica Acta* **64**(14): 2401-2416.

Christ, C.L., Clark, J.R., Evans Jr., H.T. (1995): Crystal structure of rutherfordine, UO_2CO_3, *Science* **121**: 472-473.

Coffroth, M.A. (1984): Ingestion and incorporation of coral mucus aggregates by a gorgonian soft coral, *Marine Ecology Progress Series* **17**: 193-199.

Cohen, A.L., Gaetani, G.A. (2010): Ion partitioning and the geochemistry of coral skeletons: solving the mystery of the vital effect, *EMU Notes in Mineralogy* **11** (Chapter 11): 377-397.

Cohen, A.L., Gaetani, G.A., Lundälv, T., Corliss, B.H., George, R.Y. (2006): Compositional variability in a cold-water scleractinian, *Lophelia pertusa*: New insights into 'vital effects', *Geochemistry Geophysics Geosystems* **7**(12): Q12004, doi:10.1029/2006GC001354.

Cohen, A.L., Layne, G.D., Hart, S.R. (2001): Kinetic control of skeletal Sr/Ca in a symbiotic coral: Implications for the paleotemperature proxy, *Paleoceanography* **16**(1): 20-26.

Cohen, A.L., McConnaughey, T.A. (2003): Geochemical Perspectives on Coral Mineralization, in P.M. Dove, J.J. De Yoreo, S. Winer (eds): *Biomineralization, Reviews in Mineralogy and Geochemistry* **54**, Washington: Mineralogical Society of America: 151-187.

Cohen, A.L., Owens, K.E., Layne, G.D., Shimizu, N. (2002): The Effect of Algal Symbionts on the Accuracy of Sr/Ca Paleotemperatures from Coral, *Science* **296**: 331-333.

Cohen, A.L., Sohn, R.A. (2004): Tidal modulation of Sr/Ca ratios in a Pacific reef coral, *Geophysical Research Letters* **31**: L16310. doi:10.1029/2004GL020600.

Colin, C., Frank, N., Copard, K., Douville, E. (2010): Neodymium isotopic composition of deep-sea corals from the NE Atlantic implications for past hydrological changes during the Holocene, *Quaternary Science Reviews* **29**: 2509-2517.

Constantz, B.R. (1986): Coral Skeleton Construction: A Physiochemically Dominated Process, *Palaios* **1**: 152-157.

Copard, K., Colin, C., Douville, E., Freiwald, A., Gudmundsson, G., De Mol, B., Frank, N. (2010): Nd isotopes in deep-sea corals in the North-eastern Atlantic, *Quaternary Science Reviews* **29**: 2499-2508.

Correa, T.B.S., Eberli, G.P., Grasmueck, M., Reed, J.K., Correa, A.M.S. (2012): Genesis and morphology of cold-water coral ridges in a unidirectional current regime, *Marine Geology* **326-328**: 14-27.

Croot, P.L., Laan, P., Nishioka, J., Strass, V., Cisewski, B., Boye, M., Timmermans, K.R., Bellerby, R.G., Goldson, L., Nightingale, P., de Baar, H.J.W. (2005): Spatial and temporal distribution of Fe(II) and H_2O_2 during EisenEx, an open ocean mescoscale iron enrichment, *Marine Chemistry* **95**: 65-88.

Cuif, J.-P., Dauphin, Y. (1998): Microstructural and physico-chemical characterization of 'centers of calcification' in septa of some Recent scleractinian corals, *Paläontologische Zeitschrift* **2**(3/4): 257-270.

Cuif, J.-P., Dauphin, Y. (2005a): The two-step mode of growth in the scleractinian coral skeletons from the micrometre to the overall scale, *Journal of Structural Biology* **150**: 319-331.

Cuif, J.-P., Dauphin, Y. (2005b): The Environment Recording Unit in coral skeletons - a synthesis of structural and chemical evidence for a biochemically driven, stepping-growth process in fibres, *Biogeosciences* **2**: 61-73.

Cuif, J.-P., Dauphin, Y., Doucet, J., Salome, M., Susini, J. (2003): XANES mapping of organic sulfate in three sclerctinian coral skeletons, *Geochimica et Cosmochimica Acta* **67**(1): 75-83.

Cuif, J.-P., Dauphin, Y., Freiwald, A., Gautret, P., Zibrowius, H. (1999a): Biochemical markers of zooxanthellae symbiosis in soluble matrices of skeleton of 24 *Scleractinia* species, *Comparative Biochemistry and Physiology Part A* **123**: 269-278.

Cuif, J.-P., Dauphin, Y., Gautret, P. (1999b): Compositional diversity of soluble mineralizing matrices in some recent coral skeletons compared to fine-scale growth structures of fibres: discussion of consequences for biomineralization and diagenesis, *International Journal of Earth Sciences* **88**: 582-592.

Cunningham, M.J., Hodgson, S., Masson, D.G., Parson, L.M. (2005): An evaluation of along- and down-slope sediment transport processes between Goban Spur and Brenot Spur on the Celtic Margin of the Bay of Biscay, *Sedimentary Geology* **179**: 99-106.

Davies, A.J., Duineveld, G.C.A., Lavaleye, M.S.S., Bergman, M.J.N., van Haren, H., Roberts, J.M. (2009): Downwelling and deep-water bottom currents as food supply mechanisms to the cold-water coral *Lophelia pertusa* (Scleractinia) at the Mingulay Reef complex, *Limnology and Oceanography* **54**(2): 620-629.

Davies, A.J., Guinotte, J.M. (2011): Global Habitat Suitability for Framework-Forming Cold-Water Corals, *PLoS ONE* **6**(4): e18483. doi:10.1371/journal.pone.0018483.

Davies, A.J., Wisshak, M., Orr, J.C., Roberts, J.M. (2008): Predicting suitable habitat for the cold-water coral *Lophelia pertusa* (Scleractinia), *Deep-Sea Research* **155**: 1048-1062.

DeCarlo, T.M., Gaetani, G.A., Holcomb, M., Cohen, A.L. (2015): Experimental determination of factors controlling U/Ca of aragonite precipitated from seawater:

Implications for interpreting coral skeleton, *Geochimica et Cosmochimica Acta* **162**: 151-165.

Delaney, M.L., Linn, L.J., Druffel, E.R.M. (1993): Seasonal cycles of manganese and cadmium in coral from the Galapagos Islands, *Geochimica et Cosmochimica Acta* **57**: 347-354.

Delanghe, D., Bard, E., Hamilin, B. (2002): New TIMS constraints on the uranium-238 and uranium-234 in seawater from the main ocean basins and the Mediterranean Sea, *Marine Chemistry* **80**: 79-93.

De Mol, L,. Van Rooij, D., Pirlet, H., Greinert, J., Frank, N., Quemmerais, F., Henriet, J.-P. (2011): Cold-water coral habitats in the Penmarc'h and Guilvinec Canyons (Bay of Biscay): Deep-water versus shallow-water settings, *Marine Geology* **282**(1-2): 40-52.

De Villiers, J.P.R. (1971): Crystal structures of aragontie, strontianite, and witherite, *The American Mineralogist* **56**: 758-767.

De Villiers, S., Nelson, B.K., Chivas, A.R. (1995): Biological Controls on Coral Sr/Ca and $\delta^{18}O$ Reconstructions of Sea Surface Temperatures, *Science* **269**: 1247-1249.

Diercks, A.R., Asper, V.L. (1997): *In situ* settling speeds of marine snow aggregates below the mixed layer: Black Sea and Gulf of Mexico, *Deep-Sea Research Part I* **44**: 385-398.

Dietzel, M., Gussone, N., Eisenhauer, A. (2004): Co-precipitation of Sr^{2+} and Ba^{2+} with aragonite by memberane diffusion of CO_2 between 10 and 50°C, *Chemical Geology* **203**: 139-151.

Djogić, R., Sipos, L., Branica, M. (1986): Characterization of uranium(VI) in seawater, *Limnology and Oceanography* **31**(5): 1122-1131.

Dodds, L.A., Roberts, J.M., Taylor, A.C., Marubini, F. (2007): Metabolic tolerance of the cold-water coral *Lophelia pertusa* (Scleractinia) to temperature and dissolved oxygen change, *Journal of Experimental Marine Biology and Exology* **349**: 205-214.

Dolan, M.F.J., Grehan, A.J., Guinan, J.C., Brown, C. (2008): Modelling the local distribution of cold-water corals in relation to bathymetric variables: Adding spatial context to deep-sea video data, *Deep-Sea Research I* **55**: 1564-1579.

Domart-Coulon, I., Stolarski, J., Brahmi, C., Gutner-Hoch, E., Janiszewska, K., Shemesh, A., Meibom, A. (2014): Simultaneous extension of both basic microstructural components in scleractinian coral skeleton during night and daytime, visualized by *in situ* ^{86}Sr pulse labeling, *Journal of Structural Biology* **185**(1): 79-88.

Dorschel, B., Hebbeln, D., Foubert, A., White, M., Wheeler, A.J. (2007): Hydrodynamics and cold-water coral facies distribution related to recent sedimentary processes at Galway Mound west of Ireland, *Marine Geology* **244**: 184-195.

Douarin, M., Elliot, M., Noble, S.R., Sinclair, D., Henry, L.-A., Long, D., Moreton, S.G., Roberts, J.M. (2013): Growth of north-east Atlantic cold-water coral reefs and mounds during the Holocene: A high resolution U-series and ^{14}C chronology, *Earth and Planetary Science Letters* **375**: 176-187.

Ducklow, H.W., Mitchell, R. (1979a): Bacterial Populations and Adaptations in the Mucus Layers on Living Corals, *Limnology and Oceanography* **24**(4): 715-725.

Ducklow, H.W., Mitchell, R. (1979b): Composition of Mucus Released by Coral Reef Coelenterates, *Limnology and Oceanography* **24**(4): 706-714.

Duggen, S., Croot, P., Schacht, U., Hoffmann, L. (2007): Subduction zone volcanic ash can fertilize the surface ocean and stimulate phytoplankton growth: Evidence from biogeochemical experiments and satellite data, *Geophysical Research Letters* **34**: L01612. doi:10.1029/2006GL027522.

Duggen, S., Olgun, N., Croot, P., Hoffmann, L., Dietze, H., Delmelle, P., Teschner, C. (2010): The role of airborne volcanic ash for the surface ocean biogeochemical iron-cycle: a review, *Biogeosciences* **7**: 827-844.

Duineveld, G.C.A., Lavaleye, M.S.S., Bergman, M.J.N., de Stigter, H., Mienis, F. (2007): Trophic structure of a cold-water coral mound community (Rockall Bank, NE Atlantic) in relation to the near-bottom particle supply and current regime, *Bulletin of Marine Science* **81**(3): 449-467.

Duineveld, G.C.A., Lavaleye, M.S.S., Berghuis, E.M. (2004): Particle flux and food supply to a seamount cold-water coral community (Galicia Bank, NW Spain), *Marine Ecology Progress Series* **277**: 13-23.

Dullo, W.C., Flögel, S., Rüggeberg, A. (2008): Cold-water coral growth in relation to the hydrography of the Celtic and Nordic European continental margin, *Marine Ecology Progress Series* **371**: 165-176.

Duncan, P.M. (1877): On the Rapidity of Growth and Variability of Some Madreporaria on an Atlantic Cable, with Remarks upon the Rate of Accumulation of Foraminiferal Deposits, *Proceedings of the Royal Society of London* **26**: 133-137.

Emiliani, C., Hudson, J.H., Shinn, E.A., George, R.Y. (1978): Oxygen and Carbon Isotopic Growth Record in a Reef Coral from the Florida Keys and a Deep-Sea Coral from Blake Plateau, *Science*, New Series **202**(4368): 627-629.

Fallon, S.J., Thresher, R.E., Adkins, J. (2014): Age and growth of the cold-water scleractinian *Solenosmilia variabilis* and its reef on SW Pacific seamounts, *Coral Reefs* **33**: 31-38.

Fietzke, J., Heinemann, A., Taubner, I., Böhm, F., Erez, J., Eisenhauer, A. (2010): Boron isotope ratio determination in carbonates via LA-MC-ICP-MS using soda-lime glass standards as reference material, *Journal of Analytical Atomic Spectrometry* **25**: 1953-1957.

Foley, N.S., Armstrong, C.W., Kahui, V., Mikkelsen, E., Reithe, S. (2012): A Review of Bioeconomic Modelling of Habitat-Fisheries Interactions, *International Journal of Ecology*: ID 861635. doi: 10.1155/2012/861635.

Fones, G.R., Davison, W., Hamilton-Taylor, J. (2004): The fine-scale remobilization of metals in the surface sediment of the North-East Atlantic, *Continental Shelf Research* **24**: 1485-1504.

Form, A.U., Riebesell, U. (2012): Acclimation to ocean acidification during long-term CO_2 exposure in the cold-water coral *Lophelia pertusa*, *Global Change Biology* **18**: 843-853.

Fosså, J.H., Mortensen, P.B., Furevik, D.M. (2002): The deep-water coral *Lophelia pertusa* in Norwegian waters: distribution and fishery impacts, *Hydrobiologia* **471**: 1-12.

Foubert, A., Huvenne, V.A.I., Wheeler, A., Kozachenko, M., Opderbecke, J., Henriet, J.-P. (2011): The Moira Mounds, small cold-water mounds in the Porcupine Seabight, NE Atlantic: Part B - Evaluating the impact of sediment dynamics through high-resolution ROV-borne bathymetric mapping, *Marine Geology* **282**: 65-78.

Fowler, S.W., Knauer, G.A. (1986) Role of Large Particles in the Transport of Elements and Organic Compounds Through the Oceanic Water Column, *Progress in Oceanography* **16**(3): 147-194.

Frank, N., Freiwald, A., López Correa, M., Wienberg, C., Eisele, M., Hebbeln, D., Van Rooij, D., Henriet, J.-P., Colin, C., Van Weering, T., De Haas, H., Buhl-Mortensen, P., Roberts, J.M., De Mol, B., Douville, E., Blamart, D., Hattè, C. (2011): Northeastern Atlantic cold-water coral reefs and climate, *Geology* **39**(8): 743-746.

Freiwald, A. (1998): Geobiology of *Lophelia pertusa* (Scleractinia) reefs in the North Atlantic, Habilitationsschrift, Fachbereich Geowissenschaften, Universität Bremen.

Freiwald, A., Beuck, L., Rüggeberg, A., Taviani, M., Hebbeln, D., R/V Meteor Cruise M70-1 participants (2009): White Coral Community in the Central Mediterranean Sea Revealed by ROV Surveys, *Oceanography* **22**(1): 58-74.

Freiwald, A., Fosså, J.H., Grehan, A., Koslow, T., Roberts, J.M. (2004): Cold-water Coral Reefs, *UNEP-WCMC, Cambridge, UK.*

Freiwald, A., Henrich, R., Pätzold, J. (1997): Anatomy of a deep-water coral reef mound from Stjernsund, west Finnmark, Northern Norway, *SEPM Special Publication* **56**: 141-162.

Freiwald A., Roberts J.M. (eds.) (2005): *Cold-water Corals and Ecosystems*, Berlin Heidelberg: Springer Verlag.

Freiwald, A., Wilson, J.B. (1998): Taphonomy of modern deep, cold-temperate water coral reefs, *Historical Biology: International Journal of Paleobiology* **13**(1): 37-52.

Frogner, P., Gíslason, S.R., Óskarsson, N. (2001): Fertilizing potential of volcanic ash in ocean surface water, *Geology* **29**(6): 487-490.

Gabitov, R.I., Gaetani, G.A., Watson, E.B., Cohen, A.L., Ehrlich, H.L. (2008): Experimental determination of growth rate effect on U^{6+} and Mg^{2+} partitioning between aragonite and fluid at elevated U^{6+} concentration, *Geochimica et Cosmochimica Acta* **72**(16): 4058-4068.

Gabitov, R.I., Sadekov, A., Leinweber, A. (2014): Crystal growth rate effect on Mg/Ca and Sr/Ca partitioning between calcite and fluid: An *in situ* approach, *Chemical Geology* **367**: 70-82.

Gaetani, G.A., Cohen, A.L. (2006): Element partitioning during precipitation of aragonite from seawater: A framework for understanding paleoproxies, *Geochimica et Cosmochimica Acta* **70**: 4617-4634.

Gaetani, G.A., Cohen, A.L., Wang, Z., Crusius, J. (2011): Rayleigh-based, multi-element coral thermometry: A biomineralization approach to developing climate proxies, *Geochimica et Cosmochimica Acta* **75**: 1920-1932.

Gagnon, A.C., Adkins, J.F., Erez, J. (2012): Seawater transport during coral biomineralization, *Earth and Planetary Science Letters* **329**: 150-161.

Gagnon, A.C., Adkins, J.F., Erez, J., Eiler, J.M., Guan, Y. (2013): Sr/Ca sensitivity to aragonite saturation state in cultured subsamples from a single colony of coral: Mechanism of biomineralization during ocean acidification, *Geochimica et Cosmochimica Acta* **105**: 240-254.

Gagnon, A.C., Adkins, J.F., Fernandez, D.P., Robinson, L.F. (2007): Sr/Ca and Mg/Ca vital effects correlated with skeletal architecture in a scleractinian deep-sea coral and the role of Rayleigh fractionation, *Earth and Planetary Science Letters* **261**: 280-295.

Galkiewicz, J.P., Pratte, Z.A., Gray, M.A., Kellogg, C.A. (2011): Characterization of culturable bacteria isolated from the cold-water coral *Lophelia pertusa*, *FEMS Microbiology Ecology* **77**: 333-346.

Gass, S.E., Roberts, J.M. (2011): Growth and branching patterns of *Lophelia pertusa* (Scleractinia) from the North Sea, *Journal of the Marine Biological Association of the United Kingdom*: 1-5. doi: 10.1017/S002531541000055X.

Gass, S.E., Roberts, J.M. (2006): The occurrence of the cold-water coral *Lophelia pertusa* (Scleractinia) on oil and gas platforms in the North Sea: Colony growth, recruitment and environmental controls on distribution, *Marine Pollution Bulletin* **52**: 549-559.

Gautret, P., Cuif, J.-P., Freiwald, A. (1997): Composition of Soluble Mineralizing Matrices in Zooxanthellate and Non-zooxanthellate Scleractinian Corals: Biochemical Assessment of Photosynthetic metabolism through the Study of a Skeletal Feature, *Facies* **36**: 189-184.

Gautret, P., Cuif, J.-P., Stolarski, J. (2000): Organic components of the skeleton of scleractinian corals - evidence from *in situ* acridine orange staining, *Acta Palaeontologica Polonica* **45**(2): 107-118.

Genin, A., Dayton, P.K., Lonsdale, P.F., Spiess, F.N. (1986): Corals on seamount peaks provide evidence of current acceleration over deep-sea topography, *Nature* **322**: 59-61.

Gillikin, D.P., Dehairs, F. (2013): Uranium in aragonitic marine bivalve shells, *Palaeogeography, Palaeoclimatology, Palaeoecology* **373**: 60-65.

Gooday, A.J. (2002): Biological responses to seasonally varying fluxes of organic matter to the ocean floor: a review, *Journal of Oceanography* **58**: 305-332.

Guihen, D., White, M., Lundälv, T. (2013): Boundary layer flow dynamics at a cold-water coral reef, *Journal of Sea Research* **78**: 36-44.

Guinan, J., Brown, C., Dolan, M.F.J., Grehan, A.J. (2009a): Ecological niche modelling of the distribution of cold-water coral habitat using underwater remote sensing data, *Ecological Informatics* **4**: 83-92.

Guinan, J., Grehan, A.J., Dolan, M.F.J., Brown, C. (2009b): Quantifying relationships between video observations of cold-water coral cover and seafloor features in Rockall Trough, west of Ireland, *Marine Ecology Progress Series* **375**: 125-138.

Guinotte, J.M., Davies, A.J. (2014): Predicted Deep-Sea Coral Habitat Suitability for the U.S. West Coast, *PLoS ONE* **9**(4): e93918. doi:10.1371/journal.pone.0093918.

Guinotte, J.M., Orr, J., Cairns, S., Freiwald, A., Morgan, L., George, R. (2006): Will human-induced chagnes in seawater chemistry alter the distribution of deep-sea scleractinian corals? The Ecological Society of America, *Frontiers in Ecology and the Environment* **4**(3): 141-146.

Hamme, R.C., Webley, P.W., Crawford, W.R., Whitney, F.A., DeGrandpre, M.D., Emerson, S.R., Eriksen, C.C., Giesbrecht, K.E., Gower, J.F.R., Kavanaugh, M.T., Peña, M.A., Sabine, C.L., Batten, SD, Coogan, L.A., Grundle, D.S., Lockwood, D. (2010): Volcanic ash fuels anomalous plankton bloom in subarctic northeast Pacific, *Geophysical Research Letters* **37**: L19604. doi:10.1029/2010GL044629.

Hansson, L., Agis, M., Maier, C., Weinbauer, M.G. (2009): Community composition of bacteria associated with cold-water coral *Madrepora oculata*: within and between colony variability, *Marine Ecology Progress Series* **397**: 89-102.

Hassenrueck, C., Jantzen, C., Försterra, G., Häussermann, V., Willenz, P. (2013): Rates of apical septal extension of *Desmophyllum dianthus*: effect of association with endolithic photo-autotrophs, *Marine Biology* **160**: 2919-2927.

Hathorne, E.C., Felis, T., Suzuki, A., Kawahata, H., Cabioch, G. (2013a): Lithium in the aragonite skeletons of massive Porites corals: A new tool to reconstruct tropical sea surface temperatures, *Paleoceanography* **28**: 143-152.

Hathorne, E.C., Gagnon, A., Felis, T., Adkins, J., Asami, R., Boer, W., Caillon, N., Case, D., Cobb, K.M., Douville, E., deMenocal, P., Eisenhauer, A., Garbe-Schöneberg, D., Geibert, W., Goldstein, S., Hughen, K., Inoue, M., Kawahata, H., Kölling, M., Cornec, F.L., Linsley, B.K., McGregor, H.V., Montagna, P., Nurhati, I.S., Quinn, T.M., Raddatz, J., Rebaubier, H., Robinson, L., Sadekov, A., Sherrell, R., Sinclair, D., Tudhope, A.W., Wei, G., Wong, H., Wu, H.C., You, C.-F. (2013b): Interlaboratory study for coral Sr/Ca and other element/Ca ratio measurements, *Geochemistry Geophysics Geosystems* **14**(9): 3730-3750.

Heikoop, J.M., Dunn, J.J., Risk, M.J., Schwarcz, H.P., McConnaughey, T.A, Sandeman, I.M. (2000): Separation of kinetic and metabolic isotope effects in carbon-13 records preserved in reef coral skeletons, *Geochimica et Cosmochimica Acta* **64**: 975-987.

Helmle, K.P., Dodge, R.E. (2011): Sclerochronology, In: Hopley, D. (ed.) *Encyclopedia of Modern Coral Reefs*, Encyclopedia of Earth Sciences Series: Springer Science-Business Media: 958-966.

Henry, L.-A., Davies, A.J., Roberts, J.M. (2009): Beta diversity of cold-water coral reef communities off western Scotland, *Coral Reefs* **29**: 427-436.

Henry, L.-A., Frank, N., Hebbeln, D., Wienberg, C., Robinson, L., van de Flierdt, T., Dahl, M., Douarin, M., Morrison, C.L., López Correa, M., Rogers, A.D., Ruckelshausen, M., Roberts, J.M. (2014): Global ocean conveyor lowers extinction risk in the deep sea, *Deep-Sea Research I* **88**: 8-16.

Henson, S.A., Painter, S.C., Holliday, N.P., Stinchcombe, M.C., Giering, S.L.C. (2013): Unusual subpolar North Atlantic phytoplankton bloom in 2010: Volcanic fertilization or North Atlantic Oscillation? *Journal of Geophysical Research* **118**(10): 4771-4780.

Hirata, T. (2004): New technique for isobaric interferences on Ba using ICP-mass spectrometry, *Journal of The American Society for Mass Spectrometry JPN* **52**(4): 171-176.

Holcomb, M., Cohen, A.L., Gabitow, R.I., Hutter, J.L. (2009): Compositional and morphological features of aragonite precipitated experimentally from seawater and biogenically by corals, *Geochimica et Cosmochimica Acta* **73**: 4166-4179.

Houk, R.S. (1986) Mass Spectrometry of Inductively Coupled Plasmas, *Analytical Chemistry* **58**(1): 97A-105A.

Huettel, M., Wild, C., Gonelli, S. (2006): Mucus trap in coral reefs: formation and temporal evolution of particle aggregates caused by coral mucus, *Marine Ecology Progress Series* **307**: 69-84.

Huvenne, V.A.I., Tyler, P.A., Masson, D.G., Fisher, E.H., Hauton, C., Hühnerbach, V., Le Bas, T.P., Wolff, G.A. (2011): A Picture on the Wall: Innovative Mapping Reveals Cold-Water Refuge in Submarine Canyon, *PLoS ONE* **6**(12): e28755. doi:10.1371/journal.pone.0028755.

Huvenne, V.A.I., Van Rooij, D., De Mol, B., Thierens, M., O'Donnell, R., Foubert, A. (2009): Sediment dynamics and palaeo-environmental context at key stages in the Challenger cold-water coral mound formation: Clues from sediment deposits at the mound base, *Deep-Sea Research Part I* **56**: 2263-2280.

Inoue, M., Suwa, R., Suzuki, A., Sakai K., Kawahata, H. (2011): Effects of seawater pH on growth and skeletal U/Ca ratios of Acropora digitifera coral polyps, *Geophysical Research Letters* **38**: L12809. doi:10.1029/2011GL047786.

Ip, Y.K., Lim, A.L.L. (1991): Short Communication: Are calcium and strontium transported by the same mechanism in the hermatypic coral *Galaxea fascicularis*? *Journal of Experimental Biology* **159**: 507-513.

Isa, Y., Ikehara, N., Yamazato, K. (1980): Evidence for the occurrence of Ca2+-dependent adenosine triphosphatase in a hermatypic coral, Acropora hebes (Dana), *Sesoko Marine Science Lab Technical Report* **7**: 19-25.

Järnegren, J., Kutti, T. (2014): *Lophelia pertusa* in Norwegian waters. What have we learned since 2008? *NINA Report 1028, Norwegian Institute for Nature Research, Trondheim.*

Jantzen, C., Laudien, J., Sokol, S., Förstera, G., Häussermann, V., Kupprat, F., Richter, C. (2013): *In situ* short-term growth rates of a cold-water coral, *Marine and Freshwater Research* **64**(7): 631-641.

Jensen, A., Frederiksen, R. (1992): The fauna associated with the bank-forming deepwater coral *Lophelia pertusa* (Scleractinia) on the Faroe shelf, *Sarsia* **77**: 53-69.

Jochum, K.P., Weis, U., Stoll, B., Kuzmin, D., Yang, Q., Raczek, I., Jacob, D.E., Stracke, A., Birbaum, K., Frick, D.A., Günther, D., Enzweiler, J. (2011): Determination of Reference Values for NIST SRM 610-617 Glasses Following ISO Guidelines, *Geostandards and Geoanalytical Research* **35**(4): 397-429.

Johnson, M.P., White, M., Wilson, A., Wurzberg, L., Schwabe, E., Folch, H., Allcock, A.L. (2013): A Vertical Wall Dominated by *Acesta excavata* and *Neopycnodonte zibrowii*, Part of an Undersampled Group of Deep-Sea Habitats, *PLoS ONE* **8**(11): e79919. doi: 10.1371/journal.pone0079917.

Juillet-Leclerc, A., Reynaud, S., Rollion-Bard, C., Cuif, J.P., Dauphin, Y., Blamart, D., Ferrier-Pagès, C., Allemand, D. (2009): Oxygen isotopic signature of the skeletal microstructures in cultured corals: Idendification of vital effects, *Geochimica et Cosmochimica Acta* **73**: 5320-5332.

Kaczmarek, K., Horn, I., Nehrke, G., Bijma, J. (2015): Simultaneous determination of δ^{11}B and B/Ca ratio in marine biogenic carbonates at nanogram level, *Chemical Geology* **392**: 32-42.

Keller, N.B., Os'kina, N.S. (2008): Habitat Temperature Ranges of Azooxantellate Scleractinian Corals in the World Ocean, *Oceanology* **48**(1): 77-84.

Kennish, M.J. (Ed.) (2000): Practical Handbook of Marine Science, 3rd Edition, CRC Press, New York. ISBN-13: 978-0849323911.

Khripounoff, A., Caprais, J.-C., Le Bruchec, J., Rodier, P., Noel, P., Cathalot, C. (2014): Deep cold-water coral ecosystems in the Brittany submarine canyons (Northeast Atlantic): Hydrodynamics, particle supply, respiration, and carbon cycling, *Limnology and Oceanography* **59**(10): 87-98.

Kiriakoulakis, K., Fisher, E., Wolff, G.A., Freiwald, A., Grehan, A., Roberts, J.M. (2005): Lipids and nitrogen isotopes of two deep-water corals from the North-East Atlantic: initial results and implications for their nutrition, in A. Freiwald, J.M. Roberts (eds): *Cold-water Corals and Ecosystems*, Berlin Heidelberg: Springer Verlag: 715-729.

Kiriakoulakis, K., Freiwald, A., Fisher, E., Wolff, G.A. (2007): Organic matter quality and supply to deep-water coral/mound systems of the NW European Continental Margin, *International Journal of Earth Science (Geologische Rundschau)* **96**: 159-170.

Klitgaard, A.B., Tendal, O.S., Westerberg, H. (1997): Mass occurrence of large sponges (Porifera) in Faeroe Island (NE Atlantic) shelf and slope areas: characteristics, distribution and possible causes, In: L.E. Hawkins, S. Hutchins (eds) *The Responses of Marine Organisms to their Environments*, Southampton Oceanographic Centre, University of Southampton: 129-141.

Klochko, K., Kaufman, A.J., Yao, W., Byrne, R.H., Tossell, J.A. (2006): Experimental measurement of boron isotope fractionation in seawater, *Earth and Planetary Science Letters* **248**: 261-270.

Klochko, K., Cody, G.D., Tossell, J.A., Dera, P., Kaufman, A.J. (2009): Re-evaluating boron speciation in biogenic calcite and aragonite using ^{11}B MAS NMR, *Geochimica et Cosmochimica Acta* **73**: 1890-1900.

Kunioka, D., Shirai, K., Takahata, N., Sano, Y., Toyofuku, T., Ujiie, Y. (2006): Microdistribution of Mg/Ca, Sr/Ca, and Ba/Ca ratios in Pulleniatina obliquiloculata test by using a NanoSIMS: Implication for the vital effect mechanism, *Geochemistry Geophysics Geosystems* **7**(12): Q12P20. doi:10.1029/2006GC001280.

Ku, T.-L., Knauss, K.G., Mathieu, G.G. (1977): Uranium in open ocean: concentration and isotopic composition, *Deep-Sea Research* **24**: 1005-1017.

Langmann, B., Zakšek, K., Hort, M., Duggen, S. (2010): Volcanic ash as fertiliser for the surface ocean, *Atmospheric Chemistry and Physics* **10**: 3891-3899.

Larsson, A.I., Järnegren, J., Strömberg, S.M., Dahl, M.P., Lundälav, T., Brooke, S. (2014): Embryogenesis and larval biology of the cold-water coral *Lophelia pertusa*, *PLoS ONE* **9**(7): e102222. doi:10.1371/journal.pone.0102222.

Larsson, A.I., Purser, A. (2011): Sedimentation on the cold-water coral Lophelia pertusa: Cleaning efficiency from natural sediments and drill cuttings, *Marine Pollution Bulletin* **62**: 1159-1168.

Lartaud, F., Pareige, S., De Rafelis, M., Feuillassier, L., Bideau, M., Peru, E., Romans, P., Alcala, F., Le Bris, N. (2013): A new approach for assessing cold-water coral growth *in situ* using fluorescent calcein staining, *Aquatic Living Resources* **26**: 187-196.

LaVigne, M., Field, M.P., Anagnostou, E., Grottoli, A.G., Wellington, G.M., Sherrell, R.M. (2008): Skeletal P/Ca tracks upwelling in Gulf of Panama coral: Evidence for a new seawater phosphate proxy, *Geophysical Research Letters* **35**: L05604. doi:10.1029/2007GL031926.

LaVigne, M., Hill, T.M., Spero, H.J., Guilderson, T.P. (2011): Bamboo coral Ba/Ca: Calibration of a new deep ocean refractory nutrient proxy, *Earth and Planetary Science Letters* **312**: 506-515.

Lazier, A.V., Smith, J.E., Risk, M.J., Schwarcz, H.P. (1999): The skeletal structure of *Desmophyllum cristagalli*: the use of deep-water corals in sclerochronology, *Lethaia* **32**: 119-130.

Lea, D.W., Shen, G.T., Boyle, E.A. (1989): Coralline barium records temporal variability in equatorial Pacific upwelling, *Nature* **340**: 373-376.

Le Goff-Vitry, M.C., Pybus, O.G., Rogers, A.D. (2004a): Genetic structure of the deep-sea coral *Lophelia pertusa* in the northeast Atlantic revealed by microsatellites and internal transcribed spacer sequences, *Molecular Ecology* **13**: 537-549.

Le Goff-Vitry, M.C., Rogers, A.D., Baglow, D. (2004b): A deep-sea slant on the molecular phylogeny of the Scleractinia, *Molecular Phylogenetics and Evolution* **30**: 167-177.

Le Goff-Vitry, M.C., Rogers, A.D. (2005): Molecular ecology of *Lophelia pertusa* in the NE Atlantic, in A. Freiwald, J.M. Roberts (Eds): *Cold-water Corals and Ecosystems*, Berlin Heidelberg: Springer Verlag: 653-662.

Le Moigne, F.A.C., Moore, M.C., Sanders, R.J., Villa-Alfageme, M., Steigenberger, S., Achterberg, E.P. (2014): Sequestration efficiency in the iron-limited North Atlantic: Implications for iron supply mode to fertilized blooms, *Geophysical Research Letters* **47**: 4619-4627.

Lo Bue, N., Sgroi, T., Gionanetti, G., Marinaro, G., Favali, P. (2014): Original recording of the 2013 Etna pyroclastic activity through the ADCP sensor of NEMO-SN1 multidisciplinary seafloor abservatory, poster 1047, AGU meeting, San Franscisco, 15-19 December.

Longerich, H.P., Jenner, G.A., Fryer, B.J., Jackson, S.E. (1990): Inductively coupled plasma-mass spectrometric analysis of geological samples: A critical evaluation based on case studies, *Chemical Geology* **83**: 105-118.

Longerich, H.P., Jackson, S.E., Günther, D. (1996): Laser Ablation Inductively Coupled Plasma Mass Spectrometric Transient Signal Data Acquisition and Analyte Concentration Calculation, *Journal of Analytical Atomic Spectrometry* **11**: 899-904.

López Correa, M., Montagna, P., Vendrell-Simón, B., McCulloch, M., Taviani, M. (2010): Stable isotopes ($\delta^{18}O$ and $\delta^{13}C$), trace and minor element compositions of Recent scleractinians and Last Glacial bivalves at the Santa Maria di Leuca deep-water coral province, Ionian Sea, *Deep-Sea Research Part II* **57**: 471-486.

Lumsden, S.E., Hourigan, T.F., Bruckner, A.W., Dorr, G. (Eds) (2007): The State of Deep Coral Ecosystems of the United States, *NOAA Technical Memorandum CRCP3, Silver Spring MD.*

Maier, C., Bils, F., Winbauer, M.G., Watremez, P., Peck, M.A., Gattuso, J.-P. (2013b): Respiration of Mediterranean cold-water corals is not affected by acean acidification as projected for the end of the century, *Biogeosciences* **10**: 5671-5680.

Maier, C., Hegeman, J., Weinbauer, M.G., Gattuso, J.-P. (2009): Calcification of the cold-water coral Lophelia pertusa under ambient and reduced pH, *Biogeosciences* 6: 1875-1901.

Maier, C., Schubert, A., Berzunza Sánchez, M.M., Weinbauer, M.G., Watremez, P., Gattuso, J.-P. (2013a): End of the Century pCO_2 Levels Do Not Impact Calcification in Mediterranean Cold-Water Corals, *PLoS ONE* **8**(4): e6255. doi:10.1371/journal.pone.0062655.

Maier, C., Watremex, P., Taviani, M., Winbauer, M.G., Gattuso, J.P. (2012): Calcification rates and the effect of ocean acidification on Mediterranean cold-water corals, *Proceedings of the Royal Society B* **279**: 1716-1723.

Marali, S., Wisshak, M., Lopez Correa, M., Freiwald, A. (2013): Skeletal microstructure and stable isotope signature of three bathyal solitary cold-water corals from the Azores, *Palaeogeography Palaeoclimatology Palaeoecology* **373**: 25-38.

Marin, F., Smith, M., Isa, Y., Muyzer, G., Westbroek, P. (1996): Skeletal matrices, muci, and the origin of invertebrate calcification, *Proceedings of the National Academy of Sciences USA* **93**: 1554-1559.

Martinez, E., Antoine, D., D'Ortenzio, F., de Boyer Montégut, C. (2011): Phytoplankton spring and fall blooms in the North Atlantic in the 1980s and 2000s, *Journal of Geophysical Research* **116**: C11029. doi:10.1029/2010JC006836.

Masson, D.G., Bett, B.J., Billett, D.S.M., Jacobs, C.L., Wheeler, A.J., Wynn, R.B. (2003): The origin of deep-water, coral-topped mounds in the northern Rockall Trough, Northeast Atlantic, *Marine Geology* **194**: 159-180.

Mastrototaro, F., D'Onghia, G., Corriero, G., Matarrese, A., Maiorano, P., Panetta, P., Gherardi, M., Longo, C., Rosso, A., Sciuto, F., Sanfilippo, R., Gravili, C., Boero, F., Taviani, M., Tursi, A. (2010): Biodiversity of the white coral bank off Cape Santa Maria di Leuca (Mediterranean Sea): An update, *Deep-Sea Research Part II* **57**: 412-430.

Matthews, K.A., Grottoli, A.G., McDonough, W.F., Palardy, J.E. (2008): Upwelling, species, and depth effects on coral skeletal cadmium-to-calcium ratios (Cd/Ca), *Geochimica et Cosmochimica Acta* **72**: 4537-4550.

Mayer, F.W., Wild, C. (2010): Coral mucus release and following particle trapping contribute to rapid nutrient recycling in a Northern Red Sea fringing reef, *Marine and Freshwater Research* **61**: 1006-1014.

May, T.W., Wiedmeyer, R.H. (1998): A Table of Polyatomic Interferences in ICP-MS, *Atomic Spectroscopy* **19**(5): 150-155.

McConnaughey, T. (1989a): ^{13}C and ^{18}O isotopic disequilibrium in biological carbonates: I. Patterns, *Geochimica et Cosmochimica Acta* **53**(1): 151-162.

McConnaughey, T. (1989b): ^{13}C and ^{18}O isotopic disequilibrium in biological carbonates: II. In vitro simulation of kinetic isotope effects, *Geochimica et Cosmochimica Acta* **53**: 163-171.

McConnaughey, T.A., Burdett J., Whelan J.F. and Paull C.K. (1997): Carbon isotopes in biological carbonates: Respiration and photosynthesis, *Geochimica et Cosmochimica Acta* **61**(3): 611-622.

McCulloch, M., Trotter, J., Montagna, P., Falter, J., Dunbar, R., Freiwald, A., Försterra, G., López Correa, M., Maier, C., Rüggeberg, A., Taviani, M. (2012): Resilience of cold-water scleractinian corals to ocean acidification: Boron isotopic systematics of pH and saturation state up-regulation, *Geochimica et Cosmochimica Acta* **87**: 21-34.

Meibom, A., Cuif, J.-P., Hillion, F., Constantz, B.R., Juillet-Leclerc, A., Dauphin, Y., Watanabe, T., Dunbar, R.B. (2004): Distribution of magnesium in coral skeleton, *Geophysical Research Letters* **31**: L23306. doi/10.1029/2004GL021313/abstract.

Meibom, A., Cuif, J.-P., Houlbreque, F., Mostefaoui, S., Dauphin, Y., Meibom, K.L., Dunbar, R. (2008): Compositional variations at ultra-structure length scales in coral skeleton, *Geochimica et Cosmochimica Acta* **72**(6): 1555-1569.

Meibom, A., Stage, M., Wooden, J., Constantz, B.R., Dunbar, R.B., Owen, A., Gumet, N., Bacon, C.R., Chamberlain, C.P. (2003): Monthly Strontium/Calcium oscillations in symbiotic coral aragonite: Biological effects limiting the precision of the paleotemperature proxy, *Geophysical Research Letters* **30**(7): 1418. doi:10.1029/2002GL016864.

Mienis, F., van der Land, C., de Stigter, H.C., van de Vorstenbosch, M., de Haas, H., Richter, T., van Weering, T.C.E. (2009): Sediment accumulation on a cold-water carbonate mound at the Southwest Rockall Trough margin, *Marine Geology* **265**: 40-50.

Mikkelsen, N., Erlenkeuser, H., Killingsley, J.S, Berger, W.H. (1982): Norwegian corals: radiocarbon and stable isotopes in *Lophelia pertusa*, *Boreas* **11**: 163-171.

Miller, K., Williams, A., Rowden, A.A., Knowles, C., Dunshea, G. (2010): Conflicting estimates of connectivity among deep-sea coral populations, *Marine Ecology* **31** (suppl. 1): 144-157.

Min G.R., Edwards, R. L., Taylor, F.W., Recy J., Gallup, C.D., Beck, J.W. (1995): Annual cycles of U/Ca in coral skeletons and U/Ca thermometry, *Geochimica et Cosmochimica Acta* **59**: 2025-2042.

Mitsuguchi, T., Kawakami, T. (2012): Potassium and other minor elements in *Porites* corals: implications for skeletal geochemistry and paleoenvironmental reconstruction, *Coral Reefs* **31**: 671-681.

Montagna, P., McCulloch, M., Douville, E., López Correa, M., Trotter, J., Rodolfo-Metalpa, R., Dissard, D., Ferrier-Pagès, C., Frank, N., Freiwald, A., Goldstein, S., Mazzoli, C., Reynaud, S., Rüggeberg, A., Russo, S., Taviani, M. (2014): Li/Mg systematics in scleractinian corals: Calibration of the thermometer, *Geochimica et Cosmochimica Acta* **132**: 288-310.

Montagna, P., McCulloch, M., Taviani, M., Remin, A., Rouse, G. (2005): High-resolution trace and minor element compositions in deep-water scleractinian corals (*Desmophyllum dianthus*) from the Mediterranean Sea and the Great Australian Bight, in A. Freiwald, J.M. Roberts (Eds): *Cold-water Corals and Ecosystems*, Berlin Heidelberg: Springer Verlag: 1109-1126.

Montagna, P., López Correa, M., Rüggeberg, A., McCulloch, M., Rodolfo-Metalpa, R., Dullo, W.C. (2008): Coral Li/Ca in micro-structural domains as a temperature proxy, *Geochimica et Cosmochimica Acta* **72**(12): A645-A645.

Montero-Serrano, J.-C., Frank, N., Tisnérat-Laborde, N., Colin, C., Wu, C.-C., Lin, K., Shen, C.-C., Copard, K., Orejas, C., Gori, A., De Mol, L., Van Rooij, D., Reverdin, G., Douville, E. (2013): Decadal changes in the mid-depth water mass dynamic of the Northeastern Atlantic margin (Bay of Biscay), *Earth and Planetary Science Letters* **364**: 134-144.

Morris, K.J., Tyler, P.A., Masson, D.G., Huvenne, V.I.A., Rogers, A.D. (2013): Distribution of cold-water corals in the Whittard Canyon, NE Atlantic, *Deep-Sea Research Part II* **92**: 136-144.

Morrison, C.L., Eackles, M.S., Johnson, R.L., King, T.L. (2008a): Characterization of 13 microsatellite loci for the deep-sea coral, *Lophelia pertusa* (Linnaeus 1758), from the western North Atlantic Ocean and Gulf of Mexico, *Molecular Ecology Resources* **8**: 1037-1039.

Morrison, C.L., Johnson, R.L., King, T. L., Ross, S.W., Nizinski, M.S. (2008b): Molecular Assessment of Deep-sea Scleractinian Coral Biodiversity and Populations Structure of *Lophelia pertusa* in the Gulf of Mexico, In: K.J. Sulak (Ed): *Characterization of Northern Gulf of Mexico deepwater hard bottom communities with emphasis on Lophelia coral - Lophelia reef megafaunal community structure biotopes, genetics, microbial ecology, and geology (2004-2006)* (4-78). USGS open file report 2008-1145; OCS study MMS 2008-015, Minerals Management Service, New Orleans, LA, USA.

Morrison, C.L., Ross, S.W., Nizinski, M.S., Brooke, S., Järnegren, J., Waller, R.G., Johnson, R.L., King, T.L. (2011): Genetic discontinuity among regional populations of *Lophelia pertusa* in the North Atlantic Ocean, *Conservation Genetics* **12**: 713-729.

Mortensen, P.B. (2001): Aquarium observations on the deep-water coral Lophelia pertusa (L., 1758) (Scleractinia) and selected associated invertebrates, *Ophelia* **54**: 83-104.

Mortensen, P.B., Hovland, M.T., Fosså, J.H., Furevik, D.M. (2001): Distribution, abundance and size of *Lophelia pertusa* coral reefs in mid-Norway in relation to seabed characteristics, *Journal of the Marine Biological Association U.K.* **81**: 581-597.

Mortensen, P.B., Rapp, H.T. (1998): Oxygen and carbon isotope ratios related to growth line patterns in skeletons of *Lophelia pertusa* (L) (Anthozoa, Scleractinia): Implications for determination of linear extension rates, *Sarsia* **83**: 433-446.

Motai, S., Nagai, T., Sowa, K., Watanabe, T., Sakamoto, N., Yurimoto, H., Kawano, J. (2012): Needle-like grains across growth lines in the coral skeleton of *Porites lobata*, *Journal of Structural Biology* **180**: 389-393.

Mouchi, V., Crowley, Q.G., Jackson, A., McDermott, F., Monteys, X., De Rafélis, M., Rueda, J.L., Lartaud, F. (2014): Potential seasonal calibration for palaeoenvironmental reconstruction using skeletal microstructures and strontium measurements from the cold-water coral *Lophelia pertusa*, *Journal of Quaternary Science*, **29**(8): 803-814.

Mueller, C.E., Larsson, A.I., Veuger, B., Middelburg, J.J., van Oevelen, D. (2014): Opportunistic feeding on various organic food sources by the cold-water coral *Lophelia pertusa*, *Biogeosciences* **11**: 123-133.

Mueller, C.E., Lundälv, T., Middelburg, J.J., van Oevelen, D. (2013): The Symbiosis between Lophelia pertusa and *Eunice norvegica* Stimulates Coral Calcification and Worm Assimilation, *PLoS ONE* **8**(3): e58660. doi: 10.1371/journal.pone.0058660.

Naumann, M.S., Orejas, C., Wild, C., Ferrier-Pagés, C. (2011): First evidence for zooplankton feeding sustaining key physiological processes in a scleractinian cold-water coral, *The Journal of Experimental Biology* **214**: 3570-3576.

Naumann, M.S., Orejas, C., Ferrier-Pagès, C. (2013): High thermal tolerance of two Mediterranean cold-water coral species maintained in aquaria, *Coral Reefs* **32**: 749-754.

Neulinger, S.C., Gärtner, A., Järnegren, J., Ludvigsen, M., Lochte, K., Dullo, W.-C. (2009): Tissue-Associated "*Candidatus* Mycoplasma corallicola" and Filamentous Bacteria on the Cold-Water Coral *Lophelia pertusa* (Scleractinia), *Applied and Environmental Microbiology* **75**(5): 1437.

Neulinger, S.C., Järnegren, J., Ludvigsen, M., Lochte, K., Dullo, W.-C. (2008): Phenotype-Specific Bacterial Communities in the Cold-Water Coral *Lophelia pertusa* (Scleractinia) and Their Implications for the Coral's Nutrition, Health, and Distribution, *Applied and Environmental Microbiology* **74**(23): 7272.

Nielsdóttir, M.C., Moore, C.M., Sanders, R., Hinz, D.J., Achterberg, E.P. (2009): Iron limitation of the postbloom phytoplankton communities in the Iceland Basin, *Global Biogeochemical Cycles* **23**: GB3001.

O'Connor, M.I., Bruno, J. F., Gaines, SD, Halpern, B.S., Lester, S.E., Kinlan, B.P., Weiss, J.M. (2007): Temperature control of larval dispersal and the implications for marine ecology, evolution, and conservation, *Proceedings of the National Academy of Sciences of the United States of America* **104**(4): 1266-1271.

Ogilvie, M.M. (1896): Microscopic and systematic study of madreporarian type of corals, *Philosophical Transactions of theRoyal Society of London* **187B**: 83- 345.

Okai, T., Suzuki, A., Kawahata, H., Terashima, S., Imai, N. (2002) Preparation of a New Geological Survey of Japan Geochemical Reference Material: Coral JCp-1, *Geostandards Newsletter* **26**(1): 95-99.

Orejas, C., Ferrier-Pagès, C., Reynaud, S., Tsounis, G., Allemand, D., Gili, J.M. (2011): Experimental comparison of skeletal growth rates in the cold-water coral *Madrepora oculata* Linnaeus, 1758 and three tropical scleractinian corals, *Journal of Experimental Marine Biology and Ecology* **405**: 1-5.

Orejas, C., Gori, A., Gili, J.M. (2008): Growth rates of live *Lophelia pertusa* and *Madrepora oculata* from the Mediterranean Sea maintained in aquaria, *Coral Reefs* **27**: 255.

Orejas, C., Gori, A., Lo Iacono, C., Puig, P., Gili, J.-M., Dale, M.R.T. (2009): Cold-water corals in the Cap de Creus canyon, northwestern Mediterranean: spatial distribution, density and anthropogenic impact, *Marine Ecology Progress Series* **397**: 37-51.

Owens, S.A., Buesseler, K.O., Sims, K.W.W. (2011): Re-evaluating the ^{238}U-salinity relationship in seawater: Implications for the ^{238}U-^{234}Th disequilibrium method, *Marine Chemistry* **127**: 31-39.

Pagini, M., Lemarchand, D., Spivack, A., Gaillardet, J. (2005): A critical evaluation of the boron isotope-pH proxy: The accuracy of ancient ocean pH estimates, *Geochimica et Cosmochimica Acta* **69**(4): 953-961.

Painter, S.C., Henson, S.A., Forryan, A., Steigenberger, S., Klar, J., Stinchcombe, M.C., Rogan, N., Baker, A.R., Achterberg, E.P., Moore, C.M. (2014): An assessment of the vertical diffusive flux of iron and other nutrients to the surface waters of the subpolar North Atlantic Ocean, *Biogeosciences* **11**: 2113-2130.

Park, Y.-H., Gambéroni, L., Charriaud, E. (1991): Frontal structure and transport of the Antarctic Circumpolar Current in the south Indian Ocean sector, 40-80°E, *Marine Chemistry* **35**: 45-62.

Pates, J.M., Muir, G.K.P. (2007): U-salinity relationships in the Mediterranean: Implications for 234Th:238U particle flux studies, *Marine Chemistry* **106**(3-4): 530-545.

Paton, C., Hellstrom, J., Paul, B., Woodhead, J., Hergt, J. (2011): Iolite: Freeware for the visualisation and processing of mass spectrometric data, *Journal of Analytical Atomic Spectrometry* **26**: 2508-2518.

Pires, D.O., Silva, J.C., Bastos, N.D. (2014): Reproduction of deep-sea reef building corals from the southwestern Atlantic, *Deep-Sea Research Part II* **99**: 51-63.

Politi, Y., Batchelor, D.R., Zaslansky, P., Chmelka, B.F., Weaver, J.C., Sagi, I., Weiner, S., Addadi, L. (2010): Role of Magnesium Ion in the Stabilization of Biogenic Amorphous Calcium Carbonate: A Structure - Function Investigation, *Chemistry of Materials* **22**: 161-166.

Pons-Branchu, E., Hillaire-Marcel, C., Deschamps, P., Ghaleb, B., Sinclair, D.J. (2005): Early diagenesis impact on precise U-series dating of deep-sea corals: Example of a 100-200-year old *Lophelia pertusa* sample from the northeast Atlantic, *Geochimica et Cosmochimica Acta* **69**(20): 4865-4879.

Pretet, C., Reynaud, S., Ferrier-Pagès, C., Gattuso, J.-P., Kamber, B.S., Samankassou, E. (2014): Effect of salinity on the skeletal chemistry of cultured scleractinian

zooxanthellate corals: Cd/Ca ratio as a potential proxy for salinity reconstruction, *Coral Reefs* **33**: 169-180.

Puig, P., Canals, M., Company, J.B., Martín, J., Amblas, D., Lastras, G., Palanques, A., Calafat, A.M. (2012): Ploughing the deep sea floor, *Nature* **489**: 286-290.

Purser, A., Orejas, C., Gori, A., Tong, R., Unnithan, V., Thomsen, L. (2013): Local variation in the distribution of benthic megafauna species associated with cold-water coral reefs on the Norwegian margin, *Continental Shelf Research* **54**: 37-51.

Putten, E.V., Dehairs, F., Keppens, E., Baeyens, W. (2000): High resolution distribution of trace elements in the calcite shell layer of modern Mytilus edulis: Environmental and biological controls, *Geochimica et Cosmochimica Acta* **64**(6): 997-1011.

Raddatz, J., Liebetrau, V., Rüggeberg, A., Hathorne, E., Krabbenhöft, A., Eisenhauer, A., Böhm, F., Vollstaedt, H., Fietzke, J., López Correa, M., Freiwald, A., Dullo, W.-C. (2013): Stable Sr-isotope, Sr/Ca, mg/Ca, Li/Ca and Mg/Li ratios in the scleractinian cold-water coral *Lophelia pertusa*, *Chemical Geology* **352**: 143-152.

Raddatz, J., Rüggeberg, A., Flögel, S., Hathorne, E.C., Liebetrau, V., Eisenhauer, A., Dullo, W.-C. (2014): The influence of seawater pH on U/Ca ratios in the scleractinian cold-water coral *Lophelia pertusa*, *Biogeosciences* **11**: 1863-1871.

Reitner, J. (2005): Calcifying extracellular mucus substrates (EMS) of *Madrepora oculata* - a first geobiological approach, in A. Freiwald, J.M. Roberts (Eds): *Cold-water Corals and Ecosystems*, Berlin Heidelberg: Springer Verlag: 731-744.

Rengstorf, A.M., Yesson, C., Brown, C., Grehan, A.J. (2013): High-resolution habitat suitability modelling can improve conservation of vulnerable marine ecosystems in the deep sea, *Journal of Biogeography* **40**: 1702-1714.

Risk, M.J., Heikoop, J.M., Snow, M.G., Beukens, R. (2002): Lifespans and growth patterns of two deep-sea corals: *Primnoa resedaeformis* and *Desmophyllum cristagalli*, *Hydrobiologia* **471**: 125-131.

Rix, L., de Goeij, J.M., Mueller, C.E., Struck, U., Middelburg, J.J., van Duyl, F.C., Al-Horani, F.A., Wild, C., Naumann, M.S., van Oevelen, D. (2016) Coral mucus fuels the sponge loop in warm- and cold-water coral reef ecosystems, *Scientific Reports* **6**: 18715. doi:10.1038/srep18715.

Roberts, J.M. (2002): The occurrence of the coral *Lophelia pertusa* and other conspicuous epifauna around an oil platform in the North Sea, *Journal of the Society for Underwater Technology* **25**: 83-91.

Roberts, J.M. (2005): Reef-aggregating behaviour by symbiotic eunicid polychaetes from cold-water corals: do worms assemble reefs? *Journal of the Marine Biological Association of the United Kingdom* **85**: 813-819.

Roberts, J.M., Davies, A.J., Henry, L.A., Dodds, L.A., Duineveld, G.C.A., Lavaleye, M.S.S., Maier, C., van Soest, R.W.M., Bergman, M.J.N., Hühnerbach, V., Huvenne, V.A.I., Sinclair, D.J., Watmough, T., Long, D., Green, S.L., van Haren, H. (2009a): Mingulay reef complex: an interdisciplinary study of cold-water coral habitat, hydrography and biodiversity, *Marine Ecology Progress Series* **397**: 139-151.

Roberts, J.M., Long, D., Wilson, J.B., Mortensen, P.B., Gage, J.D. (2003): The cold-water coral *Lophelia pertusa* (Scleractinia) and enigmatic seabed mounds along the north-east Atlantic margin: are they related? *Marine Pollution Bulletin* **46**: 7-20.

Roberts, J.M., Wheeler, A.J., Freiwald, A., Cairns, SD (2009b): *Cold-water corals: The biology and Geology of Deep-Sea Coral Habitats*, Cambridge: Cambridge University Press. ISBN 978-0-521-88485-3.

Robinson L.F., Adkins J.F., Fernandez D.P., Burnett D.S., Wang S.-L., Gagnon A.C. and Krakauer N. (2006): Primary U distribution in scleractinian corals and its implications for U series dating, *Geochemistry Geophysics Geosystems* **7**(5): Q05022. doi:10.1029/2005GC001138.

Rollion-Bard, C., Blamart, D. (2015): Possible controls on Li, Na, and Mg incorporation into aragonite coral skeletons, *Chemical Geology* **396**: 98-111.

Rollion-Bard, C., Blamart, D., Cuif, J.-P., Dauphin, Y. (2010): *In situ* measurements of oxygen isotopic composition in deep-sea coral, *Lophelia pertusa*: Re-examination of the current geochemical models of biomineralization, *Geochimica et Cosmochimica Acta* **74**: 1338-1349.

Rollion-Bard, C., Blamart, D., Cuif, J.-P., Juillet-Leclerc, A. (2003): Microanalysis of C and O isotopes of azooxanthellate and zooxanthellate corals by ion microprobe, *Coral Reefs* **22**, 405-415.

Rollion-Bard, C., Blamart, D., Trebosc, J., Tricot, G., Mussi, A., Cuif, J.-P. (2011): Boron isotopes as pH proxy: A new look at boron speciation in deep-sea corals using ^{11}B MAS NMR and EELS, *Geochimica et Cosmochimica Acta* **75**: 1003-1012.

Rollion-Bard, C., Vigier, N., Meiborn, A., Blamart, D., Reynaud, S., Rodolfo-Metalpa, R., Martin, S., Gattuso, J.-P. (2009): Effect of environmental conditions and skeletal ultrastructure on the Li isotopic composition of scleratinian corals, *Earth and Planetary Science Letters* **286**: 63-70.

Rüggeberg, A., Fietzke, J., Liebetrau, V., Eisenhauer, A., Dullo, W.-C., Freiwald, A. (2008): Stable strontium isotope ($\delta^{88/86}$Sr) in cold-water corals - a new proxy for reconstruction of intermediate ocean water temperatures, *Earth and Planetary Science Letters* **269**(3/4): 570-575.

Ryan-Keogh, T.J., Macey, A.I., Nielsdóttir, M.C., Lucas, M.I., Steigenberger, S.S., Stinchcombe, M.C., Achterberg, E.P., Bibby, T.S., Moore, C.M. (2013): Spatial and temporal development of phytoplankton iron stress in relation to bloom dynamics

in the high-latitude North Atlantic Ocean, *Limnology and Oceanography* **58**(2): 533-545.

Sabatier, P., Reyss, J.-L., Hall-Spencer, J.M., Colin, C., Frank, N., Tisnérat-Laborde, N., Bordier, L., Douville, E. (2012): ^{210}Pb-^{226}Ra chronology reveals rapid growth rate of *Madrepora oculata* and *Lophelia pertusa* on world's largest cold-water coral reef, *Biogeosciences* **9**: 1253-1265.

Saenger, C., Cohen, A.L., Oppo, D.W., Hubbard, D. (2008): Interpreting sea surface temperature from strontium/calcium ratios in *Montastrea* corals: Link with growth rate and implications for proxy reconstructions, *Paleoceanography* **23**: PA3102. doi:10.1029/2007PA001572.

Savini, A., Vertino, A., Marchese, F., Beuck, L., Freiwald, A. (2014): Mapping Cold-Water Coral Habitats at Different Scales within the Northern Ionian Sea (Central Mediterranean): An Assessment of Coral Coverage and Associated Vulnerability, *PLoS ONE* **9**(2): e102406. doi:10.1371/journal.pone.0102405.

Schmidt, G.A., Bigg, G.R., Rohling, E.J. (1999): Global Seawater Oxygen-18 Database - v1.21. `http://data.giss.nasa.gov/o18data/`

Schmidt, S. (2006): Impact of the Mediterranean Outflow Water on particle dynamics in intermediate waters of the Northeast Atlantic, as revealed by ^{234}Th and ^{228}Th, *Marine Chemistry* **100**(3-4): 289-298.

Schöttner, S., Hoffmann, F., Wild, C., Rapp, H.T., Boetius, A., Ramette, A. (2009): Inter- and intra-habitat bacterial diversity associated with cold-water corals, *The International Society for Microbial Ecology Journal* **3**: 756-759.

Schott, F.A., McCreary Jr, J.P. (2001): The monsoon circulation of the Indian Ocean, *Progress in Oceanography* **51**: 1-123.

Schroeder, W.W. (2002): Observations of *Lophelia pertusa* and the surficial geology at a deep-water site in the northeastern Gulf of Mexico, *Hydrobiologia* **471**: 29-33.

Shanks, A.L., Trent, J.D. (1980) Marine snow: sinking rates and potential role in vertical flux, *Deep-Sea Research* **27A**: 137-143.

Shelton, G.A.B (1980): *Lophelia pertusa* (L.): Electrical conduction and behaviour in a deep-water coral, *Journal of the Marine Biological Association of the United Kingdom* **60**: 517-528.

Shen, G.T., Boyle, E.A. (1988): Determination of Lead, Cadmium and other trace metals in annually-banded corals, *Chemical Geology* **67**: 47-62.

Shen, G.T., Boyle, E.A., Lea, D.W. (1987): Cadmium in corals as a tracer of historical upwelling and industrial fallout, *Nature* **328**: 794-796.

Shen, G.T., Dunbar, R.B. (1995): Environmental controls on uranium in reef corals, *Geochimica et Cosmochimica Acta* **59**(10): 2009-2024.

Shirai, K., Kusakabe, M., Nakai, S., Ishii, T., Watanabe, T., Hiyagon, H., Sano, Y. (2005): Deep-sea coral geochemistry: Implication for the vital effect, *Chemical Geology* **224**: 212-222.

Siegel, D.A., Deuser, W.G. (1997) Trajectories of sinking particles in the Sargasso Sea: modeling of statistical funnels above deep-ocean sediment traps, *Deep-Sea Research Part I* **44**(9-10): 1519-1541.

Sinclair, D.J., Risk, M.J. (2006): A numerical model of trace-element coprecipitation in a physicochemical calcification system: Application to coral biomineralization and trace-element 'vital effects', *Geochimica et Cosmochimica Acta* **70**: 3855-3868.

Sinclair, D.J., Williams, B., Risk, M. (2006): A biological origin for climate signals in corals - Trace element 'vital effects' are ubiquitous in Scleractinian coral skeletons, *Geophysical Research Letters* **33**: L17707. doi:10.1029/2006GL027183.

Smith, J.E., Schwarcz, H.P., Risk, M.J. (2000): Paleotemperatures From Deep-Sea Corals: Overcoming 'Vital Effects', *Palaios* **15**: 25-32.

Smith, J.E., Schwarcz, H.P., Risk, M.J. (2002): Patterns of isotopic disequilibria in azooxanthellate coral skeleton, *Hydrobiologia* **471**: 111-115.

Speer, J.A. (1983): Crystal chemistry and phase relations of orthorhombic carbonates, *Reviews in Mineralogy and Geochemistry* **11**: 145-190.

Spiro, B., Roberts, M., Gage, J., Chenery, S. (2000): $^{18}O/^{16}O$ and $^{13}C/^{12}C$ in an ahermatypic deep-water coral *Lophelia pertusa* from the North Atlantic: a case of disequilibrium isotope fractionation, *Rapid Communications in Mass Spectrometry* **14**: 1332-1336.

Stecher III, H.A., Krantz, D.E., Lord III, C.J., Luther III, G.W., Bock, K.W. (1996): Profiles of strontium and barium in Mercenaria mercenaria and Spisula solidissima shells, *Geochimica et Cosmochimica Acta* **60**(18): 3445-3456.

Steel, C., Henchman, M. (1998) Understanding the Quadrupole Mass Filter through Computer Simulation, *Journal of Chemical Education* **75**(8): 1049-1054.

Stevenson, A., Rocha, C. (2013): Evidence for the bioerosion of deep-water corals by echinoids in the Northeast Atlantic, *Deep-Sea Research Part I* **71**: 73-78.

Stolarski, J. (2003): Three-dimensional micro- and nanostructural characteristics of the scleractinian coral skeleton: A biocalcification proxy, *Acta Palaeontologica Polonica* **48**(4): 497-530.

Strömberg, S.M., Lundälv, T., Goreau, T.J. (2010): Suitability of mineral accretion as a rehabilitation method for cold-water coral reefs, *Journal of Experimental Marine Biology and Ecology* **395**: 153-161.

Swart, P.K., Hubbard, J.A.E.B. (1982): Uranium in Scleractinian Coral Skeletons, *Coral Reefs* **1**: 13-19

Tambutté, E. Allemand D., Mueller, E., Jaubert J. (1996): A compartmental approach to the mechanism of calcification in hermatypic corals, *The Journal of Experimental Biology* **199**: 1029-1041.

Tambutté, E., Tambutté, S., Segonds, N., Zoccola, D., Venn, A., Erez J., Allemand, D. (2011): Calcein labelling and electrophysiology: insights on coral tissue permeability and calcification, *Proceedings of the Royal Society B* **279**(1726): 19-27.

Taviani, M., Freiwald, A., Zibrowius, H. (2005): Deep coral growth in the Mediterranean Sea: an overview, in A. Freiwald, J.M. Roberts (eds.): *Cold-water Corals and Ecosystems*, Berlin Heidelberg: Springer Verlag: 137-156.

Thiem, Ø, Ravagnan, E., Fosså, J.H., Berntsen, J. (2006): Food supply mechanisms for cold-water corals along a continental shelf edge, *Journal of Marine Systems* **60**: 207-219.

Thomas, R. (2013) Practical Guide to ICP-MS: a tutorial for beginners, 3^{rd} edition, CRC Press, Taylor & Francis Group, Boca Raton, FL, USA.

Towle, E.K., Enochs, I.C., Langdon, C. (2015): Threatened Caribbean Coral Is Able to Mitigate the Adverse Effects of Ocean Acidification on Calcification by Increasing Feeding Rate, *PLoS ONE* **10**(4): e0123394. doi:10.1371/journal.pone.0123394.

Trotter, J., Montagna, P., McCulloch, M., Silenzi, S., Reynaud, S., Mortimer, G., Martin, S., Ferrier-Pagès, C., Gattuso, J.-P., Rodolfo-Metalpa, R. (2011): Quantifying the pH 'vital effect' in the temperate zooxanthellate coral *Cladocora caespitosa*: Validation of the boron seawater pH proxy, *Earth and Planetary Science Letters* **303**: 163-173.

Tveteraas, A., Bryant, P. (2003): Norwegian coldwater coral protection - Setting an international example in marine conservation, WWF newsletter, *Gift to the Earth* **86**: 1-2.

Twining, B.S., Nodder, SD, King, A.L., Hutchins, D.A., LeCleir, G.R., DeBruyn, J.M., Maas, E.W., Vogt, S., Wilhelm, S.W., Boyd, P.W. (2014): Differential remineralization of major and trace elements in sinking diatoms, *Limnology and Oceanology* **59**(3): 689-704.

Ubide, T., McKenna, C.A., Chew, D.M., Kamber, B.S. (2015): High-resolution LA-ICP-MS trace element mapping of igneous minerals: In search of magma histories, *Chemical Geology* **409**: 157-168.

van de Locht, R., Verch, A., Saunders, M., Dissard, D., Rixen, T., Moya, A., Krüger, R. (2013): Microstructural evolution and nanoscale crystallography in scleractinian coral spherulites, *Journal of Structural Biology* **183**: 57-65.

Waller, R.G., Tyler, P.A. (2005): The reproductive biology of two deep-water, reef-building scleractinians from the NE Atlantic Ocean, *Coral Reefs* **24**: 514-522.

Wall, M., Ragazzola, F., Foster, L.C., Form, A., Schmidt, D.N. (2015): Enhanced pH up-regulation enables the cold-water coral *Lophelia pertusa* to sustain growth in aragonite undersaturated conditions, *Biogeosciences* **12**: 6757-6781.

Watson, B. E. (1996): Surface enrichment and trace-element uptake during crystal growth, *Geochimica et Cosmochimica Acta* **60**: 5013-5020.

Weaver, P., Boetius, A., Danovaro, R., Freiwald, A., Gunn, V., Heussner, S., Morato, T., Schewe, I., van den Hove, S. (2009): The Future of Integrated Deep-Sea Research in Europe: The HERMIONE Project, HERMES Special Issue Feature, *Oceanography* **22**(1): 170-183.

Weiner, S., Dove, P.M. (2003): An Overview of Biomineralization Processes and the Problem of the Vital Effect, in P.M. Dove, J.J. De Yoren, S. Winer (Eds): *Biomineralization, Reviews in Mineralogy and Geochemistry* **54**, Washington, U.S.A: Mineralogical Society of America: 1-29.

Wheeler, A.J., Kozachenko, M., Henry, L.-A., Foubert, A., de Haas, H., Huvenne, V.A.I., Masson, D.G., Olu, K. (2011): The Moira Mounds, small cold-water coral banks in the Porcupine Seabight, NE Atlantic: Part A - an early stage growth phase for future coral carbonate mounds? *Marine Geology* **282**: 53-64.

White, M., Dorschel, B. (2010): The importance of the permanent thermocline to the cold water coral carbonate mound distribution in the NE Atlantic, *Earth and Planetary Science Letters* **296**: 395-402.

White, M., Mohn, C., de Stigter, H., Mottram, M. (2005): Deep-water coral development as a function of hydrodynamics and surface productivity around the submarine banks of the Rockall Trough, NE Atlantic In: A. Freiwald, J.M. Roberts (eds.): *Cold-water Corals and Ecosystems*, Berlin Heidelberg: Springer Verlag: 503-514.

White, M., Mohn, C., Orren, M.J. (1998): Nutrient distributions across the Porcupine Bank, *ICES Journal of Marine Science* **55**: 1082-1094.

White, M., Roberts, J.M., van Weering, T. (2007): Do bottom-intensified diurnal tidal currents shape the alignment of carbonate mounds in the NE Atlanic? *Geo-Marine Letters* **27**: 391-397.

Wienberg, C., Wintersteller, P., Beuck, L., Hebbeln, D. (2013): Coral Patch seamount (NE Atlantic) - a sedimentological and megafaunal reconnaissance based on video and hydroacoustic surveys, *Biogeoscience* **10**: 3421-3443.

Wild, C., Naumann, M., Niggl, W., Haas, A. (2010): Carbohydrate composition of mucus released by scleractinian warm- and cold-water reef corals, *Aquatic Biology* **10**: 41-45.

Wild, C., Rasheed, M., Werner, U., Franke, U., Johnstone, R., Huettel, M. (2004): Degradation and Mineralization of Coral Mucus in Reef Environments, *Marine Ecology Progress Series* **267**: 159-171.

Wilson, J.B. (1979): 'Patch' development of the deep-water coral *Lophelia pertusa* (L.) on Rockall Bank, *Journal of the Marine Biological Association of the United Kingdom* **59**: 165-177.

Wilson, A.M., Raine, R., Mohn, C., White, M. (2015): Nepheloid layer distribution in the Whittard Canyon, NE Atlantic Margin, *Marine Geology* **367**: 130-142.

Wilson, M.F.J., O'Connell, B., Brown, C., Guinan, J.C., Grehan, A.J. (2007): Multiscale Terrain Analysis of Multibeam Bathymetry Data for Habitat Mapping on the Continental Slope, *Marine Geology* **30**: 3-35.

Zeebe, R.E. (2005): Stable boron isotope fractionation between dissolved $B(OH)_3$ and $B(OH)_4^-$, *Geochimica et Cosmochimica Acta* **69**(11): 2753-2766.

Zoccola, D., Tambutté, E., Kulhanek, E., Puverel, S., Scimeca, J.-C., Allemand, D., Tambutté, S. (2004): Molecular cloning and localization of a PMCA P-type calcium ATPase from the coral *Stylophora pistillata*, *Biochimica et Biophysica Acta (BBA) - Biomembranes* **1663**(1-2): 117-126.

Zoccola, D., Tambutté, E., Sénégas-Balas, F., Michiels, J.-F., Failla, J.-P., Jaubert, J., Allemand, D. (1999): Cloning of a calcium channel $\alpha 1$ subunit from the reef-building coral, Stylophora pistillata, *Gene* **227**(2): 157-167.

Part VI

Appendix

Appendix A

Selected scleractinian species from the Irish shelf

A.1 *Lophelia pertusa* Specimens

1033	Porcupine Bank: *L. pertusa* branch with *Eunice norvegica* tube along most of the growth strengthening the central branch.
1036	Porcupine Bank: *L. pertusa* branch with partly uncalcified *E. norvegica* tube.
1587	Whittard Canyon: *L. pertusa* colony with a system of *E. norvegica* tubes integrated between the branches.
1447	Whittard Canyon: White *L. pertusa* colony with *E. norvegica* tube in an earlier stage stabilizing the base.
1446	Whittard Canyon: Pink *L. pertusa* (with *E. norvegica* tube) collected together with white specimen 1447. Both samples show grew in direct contact but show distinct differences in branch morphology and thickening.
1029	Porcupine Bank: Thin-branched *L. pertusa* grew in symbiosis with a number of molluscs and octocorals.
1534	Whittard Canyon: The colony of *L. pertusa* settled on and with a accumulation of short-cupped *D. dianthus* and octocorals.
1450	Whittard Canyon: A large dead colony of *L. pertusa* not only provides the ground for new *L. pertusa* settlement but also allows *E. norvegica* to move from the dead corals to the live ones.
1540	Whittard Canyon: *L. pertusa* branch piece with rests of organic *E. norvegica* tube.

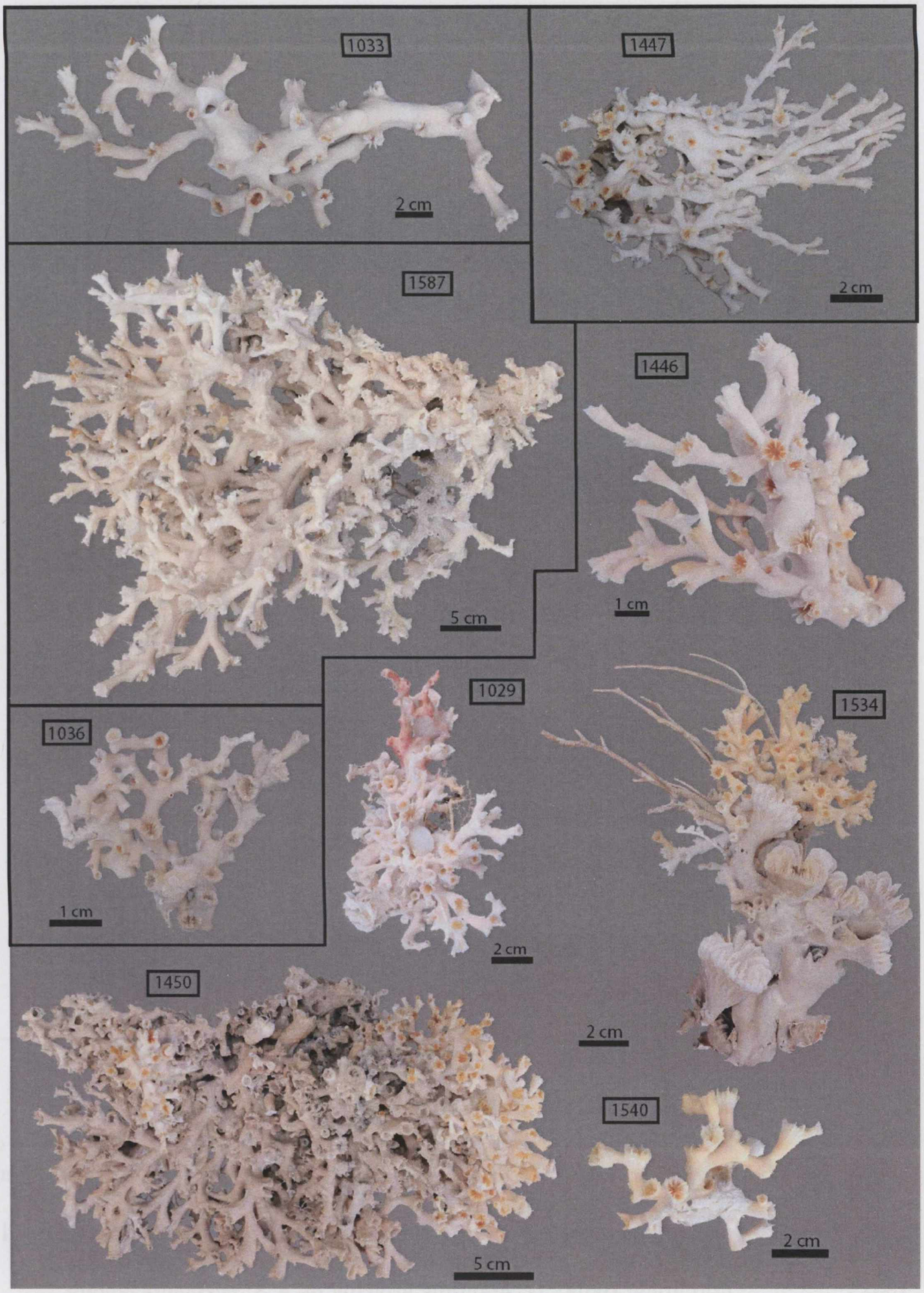


Figure A.1: *Lophelia pertusa* specimens collected from the Whittard Canyon and Porcupine Bank during CE13008. Samples selected for geochemical analysis in boxes.

A.2 *Desmophyllum dianthus* Specimens

1526	Whittard Canyon: Two *D. dianthus* attached at base. The samples show a lighter layer covering a large part underneath the septal face.
1535	Whittard Canyon: A group of *D. dianthus* with lower cup height provides the base for an assemblage of hexa- and octocorals to grow on.
1453	Whittard Canyon: Three *D. dianthus* growing attached to each other. It appears that the left cup developed the wider calice seen in more mature specimens and then either reassumed growth or was resettled by another *D. dianthus*.
1352	Porcupine Bank: *D. dianthus* growing on a *S. variabilis* colony.
1088	Porcupine Bank: Three *D. dianthus* cup corals grow on a dead soft coral branch. The cups are fastened by extensive calcification.
458-C1 to -C4	Whittard Canyon: the four *D. dianthus* specimens collected during CE12006 show different states of bioerosion along the lower part of the corallite. C3 and C4 show pseudo-branching with a younger *D. dianthus* attached to the side of the corallite.

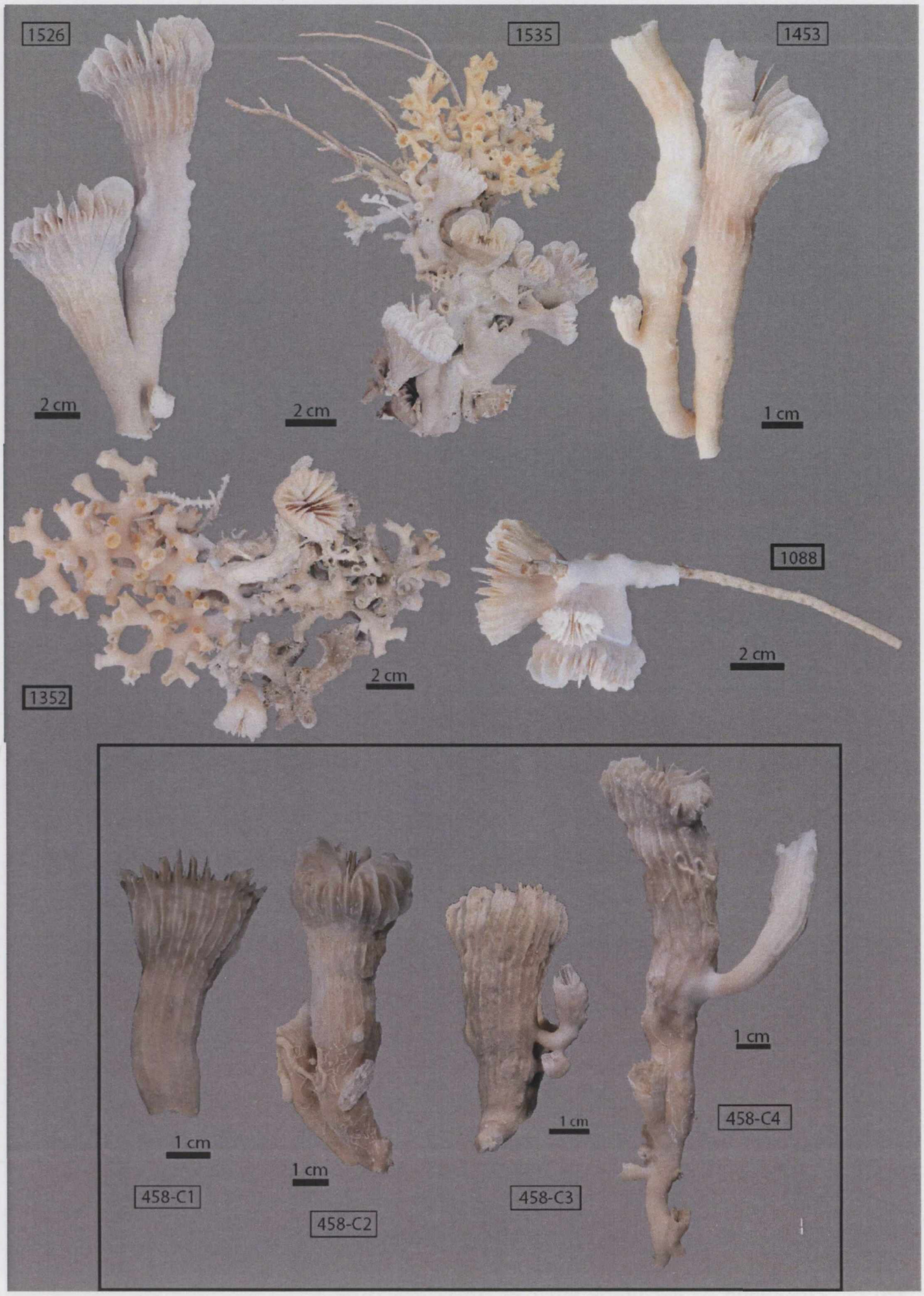


Figure A.2: *Desmophyllum dianthus* specimens collected from the Whittard Canyon and Porcupine Bank during CE12006 and CE13008. Samples selected for geochemical analysis in boxes.

A.3 *Solenosmilia variabilis* Specimens

1239	*S. variabilis* colony on dead colony. Bamboo corals are often found growing with *S. variabilis.*
1247	*S. variabilis* on dead *Enallopsammia rostrata* branch.
1351	*S. variabilis* with *Eunice norvegica* tube growing on dead colony.
1372	Thickened *S. variabilis* with *E. norvegica* tube.
1355	Thin-branched *S. variabilis* growing on dead colony.
1361	Thickened *S. variabilis* in symbiosis with *E. norvegica.*
1226	Thin-branched *S. variabilis* with long distances between corallites. Budding events here appear less regular.
1151	Thickened *S. variabilis.*
1353	*S. variabilis* with octocoral growing in and around the encalcified *E. norvegica* tubes.

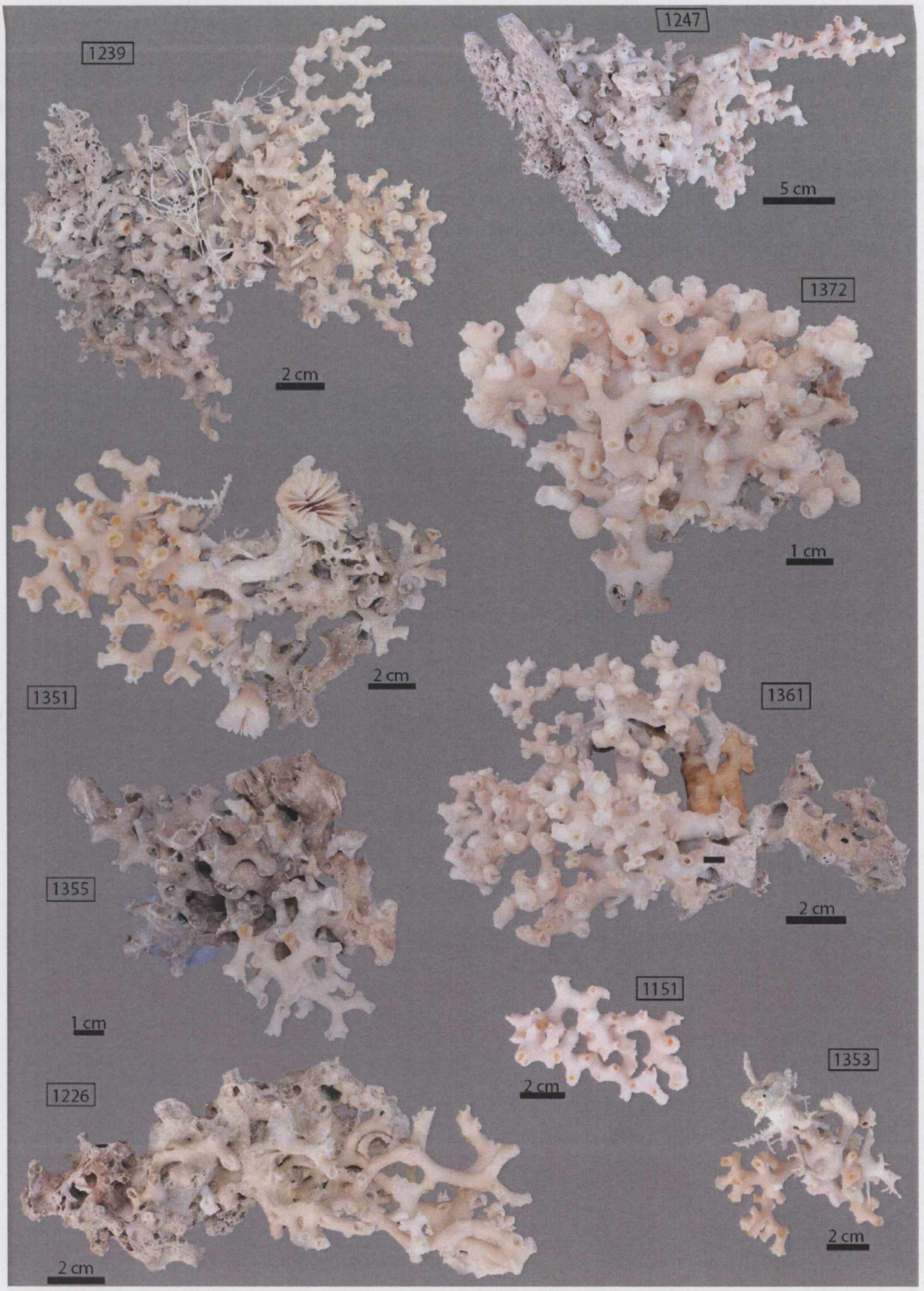


Figure A.3: *Solenosmilia variabilis* specimens collected from the Porcupine Bank during CE13008.

A.4 *Madrepora oculata* Specimens

1009	Porcupine Bank: *M. oculata* colony strengthened by network of *E. norvegica* tubes.
1051	Porcupine Bank: Thickened *M. oculata* branches with additional *E. norvegica* tube strengthening.
1589	Whittard Canyon: Thin-branched *M. oculata* colony stabilized by *E. norvegica* tubes.
459-M1	Whittard Canyon: *M. oculata* branches with *E. norvegica* grow in all directions.
459-M2	Whittard Canyon: *M. oculata* with *E. norvegica* tubes.

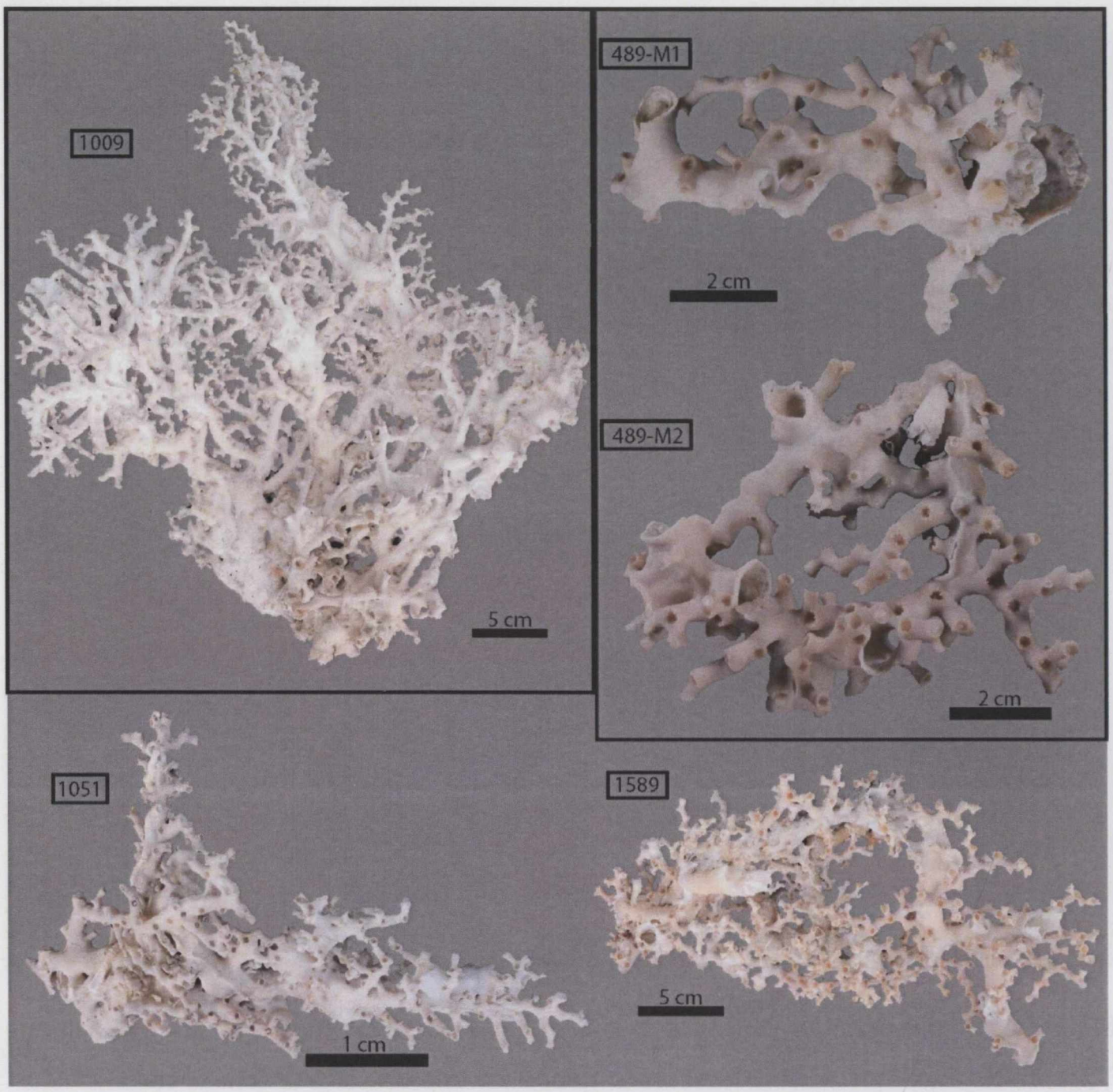


Figure A.4: *Madrepora oculata* specimens collected from the Whittard Canyon and Porcupine Bank during CE12006 and CE13008. Samples selected for geochemical analysis in boxes.

A.5 *Enallopsammia rostrata* Specimens

1233/1234	Fan-shaped colony of *E. rostrata* with *S. variabilis* growing in the center. No polychaete tubes are found in connection with *E. rostrata*.
1221	Dead (top part, greyish colour) and live portion (in white) of *E. rostrata*. Polyps only sit on one side of the branches in the center of the sheltering fan-shape.

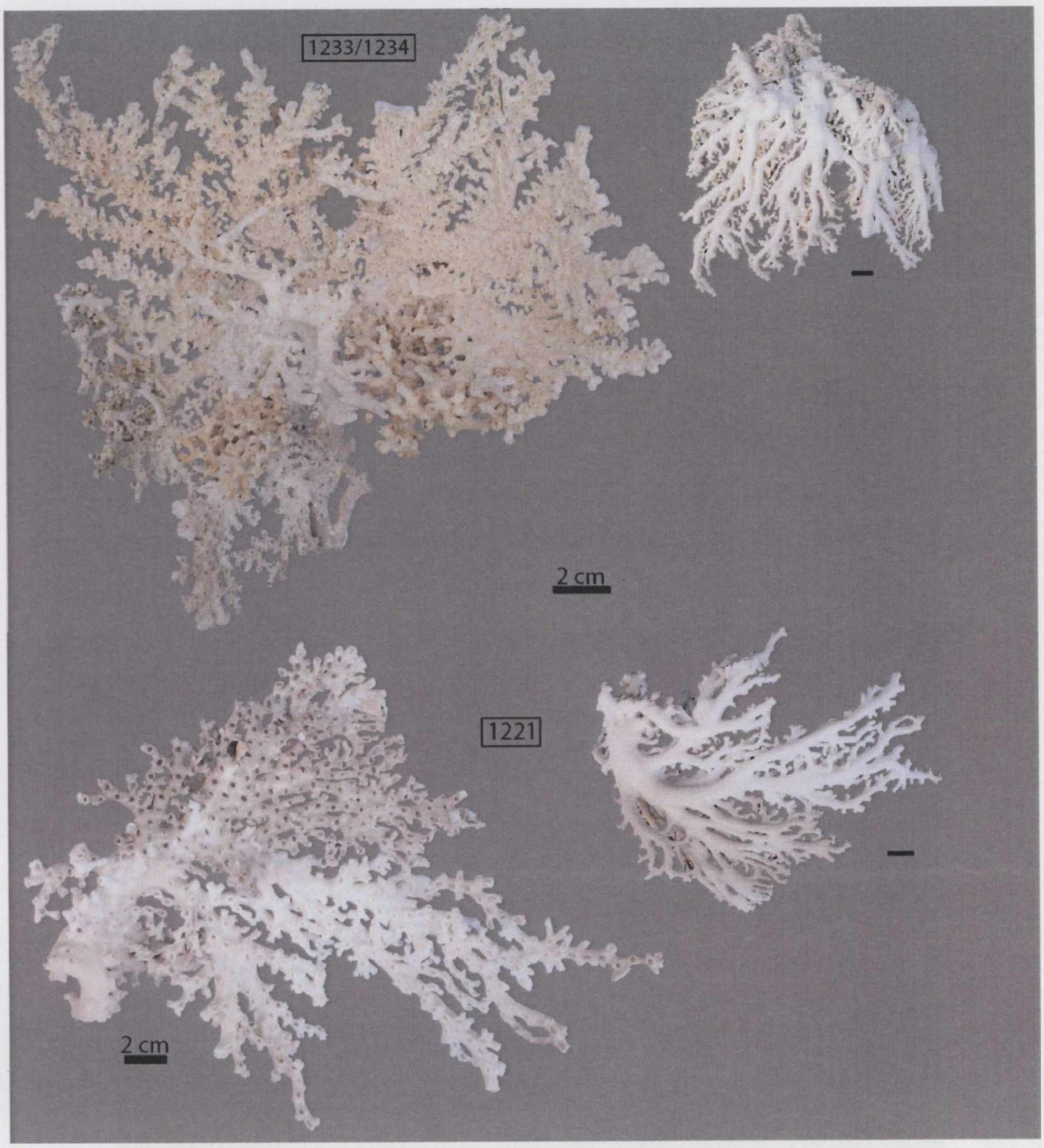


Figure A.5: *Enallopsammia rostrata* specimens collected from the Porcupine Bank during CE12006 and CE13008.

Appendix B

M. oculata Branches for Temperature Reconstruction

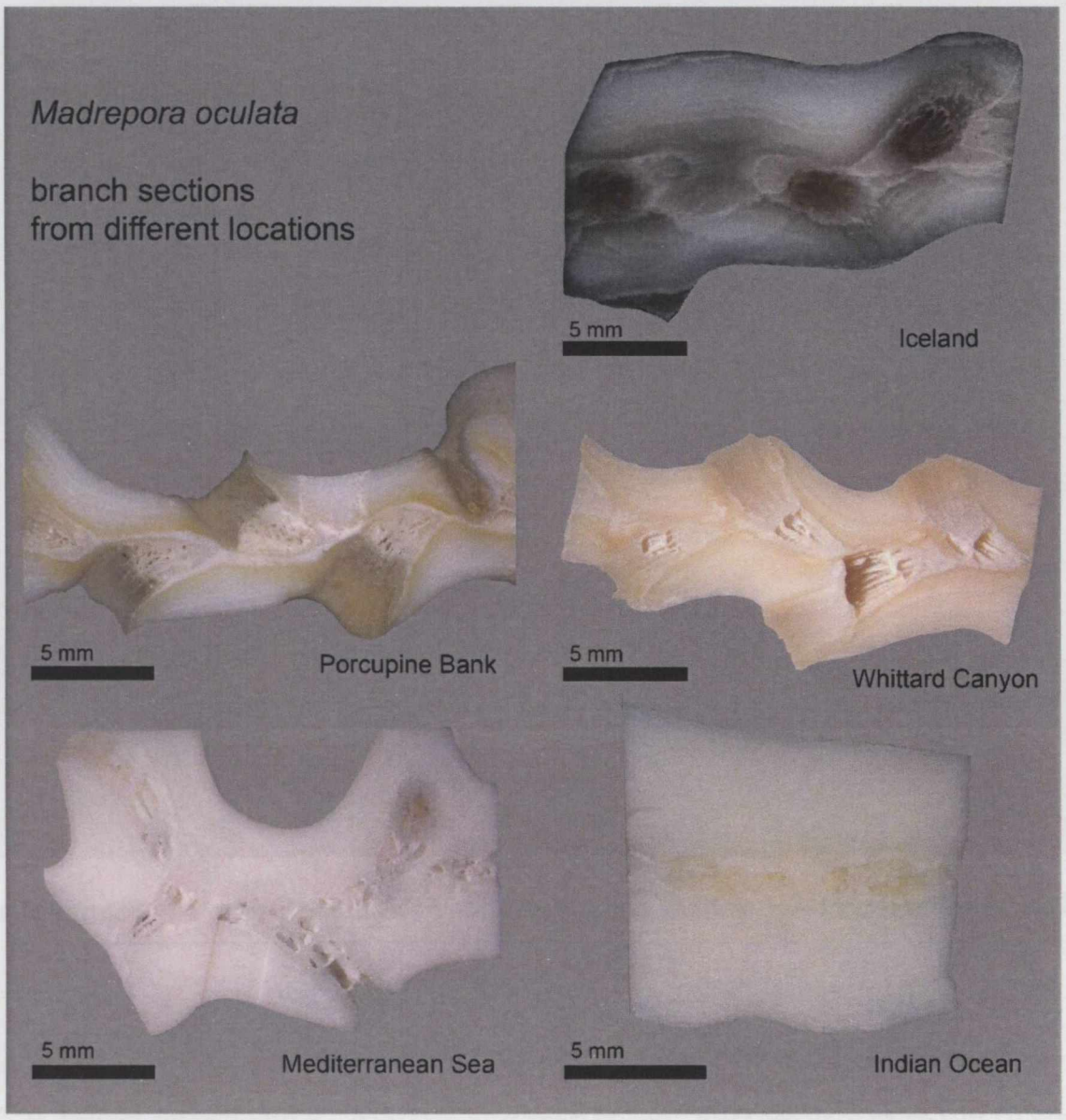


Figure B.1: Microstructural layers visible in the *M. oculata* branch cross sections from different locations.

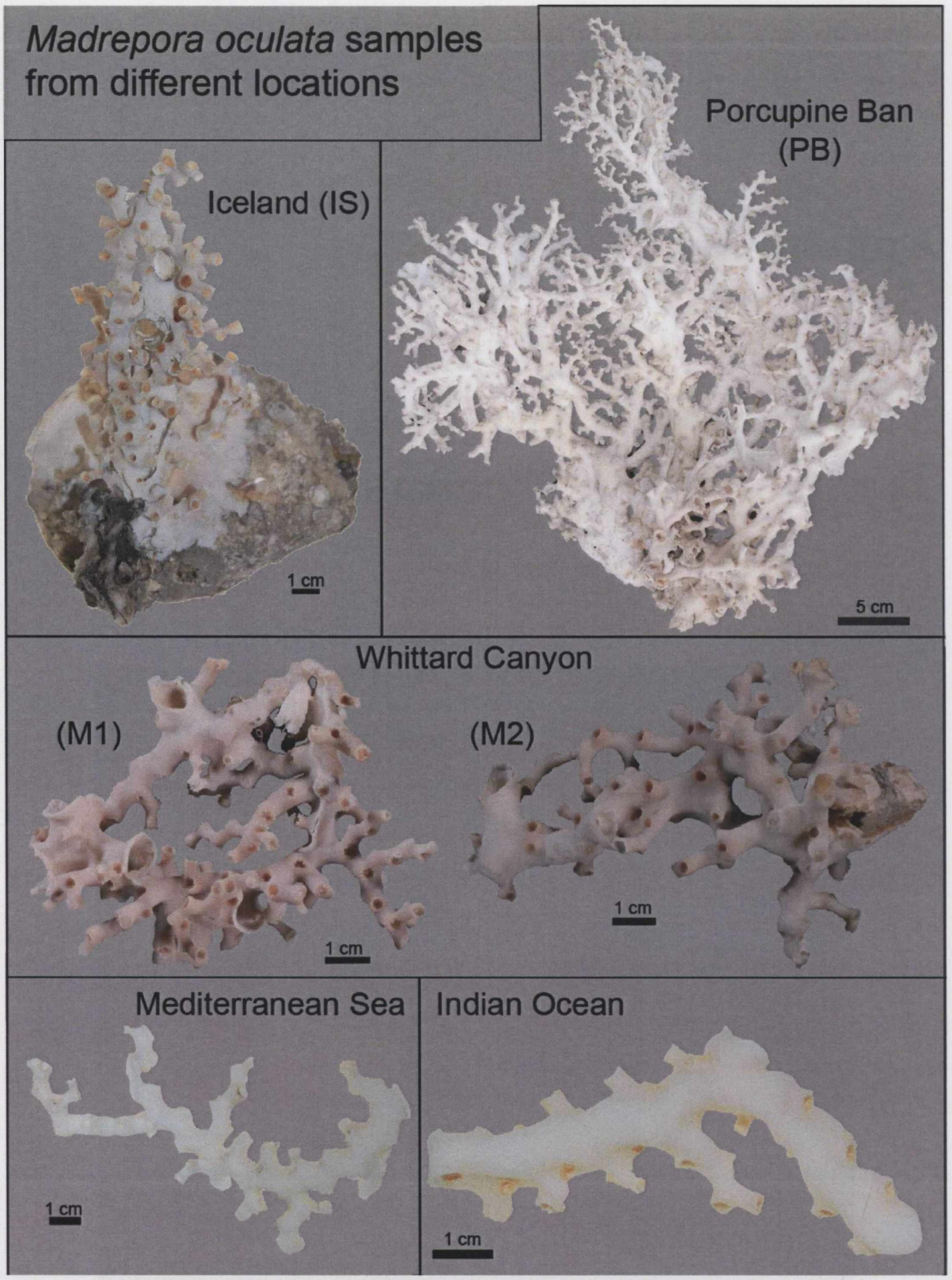


Figure B.2: A selection of *M. oculata* colony provides the basis for testing temperature reconstruction.

Appendix C

Initial Tests for LA-ICP-MS

In order to specify appropriate analytes, spotsizes and scan speeds for the study a series of initial tests was run along the cross section of the *L. pertusa* theca prior to analysis. The cross section displays a number of visible white layers. The laser ablation lines for the initial tests are positioned perpendicular to the layer orientation. Each set of three lines is bracketed by two NIST612 ablation lines which is insufficient for information on precision but gives insight into the accuracy.

C.1 Specifying Spotsize and Scan Speed

Table C.1: Initial test 1 - spotsize and scan speed: First set of tested elements and their concentrations in standard material and sample. Spotsize 8 μm was run at 4 μm/s, spotsize 15 μm at 6 μm/s, spotsize 30 μm at 10 μm/s.

		NIST612		**sample**		
Spotsize	Element	$Conc_{meas}$	$Conc_{accept}$	$Conc_{meas}$	2 SD	RSD
8μm	^{25}Mg	68.0	68.0	883	49	5.6%
	^{88}Sr	78.4	78.4	8571	74	0.87%
	^{137}Ba	39.3	39.3	14.47	0.94	6.5%
	^{238}U	37.38	37.38	3.32	0.22	6.7%
15μm	^{25}Mg	68.0	68.0	847	12	1.4%
	^{88}Sr	78.4	78.4	8381	10	0.12%
	^{137}Ba	39.3	39.3	12.81	0.61	4.7%
	^{238}U	37.38	37.38	3.42	0.082	2.4%
30μm	^{25}Mg	68.0	68.0	814	29	3.5%
	^{88}Sr	78.4	78.4	7820	160	2.1%
	^{137}Ba	39.3	39.3	11.93	0.38	3.2%
	^{238}U	37.37	37.38	3.24	0.33	10%

Table C.2: Initial tests 2 and 3 - spotsize and scan speed: Further sets were run to test elements of interest and their concentrations in standard material and sample. Spotsize 8 μm was run at 4 μm/s, spotsize 15 μm at 6 μm/s, spotsize 30 μm at 10 μm/s.

		NIST612		sample		
Spotsize	Element	$Conc_{meas}$	$Conc_{accept}$	$Conc_{meas}$	2 SD	RSD
8 μm	^{7}Li	40.2	40.2	0.91	0.70	77%
	^{11}B	34.4	34.3	58.6	3.3	5.6%
	^{31}P	275.5	46.6	36.0	18.0	50%
	^{232}Th	37.8	37.79	0.006	0.020	320%
15 μm	^{7}Li	40.2	40.2	0.97	0.24	25%
	^{11}B	34.3	34.3	61.4	2.9	4.7%
	^{31}P	46.6	46.6	27.0	5.7	21%
	^{232}Th	37.79	37.79	0.00123	0.00048	39%
30 μm	^{7}Li	40.2	40.2	0.788	0.14	17%
	^{11}B	34.3	34.3	61.72	0.32	0.52%
	^{31}P	46.6	46.6	22.7	3.4	15%
	^{232}Th	37.79	37.79	0.00127	0.00050	39%
8 μm	^{51}V	39.0	38.8	0.420	0.620	150%
	^{55}Mn	38.0	38.7	3.10	6.80	220%
	^{57}Fe	50.2	51.0	102.5	3.6	3.5%
	^{86}Sr	78.4	78.4	8600	460	5.4%
15 μm	^{51}V	39.0	38.8	0.129	0.059	45%
	^{55}Mn	38.0	38.7	1.01	0.23	210%
	^{57}Fe	51.0	51.0	119.4	0.6	0.52%
	^{86}Sr	78.4	78.4	8560	85	0.99%
30 μm	^{51}V	39.0	38.8	0.095	0.008	8.1%
	^{55}Mn	38.0	38.7	0.77	0.15	20%
	^{57}Fe	51.0	51.0	129.1	2.3	1.8%
	^{86}Sr	78.4	78.4	8070	100	1.2%

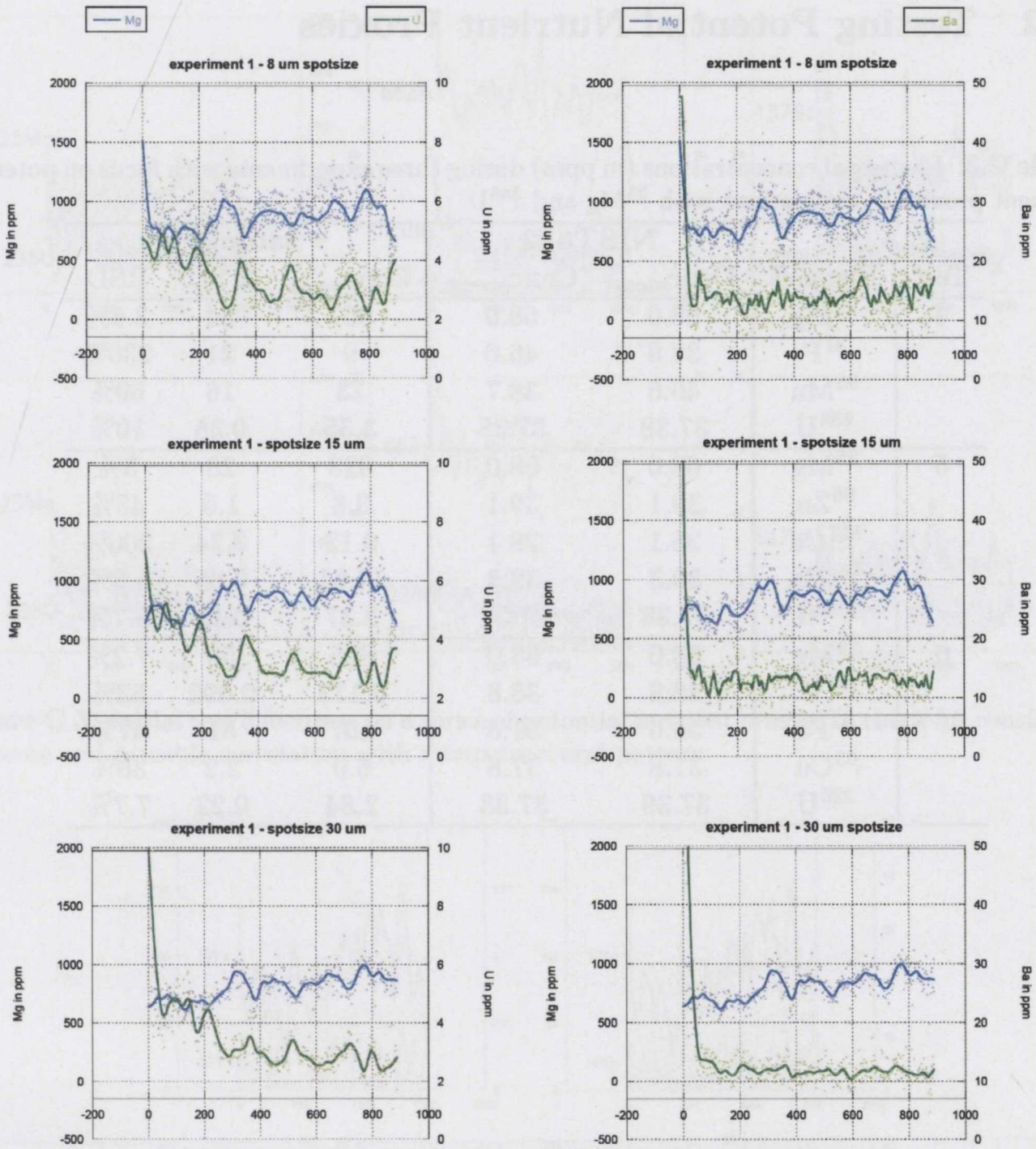


Figure C.1: Results for ^{25}Mg-^{238}U and ^{25}Mg-^{137}Ba patterns for different ablation spotsize. From top to bottom the variations in ^{25}Mg and ^{238}U and in ^{25}Mg and ^{137}Ba along each of the lines is shown for increaseing spotsizes.

The first experiment from the pretests along *L. pertusa* growth (L1) revealed a clear antithetical correlation between ^{25}Mg and ^{238}U but also some degree of correlation for ^{25}Mg and ^{137}Ba (fig. C.1). The variations in ^{25}Mg and ^{238}U are also correlated with visible alternating white and beige microstructural layers in the CWC skeleton with high ^{25}Mg concentrations correlated with white layers. While the prominent peaks in ^{25}Mg and ^{238}U are clear for all of the tested spotsizes when data points are weighted at 5% in Kaleidograph the larger spotsizes shows patterns more pronounced and less distorted by background noise. Therefore, a spotsize between 15 and 30 μm seems most suitable (see also tables C.1 and C.2).

C.2 Testing Potential Nutrient Proxies

Table C.3: Elemental concentrations (in ppm) during three experiments with focus on potential nutrient proxies in comparison with ^{25}Mg and ^{238}U.

		NIST612		sample		
Test	Element	$Conc_{meas}$	$Conc_{accept}$	$Conc_{meas}$	2 SD	RSD
4	^{25}Mg	68.0	68.0	957	34	3.6%
	^{31}P	38.8	46.6	9	21	230%
	^{55}Mn	46.6	38.7	23	16	69%
	^{238}U	37.38	37.38	3.35	0.35	10%
5	^{25}Mg	68.0	68.0	923	28	3%
	^{66}Zn	39.1	39.1	3.8	1.6	43%
	^{111}Cd	28.1	28.1	0.12	0.24	200%
	^{137}Ba	39.3	39.3	14.61	0.85	5.8%
	^{238}U	37.38	37.38	3.37	0.19	5.7%
6	^{25}Mg	68.0	68.0	805	58	7.2%
	^{51}V	38.8	38.8	0.173	0.092	53%
	^{57}Fe	50.6	51.0	107	51	47%
	^{63}Cu	37.8	37.8	6.0	2.2	36%
	^{238}U	37.39	37.38	2.84	0.22	7.7%

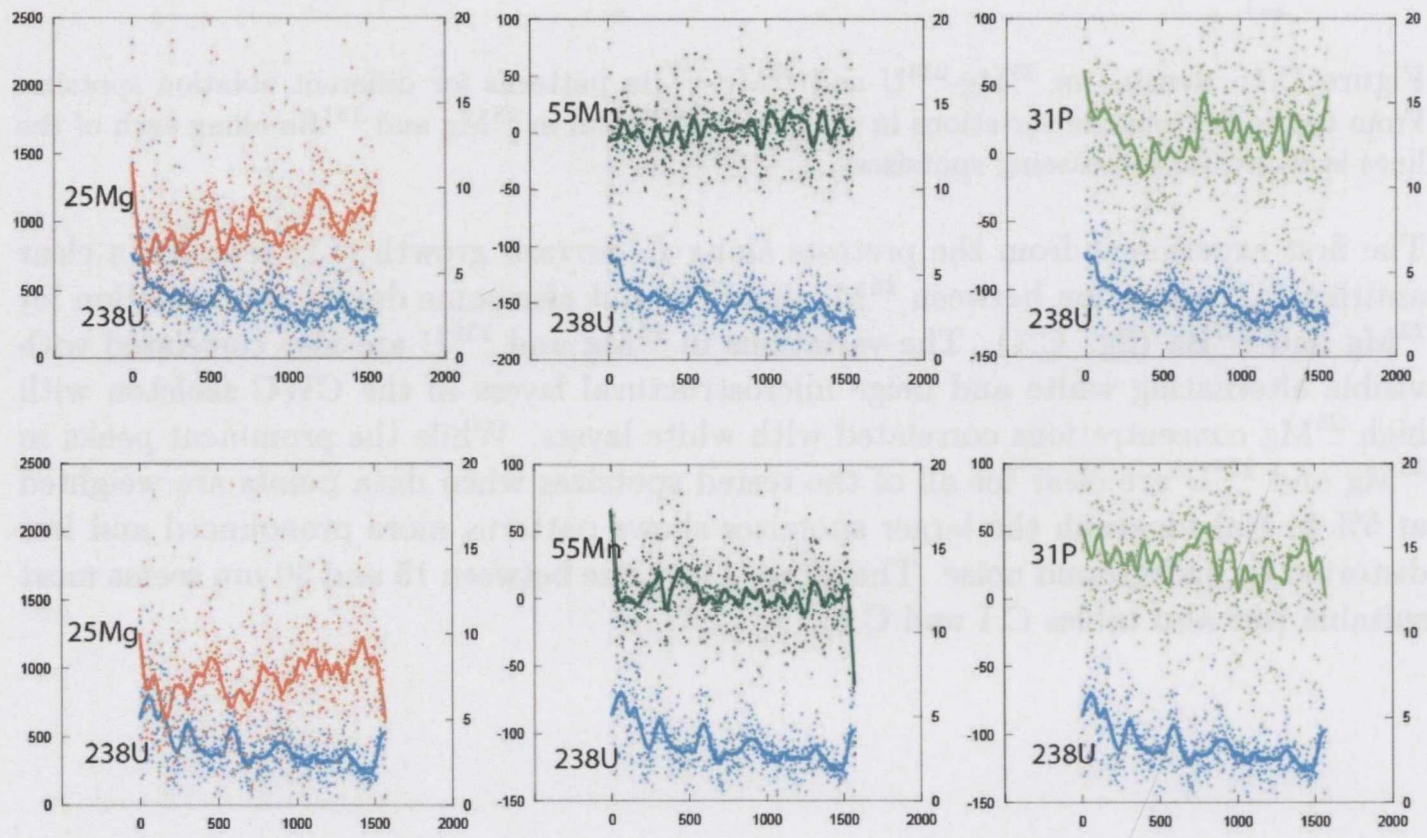


Figure C.2: Initial test 4 - ^{25}Mg, ^{238}U, Mn, P: No clear correlation with ^{25}Mg or ^{238}U .

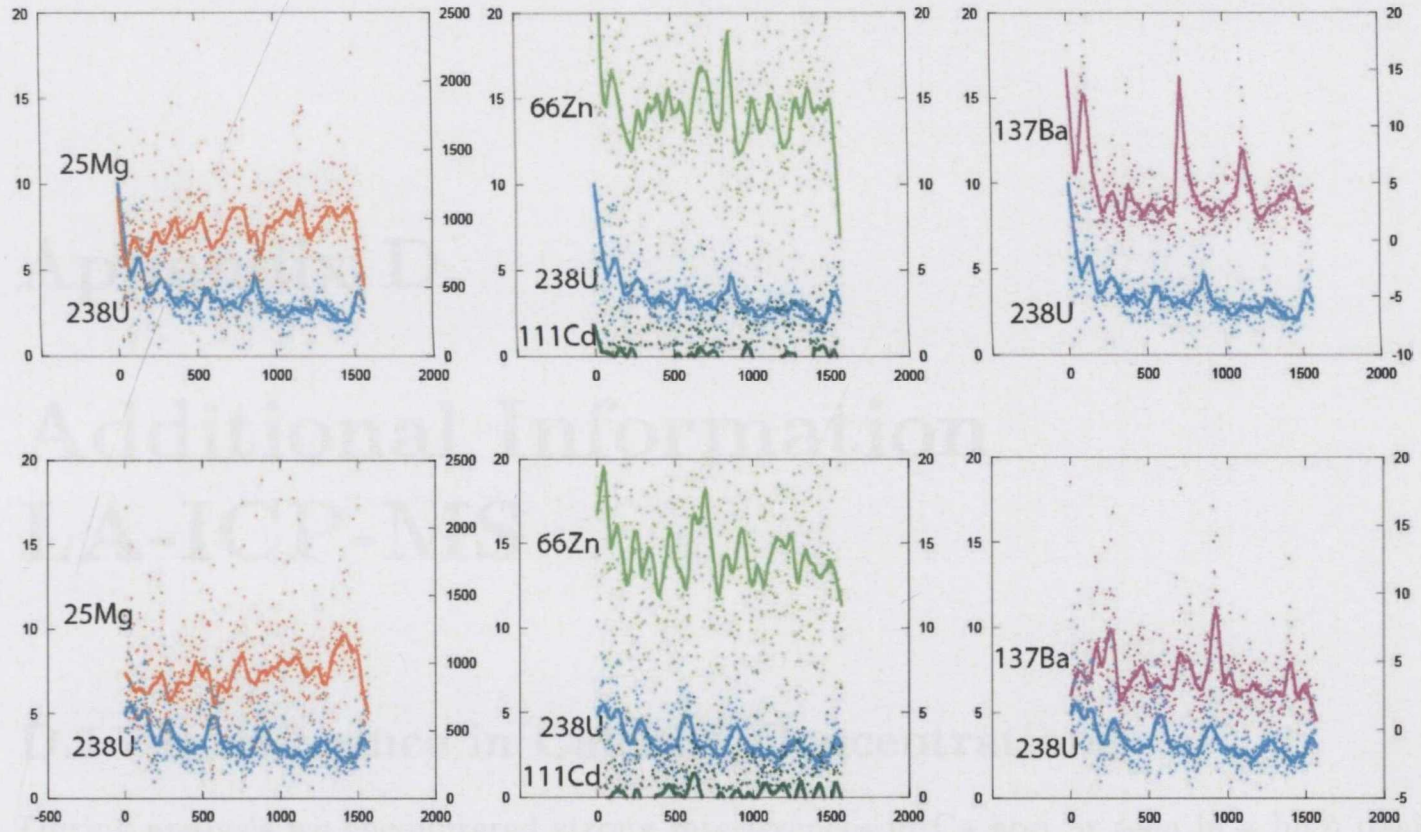


Figure C.3: Initial test 5 focusses on a series of potential nutrient proxies to check for consistent patterns and possible correlation with microstructural pattern.

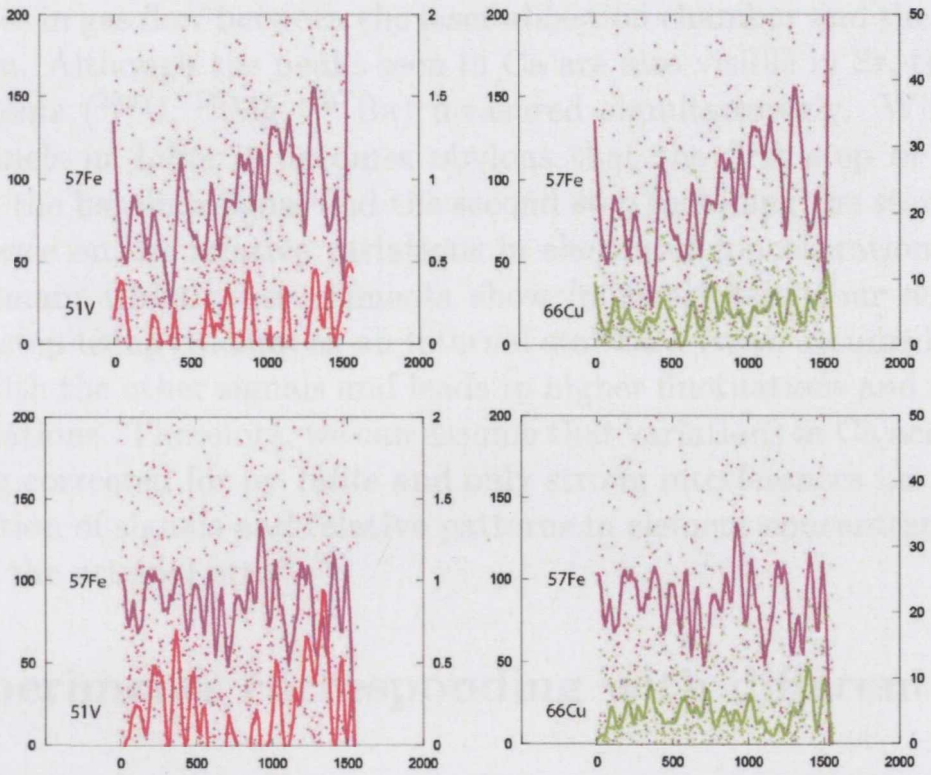


Figure C.4: Initial test 6 focusses on a series of potential nutrient proxies to check for consistent patterns and possible correlation with microstructural pattern.

The consistent antithetical behaviour of ^{25}Mg and ^{238}U in correlation with microstructures is used as a basis for the search of correlated nutrient proxies. The three experiments are set up like the first pretests with a small spotsize of 10 μm and a scan speed of 6 μm/s. Mn variations show a more or less consistent degree without apparent correlation with microstructures. P exhibits two to three peaks but appears to be distorted by low accuracy (table C.3). Zn displays indications of peaks which donnot appear to repeat over several lines. Barium, on the other hand, shows several pronounced peaks which partly appear inversely correlated to ^{238}U peaks (table C.3).

Appendix D

Additional Information LA-ICP-MS

D.1 Interference in Calcium Concentrations

During analysis we encountered strong interferences in Ca and Sr seen in a high peak in both elements. These peaks occurred within single ablation lines as well as across several neighbouring lines and were best visible when zooming out (see e.g. the central lines in E.2). The origin of these peaks is not clear and it is suspected that it is caused by irregularities in gas flow between the laser ablastion chamber and the ICP-MS during data aquisition. Although the peaks seen in Ca are also visible in Sr, they are not seen in other elements (^{238}U, ^{25}Mg, ^{137}Ba) measured simultaneously. When we compare different channels in *Iolite* it becomes obvious that the first step of data correction which reduces the baseline signal and the second step including the standard correction have no influence on the relative variations in elemental concentrations. The peaks in Ca and Sr remain while other elements show 'normal' behaviour across variations. Only the last step using calcium as an internal standard (with assumed 40.04%) causes interference with the other signals and leads to higher fluctuations and distortion of the elemental variations. Therefore, we can assume that variations in Ca across the ablation lines are being corrected for by *Iolite* and only strong interferences i.e. machine errors, cause a distortion of signals and relative patterns in element concentrations which were unaffected by the original error.

D.2 Experiments corresponding with different chapters

Table D.1: Thesis chapters and corresponding LA-Q-ICP-MS experiments

Chapter	Species	Sample Number	Focus	Experiment
7	*L. pertusa*	L1	full theca	12-18, 20
8	*M. oculata*	459-M1	full theca	21-23, 30
8	*M. oculata*	459-M1	branch	43-45a
8	*M. oculata*	1009	branch	34-37
9	*M. oculata*	459-M1-E	contact corallite-tube	24, 29, 30
9	*M. oculata*	459-M2-E	contact corallite-tube	41
9	*M. oculata*	1009-E	contact corallite-tube	40, 42
9	*L. pertusa*	1033-E	contact corallite-tube	46
9	*L. pertusa*	1036-E	contact corallite-tube	45b
9	*L. pertusa*	1447-E	contact corallite-tube	54
9	*L. pertusa*	1587-E	contact corallite-tube	55

D.3 Signal-Noise-Ratios (SNRs)

Table D.2: Signal-Noise-Ratios (SNRs) of individual experiments (Exp) in comparison. Baseline (noise) and sample (signal) measurement are given in cps. The columns n_{noise} and n_{sample} give the number of samples per experiment.

Exp	Element	Baseline	SD	Sample	SD	SNR	n_{noise}	n_{sample}
01	Mg	84.6	7.8	6720	430	79		
(8 μm)	Ca	799	51	72000	3900	90		
	Sr	80	220	1466000	72000	18325		
	Ba	4.8	3.1	404	26	84		
	U	2	11	920	100	460		
01	Mg	89.9	8.8	25290	480	281		
(15 μm)	Ca	883	66	278200	8500	315		
	Sr	270	800	5620000	220000	20815		
	Ba	5.1	3.5	1442	98	283		
	U	13	27	3711	52	285		
01	Mg	95	14	85100	5400	896		
(30 μm)	Ca	900	190	987000	50000	1097		
	Sr	160	400	17940000	790000	112125		
	Ba	4.5	6.0	4420	160	982		
	U	8	20	11020	630	1378		
02	Li	4390	670	4520	300	1		
(8 μm)	B	2390	750	3890	390	2		
	P	12900	1400	13670	330	1		
	Ca	898	54	74200	5100	83		
	Th	3.9	6.6	2.92	0.87	1		
02	Li	4390	670	5000	120	1		
(15 μm)	B	2390	750	7010	100	3		
	P	12900	1400	14213	53	1		
	Ca	898	54	253200	3300	282		
	Th	3.90	6.60	3.20	0.54	1		
02	Li	4390	670	4880	170	1		
(30 μm)	B	2390	750	14330	890	6		
	P	12900	1400	13960	110	1		
	Ca	898	54	835000	15000	930		
	Th	3.90	6.60	4.12	0.52	1		
03	Ca	447	53	65300	3500	146		
(8 μm)	V	482	18	493.9	4.9	1		
	Mn	14810	700	18180	330	1		
	Fe	5510	290	6200	210	1		
	Sr	2490	150	151000	10000	61		
03	Ca	968	97	240400	7100	248		
(15 μm)	V	490	39	526	14	1		
	Mn	15300	1500	15480	170	1		
	Fe	5610	410	7920	180	1		
	Sr	2400	590	539000	18000	225		
03	Ca	968	97	837000	15000	865		
(30 μm)	V	490	39	596.3	8.8	1		
	Mn	15300	1500	16990	690	1		
	Fe	5610	410	13350	240	2		
	Sr	2400	590	1782000	69000	743		

Exp	Element	Baseline	SD	Sample	SD	SNR	n_{noise}	n_{sample}
05	Mg	427	25	8500	1000	20		
	Ca	814	64	134000	17000	165		
	V	746	29	774	13	1		
	Fe	18800	1000	20010	310	1		
	Cu	7630	250	8160	110	1		
	U	0.8	2.0	1720	170	2150		
06	Mg	414	16	8760	540	21		
	Ca	791	57	921000	37000	1164		
	Zn	716	36	1160	140	2		
	Cd	81.7	5.9	84	9	1		
	Ba	11.5	3.0	660	16	57		
	U	0.6	1.9	1774	79	2957		
07	Mg	438	23	6450	620	15		
	P	9800	1200	9900	690	1		
	Ca	848	48	66200	2400	78		
	Mn	99000	5200	99570	4300	1		
	U	8	32	1169	54	146		
12	Mg	1580	560	32400	5400	21	13	40
	Ca	2490	340	346000	42000	139		
	Sr	1500	2900	94000	2300000	63		
	Ba	20	66	2700	230	135		
	U	90	380	8700	1100	97		
13	Mg	1240	110	25600	1900	21	7	24
	Ca	2290	260	294700	3000	129		
	Sr	440	440	66100	1900	150		
	Cd	22.1	5	34.1	5.4	2		
	Ba	8.8	9.6	2370	160	269		
	U	60	100	8400	670	140		
14	Mg	1400	130	29100	3000	21	11	30
	Ca	2480	210	350000	93000	141		
	Sr	570	610	9700000	3900000	17018		
	Cd	22.4	5.9	33	4.4	1		
	Ba	5.8	6.1	2680	250	462		
	U	33	66	8800	1000	267		
15	Mg	87	13	13000	1100	149	24	24
	Ca	810	100	167000	24000	206		
	Sr	19	25	5500000	2300000	289474		
	Cd	3.8	2.3	12	2.9	3		
	Ba	0	0	1670	140			
	U	0.5	4.7	7400	1100	14800		
16	Mg	95.4	12	12520	1100	131	36	40
	Ca	789	79	148000	1100	188		
	Sr	25.1	34	4492000	2800000	178964		
	Cd	2.6	2.9	9.1	5.7	4		
	Ba	0	0	1570	110			
	U	0	0	61100	690			
17	Mg	12.8	5.5	16900	1100	1320	24	40
	Ca	1320	350	222000	2200	168		
	Sr	160	280	7400000	3500000	46250		
	Cd	6.9	6	19.1	8.5	3		
	Ba	0.12	0.84	1980	260	16500		
	U	2	11	5910	570	2955		

Exp	Element	Baseline	SD	Sample	SD	SNR	n_{noise}	n_{sample}
18	Mg	14.6	8.2	15200	3800	1041	51	48
	Ca	1160	130	200000	66000	172		
	Sr	800	1300	6500000	4300000	8125		
	Cd	7	7.2	13.2	3.2	2		
	Ba	1.9	6.3	1570	390	826		
	U	27	86	5300	1500	196		
20	^{10}B	68	14	902	47	13	22	14
	^{11}B	318	54	3980	220	13		
	Mg	15	16	15790	340	1053		
	Ca	1060	130	209000	5300	197		
	Ba	1.6	4.3	1936	80	1210		
	U	15	40	6050	450	403		
21	Mg	20	11	17500	1800	875	45	24
	Ca	1240	190	241000	2200	194		
	Sr	1200	2200	7100000	2100000	5917		
	Cd	8	10	11.4	1.8	1		
	Ba	2.7	9.3	1800	180	667		
	U	30	130	7350	810	245		
22	Mg	14.4	5.9	17000	810	1181	28	24
	Ca	1070	160	234000	1800	219		
	Sr	500	1900	8000000	3500000	16000		
	Cd	6.2	4.8	10.1	1.9	2		
	Ba	2	16	1753	81	877		
	U	15	55	7220	750	481		
23	Mg	15.7	9.6	13930	240	887	8	19
	Ca	1030	190	186000	4500	181		
	Sr	800	2500	6500000	2500000	8125		
	Cd	5.2	7	9.6	1.8	2		
	Ba	1.6	4.9	1451	66	907		
	U	7	42	5810	410	830		
24a	Mg	5.9	3.2	18000	1700	3051	19	24
	Ca	1249	98	199000	1200	159		
	Sr	110	160	5290000	320000	48091		
	Cd	8.9	4.4	13	5	1		
	Ba	0.03	0.24	1470	190	49000		
	U	0.7	2.4	6480	380	9257		
29	^{10}B	51	15	909	61	18	18	23
	^{11}B	236	28	4000	290	17		
	Mg	5.1	3.9	14100	1400	2765		
	Ca	1030	110	15600	6300	15		
	Sr	110	170	4250000	140000	38636		
	Ba	0	0	1195	65			
	U	0.3	1.7	6210	620	20700		
30	^{10}B	45.1	6.9	889	76	20	14	14
	^{11}B	227	26	3880	370	17		
	Mg	5	4.4	14200	1800	2840		
	Ca	1016	99	156200	7500	154		
	Sr	80	130	4180000	200000	52250		
	Ba	0.03	0.21	1177	78	39233		
	U	3	12	5960	680	1987		

Exp	Element	Baseline	SD	Sample	SD	SNR	n_{noise}	n_{sample}
31	Mg	90	560	23600	8600	262	33	36
	^{31}P	212000	30000	217000	27000	1		
	Ca	1800	500	310000	110000	172		
	Fe	1230	320	6500000	2000	5285		
	Ba	20	130	1410	320	71		
	U	30	150	3900	1200	130		
32	^{32}S	12050000	500000	12640000	590000	1	6	7
	Ca	1612	39	322000	57000	200		
	^{48}Ti	2370	650	552000	98000	233		
	^{51}V	701	29	930	120	1		
	^{55}Mn	201900	1800	201760	810	1		
	^{75}As	251	40	265	29	1		
	^{85}Rb	164	94	225	89	1		
	^{89}Y	2.8	3	61	14	22		
	^{90}Zr	60	120	250	280	4		
	^{111}Cd	9	11	13.6	4.9	2		
	Sb	63	17	122	59	2		
33	Li	237	17	544	42	2	13	8
	^{23}Na	46600	1200	1680000	200000	36		
	Mg	39	42	27100	3500	695		
	^{35}Cl	104200	4900	1048000	6000	10		
	Ca	1540	150	319000	45000	207		
	U	8	18	3730	620	466		
34	Mg	28	25	27800	3200	993	22	23
	Ca	1420	110	316000	28000	223		
	Fe	822	99	4820	480	6		
	Sr	390	790	6500000	550000	16667		
	Ba	2.1	3.8	1192	76	568		
	U	3.8	3.7	4130	280	1087		
35	Mg	39	72	35200	5600	903	28	23
	Ca	1490	290	405000	61000	272		
	Fe	1090	230	7100	2100	7		
	Sr	700	1300	5710000	770000	8157		
	Ba	8	34	1430	150	179		
	U	12	52	4490	570	374		
36	Mg	38	66	35900	2300	945	25	24
	Ca	1010	140	335000	28000	332		
	Fe	890	560	5400	950	6		
	Sr	190	340	5820000	560000	30632		
	Ba	9	70	1530	140	170		
	U	13	57	4650	730	358		
37	Li	310	150	692	36	2	43	44
	Mg	60	260	35700	4000	595		
	Ca	1000	1000	333000	41000	333		
	Sr	290	810	5780000	820000	19931		
	Ba	9	75	1470	150	163		
	U	40	380	4460	630	112		
38	Li	273	29	500	20	2	28	31
	Mg	70	490	22800	2200	326		
	Ca	890	130	230000	22000	258		
	Sr	180	270	4040000	420000	22444		
	Ba	1.8	6	1150	380	639		
	U	3.2	4.6	3860	740	1206		

Exp	Element	Baseline	SD	Sample	SD	SNR	n_{noise}	n_{sample}
40a	Li	260	27	661	65	3	18	15
	Mg	30	32	35200	5900	1173		
	Ca	930	150	334000	61000	359		
	Sr	380	700	5800000	1100000	15263		
	Ba	4.1	6	1470	250	359		
	U	10	23	4670	830	467		
40b	Li	283	28	689	95	2	31	34
	Mg	70	270	34600	6100	494		
	Ca	890	180	332000	48000	373		
	Sr	280	600	5830000	940000	20821		
	Ba	3.4	4.9	1540	200	453		
	U	8	17	5400	1500	675		
41	Li	306	76	680	330	2	47	45
	Mg	1000	10000	500000	110000	500		
	Ca	40000	43000	264000	43000	7		
	Sr	500000	720000	4420000	760000	9		
	Ba	20	230	1500	1300	75		
	U	50	550	3600	1200	72		
42	Li	304	22	668	71	2	32	36
	Mg	41	61	31400	5800	766		
	Ca	870	110	314000	46000	361		
	Sr	470	930	5300000	740000	11277		
	Ba	2.6	6.2	1390	140	535		
	U	6	16	4250	670	708		
43	Li	300	1900	308	28	1	25	36
	Mg	60	300	22300	1700	372		
	Ca	1500	7600	232000	15000	155		
	Sr	1400	7000	4630000	190000	3307		
	Ba	80	720	1371	76	17		
	U	700	7100	3840	190	5		
44	Li	97	61	352	12	4	39	36
	Mg	11	21	23720	900	2156		
	Ca	760	140	250700	7900	330		
	Sr	280	490	4440000	120000	15857		
	Ba	1.9	7.3	1369	63	721		
	U	20	120	3730	160	187		
45a	Li	86	49	324	32	4	34	30
	Mg	30	110	22600	2100	753		
	Ca	690	160	245000	10000	355		
	Sr	370	810	4500000	1100000	12162		
	Ba	2.3	7.1	1180	230	513		
	U	12	79	3720	680	310		
45b	Li	86	49	312	28	4	34	10
	Mg	30	110	23100	1200	770		
	Ca	690	160	249000	8700	361		
	Sr	370	810	5000000	1500000	13514		
	Ba	2.3	7.1	1320	130	574		
	U	12	79	4140	230	345		
46	Li	123	25	409	55	3	34	37
	Mg	120	430	29300	5800	244		
	Ca	747	86	282000	30000	378		
	Sr	340	620	4590000	500000	13500		
	Ba	6	10	1100	140	183		
	U	21	61	3220	440	153		

Exp	Element	Baseline	SD	Sample	SD	SNR	n_{noise}	n_{sample}
49	Li	134	15	992	32	7	20	16
	Mg	96.7	5	85700	3500	886		
	Ca	1440	130	922000	44000	640		
	U	71	41	29960	330	422		
50	Li	86	11	129	12	2	15	8
	Mg	76.5	8.2	4300	550	56		
	Ca	1330	120	44100	5200	33		
	U	0.2	1.2	1430	160	7150		
51a	Li	128	90	975	89	8	45	10
	Mg	88	14	82200	7500	934		
	Ca	1380	240	891000	86000	646		
	U	110	380	31660	920	288		
51b	Li	128	90	1240	78	10	45	10
	Mg	88	14	95200	6600	1082		
	Ca	1380	240	905000	70000	656		
	U	110	380	25810	890	235		
51c	Li	128	90	1007	27	8	45	10
	Mg	88	14	77600	3400	882		
	Ca	1380	240	794000	35000	575		
	U	110	380	24260	480	221		
52	Li	75	11	110.1	8.6	1	21	10
	Mg	106	30	3440	840	32		
	Ca	1750	760	37000	11000	21		
	U	9	43	1100	290	122		
53a	Li	81	39	246.4	3.5	3	12	5
	Mg	93	13	16640	2.7	179		
	Ca	1380	15	176800	3.9	128		
	U	30	330	6090	29	203		
53b	Li	106	65	717	19	7	16	5
	Mg	93	12	61000	1300	656		
	Ca	1270	190	643000	15000	506		
	U	130	310	23131	74	178		
54	^{11}B	430	170	17800	4600	41	44	40
	Mg	130	350	64000	16000	492		
	Ca	1330	180	630000	120000	474		
	Ba	10	40	3960	940	396		
	U	90	310	17400	4400	193		
55	^{11}B	307	48	17700	3900	58	46	40
	Mg	85	15	86000	43000	1012		
	Ca	1230	220	660000	200000	537		
	Ba	3	13	4020	750	1340		
	U	40	210	16000	2400	400		

Appendix E

Cellspace Images

E.1 Cellspace Images *Lophelia pertusa* L1

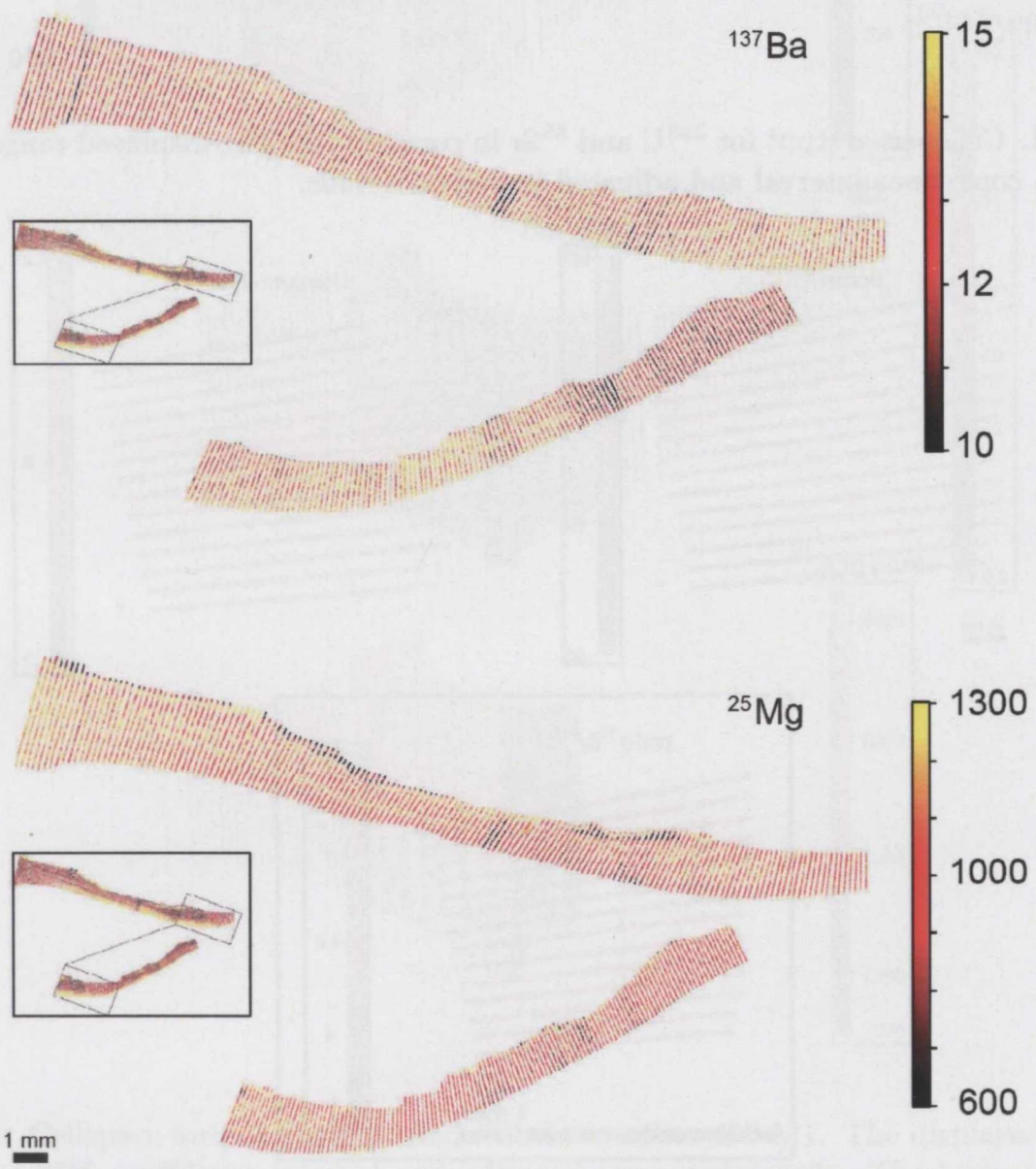


Figure E.1: Cellspace output for ^{137}Ba and ^{25}Mg in corallite L1. The displayed ranges are based on the 95% confidence interval and adjusted increased details.

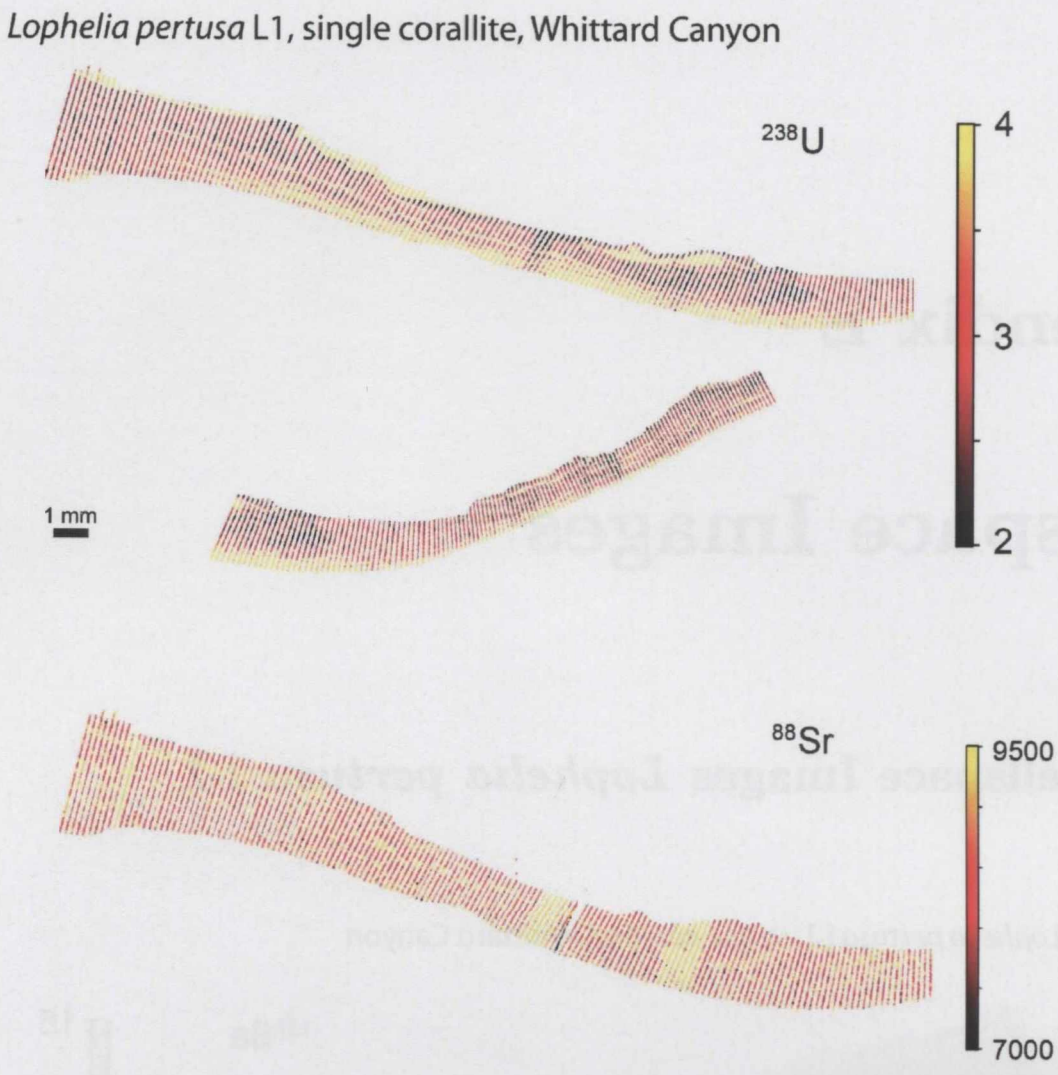


Figure E.2: Cellspace output for ^{238}U and ^{88}Sr in corallite L1. The displayed ranges are based on the 95% confidence interval and adjusted increased details.

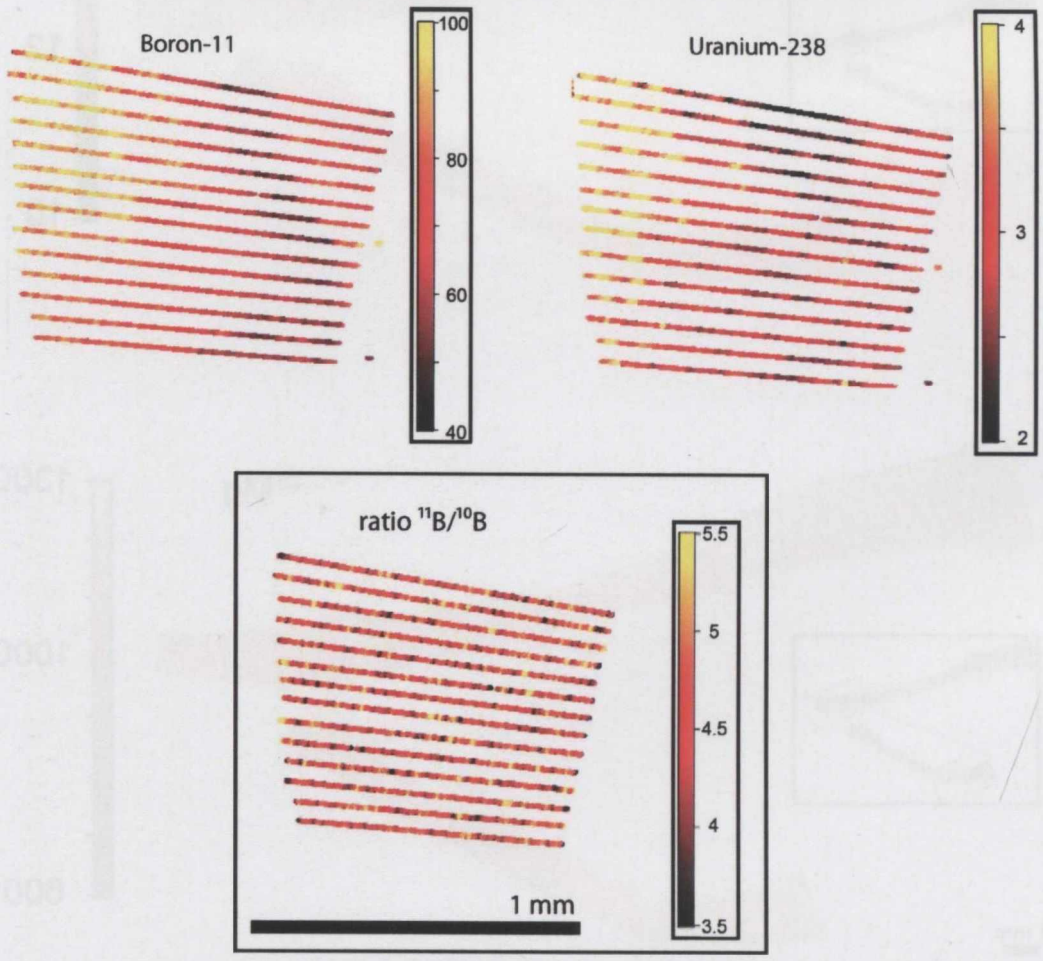


Figure E.3: Stable boron isotope ratios along ablation lines show little variations, no pronounced pattern or correlation with microstructures.

E.2 Cellspace Images *Madrepora oculata* Single Corallite

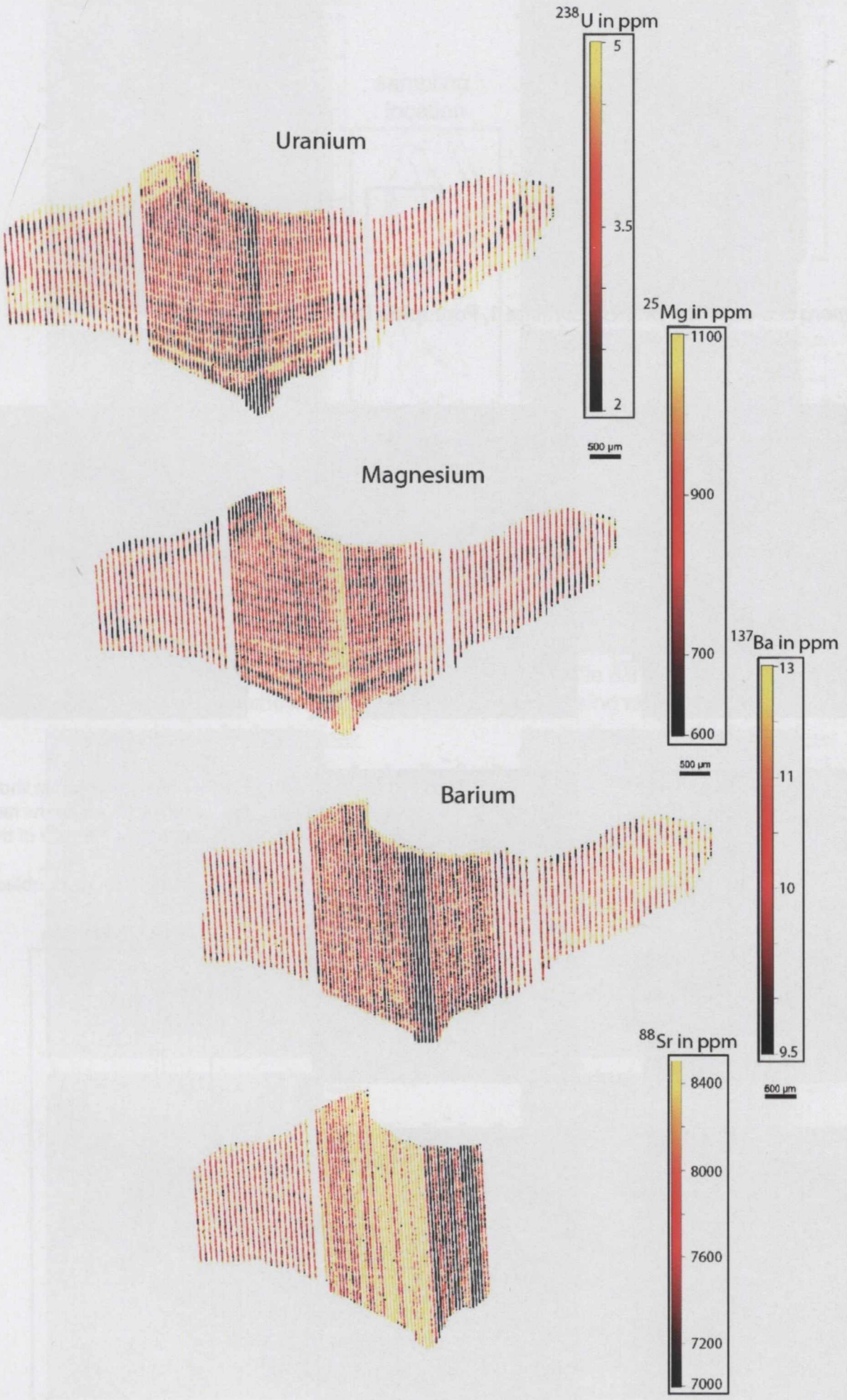


Figure E.4: Cellspace output for ^{238}U and ^{88}Sr in corallite 459-M1. The displayed ranges are based on the 95% confidence interval and adjusted increased details. The high values in the middle part of the corallite were caused by an analytical error most pronounced in Sr and Ca measurements. The general pattern in microstructure associated variations can still be retraced.

E.3 Cellspace Images *Madrepora oculata* Branches

Madrepora oculata 1009 branch, corallite 1, Porcupine Bank

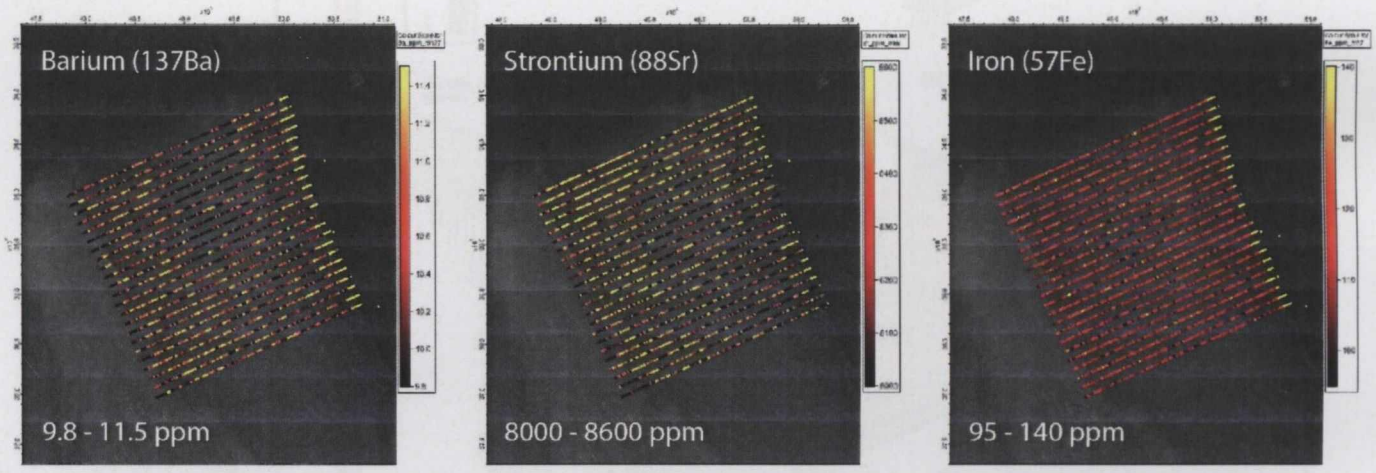
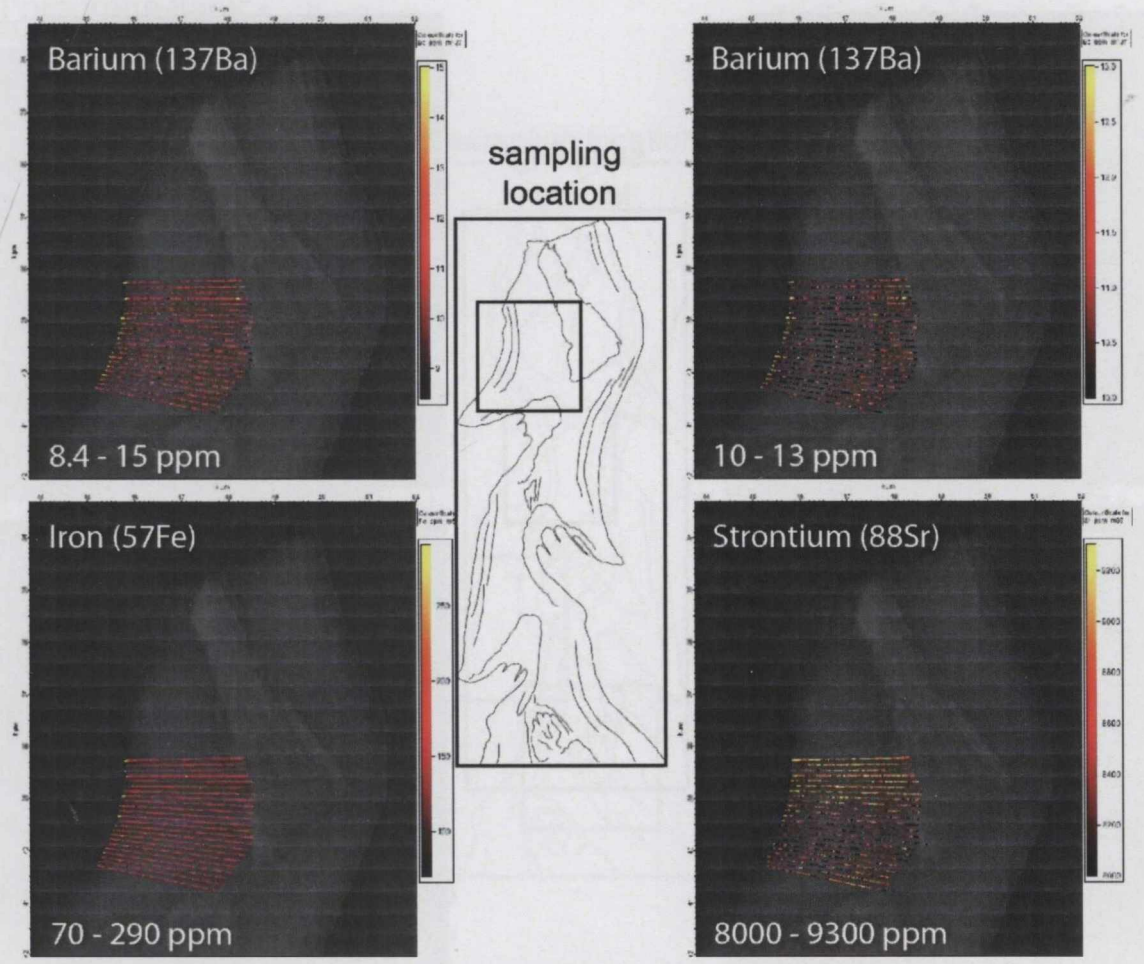


Figure E.5: Cellspace output for corallite 1 of 1009 branch. All ranges are originally based on the 95% confidence interval and in some cases additionally on adjusted range for increasing details.

Madrepora oculata 1009 branch, corallite 2, Porcupine Bank



For Uranium details increase with increasing range while Barium and Magnesium analysis shows more details with a decreasing range.

Figure E.6: Cellspace output for corallite 2 of 1009 branch. All ranges are originally based on the 95% confidence interval.

Madrepora oculata 1009 branch, corallite 3, Porcupine Bank

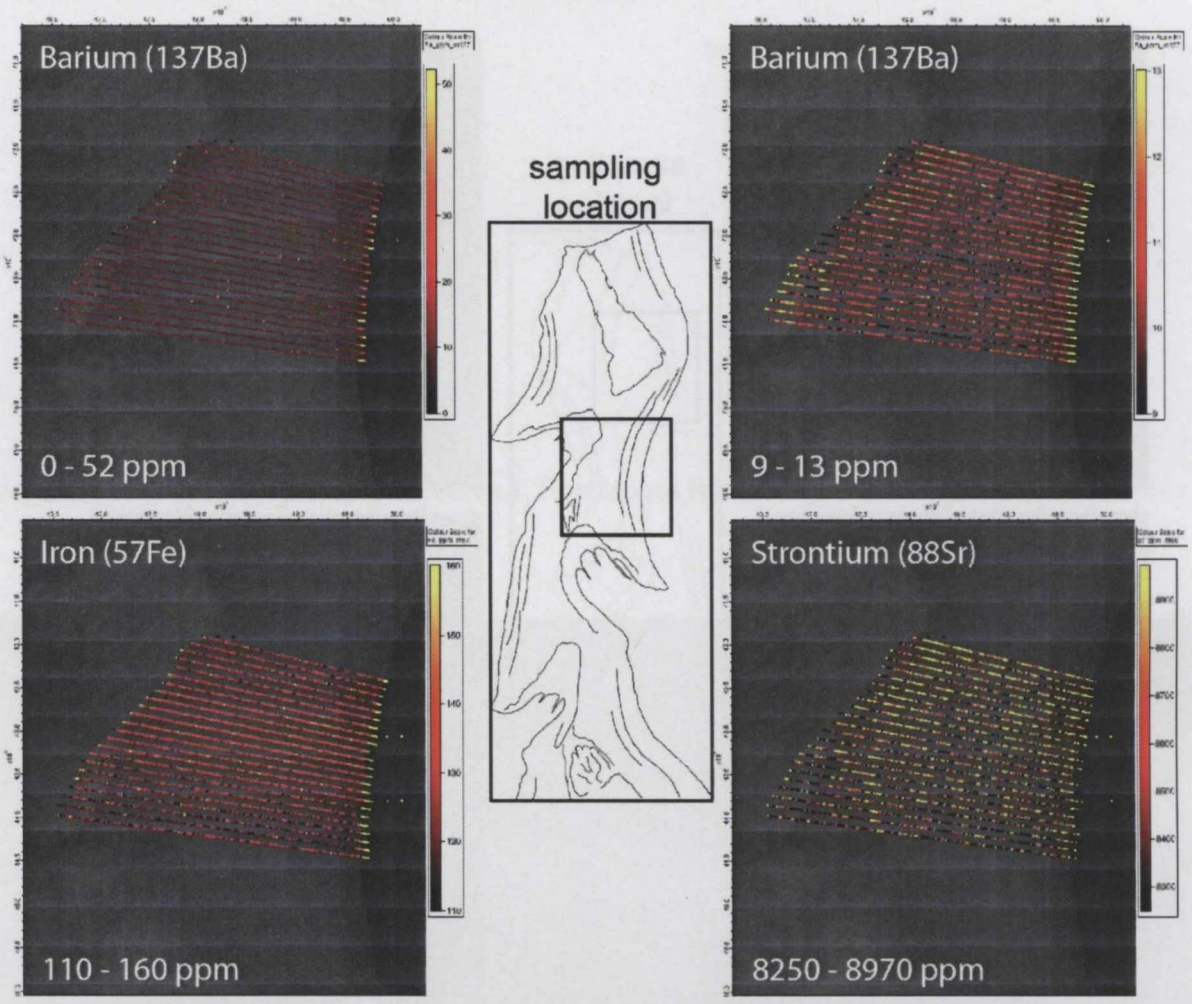
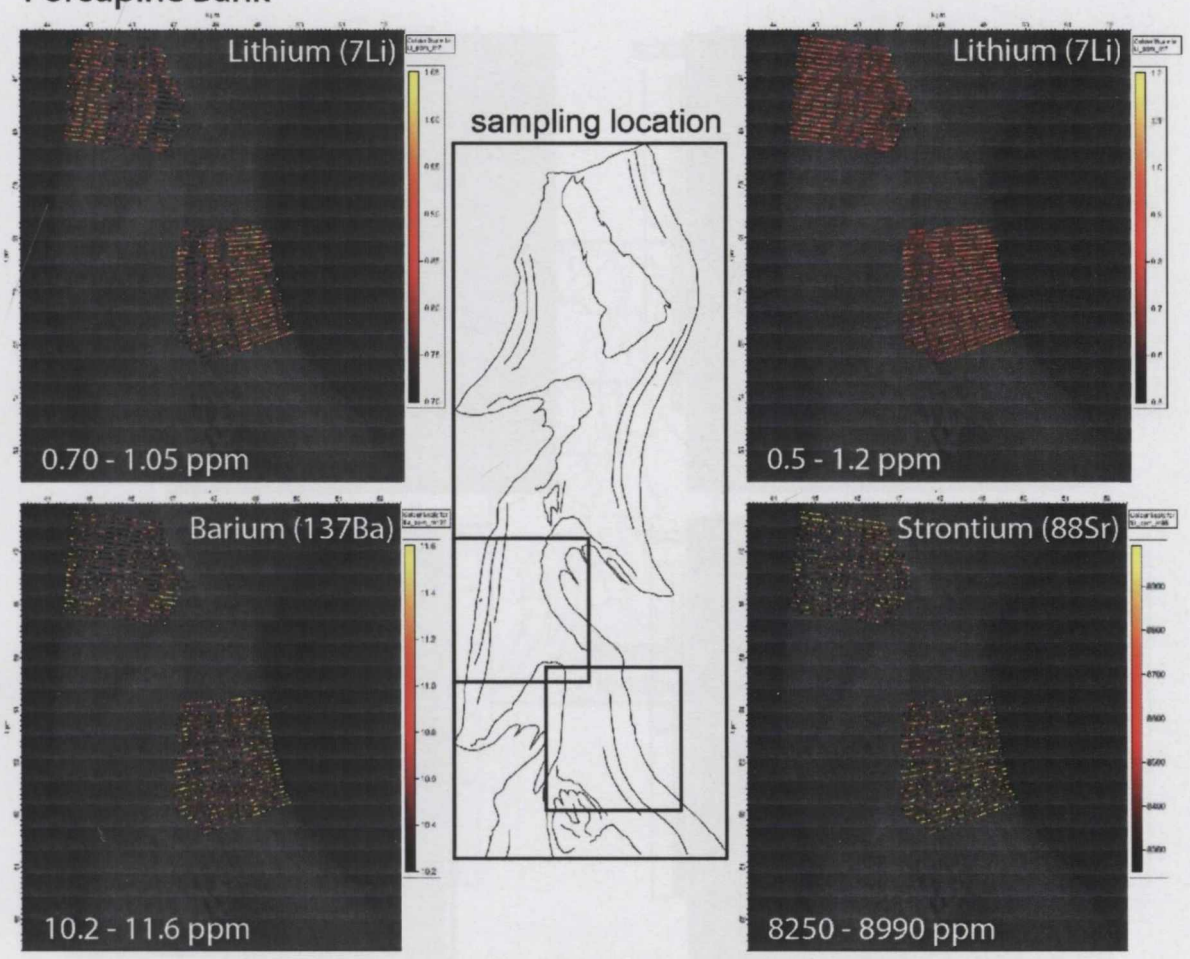


Figure E.7: Cellspace output for corallite 3 of 1009 branch. All ranges are originally based on the 95% confidence interval.

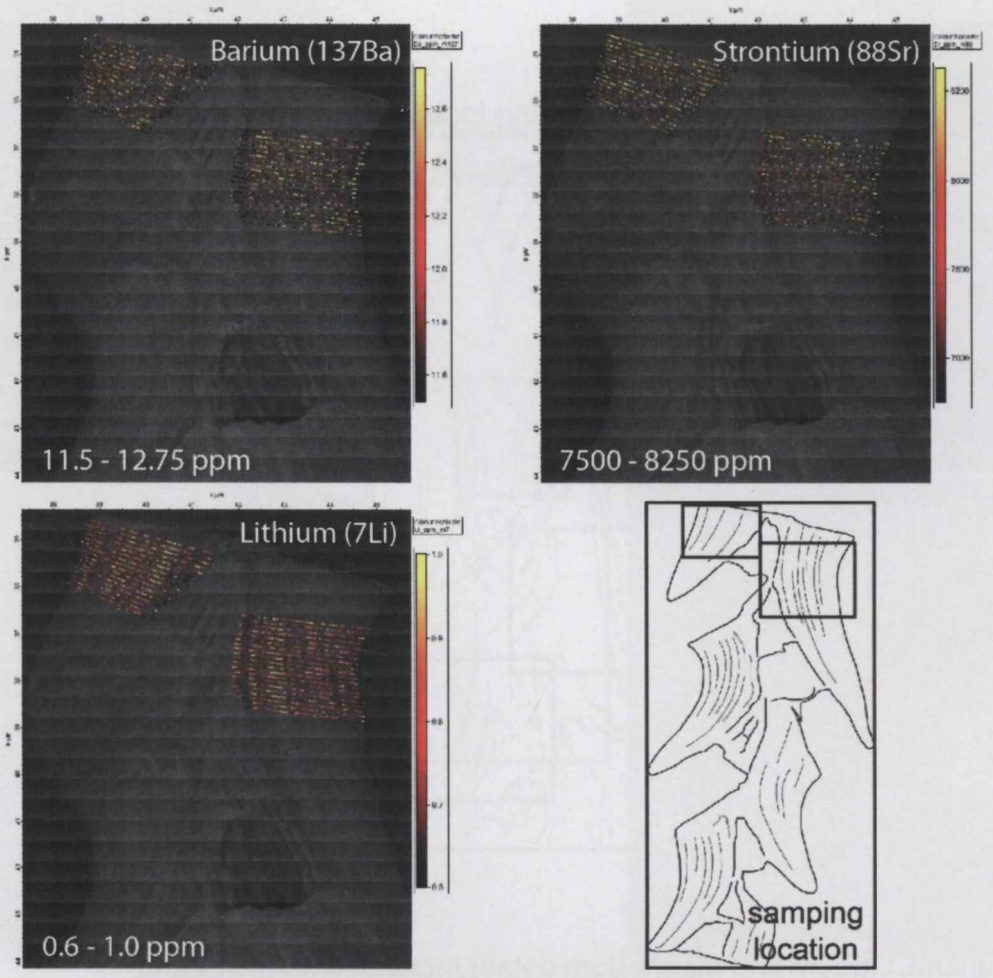
Madrepora oculata 1009 branch, corallite 4 + 5, Porcupine Bank



For Uranium, Lithium and Magnesium details increase with increasing range.

Figure E.8: Cellspace output for corallite 4 and 5 of 1009 branch. All ranges are originally based on the 95% confidence interval.

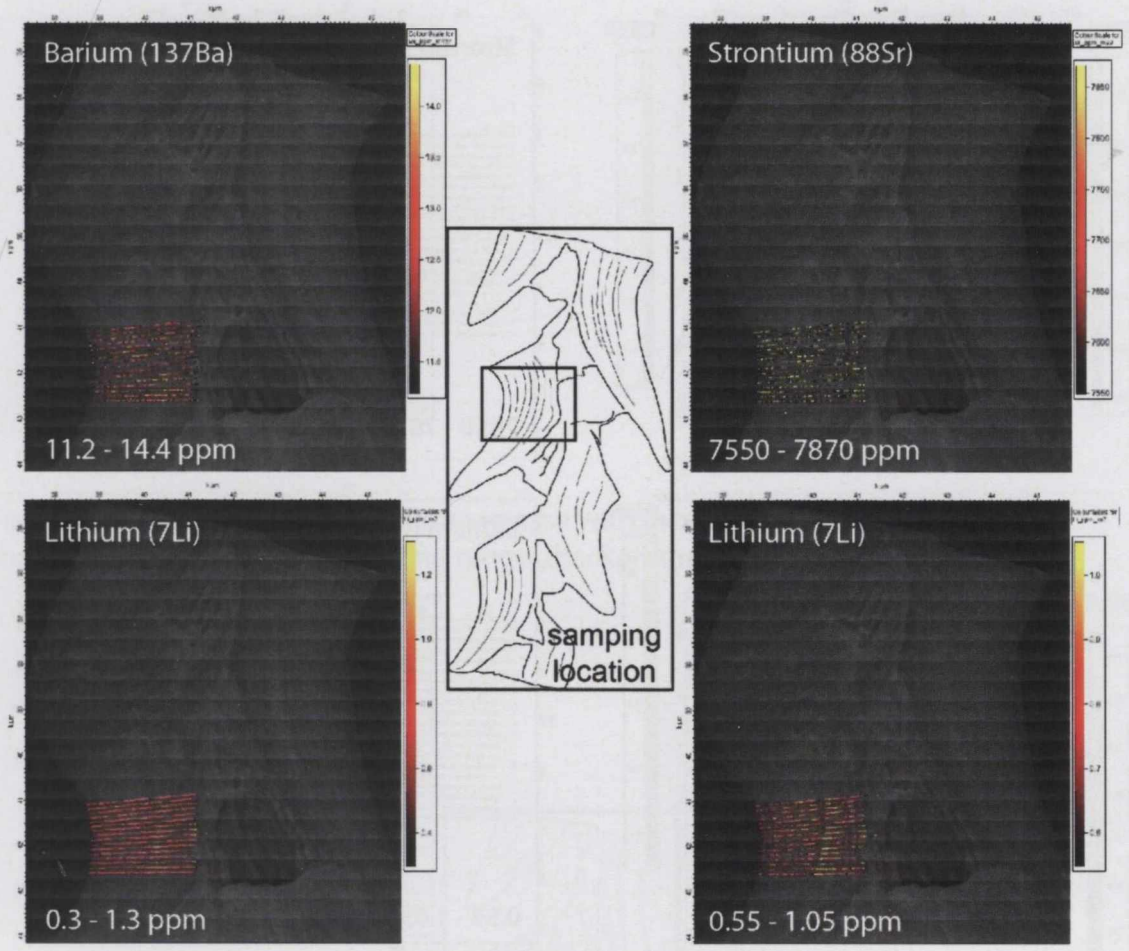
Madrepora oculata 459-M1 branch, corallite 1 + 2, Whittard Canyon



For Uranium and Magnesium details increase with increasing range.

Figure E.9: Cellspace images of branches 1 and 2 in sample 459-M1. All ranges are originally based on the 95% confidence interval.

Madrepora oculata 459-M1 branch, corallite 3, Whittard Canyon



For Uranium and Magnesium details increase with increasing range. For Lithium the details increase with decreasing range.

Figure E.10: Cellspace images of branch 3 in sample 459-M1. All ranges are originally based on the 95% confidence interval.

Madrepora oculata 459-M1 branch, corallite 5, Whittard Canyon

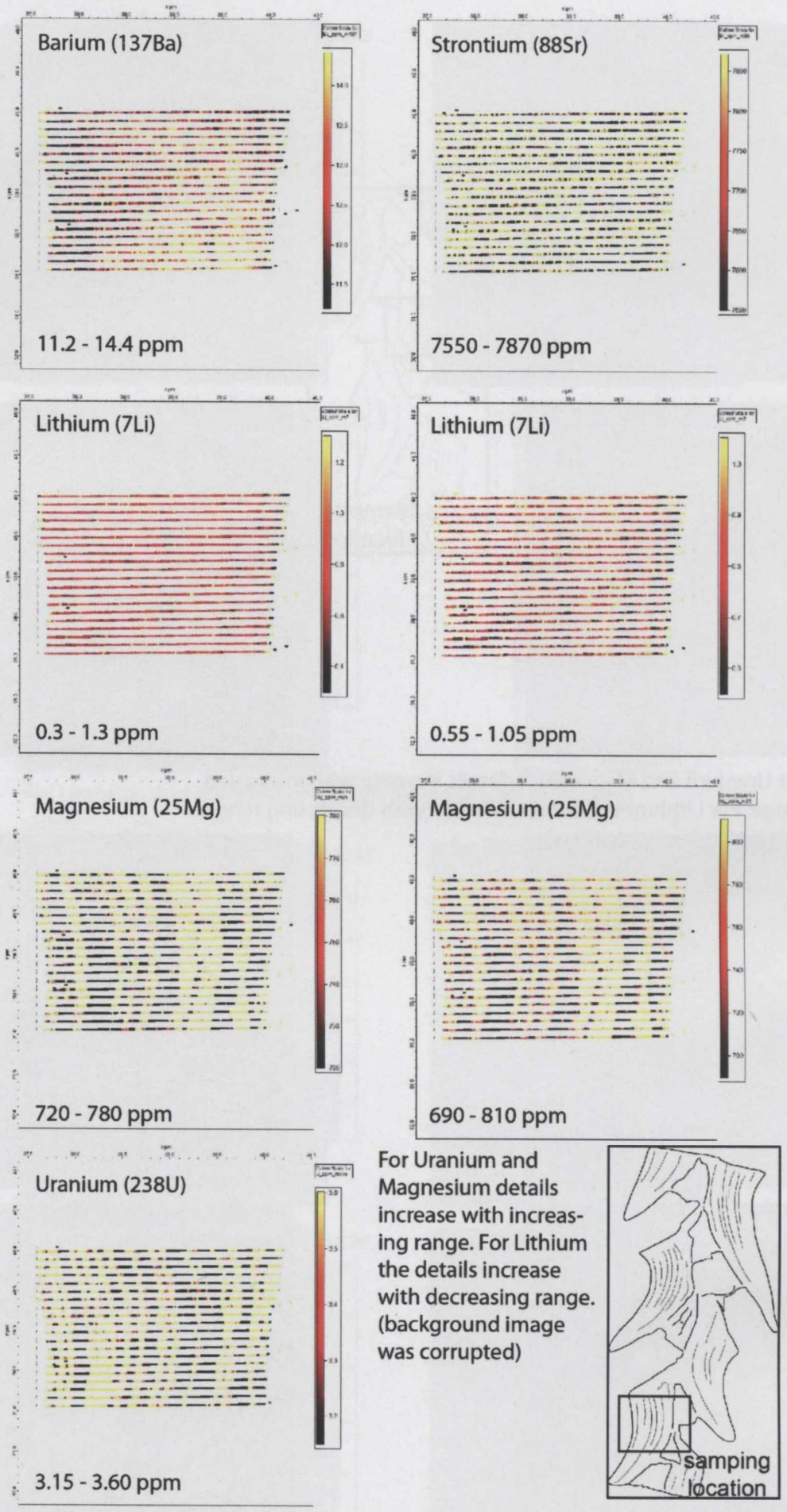
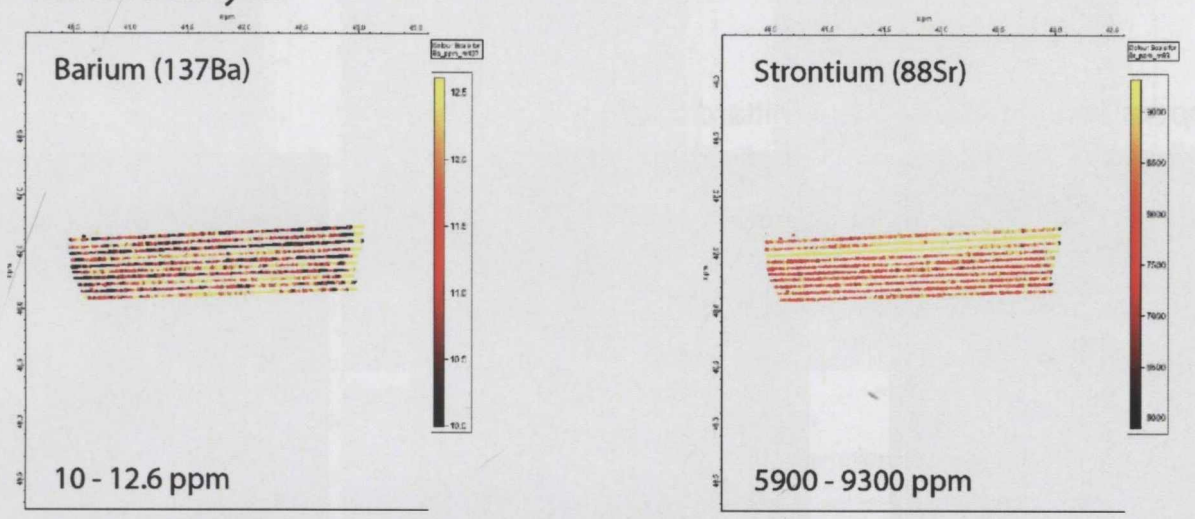


Figure E.11: Cellspace images of branch 4 in sample 459-M1. All ranges are originally based on the 95% confidence interval.

Madrepora oculata 459-M1 branch, corallite 4, Whittard Canyon



For Uranium and Magnesium details increase with increasing range. For Lithium the details increase with decreasing range. (background image was corrupted)

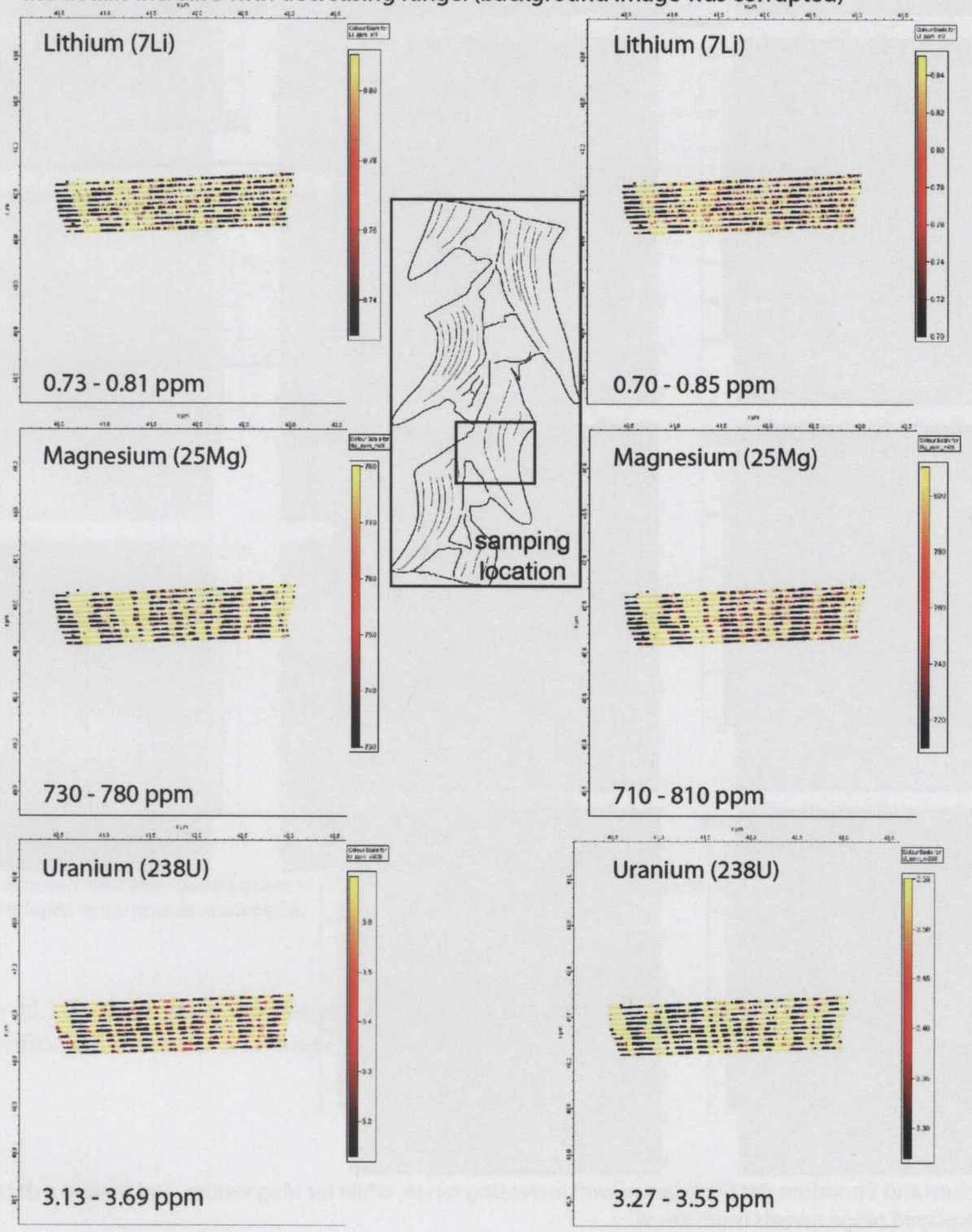
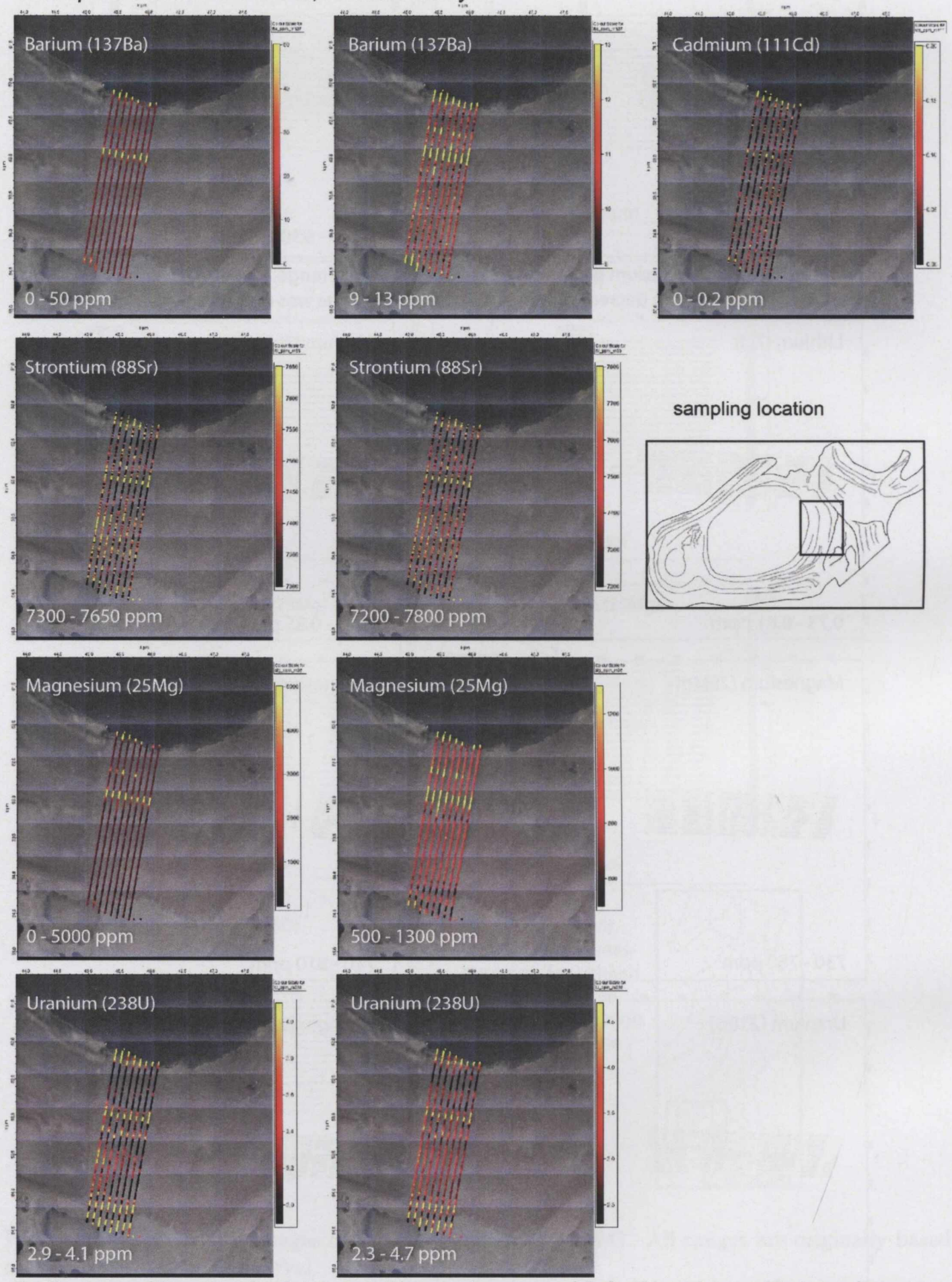


Figure E.12: Cellspace images of branch 5 in sample 459-M1. All ranges are originally based on the 95% confidence interval.

E.4 Cellspace Images *Eunice norvegica* Tubes

Madrepora oculata 459-M1-E, Whittard Canyon



For Uranium and Strontium details increase with increasing range, while for Magnesium and Barium a decrease of the displayed range reveals more detail.

Figure E.13: Cellspace images in 459-M1-E, part a. All ranges are originally based on the 95% confidence interval. For more details see chapter 9.

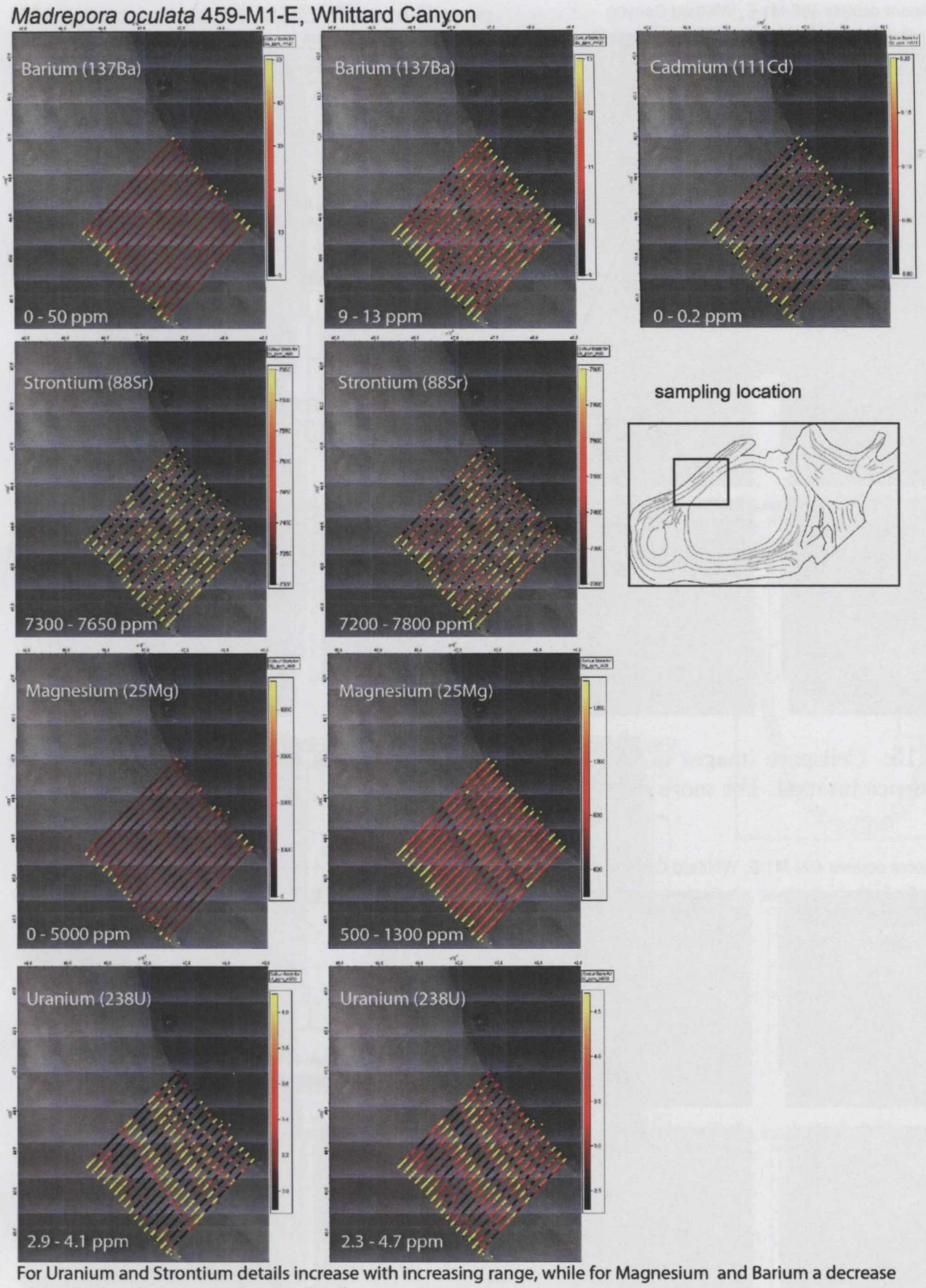


Figure E.14: Cellspace images in 459-M1-E, part b. All ranges are originally based on the 95% confidence interval. For more details see chapter 9.

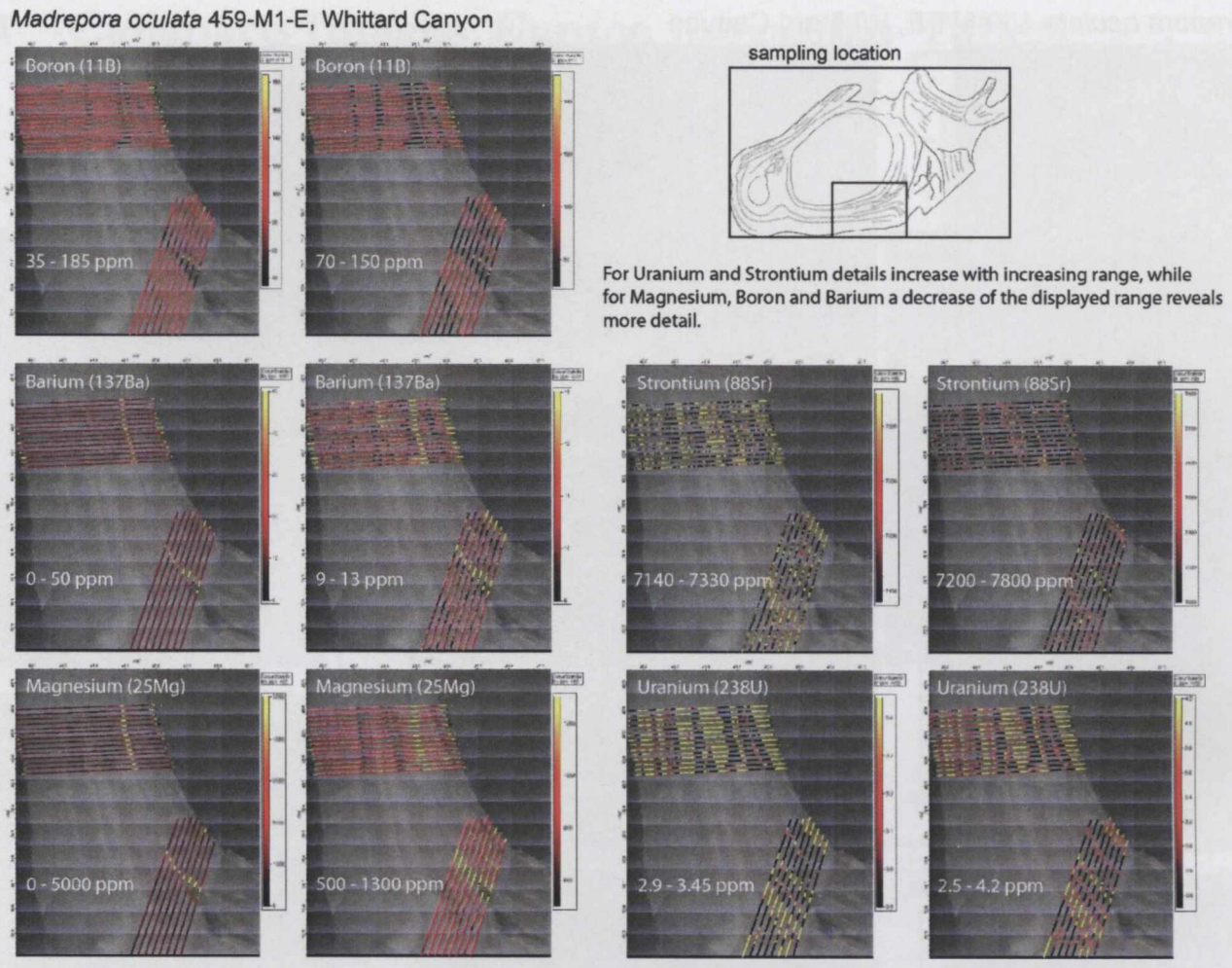


Figure E.15: Cellspace images in 459-M1-E, part c. All ranges are originally based on the 95% confidence interval. For more details see chapter 9.

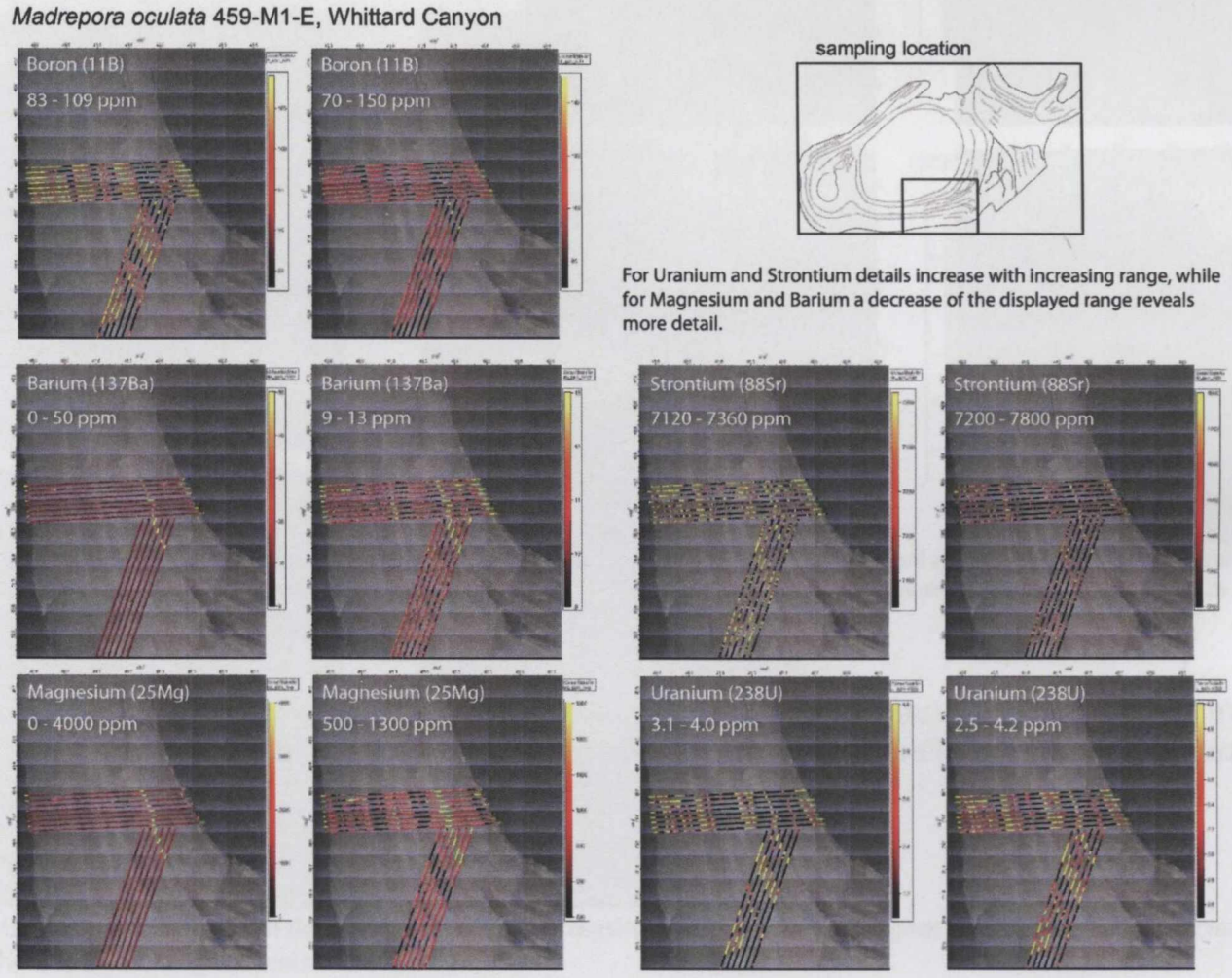
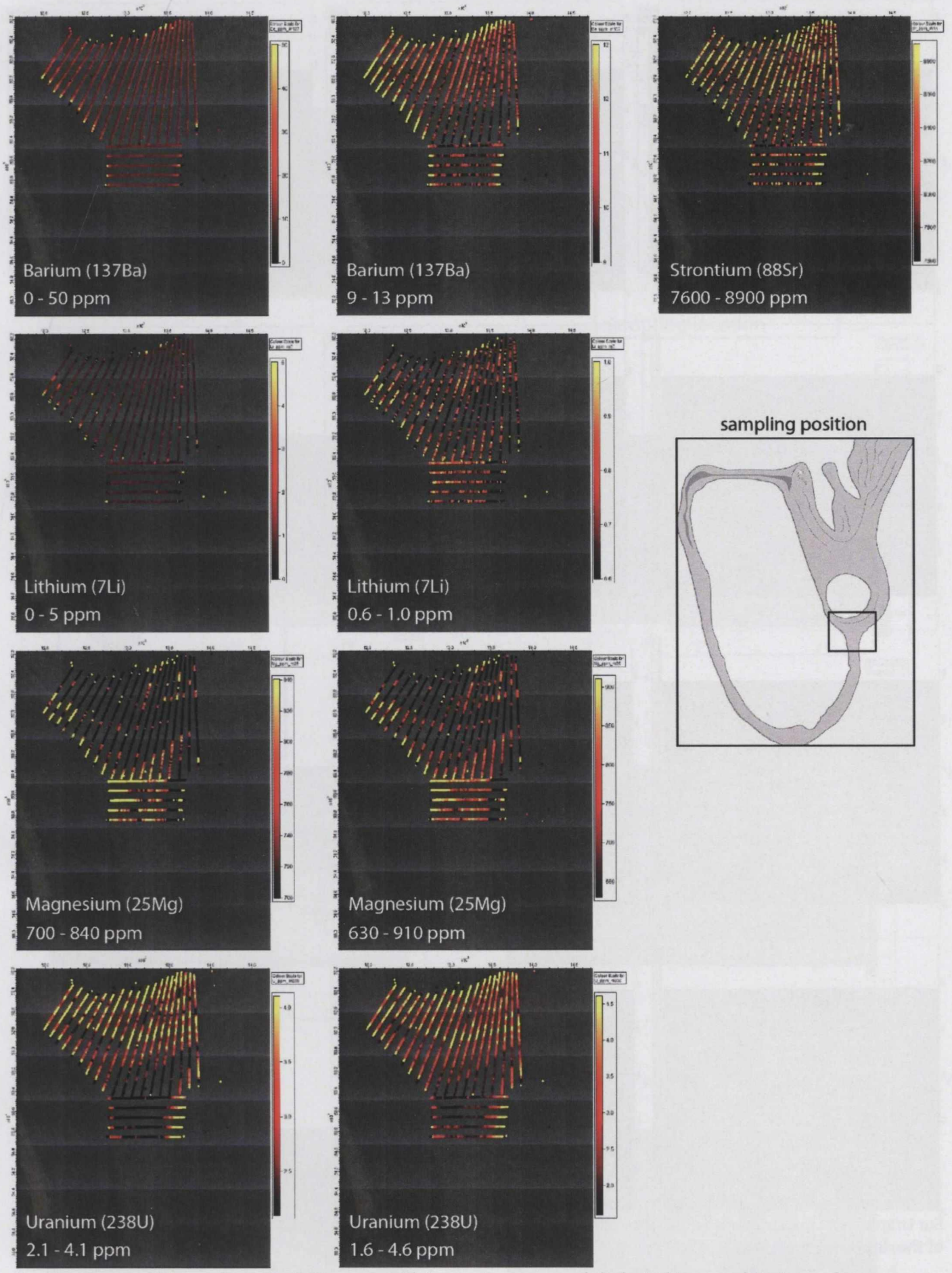


Figure E.16: Cellspace images in 459-M1-E, part d. All ranges are originally based on the 95% confidence interval. For more details see chapter 9.

Madrepora oculata 459-M2-E, Whittard Canyon



For Uranium and Magnesium details increase with increasing range, while for Lithium and Barium a decrease of the displayed range reveals more detail.

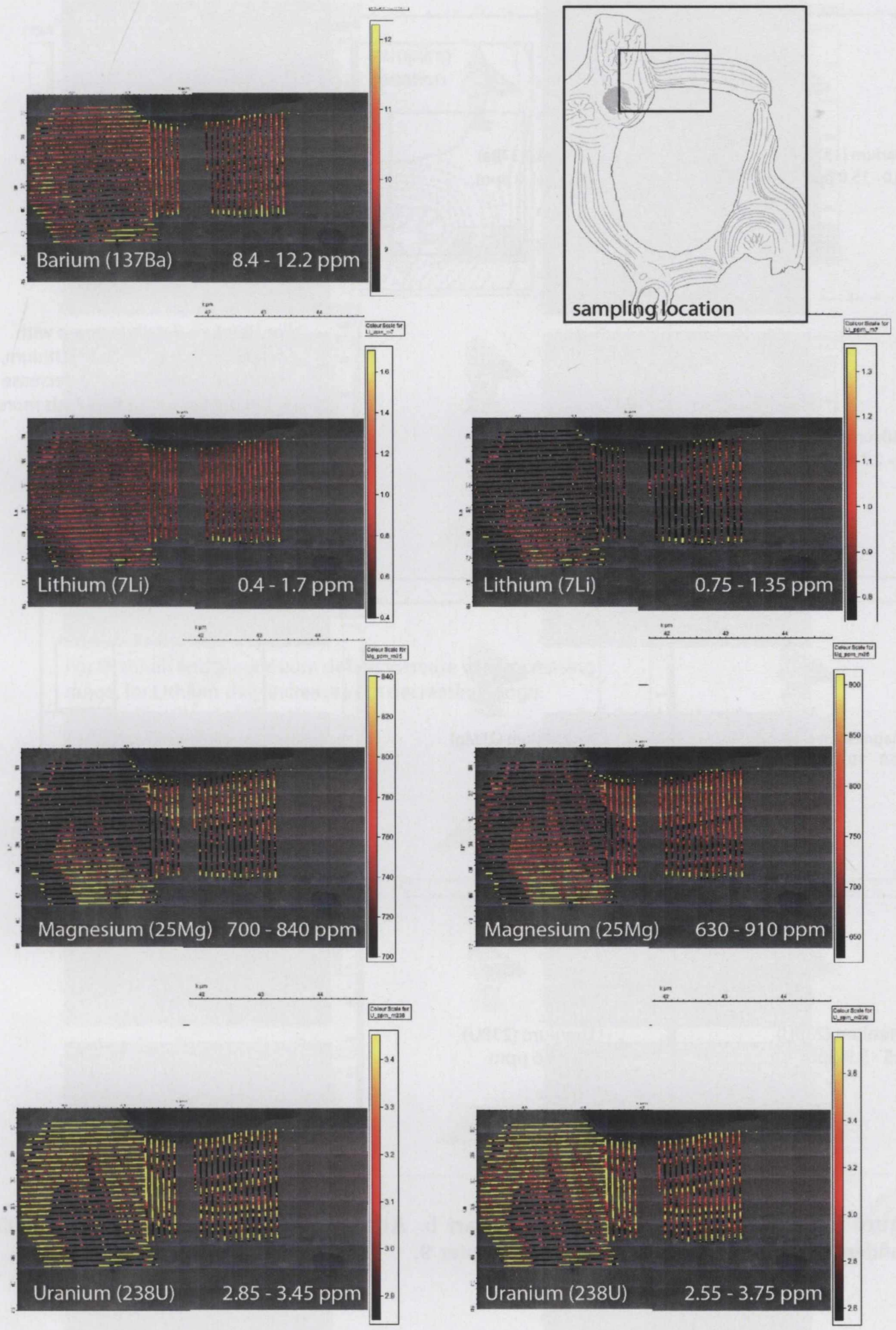
Figure E.17: Cellspace images in 459-M2-E, part a. All ranges are originally based on the 95% confidence interval. For more details see chapter 9.

Madrepora oculata 459-M2-E, Whittard Canyon



Figure E.18: Cellspace images in 459-M2-E, part b. All ranges are originally based on the 95% confidence interval. For more details see chapter 9.

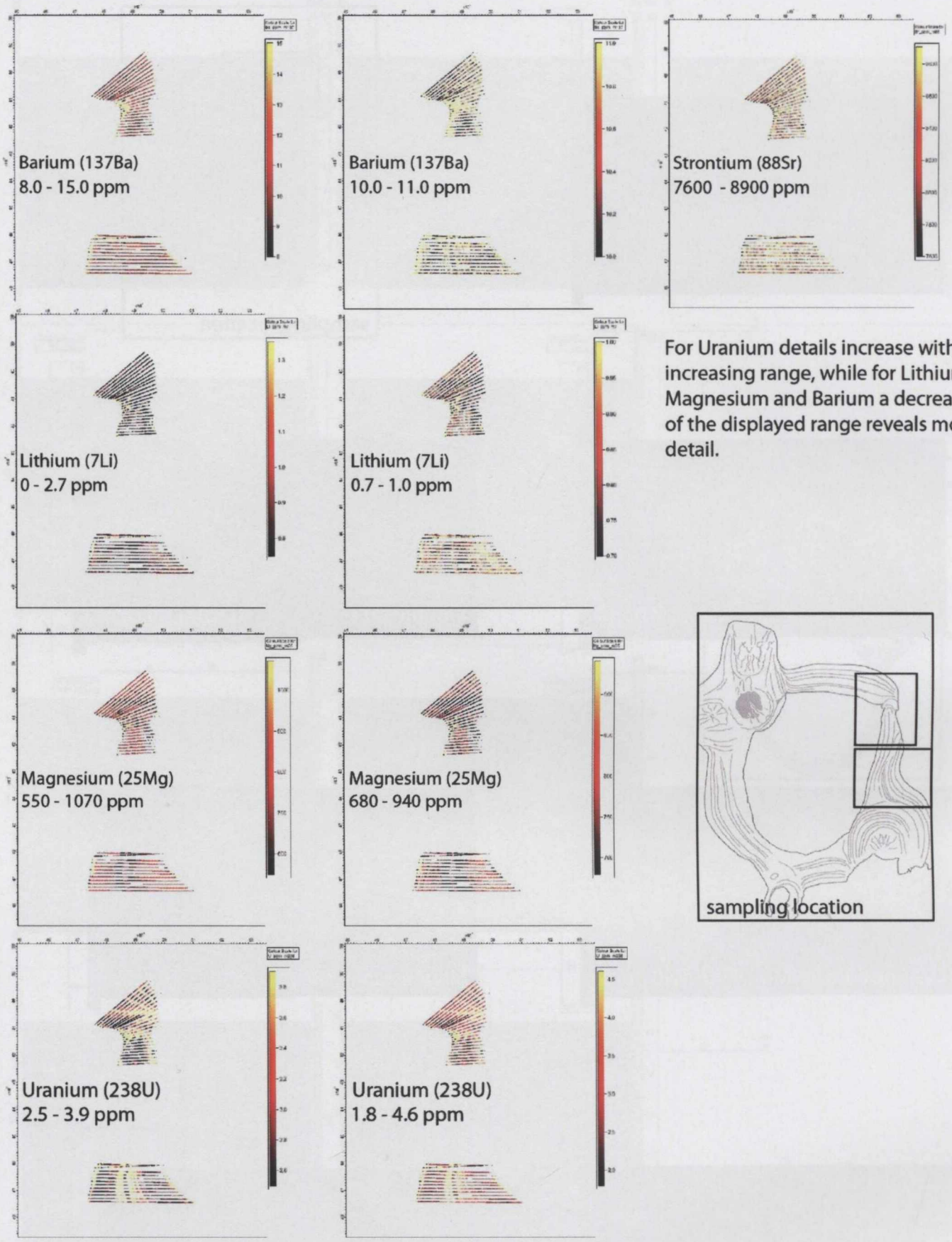
Madrepora oculata 1009-E, Porcupine Bank



For Uranium and Magnesium details increase with increasing range, while for Lithium a decrease of the displayed range reveals more detail.

Figure E.19: Cellspace images in 1009-E, part a. All ranges are originally based on the 95% confidence interval. For more details see chapter 9.

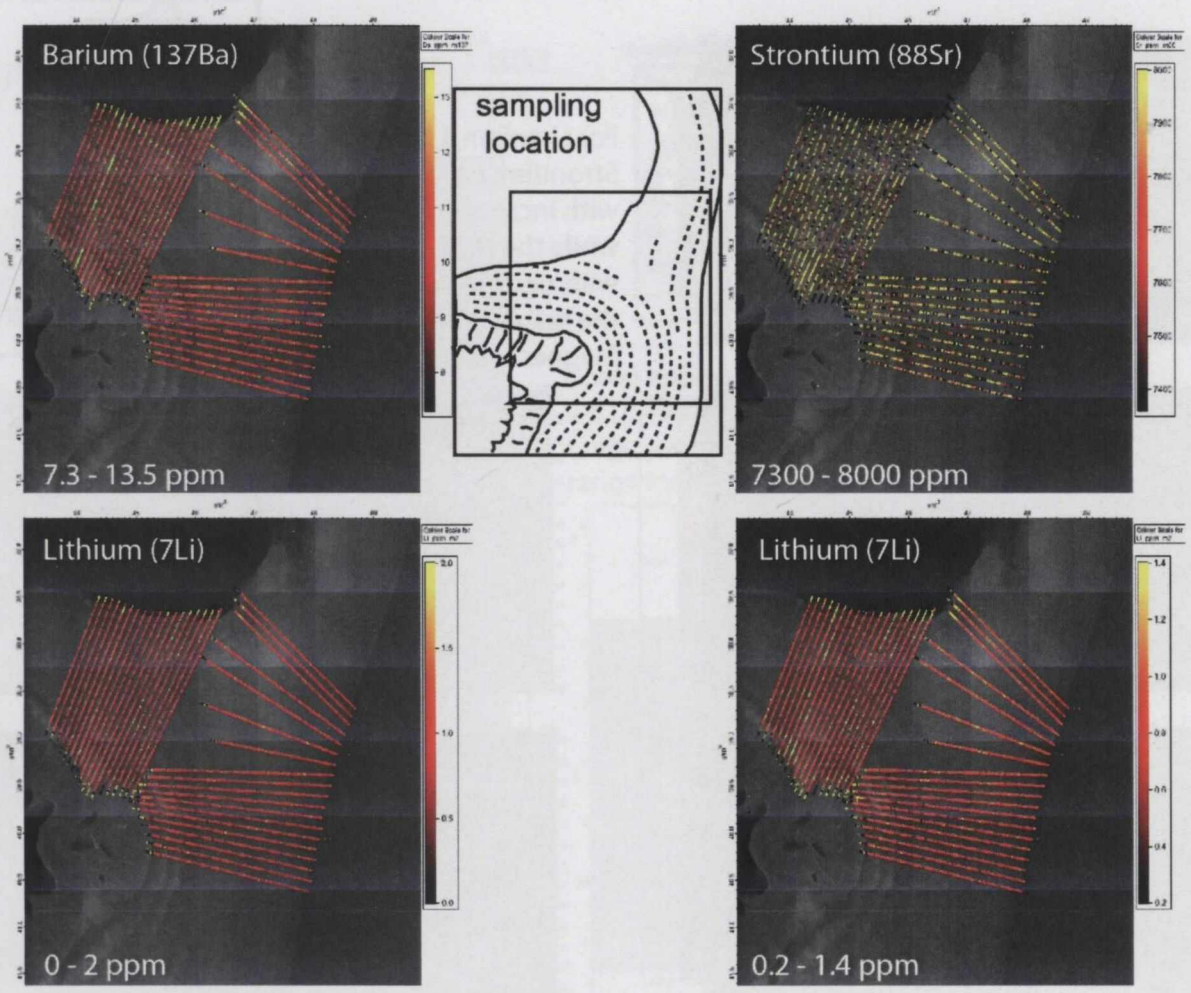
Madrepora oculata 1009-E, Porcupine Bank



For Uranium details increase with increasing range, while for Lithium, Magnesium and Barium a decrease of the displayed range reveals more detail.

Figure E.20: Cellspace images in 1009-E, part b. All ranges are originally based on the 95% confidence interval. For more details see chapter 9.

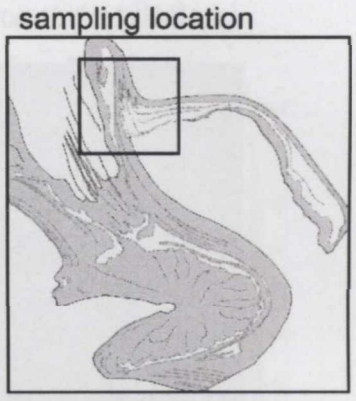
Lophelia pertusa 1033-E, Porcupine Bank

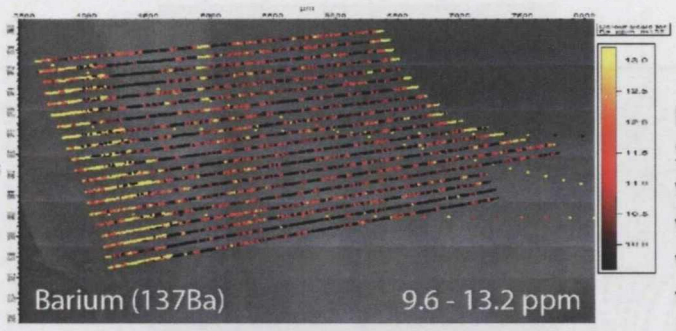


For Uranium and Magnesium details increase with increasing range, for Lithium they increase with decreasing range.

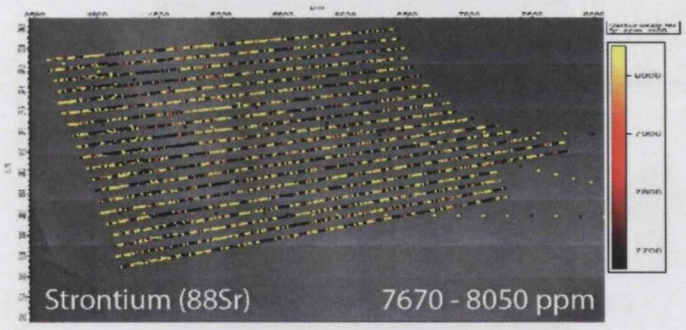
Figure E.21: Cellspace images of sample 1033-E. All ranges are originally based on the 95% confidence interval. For more details see chapter 9.

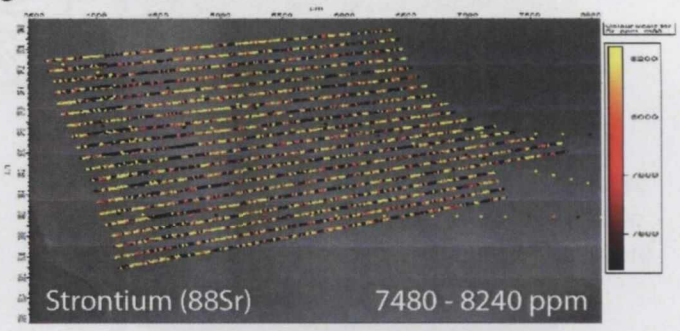
Lophelia pertusa 1036-E, Porcupine Bank

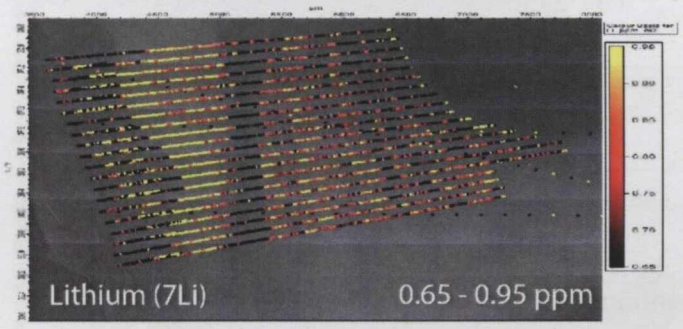


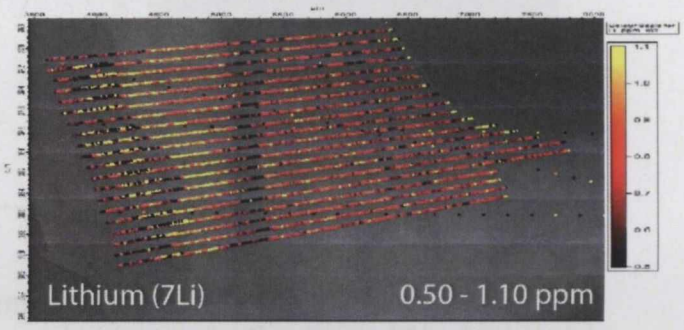


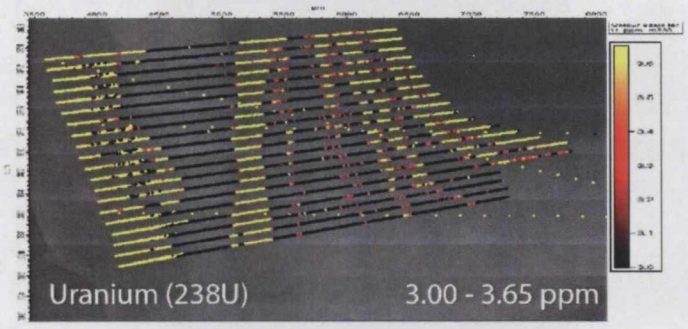
For Uranium, Lithium and Strontium details increase with increasing range, while the they increase with decreasing range for the results from Magnesium concentration











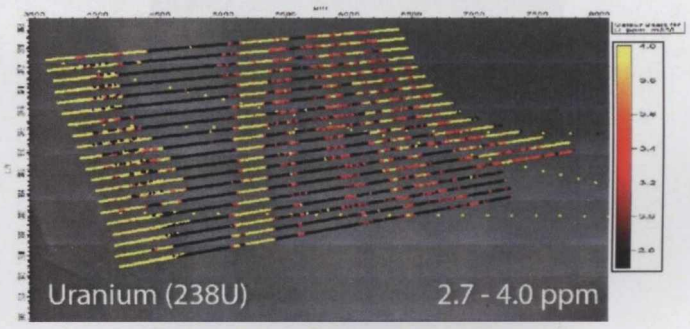
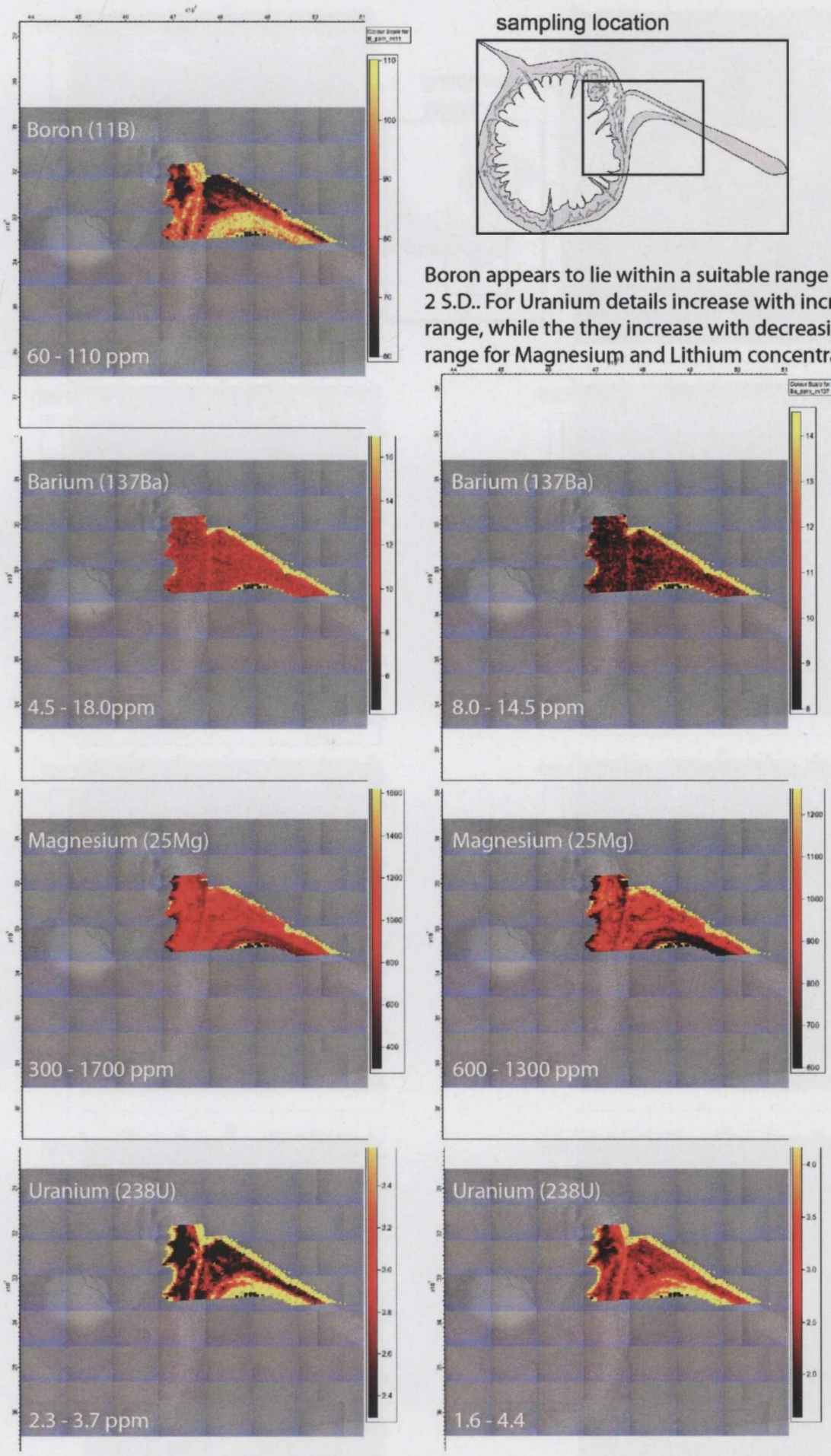


Figure E.22: Cellspace images of sample 1036-E. All ranges are originally based on the 95% confidence interval. For more details see chapter 9.

Lophelia pertusa 1447-E, Whittard Canyon



Boron appears to lie within a suitable range for 2 S.D.. For Uranium details increase with increasing range, while the they increase with decreasing range for Magnesium and Lithium concentrations.

Figure E.23: Cellspace images of sample 1447-E. All ranges are originally based on the 95% confidence interval. For more details see chapter 9.

Lophelia pertusa 1587-E, Whittard Canyon



Figure E.24: Cellspace images of sample 1587-E. All ranges are originally based on the 95% confidence interval. For more details see chapter 9.